

A Combined Theoretical- Experimental-Numerical Approach to Characterization and Modelling of Rock Fracture and Rock Burst

A Thesis Submitted for the Degree of Doctor of Philosophy

School of Civil, Environmental and Mining Engineering, the University of Adelaide



By
Rupesh Kumar Verma
June 2020

Abstract

A combined Theoretical-Experimental-Numerical Approach to Characterization and Modelling of Rock Fracture and Rock Burst

A Thesis Submitted for the Degree of Doctor of Philosophy

Rupesh Kumar Verma

School of Civil, Environmental and Mining Engineering

The University of Adelaide, June 2020.

Rock burst is a violent failure of rock in deep underground conditions, which often has severe consequences. Nevertheless, its underlying mechanism is not well understood, let alone being accurately predicted. Existing research studies do indicate the significance of strain energy storage in rock, but questions like, what material properties control strain energy characteristics? How to determine and link it with bursting? How to utilize such a framework further to unveil rock-bursting? Have always been at the center and thus formed our motivational base as well.

This research presents a systematic approach to combine theoretical, experimental, and numerical developments towards a size-dependent energy-based rockburst criterion.

Along this line, this research develops a new indirect tensile testing methodology named as ‘AUSBIT’ to control the dynamics due to excess strain energy storage in disc cracking under diametric compression. It allows capturing ‘Snap-Back’ behavior and determining inherent fracture, elastic, strength (tensile), and brittleness properties, all from one simple experiment. The devised methodology is patented in Australia as an Innovation Patent. A theoretical framework delineating the snap-back magnitude, which can be considered as a simple bursting indicator, is also developed. Advanced instrumentations such as *Digital Image Correlation* (DIC) and *Acoustic Emission* (AE) techniques are utilized to explore the benefits of controlled diametrical cracking and obtain further details on failure mechanism and its evolutions.

This thesis also develops a hybrid numerical modeling approach based on Discrete and Finite Element Methods (3DEC, by Itasca). It incorporates a new cohesive contact model with elastoplastic-damage coupling. Laboratory experiments, including uniaxial compressive strength (UCS) and conventional Brazilian disc (BD) test, are conducted

with DIC and AE applications to calibrate, validate and demonstrate the competency of the developed numerical modeling approach.

At last, this research develops a size-dependent energy-based rockburst criterion linking strength, fracture energies, and specimen size effect with stress state due to changes in boundary conditions. It results in the proposal of a bursting index (\mathbb{P}) to quantify the bursting scale. Experimental data of Bluestone rock obtained from AUSBIT and UCS tests are utilized to illustrate the capability of the proposed theoretical framework. Virtual strain-burst experiments are conducted using the developed numerical modeling approach for verification purposes. This research also provides the links between the conclusions and results from the proposed theoretical framework with the evaluation of in-situ bursting potential in rock masses around underground openings.

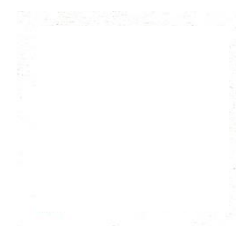
Declaration

I, Rupesh Kumar Verma, certify that this work contains no material which has been accepted for the award of any other degree or diploma in my name, in any university or other tertiary institution and, to the best of my knowledge and belief, contains no material previously published or written by another person, except where due reference has been made in the text. In addition, I certify that no part of this work will, in the future, be used in a submission in my name, for any other degree or diploma in any university or other tertiary institution without the prior approval of the University of Adelaide and where applicable, any partner institution responsible for the joint-award of this degree.

I acknowledge that copyright of published works contained within this thesis resides with the copyright holder(s) of those works.

I also give permission for the digital version of my thesis to be made available on the web, via the University's digital research repository, the Library Search and also through web search engines, unless permission has been granted by the University to restrict access for a period of time.

12th June 2020



Rupesh Kumar Verma

Acknowledgements

Foremost, I would like to express my gratitude and special thanks to my principle advisor Dr. Giang D. Nguyen for his continuous and generous support throughout my Ph.D. journey, for his immense knowledge, enthusiasm and patience. His guidance and motivation were my source of 'energy'. His insightful comments/recommendations were very helpful in my continuous improvement from the very beginning till last day of my thesis submission. His guidance, in both academic and personal life, were instrumental in handling all my ups and downs.

I would also like to express my gratitude to Dr. Murat Karakus for his knowledge, encouragement and support; Dr. Abbas Taheri for his invaluable assistance. I would also like to acknowledge the contribution of Dr. Ha H. Bui (Monash University) in the development of a generic framework for cohesive models based on damage mechanics and plasticity theory used in this study.

I would also like to have special thanks to Mr Simon Golding, Senior Technician - Labs (Processes & Controls), for his assistance in my experimentations towards the patent. Thanks, are also to all technicians, especially Mr Adam Ryntjes, Ian Ogier, Dale Hodson, and Jon Ayoub for their great support to the lab work. Support from Honours group F18G13, especially Mr Douglas Sia, in the experiments on sandstone, is also acknowledged.

The financial support from the ARC (Australian Research Council) and OZ Minerals Ltd., via Linkage Project LP150100539, as PhD scholarship for my study at the University of Adelaide is gratefully acknowledged. I would also like to acknowledge my principal supervisor, Dr. Giang D. Nguyen, and his ARC project FT140100408 for the financial assistance during my last months of my PhD study.

I greatly appreciate Dr. Sarvesh Chandra (IIT – Gandhinagar, India) and Dr. Arghya Das (IIT Kanpur, India) for introducing me to rock mechanics.

Finally, special thanks to my wife, Shaila Maheshwari for her love, support and endurance during these years of Ph.D. We both are grateful to our parents for their love and encouragement.

List of Patents

- ◆ Adelaide University Indirect Tensile Test (AUSBIT), Innovation Patent, Australia. Patent No: 2019101006. (2019).

List of Publications

- ◆ Verma, R.K., Nguyen, G.D., Karakus, M., Taheri, A., Bui, H.H. “A 3D Dis-continuum Approach to Analyze Fracture Initiation and Propagation in Hard Rocks”. (To be submitted).
- ◆ Verma, R.K., Nguyen, G.D., Karakus, M., Taheri, A., Bui, H.H. “Snap back criterion and fracture energy using lateral strain controlled Brazilian Disc test”. (To be submitted).
- ◆ Verma, R.K., Nguyen, G.D., Karakus, M., Taheri, A., Bui, H.H. “Innovative approach of controlling localized dynamics in circular disc under diametrical compression to measure uniaxial tensile strength”. (In preparation).
- ◆ Verma, R.K., Nguyen, G.D., Karakus, M., Taheri, A., Bui, H.H. “An Energy Based Strain Burst Criterion”. (In preparation).
- ◆ Verma, R.K., Pour, F.A., Dawidowski, P., Nguyen, G.D., Bui, H.H., Karakus, M., Taheri, A. (2019). “*Analyzing localization behavior of rocks using Digital Image Correlation technique*”. ICM-13 2019, 13th International Conference on the Mechanics Behavior of Material, RMIT University, Melbourne, Australia.
- ◆ Verma, R.K., Nguyen, G.D., Karakus, M., Taheri, A., Bui, H.H. (2018). “Numerical Analysis of Fracture Propagation in Brazilian Disc Test”. ACCM 2018, 3rd Australian Conference on Computational Mechanics, Deakin University, Melbourne, Australia.

Table of Contents

Abstract.....	i
Declaration.....	iii
Acknowledgements	v
List of Patents	vii
List of Publications.....	vii
List of Figures.....	V
List of Tables	XI
Chapter 1 - Introduction	1-1
1.1 Introduction	1-1
1.2 Aims and objectives of the present study.....	1-2
1.3 Outline of the thesis.....	1-7
Chapter 2 - Rock-Burst-Fracturing: State of Art	2-1
2.1 Introduction: Rock burst definition and classifications.....	2-1
2.2 Strain burst.....	2-6
2.3 Strain energy parameters evaluation: Experimental approaches	2-7
2.3.1 Rock under compression.....	2-8
2.3.2 Rock under tensile.....	2-24
2.4 Boundary conditions evaluation	2-31
2.4.1 Triaxial unloading.....	2-32
2.4.2 True-Triaxial Loading-Unloading	2-36
2.5 Numerical modeling base	2-43
2.6 Summary and discussion.....	2-47
2.7 Research aim and objectives.....	2-48

Chapter 3 - A Novel Control Method for Brazilian Disc Test to Capture the Snap Back Behavior..... 3-1

3.1 Introduction.....	3-1
3.2 Theoretical aspect: Brazilian disc test	3-2
3.2.1 Conventional (Axial strain controlled) Brazilian Disc test	3-2
3.2.2 Proposed approach: Snapback factor ($\$$) – an Energy concept.....	3-6
3.3 Proposed approach: Methodology.....	3-11
3.3.1 Testing setup	3-11
3.3.2 Technique for measuring lateral strain	3-12
3.3.3 Loading mode and strain rate determination	3-19
3.3.4 Feasibility demonstration.....	3-20
3.4 Result analysis	3-22
3.5 Benefits.....	3-29
3.5.1 Tensile strength calculation:	3-29
3.5.2 Fracture energy calculation.....	3-30
3.5.3 Fracture toughness calculation	3-30
3.5.4. Snapback factor ($\$$) calculation and validation	3-34
3.6 Discussion	3-35
3.7 Conclusion	3-36

Chapter 4 - Circular Disc under Diametrical Compression: Insights from DIC and AE based Analysis 4-1

4.1 Introduction.....	4-1
4.2 Principle: Acoustic Emission (AE) and Digital Image Correlation (DIC) techniques.....	4-3
4.3 Uncontrolled/Conventional Brazilian Disc Test.....	4-7
4.3.1 DIC validation	4-7
4.3.2 Strain Contour Evolution	4-9
4.3.3 Acoustic Emission Analysis	4-11
4.3.4 Horizontal and vertical section.....	4-13
4.3.5 Tensile strength determination.....	4-15
4.4 Lateral Strain Controlled (Conventional) Brazilian Disc Test: Sandstone.....	4-19
4.4.1 Conventional Experimental Data.....	4-20
4.4.2 Changes in global and local scale responses under servo-controlled loading	4-22
4.4.2 Tensile strength estimation.....	4-27
4.7 Conclusions.....	4-32

Chapter 5 - A 3D Dis-continuum Approach to Analyse Fracture Initiation and Propagation Mechanism in Hard Rock..... 5-1

5.1 Introduction	5-1
5.2 Dis-continuum modeling of intact rock: Numerical background.....	5-3
5.3 Crack initiation mechanism and model description.....	5-4
5.3.1 Constitutive formulation	5-6
5.3.2. Yield criterion and plastic potential	5-8
5.3.3. Model parameter determination.....	5-12
5.3.4. Stress return algorithm	5-14
5.4 Constitutive model implementation and verification.....	5-17
5.4.1 Mode-I loading (Tension)	5-18
5.4.2. Mode-2 loading (Pure shear)	5-19
5.4.3 Mixed mode loading (Shear under CNL/Shear under Tension)	5-22
5.5 Constitutive model validation	5-24
5.6 Applications: 3D numerical simulations of Uniaxial compression and Brazilian disc tests 5-27	
5.6.1 Experimental specifications	5-28
5.6.2 Numerical simulation: Uniaxial compression test	5-29
5.6.3 Numerical simulation: Brazilian disc test	5-37
5.7 Conclusions	5-40

Chapter 6 - A Size-Dependent Energy-Based Strain Burst Criterion 6-1

6.1 Introduction	6-1
6.2 An energy-based strain burst criterion	6-4
6.3 Illustration and validation: An energy-based strain burst criterion.....	6-12
6.3.1 Laboratory experiments: burst envelope and yield surface determination	6-13
6.3.2 Numerical simulations: Strain burst virtual experiments	6-17
6.4 Bursting potential quantification: Strain burst index (\mathcal{P})	6-26
6.5 Effect of material properties and confining pressure on burst potential.....	6-30
6.6 Effect of geometrical aspect on burst potential	6-31
6.6.1 Effect of aspect ratio on burst potential	6-31
6.6.2 Effect of specimen size on burst potential.....	6-34
6.7 Strain burst: the big picture	6-36
6.8 Conclusions	6-39

Chapter 7 - Conclusions and Future Work.....	7-1
7.1 Summary and Conclusions	7-1
7.1.1 AUSBIT – Adelaide University Snap Back Indirect Tensile Testing approach	7-2
7.1.2 Strength parameter determination from local-scale responses using DIC and AE techniques	7-4
7.1.3 Dis-continuum based numerical modeling development	7-5
7.1.4 A size-dependent energy-based rockburst criterion.....	7-6
7.2 Areas of improvement and recommendations for future work	7-7
References.....	1
Appendix A.....	A-1
Appendix B	B-1
Appendix C	C-1

List of Figures

Figure 2.1: Rock burst classification (a) (Tang 2000), (b) (Kaiser and Cai 2012b), (c) (He et al. 2012b), (d) (Castro et al. 2012).....	2-4
Figure 2.2: Strain burst examples: (a) (Tang 2000), (b) (Kaiser and Cai 2012b), (c) (He et al. 2012b)	2-5
Figure 2.3: Strain burst scenario	2-7
Figure 2.4: (a) Rock failure behavior classification, (b) experimental data (Hudson et al. 1971).....	2-9
Figure 2.5: (a) Relationship between E and W (Yang et al. 2018), (b) UCS complete stress-strain response (Cai 2016)	2-11
Figure 2.6: Result summary (Gong et al. 2019)	2-12
Figure 2.7: Dynamics of elastic energy transformation into post-peak rupture (Tarasov and Potvin 2013).....	2-14
Figure 2.8: Brittleness scale (Tarasov and Randolph 2011; Tarasov and Potvin 2013)..	2-16
Figure 2.9: (a) Brittleness coefficient ($K1, K2$) variation with confining pressure (Tarasov and Randolph 2011), (b) linking brittleness coefficient with aftershock activity	2-16
Figure 2.10: Relationship between rock brittleness and bursting (Feng 2018)	2-17
Figure 2.11: Synchronised load-displacement response (Verma et al. 2019b)	2-19
Figure 2.12: Synchronised load-displacement response (Verma et al. 2019b)	2-20
Figure 2.13: Synchronised load-displacement response (Dawidowski et al. 2015). ...	2-21
Figure 2.14: Synchronised load-displacement response (Tarasov and Potvin 2013)..	2-23
Figure 2.15: (a) Flake fractures, (b) sheet cleavage (Wu et al. 2010a).....	2-25
Figure 2.16: (a) Flake fractures, (b) sheet cleavage (Wu et al. 2010a).....	2-25
Figure 2.17: Rock bursting and spalling potential based on UCS and σt (Diederichs 2007)	2-26
Figure 2.18: Mobilised stress distribution (a) 0^0 , (a) 45^0 , (a) 90^0 bedding plane orientations (Aliabadian et al. 2017)	2-28
Figure 2.19: Brazilian disc tests: damage evolution (Verma et al. 2018).....	2-29
Figure 2.20: Specimen size effect (a) uniaxial tensile strength, (b) Brazilian disc test (Tomac and Gutierrez 2012).....	2-30
Figure 2.21: Energy aspect of Brazilian disc test	2-31

Figure 2.22: Stress-path (a) Displacement control, (b) Force control.....	2-32
Figure 2.23: Different loading-unloading stress paths (Feng 2018)	2-33
Figure 2.24: Time history for strain energy conversion under (a) 0.1, (b) 10 MPa/sec unloading rates. The fractured specimen in different confining pressure under (c) 0.1, (d) 10 MPa/sec unloading rates (Huang and Li 2014).....	2-34
Figure 2.25: Variation in (a) elastic strain energy, (b) dissipative strain energy with confining (Li et al. 2017).....	2-36
Figure 2.26: Change in boundary conditions (a) before, (b) after excavation	2-37
Figure 2.27: Testing setup with independent control over intermediate principle stress	2-38
Figure 2.28: Change in boundary conditions (a) before (He et al. 2010), (b) after (He et al. 2012b) excavation	2-39
Figure 2.29: True-triaxial testing results using limestone rock type (He et al. 2010).	2-40
Figure 2.30: Summary of the bursting mechanism (He et al. 2012b)	2-41
Figure 3.1: Conventional Brazilian disc test	3-3
Figure 3.2: Brazilian disc test on Hawkesbury sandstone.....	3-4
Figure 3.3: Conventional Brazilian disc test – load-displacement response.....	3-5
Figure 3.4: AUSBIT functioning	3-7
Figure 3.5: AUSBIT class-II load-displacement response.....	3-8
Figure 3.6: Variation of snapback factor with test specimen’s (a) material aspect, (b) geometrical aspect.....	3-10
Figure 3.7: Detailed overview of the testing setup.....	3-12
Figure 3.8: LVDT holder specifications (i) design details, (ii) practical applications	3-15
Figure 3.9: Strong bonding between cap and disc sample	3-16
Figure 3.10: Dust protection.....	3-17
Figure 3.11: Plasti-bond putty	3-17
Figure 3.12: Specimen and holder bonding	3-18
Figure 3.13: Finalised sample	3-18
Figure 3.14: Smooth contact between disc sample and loading plate.....	3-19
Figure 3.15: Feasibility demonstration.....	3-21
Figure 3.16: Experiment – 1: (a) Load, strain, strain energy with time, (b) load-displacement.....	3-22

Figure 3.17: Result summary (a) Iranian granite, (b) Bluestone	3-25
Figure 3.18: Result comparison – different rock types.....	3-26
Figure 3.19: (a) Evolution of ϕ and k , (b) Overall comparison	3-27
Figure 3.20: Effect of specimen dimension	3-29
Figure 3.21: Effect of mesh sensitivity on (a) poisson's ratio, (b) stiffness.....	3-32
Figure 3.22: Result summary (a) Sandstone, (b) Iranian granite, (c) Bluestone	3-33
Figure 3.23: Validation: Snapback factor	3-35
Figure 4.1: Fundamental principle behind AE and DIC functioning	4-5
Figure 4.2: DIC validation	4-8
Figure 4.3: (a) load-displacement response, (b) strain evolution DIC data.....	4-10
Figure 4.4: AE analysis: Conventional Brazilian disc test	4-11
Figure 4.5: Strain evolution in conventional Brazilian disc test: horizontal and vertical sections.....	4-13
Figure 4.6: Effect of IR size on local scale response	4-16
Figure 4.7: Conventional Brazilian disc test – local scale strain evolution.....	4-17
Figure 4.8: Cracking dynamics at local (DIC) and global (AE) scale	4-18
Figure 4.9: AUSBIT: DIC validation	4-20
Figure 4.10: AUSBIT: full-field strain evolution.	4-21
Figure 4.11: AUSBIT - sample (AE) and local scale (DIC) responses	4-24
Figure 4.12: Mechanism of servo-controlled deformation	4-27
Figure 4.13: Cracking strain determination	4-28
Figure 4.14: Effect of localized dynamics on AE energy.....	4-30
Figure 4.15: Failure envelope: tensile strength estimation	4-32
Figure 5.1:(a) Damage, (b) rough and unclean fracture surface, (c) damage-plasticity	5-5
Figure 5.2: (a) Yield surface and constitutive behavior under pure tension, compression and shear, (b) Coordinate system.....	5-10
Figure 5.3: Evolution of dilation angle with damage	5-12
Figure 5.4: Stress-return algorithm.....	5-15
Figure 5.5: (a) Yield function shrinking with damage evolution, (b) Corresponding softening in the stress-displacement plot.....	5-21

Figure 5.6: (a) Tension-Shear, (b) Compression-Shear	5-23
Figure 5.7: (a) Variation of dilation with dilation parameter (Φd), (b) variation of dilation with confinement.....	5-24
Figure 5.8: (a) sample's lower surface, (b) 3D presentation of surface (Gentier et al. 2000)	5-25
Figure 5.9: (a) 3DEC test geometry, (b) validation.....	5-27
Figure 5.10: Experimental setup	5-29
Figure 5.11: (a) UCS testing setup, (b) sensitivity analysis (i.e. block size effect)	5-30
Figure 5.12: Uniaxial compression test (a) sample scale, (b) local scale validation...	5-33
Figure 5.13: (a) Tensile stress, (b) shear stress, (c) damage	5-36
Figure 5.14: (a) Experimental observation, (b) numerical: final stage damage distribution	5-37
Figure 5.15: Conventional Brazilian disc test validation (a) Sample, (b) local scale, (c) damage evolution	5-38
Figure 6.1: (a) Initial yield surface in principle stress plane, (b) in octahedral (or π -plane) (Le et al. 2018a; Le 2019)	6-5
Figure 6.2: (a) Deep underground mine location, (b) rectangular prismatic sample, (c) strain energy in uniaxial case	6-7
Figure 6.3: Energy-based strain-burst envelope.....	6-10
Figure 6.4: (a) Uniaxial compression test, (b) AUSBIT indirect tensile strength test, (c) determination of yield surface, (d) fracture locus	6-14
Figure 6.5: (a) True-triaxial stress variations, (b) three-dimensional stress path, (c) proposed energy-based theoretical framework for burst prediction.....	6-17
Figure 6.6: Strain-burst experiments	6-19
Figure 6.7: Stress-path 1 (a) Theoretical prediction, (b) sample scale stress and strain energy evolution, (c) damage evolution, (d) rock specimen bursting, (e) burst indicator	6-22
Figure 6.8: Stress-path 2 (a) Theoretical prediction, (b) sample scale stress and energy evolution response, (c) damage evolution, (d) burst indicator	6-24
Figure 6.9: Stress-path 3 (a) Theoretical prediction, (b) sample scale stress and energy evolution response, (c) damage evolution, (d) burst indicator	6-26
Figure 6.10: Burst estimation: lateral strain-controlled UCS test (snap-back)	6-27

Figure 6.11: AUSBIT - Snap back estimation.....	6-28
Figure 6.12: Strain burst index (β)	6-29
Figure 6.13: Effect of material properties on the Burst potential	6-30
Figure 6.14: Effect of specimen dimension on burst envelope size, (b) size effect on Tianhu granite (Zhao and Cai 2015).....	6-32
Figure 6.15: Aspect ratio effect: Validation	6-33
Figure 6.16: Aspect ratio (H/B) effect along with fracture energy and peak stress.....	6-34
Figure 6.17: Effect of specimen size on the Burst potential	6-35
Figure 6.18: (a) Strain burst: Big picture, (b) theoretical link with bursting potential	6-37
Figure 6.19: Rock bolts - rockburst support system (a) (Kaiser and Cai 2012b), (b) conceptual representation	6-38

List of Tables

Table 2.1: Rock Burst Definitions	2-2
Table 3.1: Patent search result	3-1
Table 3.2: Component description	3-11
Table 3.3: LVDT holder design	3-15
Table 3.4: Input parameters	3-20
Table 3.5: Input parameters	3-34
Table 5.1: Description of cohesive model's stress return algorithm	5-16
Table 5.2: Cohesive contact model parameters	5-17
Table 5.3: Calibrated parameters	5-25
Table 5.4: Calibrated Parameters	5-31
Table 6.1: Strainburst numerical experiments	6-19

Chapter 1

Introduction

1.1 Introduction

Can contemporary human beings imagine lives without mobiles, batteries, laptops, buildings, vehicles, the internet, or household items like kitchenware, mirrors, clocks, and so forth? Probably not. These amenities are no longer seen as luxuries but as necessities for many global citizens as they organize our lives. However, they also make us dependent on minerals, many of which situate in deep undergrounds under very high in-situ pressure conditions. Complex mining processes are required to extract minerals such as copper, silver, gold, and diamonds. Such procedures could potentially induce severe instability across in-situ rocks and rock masses.

Rock burst is one of the most frequently-observed consequences of such interference in the natural geography of the land. It has been identified as a sudden and explosive failure of rock around deep underground excavations, caused by the violent release of accumulated strain energy (Durrheim et al. 1998; Durrheim 2010; Cai 2013; Zhou et al. 2016). This problem is severe in deep mines in the hard, brittle rocks often found in countries like Australia, South Africa, China, Canada, Switzerland, North, and South America (Koldas 2003; A et al. 2006; Heal 2010). Such a potential hazard raises severe concerns about workforce safety, economic drawbacks and also elevates the possibility for catastrophic disaster if it coincides with seismic events. Such incidents could be controlled or even avoided if one can reliably predict its occurrence. Nevertheless, the mechanisms controlling such hazardous phenomena are not well understood, let alone able to be predicted accurately at this point.

Whilst considerable progress has been made, researchers are still far from being accurately and reliably predict bursting events from given properties and stress conditions. Researchers have been successful in identifying types of rock-bursts and have classified them into three main categories: strain-burst, pillar-burst, and fault-slip burst (Kaiser and Cai 2012a; Zhou et al. 2016). Such events can be triggered by either static

(e.g., excavation) or dynamic (e.g., seismic activity) stress changes or by a combination of both types of events, e.g., excavation using blasting. For instance, strain-burst gets triggered by static stress changes during the excavation process. Room span (nearby stope extraction) causes pillar-burst, whilst rock mass slippages along pre-existing faults or recently-generated shear ruptures cause a fault-slip burst.

Strain-burst is among the most frequently observed rockburst type. It usually occurs in deep underground conditions, where the rock is in a deformed state due before excavation due to high in-situ stress conditions and has thus stored significant amounts of elastic strain energy. Excavation removes the confining stress and provides a free surface through which the rock can dilate, which often results in the violent release of stored strain energy, causing bursting failure of the rock surrounding underground openings. Unlike fault-slip or pillar bursts where large scale discontinuities in principle dominate the potential bursting, the behavior of rock in terms of strain energy storage and release characteristics as essential material properties is the key controlling the mechanism of burst failure inside the rock mass around underground openings (Castro et al. 2012; He et al. 2012; Kaiser and Cai 2012; Zhao and Cai 2015).

1.2 Aims and objectives of the present study

The broad aim of this research is to link the fundamental properties of rock, including strength and fracture energies, with its bursting potential. This aim has the following main objectives: (a) to identify the key material parameters that control the strain energy storage and release characteristics. After that, devise a methodology to determine the above parameters efficiently from laboratory experiments. (b) Develop a numerical modeling framework to complement the laboratory experiments and extract details of local-scale responses, which often are inaccessible in macro-scale experimental data. (c) To develop a theoretical framework that can link the energy parameters with the bursting potential of rocks. The results from the first two objectives provide a base to illustrate the reliability and efficiency of the developed theoretical framework for rock's burst potential prediction. Subsequently, this theoretical framework utilized to explain the real in-situ rock-bursting scenarios from the perspective of potential rock bursts.

An efficient way to achieve the first objective is to conduct simple experiments with full control over the dynamics associated with specimen failure. Such experiments will

enable an analysis of the rocks' intrinsic material properties, devoid of the effects of dynamic behavior, making the experiments clean and efficient. An example of such an experiment would be the lateral strain-controlled uniaxial compression (UCS) test. This experiment allows the researcher to capture potential snap-back in the post-peak regime and helps to identify instances of class-I or class-II type rock behavior (Wawersik and Fairhurst 1970; Hudson et al. 1971; Wawersik and Brace 1971; Okubo and Nishimatsu 1985; Shimizu et al. 2010). Class-II behavior demonstrates that the availability of excess strain energy at peak load and thus a qualitative indication of bursting possibility. Despite the above benefit, one can still not determine the fracture properties of rock because of the following two reasons: (a) complex stress distribution across the cylindrical sample, which often results in mixed-mode type failure; (b) difficulty in the determination of fracture surface area, which usually involves complex fracture patterns that vary with rock type and specimen dimension.

From this perspective, the conventional Brazilian Disc test is entirely appropriate. In this indirect tensile strength experiment, one compresses the circular disc-shaped specimen diametrically to cause splitting failure. Stress distribution across the sample is straightforward with tension as prime failure mode (i.e., mode-I). Fracture surface area across failed specimens is also uniform in most cases, i.e., diametrically vertical across the specimen thickness. Besides, the disc specimen is easy to prepare and economically efficient. Also, the remaining experimental setup is quite simple. Despite these advantages, applications of this experimental methodology are yet restricted to indirect tensile strength estimation only (Carneiro 1943; ISRM 1978; Tomac and Gutierrez 2012; Verma et al. 2018; Aliabadian et al. 2019a). Unlike the Uniaxial Compression, the Brazilian Disc test is highly unstable as disc samples crack in fractions of a second. Such instability in the failure mechanism is not easy to control. To the best of author's knowledge, there have been no successful attempts recorded in the literature in this direction. Overcoming this challenge is an essential part of the research in this thesis.

The above improvement in existing experimental methodology may further get benefitted from the use of advanced instrumentation such as *Digital Image Correlation* (DIC) and *Acoustic Emission* (AE). These advanced instrumentations would provide further detail on rock deformation at a scale much lower than the specimen size, which may not be feasible in conventional setups. They can also help determine the local scale strength property, which on average, is a better material representative than the one

obtained from the empirical formulation. Before that, this research requires further investigation to evaluate the effect of overall dynamics on local scale material responses. Any promising outcomes in this area will be of considerable benefit to tensile strength determination, which often demonstrates inaccuracies in the indirect testing approach if compared to Uniaxial tensile testing results (Li and Wong 2013a; Verma et al. 2018).

The other aspect of bursting potential analysis is the change in boundary conditions. During deep underground mining, rock on the excavated face undergoes unloading in minor principle stress (σ_3) direction. Consequently, the sudden release of stored strain energy causes bursting failure. In this context, the conventional rockburst experimentation methodologies available are triaxial loading and the recently developed true-triaxial loading-unloading tests (Hua and You 2001; He et al. 2010, 2012a, 2012b, 2015; Zhao et al. 2014; Du et al. 2015; Yang 2016; Li et al. 2017; Liang et al. 2017; Wang et al. 2018). Of the two, true-triaxial experimentations have been the most successful in replicating the realistic in-situ conditions up to a certain extent. However, most of such attempts are restricted to reporting the experimental data only, with little opportunity to give insight into the material's bursting potential characteristics. The reasons behind this drawback could vary from limited visual access to the specimen during rockburst experimentation, specimen size restrictions, loading constraint, and limited access to advanced experimental facilities.

With this in mind, a good alternative might be the numerical modeling approach, which can simulate rock mass under complex loading conditions in parallel with different excavation stages or methodology. It also provides details on behavior both at local and global scales, including stress/strain evolution at any location and time, and crack initiation and propagation pattern. Besides, one can acquire more statistical data by using multiple virtual experiments with varying geometrical and material parameters resulting in better conclusions on bursting potential. It also allows one to replicate the large-scale simulations of deep underground mines and obtain enough statistics of rock for further verification/validation (though this task may not be possible even in improvised laboratory experiments with advanced instrumentations).

From the above perspective, two types of numerical modeling approaches are available: Continuum and Discontinuum. Approaches in the first category assume continuity in the target domain. The influence of discontinuities is incorporated

phenomenologically up to a certain extent. However, it is not possible to entirely capture the discrete characteristics of rock material explicitly. On the other hand, approaches in the latter category assume rock to be a combination of rigid blocks commonly of circular shapes. These approaches are suitable to simulate granular material like soil (Robertson and Bolton 2001; Cheng et al. 2004; Matsushima et al. 2008; Brugada et al. 2010; Kwok and Bolton 2013). Rock is also granular; however, its material behavior is significantly different from the soil in terms of stronger inter-particle forces within the prescribed tensile or shear limit. Although, explicit imitation of rock grains is often neither feasible nor preferred due to high computational cost. Consequently, rock specimen in such simulations are often defined as a combination of grain aggregates rather than actual grains. The size of grain aggregates can further be optimized to acquire improved computational cost without compromising numerical realism.

The other aspect apart from size is the deformability of grain aggregate. Majority of Discrete Element Method (DEM) based approaches fail to incorporate this aspect. It may not influence the sample scale behavior but can undoubtedly affect the local scale response, which may not be realistic in comparison to actual rock. This aspect of the numerical model is quite essential, especially in cases where the rock specimen exposes to the loading conditions out of its calibrated data set. In this context, a hybrid (Discrete-Finite Element Method based) numerical modeling approach, i.e., 3DEC-ITASCA, could be a better alternative. The deformability of continuum elements may help to capture the local scale deformations, while inter-block contacts provide natural discreteness observed in actual rock. Therefore, the overall behavior in terms of its mechanical response and structural failure would be the collaborative effect of block deformation (i.e., idealized as grain aggregate) and inter-block contact's relative displacement. This idealization, in principle, is comparable to the actual definition of rock provided that the contact model captures the realistic intergranular (aggregates) interactions. However, this is not always the case where the available/in-built contact models are not often competent to capture complex fracture processes under different loading conditions.

In the view of the above discussion, the first objective of this research is to develop a new indirect tensile testing methodology named 'AUSBIT,' i.e., Adelaide University Snap-Back Indirect Tensile testing. It enables the control of dynamics associated with sudden cracking of disc samples under diametrical compression. It hence allows one to correctly determine the intrinsic fracture properties from a simple compression test, with

the dynamic effects excluded or minimized. It further allows the estimation of required elastic, strength (tensile), brittleness, and fracture properties, all from one simple experiment. It also enables the efficient application of advanced instrumentations such as *Digital Image Correlation* (DIC) and *Acoustic Emission* (AE) techniques to gather further details on the failure process. Overall, it makes it possible to capture the much needed 'Snap-Back' response under the indirect tensile testing framework, which in principle is related to the dynamics associated with the fracture mechanism and hence rockburst. This research also intends to develop a theoretical framework, which can delineate the snap-back magnitude and thus can act as a simple bursting indicator in compression of circular discs.

The second objective of this research is to develop a competent numerical modeling framework that can replicate the realistic rock material behavior at both sample and local scales. For this purpose, a hybrid numerical modeling approach based on Discrete and Finite Element Methods (3DEC, by Itasca) adopted after addressing the key limitations of available inter-block contact constitutive models. For this purpose, a new cohesive contact model with elastoplastic-damage coupling is developed and implemented in 3DEC-Itasca. Its operative is thoroughly verified under different loading conditions, including mode-I (or tension), mode-II (or shear) and mixed-mode, and validated against experimental data available in the literature. Laboratory experiments, including uniaxial compressive strength (UCS) and conventional Brazilian disc (BD) tests, are also conducted in collaboration with DIC and AE instrumentations. Experimental data obtained will be further utilized to calibrate, validate, and demonstrate the competency of the developed numerical modeling approach.

The final objective of this research is to perform an in-depth analysis of the burst potential of rock using previously developed numerical and experimental basis. For this purpose, this research develops a size-dependent energy-based theoretical framework that can unveil the bursting potential of rock under polyaxial loading-unloading conditions. It considers the strength, fracture energies, and effect of specimen size in addition to stress conditions, with the Bluestone rock type as an example for illustration. Experimental data from previous steps, including AUSBIT and UCS testings, are utilized in the proposed theoretical framework to make burst predictions for the given rock. For verification of the theoretical bursting criterion, the developed numerical modeling suit used to conduct virtual strain burst experiments. This research also provides the links between the

proposed theoretical framework and the actual in-situ bursting of rock in rock mass around underground openings.

In summary, this research presents a systematic approach to combine theoretical, experimental, and numerical developments with the eventual goal to develop a size-dependent energy-based rockburst criterion that can not only predict but also illustrate the bursting possibility in any given rock sample.

1.3 Outline of the thesis

The thesis contains seven chapters, including the current one, which serves as an introduction delineating the scope and aims of this study. The brief outline for the successive chapter's content is as follows.

Chapter-2 presents the detailed literature review of rockburst analysis and research gaps, highlighting the limitations of the existing methodologies and approaches. It demonstrates the relevance of energy-based approach over conventional stress-strain based methodologies to evaluate failure mechanism and eventual bursting potential in rock. This chapter also highlights the critical material parameters which control the rock's energy evolution characteristics and existing experimental methodologies (along with associated limitations) to obtain such parameters. The significance of numerical modeling approaches to assess the rock's bursting potential is also analyzed.

Chapter 3 presents the development of a new experimental methodology that can systematically control the disc sample cracking under diametrical compressive loading. The proposed experimental approach enables us to capture the required material properties controlling strain energy storing and dissipation characteristics, i.e., tensile strength, elastic properties, fracture energy/toughness, and material brittleness, all from a single test using simple circular disc sample. This chapter also presents an energy-based Snap-back criterion for circular disc under compression, which provides a preliminary overview of the rock's bursting potential.

Chapter 4 presents the detailed analysis of results obtained from advanced experimental approaches used in this study, i.e., DIC and AE, using AUSBIT and conventional (i.e., axial displacement controlled) Brazilian disc tests. The prime focus here is to provide quantifiable insights into rock's local scale properties. This chapter also

highlights the significance of local-scale dynamics affecting the applications of advanced experimentation techniques. The estimation of uniaxial tensile strength is an essential outcome of this analysis. The correlation between local-scale dynamics with sample scale AE data is also presented.

Chapter-5 presents a brief outline for the dis-continuum based numerical modeling approach, i.e., 3DEC-ITASCA, followed by a detailed description of the new cohesive contact model based on the elastoplastic-damage coupling. Further, this contact model verified under different loading conditions, including mode-I (tension), mode-II (shear), and mixed-mode at the constitutive level. After that, this contact model is implemented in 3DEC and further validated as a user-defined joint model with experimental data available in the literature review. Numerical simulation of UCS and BD test followed by rigorous validation involving behavior and features at both macro (specimen) and smaller (fracture process zone; FPZ) scales, e.g., double scale validation, are performed to ensure the competency of developed numerical modeling suit.

Chapter 6 presents the development of a size-dependent energy-based theoretical framework to evaluate the bursting potential of rock under polyaxial loading-unloading conditions. This framework incorporates the effects of strength, fracture energies, specimen size, and stress conditions. It uses the Bluestone rock test from AUSBIT, and UCS experiments make a theoretical prediction for the strain burst. The developed numerical modeling approach in Chapter 5 utilized to conduct virtual strain burst experiments for the verification of the theoretical predictions. At last, this chapter discusses the links between illustrations and conclusions from the proposed theoretical framework with the actual in-situ bursting in rock in rock mass around underground openings.

Chapter 7 concludes the study and suggests prospective research directions for future studies.

Chapter 2

Rock-Burst-Fracturing: State of Art

2.1 Introduction: Rock burst definition and classifications

Deep underground exploration has always been among the most daring pursuits of humankind. It forms an integral part of our socioeconomic measures in that we endeavor to extract additional minerals from deep underground mines or intend to construct tunnels for technical advancement as well as expansion. Under such arrangements, we are often exposed to the unexpected, making underground exploration challenging and intimidating. Rock burst is among such deadliest events.

'Rock burst' is an umbrella term used for a wide range of rock and rock mass failure around deep underground openings like mines, tunnels, caverns, and shafts. Sudden and violent expulsion of rock around underground openings after the excavation is a common trait. The phenomenon behind this violent rock failure is quite complex. Many researchers have attempted to describe this occurrence and have proposed different definitions. For instance, Blake (1972) describes rock burst as "*a sudden form of rock failure characterized by the breaking up and expulsion of rock from its surroundings accompanied by a violent release of energy*" (Blake 1972). Ortlepp (2005) summarised rock-burst using 'cause' and 'effect' terminology as opposed to an association with a seismic event defined as "*transient energy released by a sudden fracture or failure in the rock mass which results in the emission of a seismic vibration transmitted through the rock.*" Here latter defines as "*the significant damage caused to underground excavations by a seismic event*" (Ortlepp 2005). He.et.al. (2012) termed rock-burst as an explosion of a block causing a sudden rupture in the rock, which is quite common in deep underground openings (He et al. 2012b). Similarly, many other definitions of rockburst have been proposed by researchers over time, briefly summarised in table 1. Among all such definitions, one can find the following notion of failure description in-common: violent failure of rock due to sudden energy release, as underlined in table 2.1 as well. From this, we can highlight 'energy' as its conceptual basis, whereas 'violent' as its qualitative aspect.

Table 2.1: Rock Burst Definitions

Researchers	Definition
(Cook 1965)	An <u>uncontrolled</u> and <u>violent disruption</u> in rock followed with the violent release of <u>energy</u>
(Blake 1972)	a sudden form of rock failure characterized by the breaking up and expulsion of rock from its surroundings accompanied by a <u>violent release of energy</u>
(Tao 1988a)	Mechanical disturbance due to <u>significant strain energy release</u> causing <u>violent fracturing</u>
(Gill et al. 1993)	<u>Sudden rock failure</u> characterized by breaking and expulsion of rock with <u>violent energy release</u>
(Singh and Goel 1999)	<u>Violent class-II</u> failure of rock when subjected to <u>high stresses</u>
(He et al. 2007)	The phenomenon of non-linear dynamics causing <u>sudden energy release</u> along the <u>free surface of excavated rock</u>
(Dietz et al. 2018)	<u>Sudden and violent collapse</u> of rock in <u>highly stresses</u> underground cave

The available literature records several such examples that illustrate this qualitative aspect of rockburst failure. For instance, 28 out of 42 coal mines in central Europe were reported to be endangered by rockburst problems, which resulted in 190 such events over the past 20 years, causing more than 122 fatalities. Energy magnitude documented during these events was massive up to 10^{10} Joule (Goodman 1989; Mutke and Stec 1997; Ortlepp 2005). In South Africa, gold mines of great stature faced several rockburst incidents accompanied by a significant loss in lives. Whyatt et al. (2002) reported the demise of 37 miners in 2003 alone (Whyatt et al. 2002). In Australia, Kalgoorlie district has been experiencing rockburst since the early 20th century. Various mines in the Western Australia region, for example, Mount Charlotte, Darlot and Kanowna Belle, not only trigger seismic events but are also unsafe for miners (Heal 2010). Similarly, Kolar Gold Field in Mysore, India, has long been known as a region of severe rockburst (Malliga 2015). All such accidents reported in the literature indicate significant losses in life and resources.

Therefore, it becomes imperative to understand the mechanism of rockburst and work towards minimizing its hazardous impact. Available literature presents pieces of research that provide insight into rockburst's functioning and characteristic traits, which eventually form the basis of developing several rockburst classification systems. For instance,

Ortlepp (1994) describes rockburst as an energy driven seismic event and utilized source mechanism to classify it into five main categories: strain bursting, buckling, face crushing, shear rupture, and fault-slip burst (Ortlepp and Stacey 1994). Tang (2000) classifies rock-burst in three categories: strain burst, fault-slip burst, and a combination of both (Tang 2000). He categorically highlighted in his work that the majority of rockburst in deep hard rock mines is of the strain-burst type, which includes bursting because of the mine opening abutments and pillars, as shown in figure 2.1(a). Whereas, figure 2.1(b) shows the severity of rock damage based on the rockburst classification system which utilizes failure depth to categorize rock burst into minor, moderate and severe if the depth of failure is smaller than 0.25 m, higher than 0.75 m and 1.25m (Kaiser and Cai 2012b).

He et al. (2012) classifies rock burst into strain burst and impact-induced burst, as shown in figure 2.1(c) (He et al. 2012b). This work defines strain burst as a self-induced bursting type where rock surrounding underground opening fails violently due to sudden release of stored strain energy. He further classifies strain burst into the tunnel (or mining) and pillar bursts. Two sub-categories relate to instantaneous and delayed burst depending upon the bursting time after excavation. Instantaneous burst, as the word suggests, occurs instantaneously after excavation due to sudden release of excess stored strain energy. The delayed burst occurs eventually due to a timely increase in tangential stress around an opening after excavation. Pillar burst induces by pressure increase on the underground mine pillars due to an increased rate of excavation. In short, the prime difference between these burst types is the corresponding stress-paths, which vary depending upon differences in the in-situ excavation methodologies. On the other hand, impact-induced rock burst occurs due to the impact of disturbance waves generated by in-situ mining activities or shearing of distinct geological features like dikes or faults. This impact can be induced by artificial sources like in-situ blasting or by roof collapse.

In recent times, Castro et al. (2012) classified rock-burst in: strain burst, pillar burst, and fault slip burst categories, as shown in figure 2.1(d) (Castro et al. 2012). This rockburst classification is quite generalized and agrees with several other classification suggestions (He et al. 2012; Kaiser and Cai 2012). In this classification system, the mechanism of strain burst differs from pillar burst depending upon the burst locations and stress paths. High in-situ stress concentration is the only attribute common-in between

both burst types. On the other hand, slippage along geometrical dis-continuities or any other pre-existing faults are the prime mechanisms for causing fault slip burst.

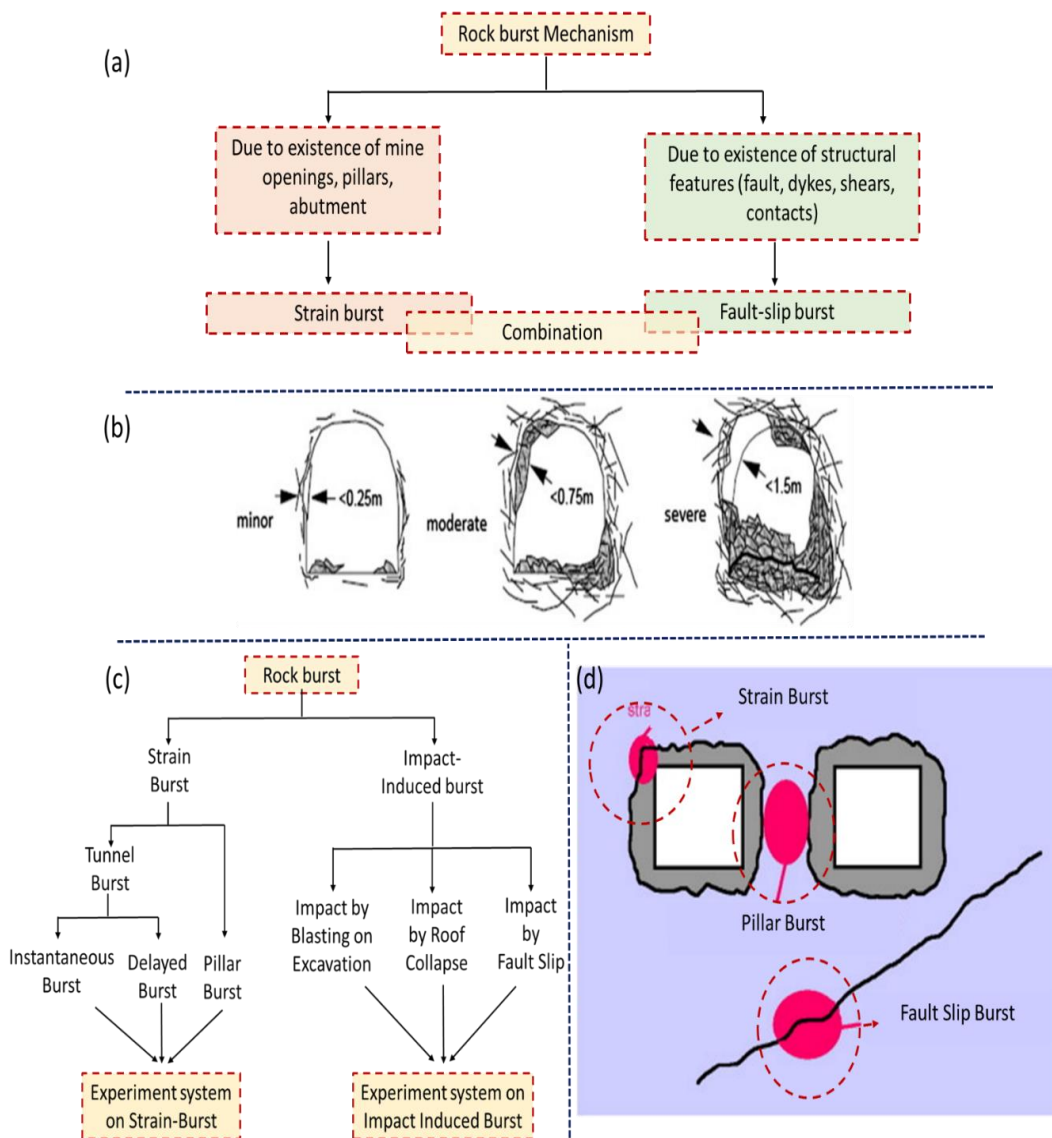


Figure 2.1: Rock burst classification (a) (Tang 2000), (b) (Kaiser and Cai 2012b), (c) (He et al. 2012b), (d) (Castro et al. 2012)

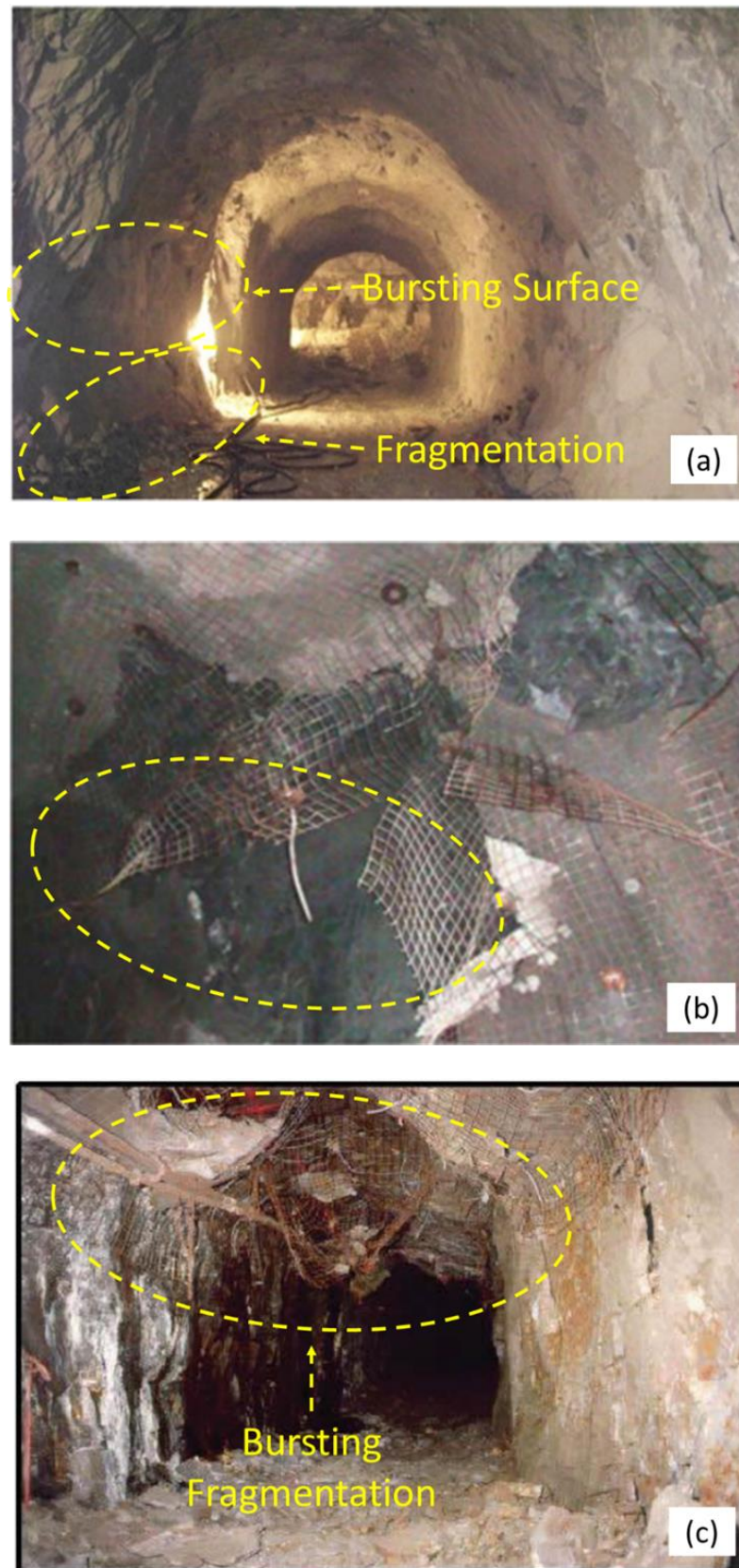


Figure 2.2: Strain burst examples: (a) (Tang 2000), (b) (Kaiser and Cai 2012b), (c) (He et al. 2012b)

Strain burst is the most common and feared rockburst type observed during deep underground excavations (Kaiser and Cai 2012; Feng et al. 2012; Zhang et al. 2012; He et al. 2015; Li et al. 2012; Zhao and Cai 2015). Figure 2.2 presents a few examples of strain burst incidents recorded in the available literature. One can observe here that each strain burst incident observes significant fragmentation, which can be severely detrimental if proper safety measures are not in place, as shown in figure 2.2(b), (c). A practical example highlighting the importance of essential safety measures is the construction of Jinping II hydropower station in China, where several intense strain burst incidents reportedly killed several workers and damaged construction equipment setups (Li et al. 2012). Given the above discussion, this study agrees with the fact that working towards reducing the impact of rockburst, especially strain burst, is quite essential and relevant.

2.2 Strain burst

Strain burst is a self-induced bursting mechanism where rock around the periphery of an underground opening fails violently into fragments due to excess strain energy release. This entire bursting mechanism has two prime aspects: bursting potential of rock and rock mass engineering. The latter refers to the full field evaluation integrating in-situ geotechnical and geological aspects, including joints/discontinuities characterization, in field porosity and water flow, in-situ stress, rock layer distribution, and other in-situ conditions. The former indicates the rock's potential to burst under certain loading-unloading conditions. If any rock does not have the potential to burst, then the possibility of rock mass bursting will also be negligible or small. From this perspective, it is essential to dissect the rock material first to evaluate its bursting capability.

In this view, figure 2.3 presents a conceptual image of in-situ rock conditions inside rock mass (excluding specific detailing on rock mass) to provide a preliminary overview of the key factors affecting its bursting tendency.

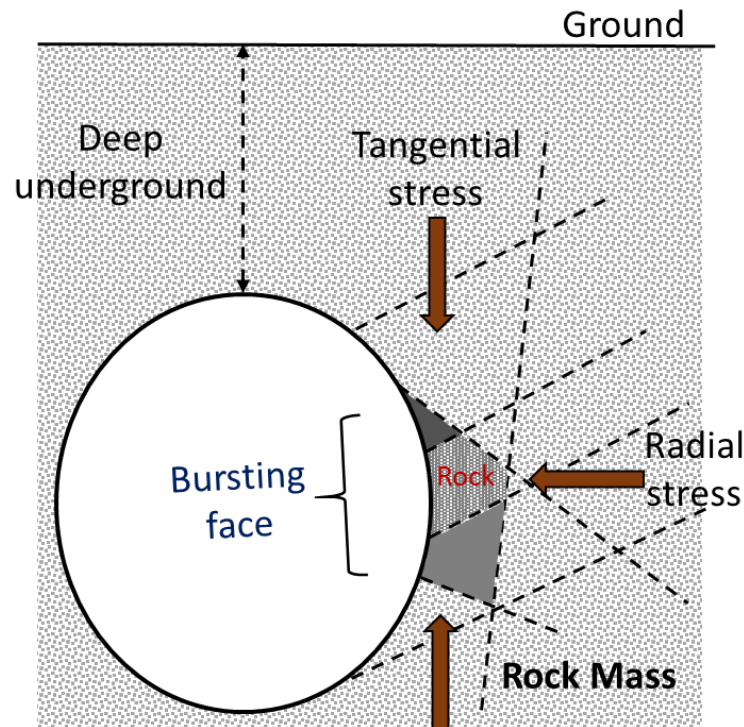


Figure 2.3: Strain burst scenario

As shown in figure 2.3, deep underground is in a high-stress state. As excavation happens, the in-situ rock gets free room to dilate. Consequently, strain energy stored inside the rock releases abruptly to cause bursting. This preliminary overview highlights the significance of the following three factors, which, in principle, controls the overall strain burst tendency: high overburden stress, rock material properties, and boundary condition changes. Rock material properties, especially in terms of strain energy storing and releasing characteristics, are of prime importance.

2.3 Strain energy parameters evaluation: Experimental approaches

Experiments that test rock under simple compression and tension would play an essential role in determining strain energy controlling rock material properties provided that one can acquire proper control over the specimen fracturing process. Subsequent subsection elaborates on this aspect and presents a detailed review of relevant experimental approaches, its applications, and critical research gaps. These research gaps will eventually form the basis of this study further to gain insight into the bursting potential of rocks.

2.3.1 Rock under compression

The uniaxial compressive strength test is a simple experiment which, along with its load-displacement response, has the potential to provide insight into the rock's strain energy storing and releasing characteristics. The pre-peak regime of this load-displacement response helps to estimate the uniaxial compressive strength (UCS) and elastic properties (i.e., Young's modulus, Poison's ratio) of rock. These material properties characterize the strain energy-storing aspect, which further provides an approximation of strain energy density whereas the post-peak response helps in the manifestation of rock's energy dissipation characteristics and provides an excellent insight into brittleness/ductility property (Goodman 1989; Harrison and Hudson 2000; Ramamurthy 2007; Piratheepan et al. 2012). Therefore, it is essential to acquire the complete load-displacement response, which could often be difficult, depending upon the stiffness of the loading frame, i.e., experimental setup, and the type of rock under consideration.

To control the effect of the former aspect (i.e., stiffness of experimental setup), infinitely stiff loading frames have been developed. Unlike the soft testing machines, these experimental setups do not store additional energy, thus nullifying the contribution of energy release from the testing frame during sample failure (Hudson et al. 1972b; Xu and Cai 2017). The other source (i.e., rock type), especially in case of hard rock where test sample stores much higher strain energy than its failure requirement, makes the process of acquiring complete load-displacement challenging. Consequently, researchers developed the servo-control mechanism inbuilt in the loading frame to optimize the axial loading rate on the cylindrical sample under the uniaxial compression (Xu and Cai 2017). It made it possible to acquire a complete load-displacement response with 'Snap-Back' characteristics, especially in case of hard rocks, as shown in figure 2.4(a) (Hudson et al. 1971).

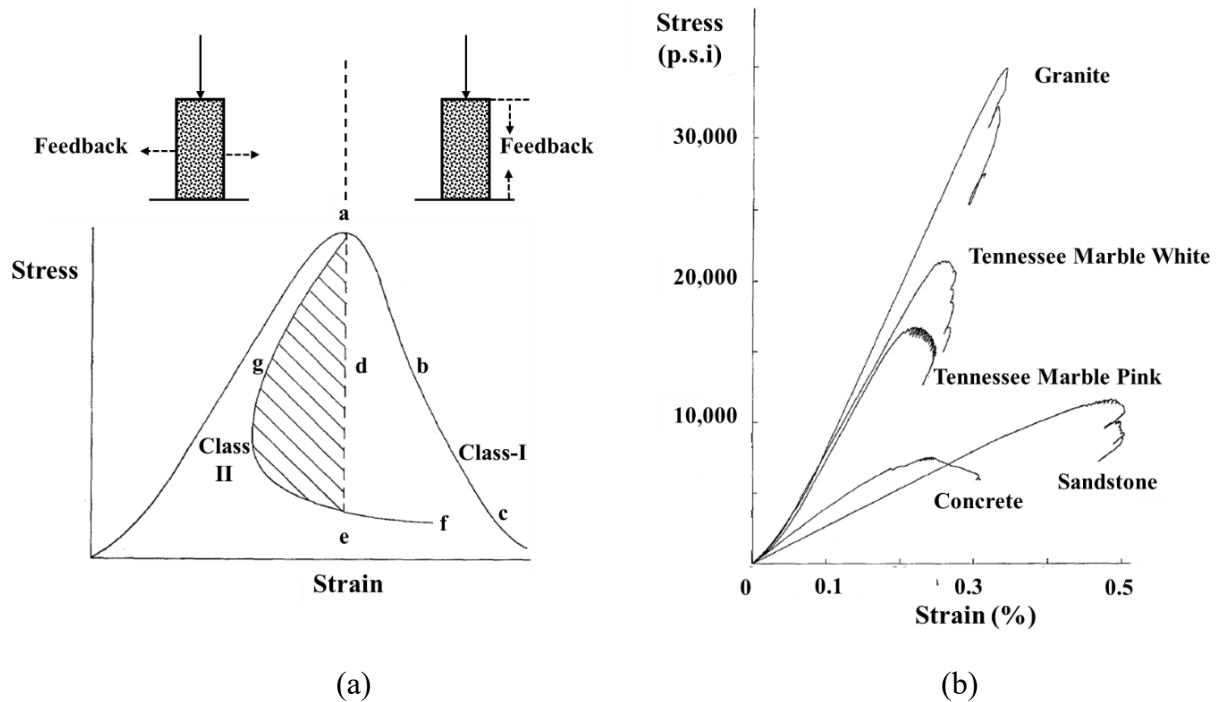


Figure 2.4: (a) Rock failure behavior classification, (b) experimental data (Hudson et al. 1971)

Overall, one can classify the load-displacement responses from different rock types into the following two categories: class-I and class-II. In class-I response, the rock sample requires uninterrupted external work via continuous downward movement of loading platen to sustain stable structural failure. It implies that the total strain energy stored at peak loading point 'a' in figure 2.4(a) is not enough to continue the stable cracking, thus requiring additional energy to further the sample failure and follow the path 'abc.' This response indicates the conventional displacement control loading approach, where feedback from the axial component of the volumetric expansion controls the overall vertical loading rate. Here, the testing approach maintains a constant axial strain rate as per the quasi-static loading requirement throughout the test. Such responses are commonly observed in weak rock types like sandstone or comparatively less brittle material types like concrete, as shown in figure 2.4(b) (Hudson et al. 1971).

On the other hand, the class-II response indicates the availability of strain energy excess to the sample's cracking requirement at the peak loading stage. Consequently, further work done by the external loading platen will supply additional energy, which makes the entire sample structure unstable resulting in uncontrolled failure, shown as an 'ade' path in figure 2.4(a). It causes a sudden drop in post-peak response. Such load-displacement response obtained from uncontrolled specimen failure may not reveal the

actual material characteristics. One solution suggested for this problem is to withdraw the additional energy component systematically inducing the 'snap-back' characteristic, shown as 'agef' in figure 2.4(a). It requires efficient utilization of a sensitive indicator of material degradation via a servo-controlled mechanism to continuously adjust the external loading rate throughout the load-displacement response (Rummel and Fairhurst 1970; Hudson et al. 1971).

In this view, volumetric expansion can be exceptionally sensitive to microstructural cracking. However, it is not a monotonically increasing parameter and thus cannot be used as mechanical feedback to control the overall axial compressive loading rate (Wawersik and Fairhurst 1970; Hudson et al. 1971). Further, unlike class-I response, additional energy available at peak loading stage in class-II type rock makes the axial component of overall volumetric expansion comparatively less sensitive to the onset of cracking. Thus it could also not be used. On these grounds, lateral component (circumferential strain) of volumetric expansion provides an efficient alternative that is not only sensitive to crack initiation but also exhibits monotonic increments even if the axial component is comparatively in an insensitive state. As a result, a lateral strain-controlled uniaxial compression test assigns a constant circumferential displacement rate to control the overall axial compressive loading. It enables to self-adjust the overall axial loading rate with increasing specimen damage. It allows the automatic control over the entire fracturing process, starting from initial loading to final bearing capacity, thus determining the complete load-displacement response. Available researches in literature review demonstrate the feasibility of such control on a wide variety of rock types, with a few examples shown in figure 2.4(b) and others (Wawersik and Fairhurst 1970; Hudson et al. 1971; Wawersik and Brace 1971; Okubo and Nishimatsu 1985).

2.3.1.1 Strain energy characteristics

The above developments facilitated various approaches to analyzing the bursting potential of rock explicitly based on its response under uniaxial compressive loading conditions. Majorities of these applications in the past aimed to develop an empirical criterion for burst prediction. For instance, uniaxial compressive strength was first used in coal mines in Poland as a coal burst propensity index (Czeczenska and Zuo 1986; Yang et al. 2018) using explicit empirical relation between elastic energy and uniaxial compressive strength as shown in figure 2.5(a). Qiao and Tian (1998) used elastic strain

energy stored at the peak loading stage under uniaxial compression of rock as a judging index to predict the rock-burst possibility (Qiao and Tian 1998). They adopted the linear theory of elasticity to compute the elastic energy (W) as follows:

$$W = \frac{\sigma^2}{2E_s} \quad (2.1)$$

Here, σ is the peak stress under uniaxial compression and E_s is the unloading secant modulus. Similarly, several researchers utilize the uniaxial compression test to define the burst energy coefficient/index (K_e) as the ratio of strain energy consumed in pre-peak (W_e) and post-peak (W_p) regime (Goodman 1989; Li et al. 1999; Cai 2016; Yang et al. 2018), as shown in figure 2.5(b).

$$K_e = \frac{W_e}{W_p} \quad (2.2)$$

Higher pre-peak energy components, in comparison with post-peak, will result in a higher coefficient indicating higher bursting potential. Cai (2016) utilized these criteria to analyze the rockburst tendency in Sanshandao gold mine, China (Cai 2016).

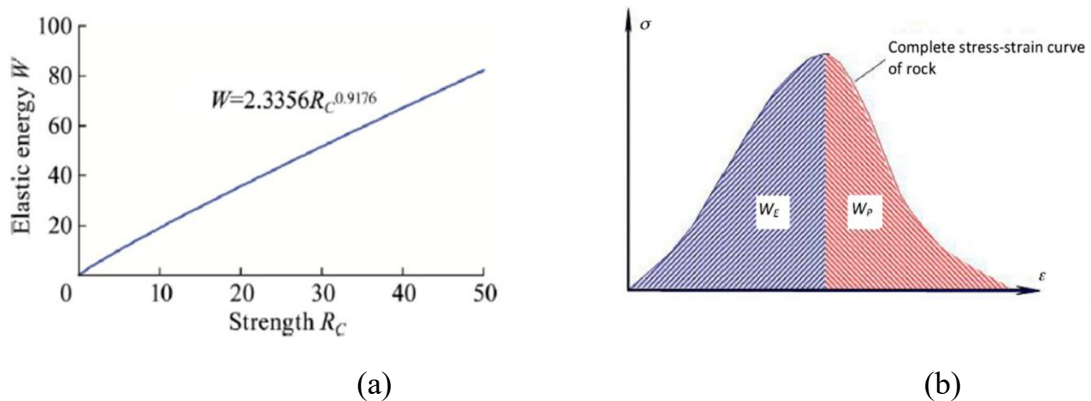


Figure 2.5: (a) Relationship between E and W (Yang et al. 2018), (b) UCS complete stress-strain response (Cai 2016)

Similarly, elastic strain energy index or burst proneness index (W_{et}) was also developed and used to analyze the rockburst potential (Kidybinski 1981; Singh 1988; Yang et al. 2018; Gong et al. 2019). This index is defined as the ratio of elastic strain energy density (u_e) to the in-elastic/dissipated strain energy density (u_d) when stress reaches 80-90% of its compressive strength under uniaxial compressive loading conditions, as shown in figure 2.6(a). The computation is as follows where u is the total strain energy:

$$u = \int_0^{\varepsilon_u} f(\varepsilon) d\varepsilon \quad (2.3)$$

$$u_e = \int_{\varepsilon_0}^{\varepsilon_u} f_1(\varepsilon) d\varepsilon \quad (2.4)$$

$$u_d = u - u_e \quad (2.5)$$

The loading and unloading curvilinear function demonstrates the total strain at peak load and the residual/permanent strain after unloading (Singh 1988; Gong et al. 2019).

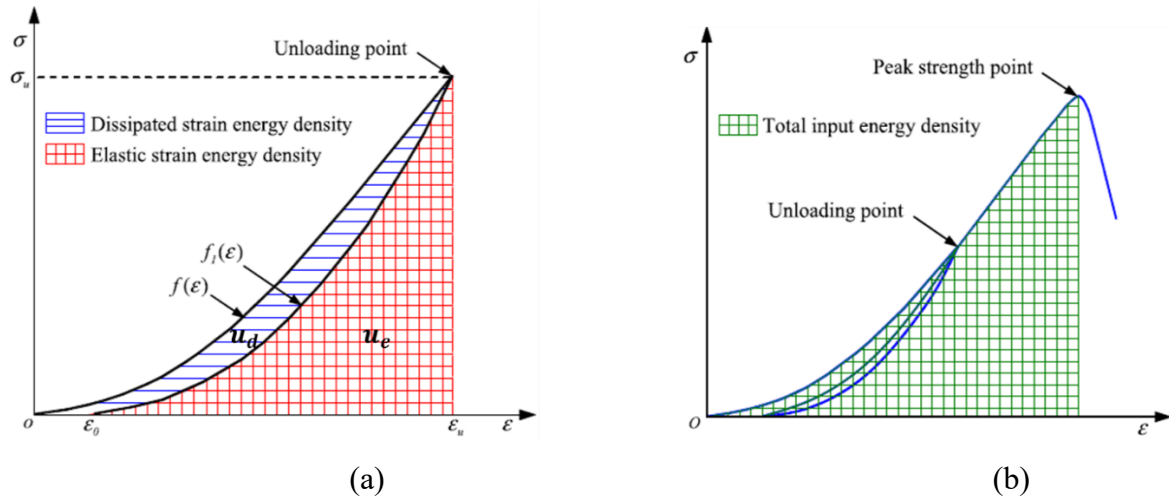


Figure 2.6: Result summary (Gong et al. 2019)

Ideally, one should define the coefficient (K_e) at peak loading stage, i.e., at compressive strength. However, the inherent heterogeneity in rock induces stochastic nature to peak load magnitude. Thus, it may not be possible to predict the peak compressive load precisely beforehand. Recently, Gong et al. (2019) attempted to address this issue by conducting a series of loading-unloading cycles in the pre-peak regime under uniaxial compression, i.e., figure 2.6(b) (Gong et al. 2019). This attempt proposed an empirical relationship between the peak loading stage and the loading-unloading response in the pre-peak regime. It made it possible to estimate the dissipated and elastic strain energy magnitudes at the peak loading stage, thus enabling the determination of K_e in a relatively precise manner. Besides, many approaches are already available, which utilize empirical relationships linking UCS directly with bursting potential (Hoek and Brown 1980; Tao 1988; Hou 1989; Wang et al. 2009; Mitri 2007). One can observe here that the prime focus of all the above approaches is to evaluate the strain energy storing capacity of rock under uniaxial compression and link it with its bursting potential. The contribution of energy dissipation characteristics is either subtle or not considered at all.

2.3.1.2 Brittleness index: Strain energy-releasing characteristics

Unlike the previous, several researchers did attempt to evaluate the post-peak characteristics of rock and consider it as a factor contributing to burst magnitude. From the perception of deformation, the post-peak response broadly provides the following critical macroscopic sample characteristics: ductility (or tenacity) and brittleness. Ductility indicates rock sample rupture after large deformation. Here, test specimen integrities and continuities sustain for a longer duration after reaching peak load accompanying gradual strength reduction, resulting in large post-peak deformation (Cook 1963). Conversely, brittleness reflects fracture without any evident or negligible deformation. The rock material loses its integrity immediately after reaching the peak load to induce instant dis-continuity at the local and global scale, complemented with a sudden drop in the sample's load-carrying capacity. Such phenomena of rock characteristics have conceptual similarities with the mechanism behind the instant release of stored energy during strain-burst in hard and brittle rocks.

Researchers made numerous attempts to quantify the rock brittleness via brittleness indexes using the uniaxial compression test and linking it with the rockburst mechanism (Aubertin et al. 1994; Zhang et al. 2003; Mitri 2007; Tarasov and Randolph 2011). Despite the absence of consensus among all such developed indexes, few approaches do provide a good base to quantify the degree of instability in brittle and hard rocks. For instance, Tarasov (2010, 2011, 2012) utilised the post-peak energy-balance approach to characterise the rock brittleness under compression (Tarasov and Randolph 2011; Tarasov 2012; Tarasov and Potvin 2012, 2013). The focus of these approaches is to analyze the intrinsic brittleness solely based on the stored elastic energy within the compressed material. Consequently, these approaches utilize the complete stress-strain response of different rock types under compression. These attempts were in line with the well-established notion of utilizing the negative or positive post-peak modulus ($M = \frac{d\sigma}{d\varepsilon}$) to characterize material brittleness. Figure 2.7 below presents a brief illustration of this proposed approach where σ is the differential stress (i.e. $\sigma_1 - \sigma_3$) while ε is an axial strain.

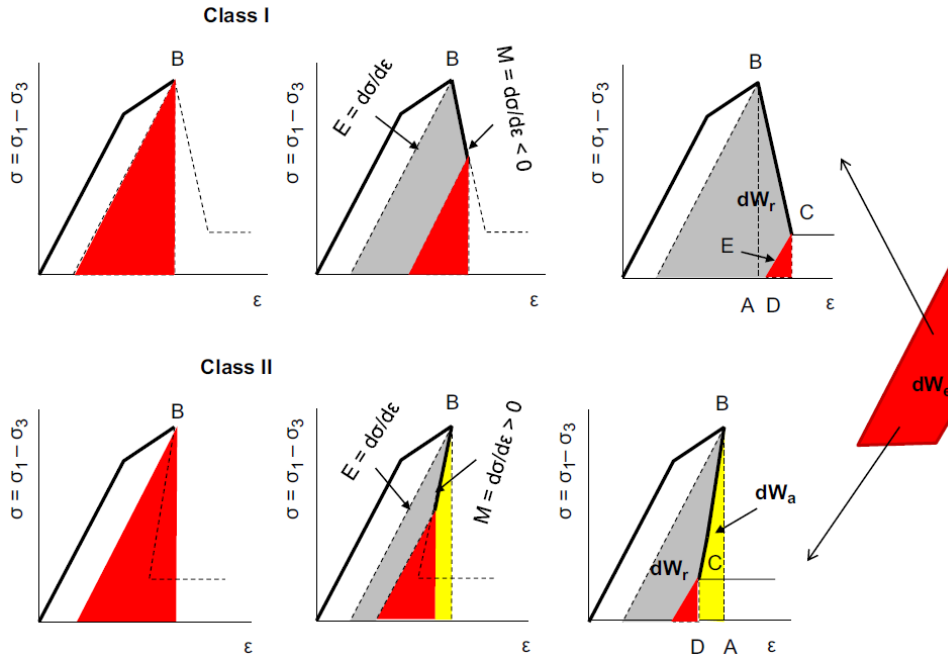


Figure 2.7: Dynamics of elastic energy transformation into post-peak rupture (Tarasov and Potvin 2013)

Figure 2.7 demonstrates energy balance at three different stages: peak load (or point B), an intermediate stage in the post-peak regime, and at the complete failure. The red-colored area shows the evolution of the elastic energy component with the above three stages. The gray area signifies post-peak rupture energy, while yellow represents the released energy component. The above illustration presents a clear distinction between class-I (i.e., $M < 0$) and class-II (i.e., $M > 0$) type of post-peak responses. For class-I response, the amount of elastic energy available at peak loading point 'B' is insufficient to continue the specimen rupture. Consequently, the external loading source provides more energy causing increased energy dissipation (a gray area increase).

On the other hand, strain energy available at peak loading point in class-II response is higher than the requirement for specimen rupture. Consequently, one can observe the self-sustaining failure with the release of excess strain energy, indicated as the yellow portion. Thus, this study considers three key energy parameters as the base to characterize rock brittleness: elastic energy removed in the post-peak regime (dW_e), post-peak rupture energy (dW_r) and additional/released energy (dW_a). Here, (dW_e) is given by:

$$dW_e = \frac{\sigma_B^2 - \sigma_C^2}{2E} \tag{2.6}$$

The differential stresses are indicated at point 'B' and 'C' while E is the elastic modulus, i.e., the same in both loading and unloading conditions. Further, the additional (or released) energy component (dW_a) is:

$$dW_a = \frac{\sigma_B^2 - \sigma_C^2}{2M} \quad (2.7)$$

Here, M is the post-peak modulus with a negative sign for the class-I response. One can deduce the expression for rupture energy (W_r) using the above formulations as follows:

$$W_r = \frac{(\sigma_B^2 - \sigma_C^2)(M-E)}{2EM} = \begin{cases} -M, & (\text{class-I}) \sim dW_r = dW_e + dW_a \\ M, & (\text{class-II}) \sim dW_r = dW_e - dW_a \end{cases} \quad (2.8)$$

Where dW_r indicates the change in rupture energy. These energy parameters form the basis of the following two brittleness indexes i.e. K_1 and K_2 , where K_1 represents the ratio of the post-peak rupture energy to the elastic energy as follows:

$$K_1 = \frac{dW_r}{dW_e} = \frac{M-E}{M} \quad (2.9)$$

While K_2 shows the ratio of released to withdrawn elastic energies:

$$K_2 = \frac{dW_a}{dW_e} = \frac{E}{M} \quad (2.10)$$

The above two brittleness indexes not only characterize the degree of rock's intrinsic instability to define overall sample brittleness but also provide a monotonous, continuous, and unambiguous scale of brittleness as shown in figure 2.8 below:

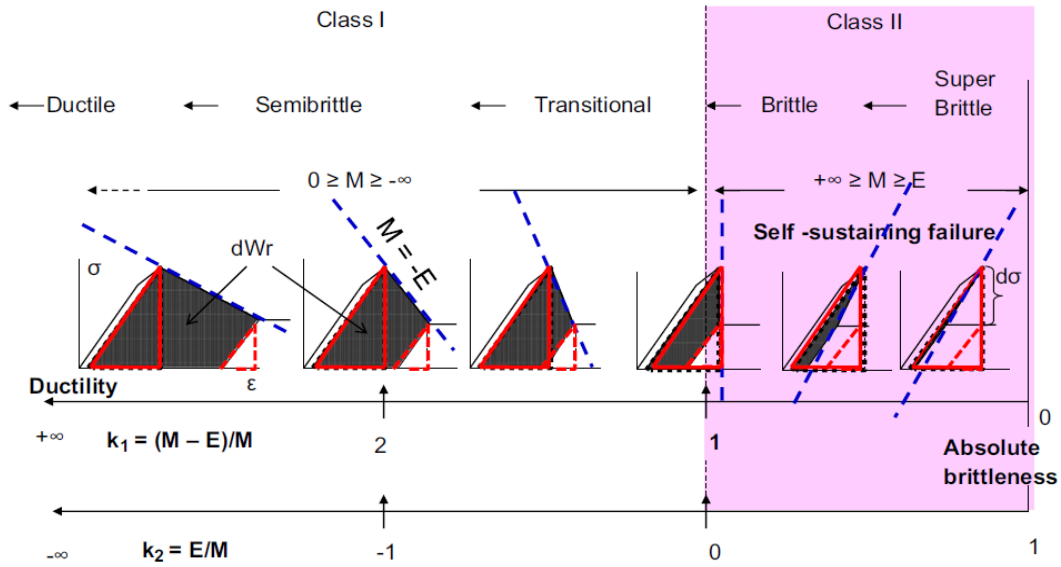


Figure 2.8: Brittleness scale (Tarasov and Randolph 2011; Tarasov and Potvin 2013)

The effect of intrinsic instability is visible in the above figure, where the range of the brittleness index $1 > K_1 > 0$ and $0 > K_2 > 1$ shows signs of self-sustaining failure demonstrating class-II behavior. Overall, the more significant difference between stored elastic energy and rupture energy components may lead to an intensification in the violent nature of sample failure. Figure 2.9(a) demonstrates the variation of the brittleness coefficient with confinement pressure. It, against the general notion of decreased post-peak ductility with increased confinement, illustrates the typical pattern of the initial increase in brittleness to acquire maximum value and then decrease eventually with confinement (Tarasov and Randolph 2011; Tarasov 2012; Tarasov and Potvin 2013).

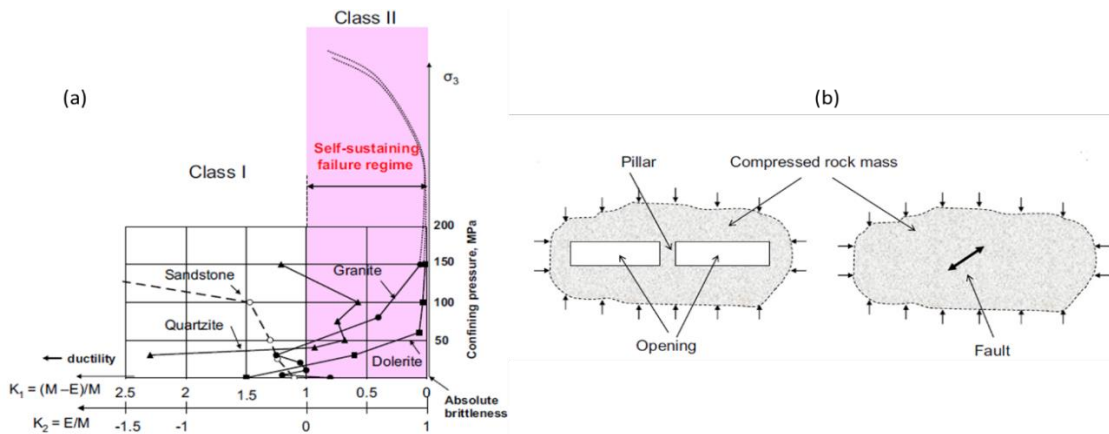


Figure 2.9: (a) Brittleness coefficient (K_1, K_2) variation with confining pressure (Tarasov and Randolph 2011), (b) linking brittleness coefficient with aftershock activity

Further, the resemblance between rock brittleness variation and aftershock activity in intact rock is used as the base to consider super brittle behavior for defining the earthquake activity. Such seismic activities, in general, occur due to the initiation of new

faults in the intact rock around the main fault, i.e., figure 2.8(b) (Tarasov and Randolph 2011; Tarasov and Potvin 2012, 2013). Also, researchers attempted to link the above relative brittleness with the mechanism of pillar-burst, as shown in figure 2.8(b).

Feng (2018), in his book Rockburst Mechanism, Monitoring, Warning And Mitigation, demonstrated the use of the following two brittleness indexes (i.e. n_b , B) to analyze rockburst intensity (Feng 2018):

$$n_b = \frac{\text{Uniaxial Compressive Strength (UCS)}}{\text{Uniaxial Tensile Strength (UTS)}} \quad (2.11)$$

$$B = 1 - \exp\left(\frac{M}{E}\right) \quad (2.12)$$

E and M are elastic and post-peak softening modulus. He utilized these indexes to evaluate the brittleness of marbles with different color, grain size, and mineral composition in the Jinping Underground laboratory phase II (CJPL-II). Different tests, including uniaxial and triaxial experiments, were conducted to determine relationships between rock brittleness and bursting potential. Figure 2.10 demonstrates the variation of rock brittleness with observed bursting potential across the section line along tunnel length as follows.

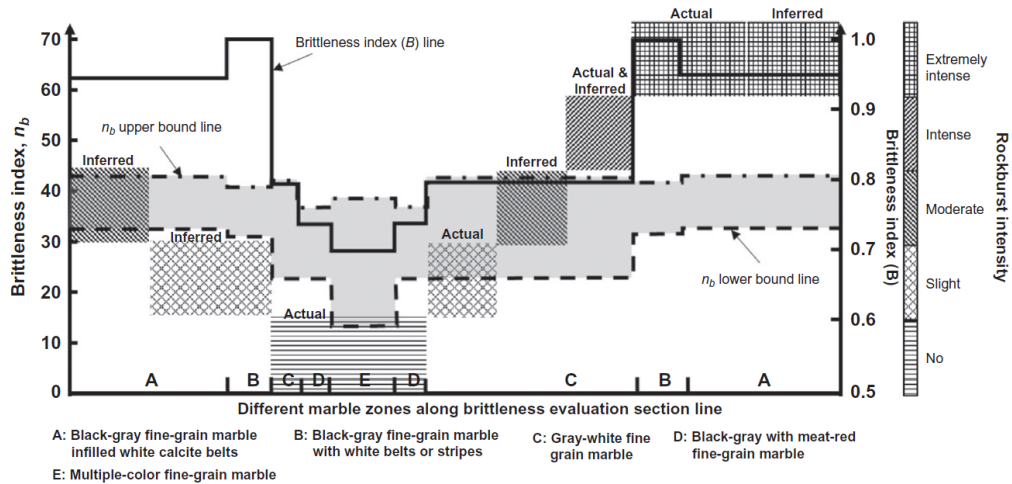


Figure 2.10: Relationship between rock brittleness and bursting (Feng 2018)

In the above figure, one can observe that the variation of brittleness index B is more prominent and sensitive in evaluating bursting potential than the parameter n_b . Overall, the results show that the bursting potential of rock increases drastically with rock brittleness and rock strength.

2.3.1.3 Stress-strain responses: Fundamental issue

Likewise, researchers made many attempts to characterize rock's brittleness using the uniaxial compression test and link it with its bursting potential (Hoek and Brown 1980; Tao 1988; Hou 1989; Wang et al. 2009; Mitri 2007). Despite providing a good insight into rock's energy storing and releasing characteristics, the fundamental correctness of such methodologies (i.e., average out the stress and strain over the entire specimen) can still be debated, especially from the viewpoint of post-peak responses. In fact, like other geo-materials such as soils and concrete, rocks exhibit a sharp strain-softening behavior beyond the peak stress, in both tension and compression (under a range of confining pressures). The localization of deformations is a direct consequence of this softening behavior, resulting in no unique stress-strain relationship (Gopalaratnam and Shah 1985). In this sense, many considered the softening branch of a stress-strain curve as a mixed material-structural property (Chen and Han 1988). Consequently, inelastic behavior and hence dissipation characteristics are dominated or governed by what happens inside the (shear) localization zone. Therefore the constitutive behavior must be analyzed and described taking into account the dissipation properties of the materials, in addition to the strength properties (Nguyen et al. 2012; Nguyen et al. 2014; Nguyen et al. 2016b). Although this concept of combining strength and dissipation properties in modeling and analyzing failure involving localization (or fracture) has long been recognized in the damage/fracture mechanics community, to the best of my knowledge, it is still in its infancy state in analyzing rock failure, given enormous studies based on stress-strain and strength only, as described in the preceding section.

One should note here that the dissipation capacity in such cases scales with the surface area created due to cracking. A homogenous stage of elastic deformation usually precedes the localized mode of failure where the energy stored in the whole volume area scales with the volume. The difference in scaling rules (energy storage scaling with volume, while energy dissipation scaling with surface area; (Nguyen et al. 2012; Nguyen et al. 2014; Nguyen et al. 2016b; Nguyen and Bui 2019) leads to the excess strain energy storage before the activation of localized failure, which is to be released via kinetic energy of rock fragments. As a consequence, the use of stress-strain and specific dissipation as the area under the stress-strain curve is inadequate, if not fundamentally incorrect, as the dissipation involved in localized failure does not scale with volume. Therefore, the surface area created due to cracking and separation, and hence the specific dissipation as

dissipated energy per unit volume is not a good representative of the failure process. The readers can refer to a series of papers on this fundamental (Nguyen et al. 2012; Nguyen et al. 2014; Nguyen et al. 2016b; Nguyen and Bui 2019) and modeling of rock/concrete/soil failure (Nguyen et al. 2016a; C T Nguyen et al. 2017; Le et al. 2018; Le et al. 2019; Wang et al. 2019; Tran et al. 2019) involving cracking and localization for further details. This combination of strength (via stress-strain behavior) and energy dissipation (via fracture energy) will form the basis for the theoretical development in this thesis.

As an illustration, the localization failure and non-uniqueness of stress-strain behavior elaborated on (Verma et al. 2019b), where three-dimensional Digital Image Correlation (DIC) technique was used to explore the behavior of rock sample both, at the sample and local scale. They conducted lateral strain-controlled uniaxial compression tests on cylindrical samples of Hawkesbury sandstone to capture complete load-displacement response. Additionally, the full-field strain data set obtained from DIC were synchronized with the overall sample response to acquire a reasonable insight to strain localization. Figures 2.11 and 2.12 present the summary of this study. Figure 2.11 shows the sample response and variation of von-mises strain with load increment. In contrast, figure 2.12 demonstrates the variation of localized strain in four different regions: across the shear band (region-1), close to the shear band (region-2), away from the shear band (region-3), and far away from the shear band (region-4).

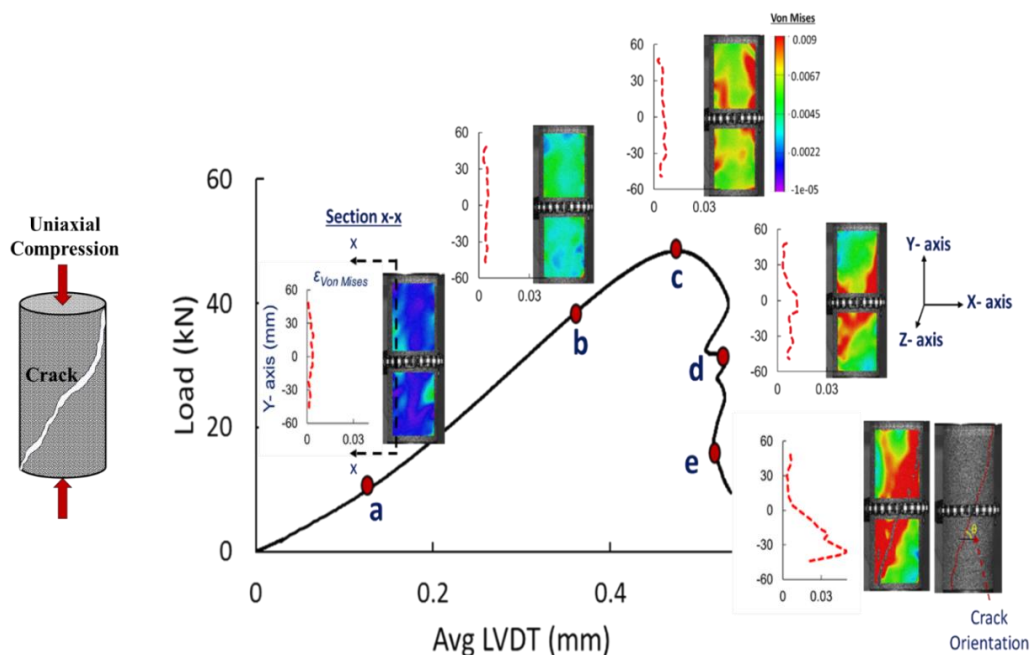


Figure 2.11: Synchronised load-displacement response (Verma et al. 2019b)

In figure 2.11, one can observe the homogeneity in strain distribution across rock samples in earlier stages 'a' and 'b' when the macroscopic load-displacement response is in its elastic regime. It indicates that all the material points across the rock sample are uniformly under compression, which is reasonable when considering the average of these localized deformations of a similar kind (compressive) when concluding the overall sample behavior.

However, as the load approaches peak point 'c,' the initiation of strain localization can be observed, which indicates deviation from strain homogeneity across the sample. Further loading strengthens this strain localization resulting in the formation of a distinct shear band visibly evident at stage 'd' and 'e.' The overall strength reduction causing a gradual load drop in the post-peak regime accompanies this strain localization. This indicates the contribution of inelastic deformation of rock material across the shear band in the degradation of the overall load-carrying capacity of rock specimens.

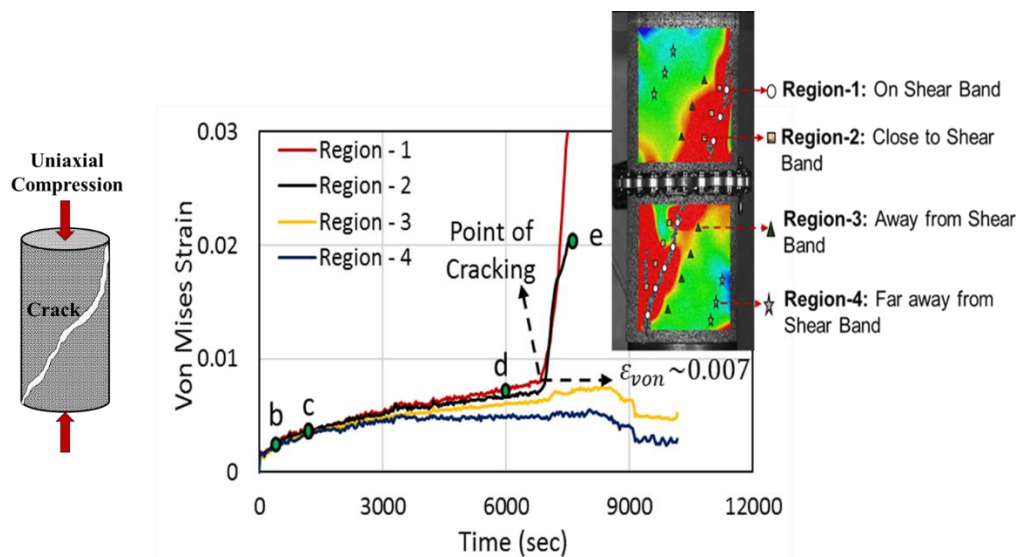


Figure 2.12: Synchronised load-displacement response (Verma et al. 2019b)

Further, strain evolution over time in four different regions across the sample in figure 2.12 shows that the von-mises strain increment in all four regions is uniform till point 'c,' i.e., global peak load. After that, it starts differing in post-peak regime with maximum increment rate (higher slope) in region-1 while minimum in region-4. This further results in localized failure indicated by the sudden jump in strain evolution across the region I and II in figure 2.12. The remaining portion of the rock sample further away from the localized shear band (regions II and IV) presents a drop in strain increment, indicating material de-stressing. The stress states in the region across (i.e., loading) and around (i.e.,

unloading) the shear band are opposite. Thus, taking the average of these opposite responses to determine the overall conclusion is fundamentally incorrect.

The other limitation of classical approaches based on macro stress-strain responses is the variation of energy characterization with the change in specimen size, i.e., size effect. One can elaborate on this using the results from the experiments conducted on the same Hawkesbury sandstone rock samples with three different lengths (L) to diameter (D) ratio (or aspect ratio) - $L/D = 1.5, 2.5$ and 3.5 (Dawidowski et al. 2015). Figure 2.13 below summarises the overall results from the above experiments.

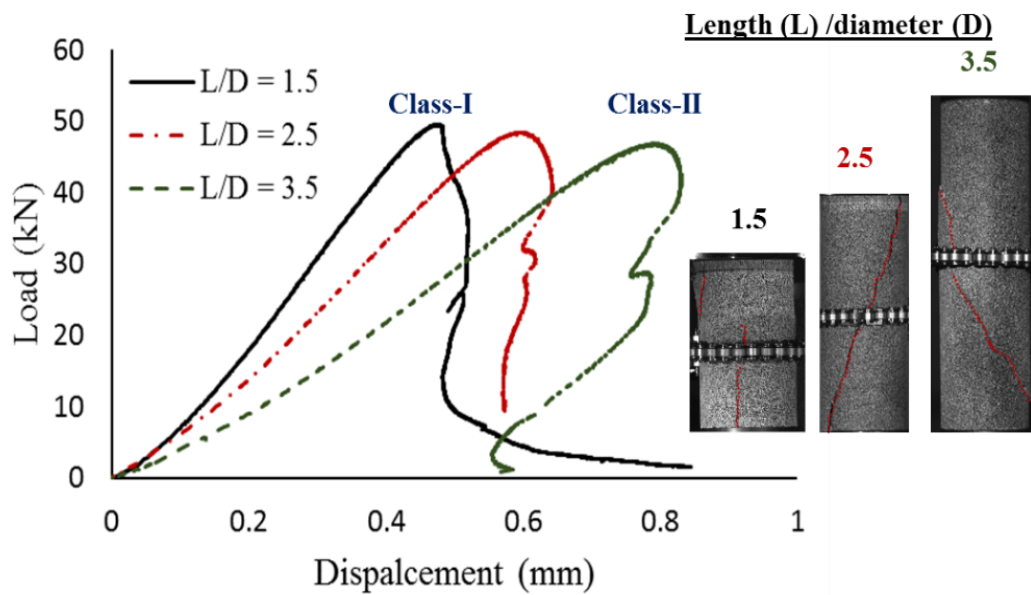


Figure 2.13: Synchronised load-displacement response (Dawidowski et al. 2015).

One can observe in figure 2.13 that, as the specimen length increases from 1.5 to 3.5 times the diameter, the overall post-peak response of the same rock type, and hence their corresponding stress-strain behavior, switches from class-I to class-II. The non-uniqueness of stress-strain behavior with specimen size is quite apparent. The key reason behind this non-uniqueness could be the increase in elastic strain energy storing capacity with specimen size. In contrast, the failure mode remains almost the same (e.g., aspect ratios of 2.5 and 3.5 above), keeping the energy requirement for structural failure consistent. Consequently, the specimen with a higher aspect ratio tends to attain a significantly higher excess energy availability at the peak loading stage. It subsequently results in uncontrolled failure in conventional axial displacement controlled loading and class-II response in lateral strain-controlled approach in uniaxial compression tests, as shown in figure 2.13. Now, the question arises: what specimen dimension could one consider ideal for deriving bursting characteristics based on post-peak response and why?

In general, ASTM suggests this ratio be between 2 and 2.5, while ISRM suggests it to be in a range of 2.5-3 times the diameter (Tuncay and Hasancebi 2009; ASTM 1994, 2000; ISRM 2007). However, there is no universal consensus on this range of aspect ratio.

Tarasov and Randolph also highlighted a similar issue (Tarasov and Randolph 2011). The focus of this research was to derive the correct approach for strain measurement to characterize the post-peak responses. Strain gauges of differing lengths (l_{g1} , l_{g2} , l_{g3} and l_{g4}) were used across one rock sample, as shown in figure 2.14(a). The strain gauge-4 covers the uncracked portion of the specimen. Each gauge measures the relative displacement between the corresponding two endpoints. Here, Δ indicates the overall axial displacement of the sample, while Δ_e and Δ_r are the elastic and inelastic/rupture components of axial displacement, as shown in figure 2.14(a). In this deformational analysis, one can observe that the inelastic displacement is localized only across the failure surface. Thus the Δ_r the component is the same for all strain gauges. It consequently affects the access strain energy measurements from three strain gauge passing through the shear band, i.e., maximum for gauge-1 and minimum for gauge-3.

One can observe the class-II behavior with negative $d\Delta$ (or positive post-peak modulus) for the strain gauge 1, i.e., most extended strain gauge. In contrast, class-I for the shortest strain gauge-3 passing through the fault with positive post-peak $d\Delta$ (or negative post-peak modulus). On the other hand, strain gauge-4 (away from fault) undergoes complete unloading, demonstrating the elastic stage of the uncracked portion. This illustration demonstrates four different post-peak responses for the same rock. Now, a similar question arises: which response should one take to estimate material brittleness and why? Additionally, if the stress state in the post-peak regime across strain gauge 1 (i.e., overall compressing/loading) and 4 (i.e., extending/relaxing) are opposite, then how can one take the average of these two responses to derive an overall conclusion? Because the principal of average requires the concerned parameters to be similar.

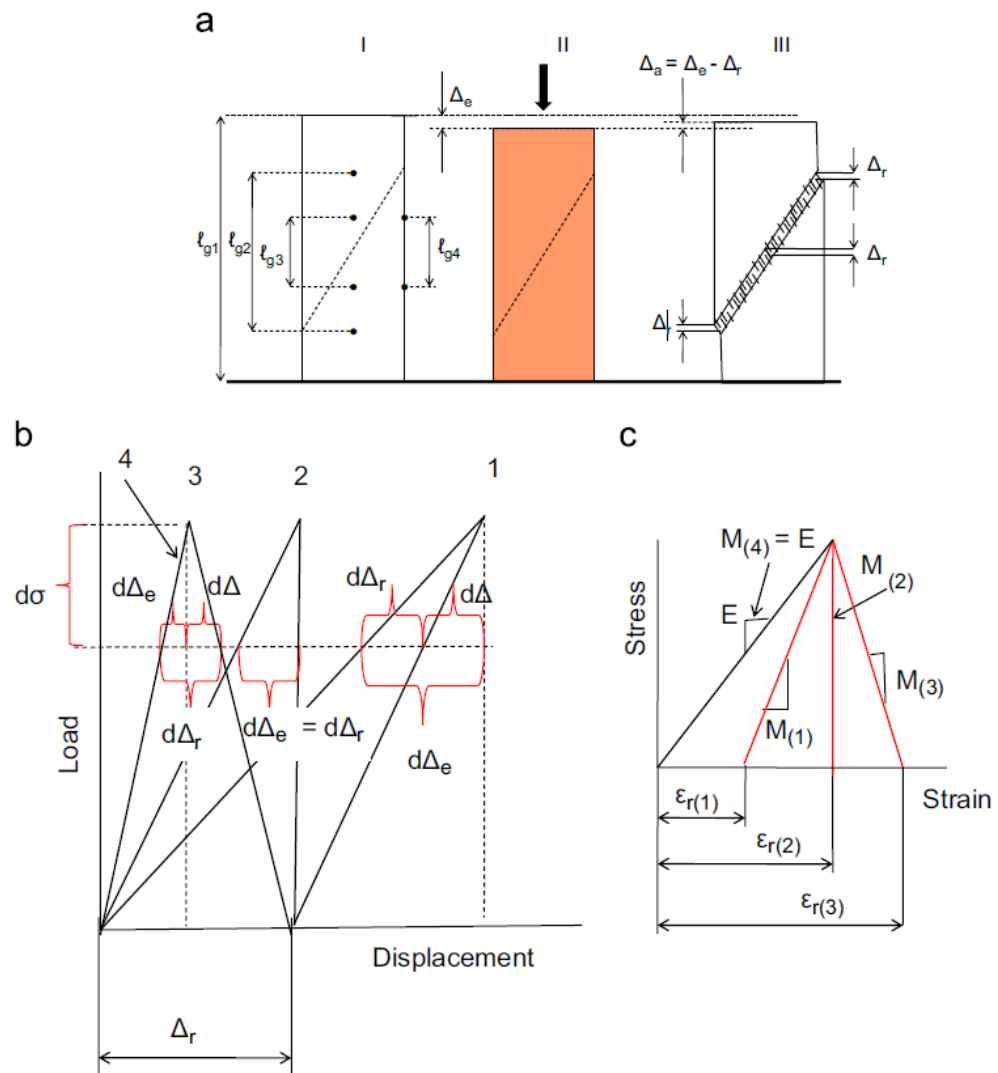


Figure 2.14: Synchronised load-displacement response (Tarasov and Potvin 2013)

The uniaxial compression test data could provide a good insight into the behavior of rock under compression or compressive shear using an advanced experimental approach. However, deriving conclusions about its bursting potential explicitly on this basis could always require empirical formulation, which does not provide much insight into the bursting mechanism and factors affecting it. One key reason behind this is the boundary conditions under which strain burst occurs. These are entirely different from uniaxial compression and affects the energy storing and dissipation components. Besides, none of such classical approaches could have had the effect of unloading on rock failure, which is an integral part of a strain-burst mechanism.

2.3.2 Rock under tensile

The majority of approaches discussed in the previous sections derive the bursting potential based on the behavior of rock under compression. Such approaches, in general, are incompetent to incorporate the contribution of rock's tensile strength property. In-fact in deep underground excavation, tensile stresses on tunnel or mining walls are among the prime factors which characterize the rock's bursting failure under high in-situ lateral pressure (Goodman 1989). It indicates that the tensile failure of rock is among the fundamental energy dissipation mode in deep underground rockburst. Thus, one should not ignore the tensile strength property of rock while analyzing its bursting potential.

2.3.2.1 Tensile strength: role in in-situ bursting

Several researchers in the literature reported the occurrence of strain burst in deep underground opening conditions when the maximum in-situ principle (σ_1) stress was considerably less than rock's uniaxial compression strength (UCS). One can explain this using the example of strain-burst at Jinping I hydropower station with a dam height of 305m, built on the Yalong river, Sichuan province. This station also has underground caverns to include a transformer chamber, leading powerhouse, and a series of tunnels. The UCS of rock (thickly layered marble) surrounding these underground openings varies from 50 to 129 MPa. Internal friction is 45° - 56° , while elastic modulus is 20-45 GPa. The surrounding rock underwent strain burst with maximum principal stress to be around 36 MPa approximately. Besides, the rock failure during the underground opening was also characterized by flake fractures at the position with a more prominent curvature or the top arch's foot (figure 2.15a) and sheet cleavage types at sidewalls (figure 2.15b). It reflects the characteristics of tensile-shear or tensile failure of rock. The secondary tensile stresses could cause such failure of rock near the excavation surface (Wu et al. 2010a).

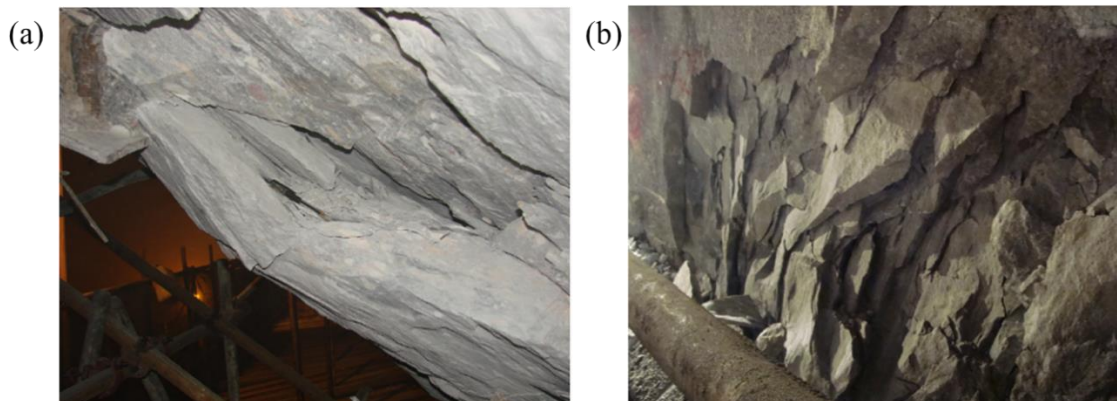


Figure 2.15: (a) Flake fractures, (b) sheet cleavage (Wu et al. 2010a)

The above rock failure features have been further explained based on theoretical and numerical solutions (Wu et al. 2010a). This analysis re-iterated the generally accepted fact: prominence of secondary tensile stresses induced by excavation to cause strain burst occurrence. One can further elaborate on this failure mechanism using Griffith theory with the following expressions for failure criterion in terms of principal stress:

$$\sigma = \sigma_t \quad (3\sigma_3 + \sigma_1 \leq 0) \quad (2.13)$$

$$(\sigma_1 - \sigma_3)^2 \sigma = 8\sigma_1(\sigma_1 - \sigma_3) \quad (3\sigma_3 + \sigma_1 > 0) \quad (2.14)$$

Where σ_t is the tensile strength while σ_1 and σ_3 are major and minor principal stress. Figure 2.16(a) shows the graphical representation of the above criterion. It indicates that if the minimum principal stress reduces below the tensile strength, the given rock material can still reach its critical state and fail irrespective of the major principal stress magnitude. This failure mechanism can explain the occurrence of strain burst with maximum in-situ principal stress smaller than rock's UCS, as observed in the Jinping I hydropower project.

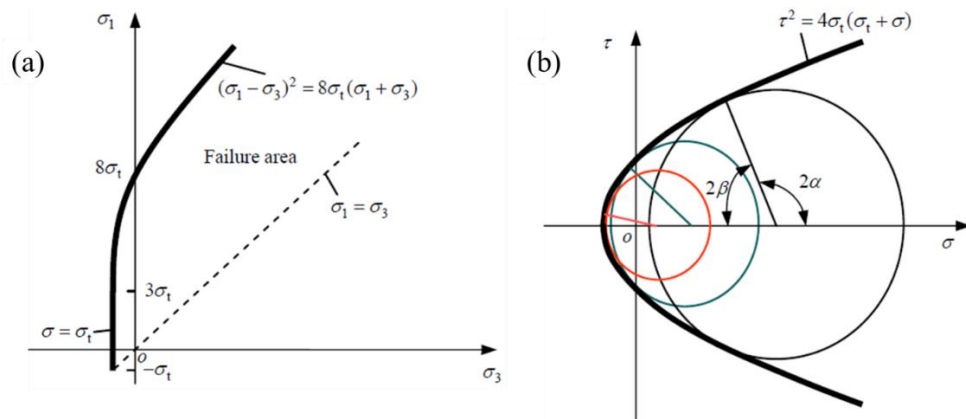


Figure 2.16: (a) Flake fractures, (b) sheet cleavage (Wu et al. 2010a)

Further, an attempt made to explain rock fragmentation types by expressing equations (2.13, 2.14) in normal (σ) and shear (τ) stress as follows:

$$\tau^2 = 4\sigma_t(\sigma_t + \sigma) \quad (2.15)$$

Figure 2.16(b) illustrates the above expression graphically. Thus, one can observe the relationship between rupture angle (α) and shear angle (β) in figure 2.16(b), i.e., gradual reduction of α to zero with normal stress approaching tensile strength (σ_t). It further explains the flake and sheet cleavage fracture characteristics of strain burst failure (i.e., figure 2.14).

Following this, Diederichs (2007) applied the Hoek-brown criterion to link the UCS with σ_t and deduce the rockburst potential, i.e., a higher ratio of UCS to σ_t results in higher bursting potential, as shown in figure 2.17 below (Diederichs 2007).

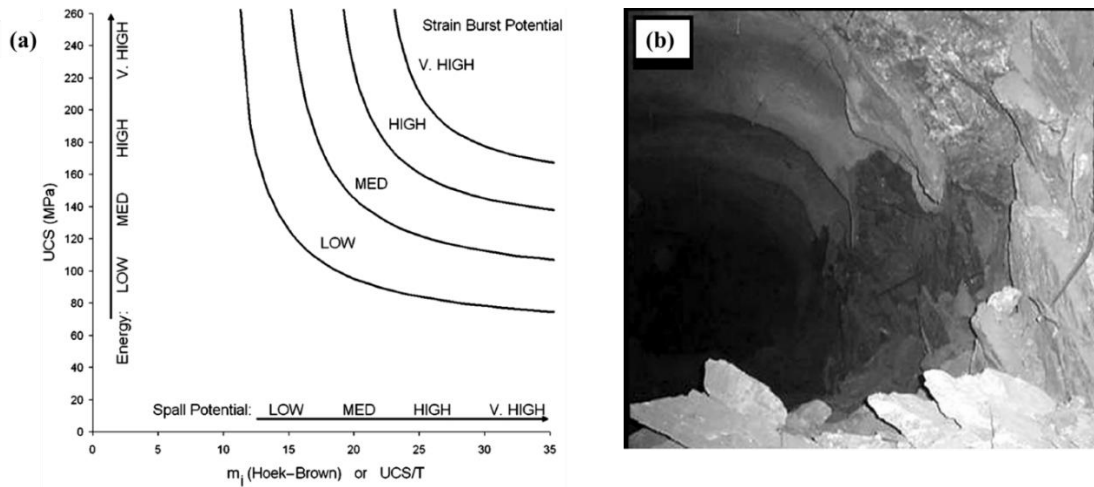


Figure 2.17: Rock bursting and spalling potential based on UCS and σ_t (Diederichs 2007)

The above figure shows that the more potent rock with very high UCS and smaller σ_t demonstrates higher bursting potential. Evidently, as the strength of rock increases, so too does the build-up of strain energy, thus cause violent failure. The practical example of strain bursting could be gneiss and granite in the Fukra train tunnel in Switzerland (figure 2.17b). As the magnitude of tensile strength increases, it dominates the crack initiation mechanism and gradually reduces the bursting magnitude. Consequently, rock failure mode switches from bursting to less violent spalling.

From the above discussion, one can observe the relevance of rock's tensile strength property, especially to understand the mechanism of rockburst mechanism under deep underground conditions. Therefore, it is vital to consider the correct and accurate representation of rock's internal tensile strength while determining or understanding the bursting magnitude or mechanism. It also highlights the significance of an efficient experimental approach to determine rock's tensile strength property.

2.3.2.2 Tensile strength experimentation

The direct tension test is the standard experimental approach to estimate the tensile strength property of any target material. It undoubtedly provides the most accurate results. However, there are several practical difficulties associated with such a standard experimental approach, especially in the case of brittle materials like rock and concrete.

Consequently, it resulted in the development of the indirect tensile strength test, commonly known as a Brazilian disc test. This experiment was proposed by Carneiro et al. (1943) based on the fact that under bi-axial loading conditions with compression (three times smaller than principal tensile stress) in one direction and tensile loading in other, the majority of rock specimens fail in tension (Carneiro 1943; Goodman 1989; Piratheepan et al. 2012). This experimental approach requires a disc-shaped specimen compressed under diametrical compressive loading. It generates uniform tensile stress perpendicular to the vertical diametrical axis of the specimen. As brittle materials like rock and concrete are usually weak in tension; this tensile stress across the vertical axis exceeds material strength and results in splitting failure. Strength to resist this failure, as in Brazilian tensile strength in MPa (σ_t), can be calculated from the following equation:

$$\sigma_t = \frac{2P}{\pi Dt} \quad (2.16)$$

Where P is the peak load (kN), D is the diameter (mm), and t is the specimen thickness (mm). Initially, this experiment developed for concrete primarily. Later on, Rock mechanics (ISRM-1978) utilized the assumptions of material homogeneity, isotropy, and pre-peak linear elasticity and recommended this experiment for testing rock as well (ISRM 1978). This test was practically more convenient to perform as compared to the direct tensile strength test. Consequently, it becomes widely accepted as a conventional tensile strength testing approach for brittle materials.

Despite widespread popularity, the Brazilian disc test has always been in controversy since its inception. The reason for the controversy is the difference in Brazilian disc and direct tensile strength test results. Many researchers attempted to explain this anomaly by linking the material tensile property with the crack initiation point in disc specimens. Ideally, cracking in discs under uniform tensile stresses should initiate from the center (ISRM 1978). It eventually formed the basis to confirm the validity of the Brazilian disc test. For instance, Jaeger et al. (1967) supported the feasibility of the Brazilian disc test based on theoretical and experimental results of tensile strength tests on three different rocks (Jaeger 1967). Yanagidani et al. (1978) analyzed strain variation on specimen surface using transient recorder (TR) and observed that cracks initiated from the tensile stress zone (Jaeger 1967). Mellor et al. (1971) suggested the use of curved-jaw loading plates to make the Brazilian disc test results compared with the uniaxial tensile strength test (Mellor and Hawkes 1971). Wang et al. (2003) suggested the use of the flattened

Brazilian disc specimen instead of the conventional round specimen in order to ensure crack initiation at the specimen center (Wang et al. 2004).

Contrarily, Fairhurst in 1964 used Griffith type fracture criterion to suggest that, for small loading angles, failure may occur away from the specimen's center resulting in under-estimation of the material tensile strength (Fairhurst 1964). Colback (1966) used high-speed photography to determine the point of fracture initiation and suggested that for any valid Brazilian disc test, the crack must initiate from the disc's center to cause axial splitting of the specimen (Colback 1966). Hudson (1972) used scanning electron micrograph technology to analyze the point of crack initiation and concluded that the use of a flat steel plate in the Brazilian test will always cause failure initiation beneath the loading point, thus questioned its feasibility (Hudson et al. 1972a).

In recent times, Aliabadian (2017) explored this issue and highlighted the significance of rock material transverse isotropy due to preferred directions of micro-cracks, bedding planes, pore, and grain orientation (Aliabadian et al. 2017). The analytical solution is applied to explore the effect of loading contact areas on the overall stress distribution. This research utilizes the combination of transverse isotropy with analytical stress distribution to identify the location of crack initiation and reported it to be away from the disc center at the loading ends for flat platens, as shown in figure 2.18 below.

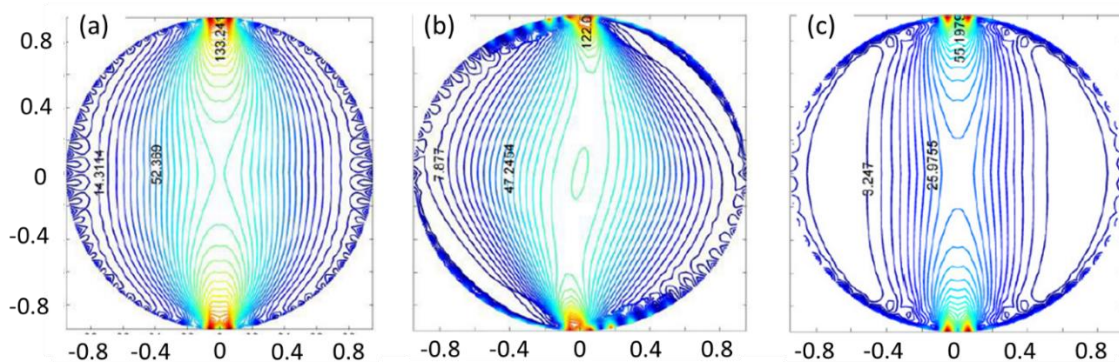


Figure 2.18: Mobilised stress distribution (a) 0° , (a) 45° , (a) 90° bedding plane orientations (Aliabadian et al. 2017)

Later on, advanced experimental approaches, including the use of DIC, were used in addition to the above method to verify the results from analytical solution coupled with failure criterion with the intent to determine crack initiation point (Aliabadian et al. 2019a). This study considered Hawkesbury sandstone to demonstrated that, for the

transverse anisotropy plane perpendicular or parallel to the loading angle, the crack would initiate at the disc center provided a larger contact area is ensured (Aliabadian et al. 2019a).

Verma et al. (2018) highlighted the effect of load concentration using the Hybrid (continuum-dis-continuum) based numerical modeling approach, which is 3DEC-Itasca (Verma et al. 2018). Figure 2.19 demonstrates the progress of material damage with loading across the disc sample. The damage first initiates near the loading end, as shown in figure 2.19(a). This study reveals that the cause of damage initiation was localized shearing at loading ends. As the applied load approaches the peak and surpasses it to the post-peak regime, the localized material damage propagates from loading ends towards the disc center. Whereas, the magnitude of damage intensification across the disc center is much higher than at the loading ends. It indicates that the central diametrical cracking, which precedes the loading ends crack initiation, in actual governs the structural failure of the disc sample. One can conclude here that the disc sample under diametrical compression fails in tension primarily. However, the localized crack initiation does affect the peak load; thus, the resultant tensile strength estimation.

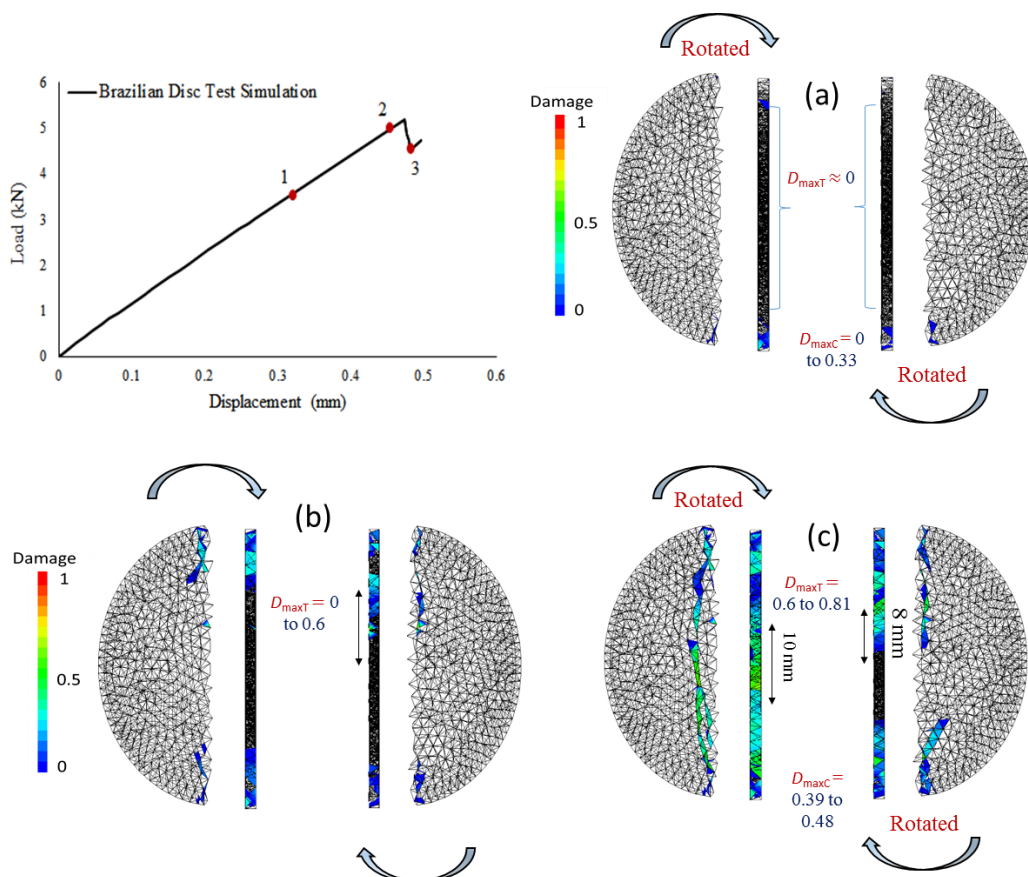


Figure 2.19: Brazilian disc tests: damage evolution (Verma et al. 2018)

On the other hand, Tomac and Gutierrez (2012) explored the size dependency facet of this experiment using micromechanical insights from DEM based numerical modeling (Tomac and Gutierrez 2012). It demonstrated the unreliability of Brazilian disc tests in tensile strength estimation because, unlike the uniaxial tensile strength experiment, results, in this case, are negatively influenced by the specimen size, as shown in figure 2.20. Here, D denotes the sample diameter, while R is the average size of particles.

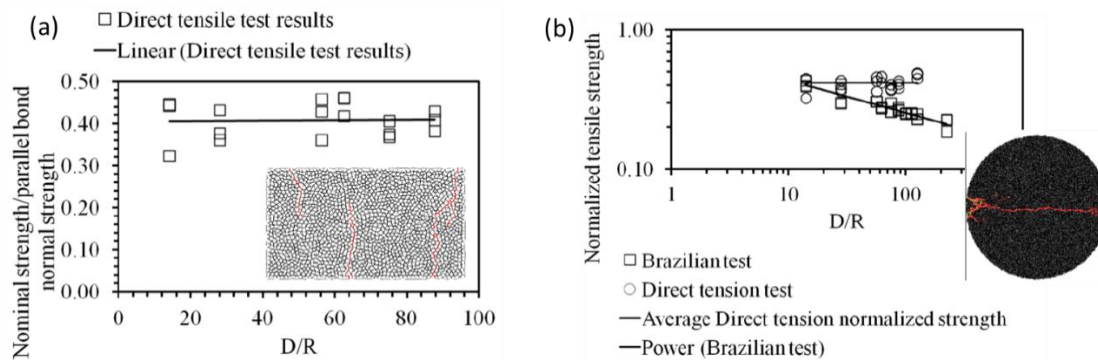


Figure 2.20: Specimen size effect (a) uniaxial tensile strength, (b) Brazilian disc test (Tomac and Gutierrez 2012)

Many researchers attempted to collaborate advanced instrumentation techniques like DIC to acquire an insight to rock material behavior in Brazilian disc testing setup (Jonsén et al. 2007; Leplay et al. 2010; Stirling et al. 2013; Liu 2014; Mazel et al. 2016; He and Hayatdavoudi 2018; Mousavi et al. 2018; Patel and Martin 2018; Xing et al. 2018; Cao et al. 2018; Zhang et al. 2018; Shara et al. 2018; Belrhiti et al. 2017; Nath and Mokhtari 2018; Wang et al. 2019; Candamano et al. 2019). DIC applications do provide an excellent base for full-field strain evolution, which conventional approaches could not. Nevertheless, the majority of these attempts yet fail to provide any significant contribution in terms of qualitative analysis.

The prime reason for the above limitation could be the experimental instability in terms of disc sample failure in the split second-time frame window. It causes the sudden drop of load immediately after reaching a peak, demonstrating the uncontrolled release of stored strain energy, as shown in figure 2.21 below.

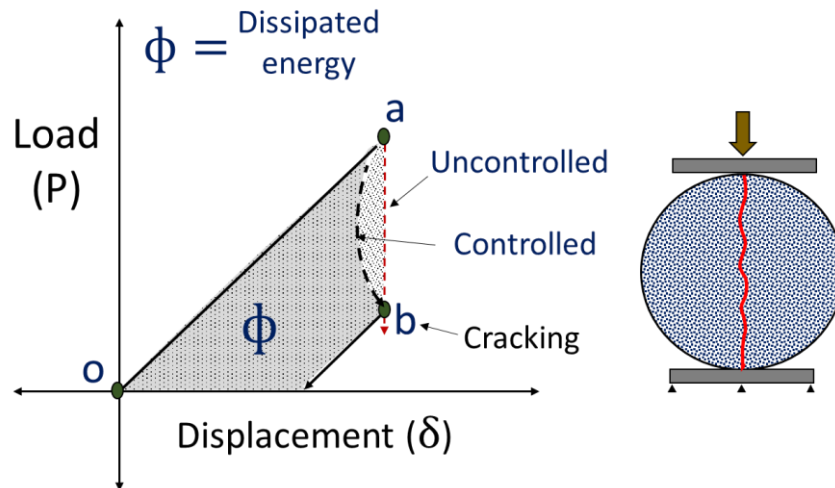


Figure 2.21: Energy aspect of Brazilian disc test

It indicates the inability to control the excess strain energy available at the peak load point. Consequently, it makes the efficient applications of advanced instrumentation for strain measurement (such as X-ray Computed Tomography, Digital Image Correlation) impossible, besides resulting in an incorrect measurement of fracture properties. Nevertheless, researchers yet fail to address this aspect of the widely used Brazilian disc test. It forces to utilize empirical formulation/s for tensile strength estimation, which, most of the time, are inaccurate when considering the crack initiation point and scale dependency aspects. Therefore, this study highlights the need for an innovative methodology to control the instant cracking mechanism of the disc sample under diametrically compressive loading. The controlled cracking of the disc specimen will allow the efficient application of advanced experimental approaches. It also enables the investigator to capture the much-needed snap back aspect in indirect testing methodology, which has potential applications towards fracture parameter determination, as highlighted in figure 2.21 as well.

2.4 Boundary conditions evaluation

The previous section described rock's behavior in uniaxial compression and indirect tension loading conditions along with the limitations, which, if addressed, would provide an improved approach for material parameters determination. Besides, it also highlights that the majority of such approaches intend to use empirical formations to link the bursting potential with rock's material properties. The prime reason behind this limitation is the absence of boundary conditions effects, which is quite essential from the in-situ

bursting point of view. From this perspective, the subsequent subsection presents a brief overview of experimental approaches developed to evaluate the effect of boundary conditions changes on the strain burst mechanism along with allied competencies and limitations.

2.4.1 Triaxial unloading

Triaxial unloading experiment is an experimental approach to evaluate the effect of unloading on the strain burst occurrence. In this experiment, cylindrical samples are triaxially loaded to the desired stress state first. After that, confining pressure is removed to create an unloading effect in line with deep underground excavation. For instance, Huang et al. (2001) conducted triaxial unloading tests on three rock types, including limestone, granite, and magmatic granite using both, displacement control and load control approaches (Huang et al. 2001). Figure 2.22 below presents a brief outline of the adopted stress-path.

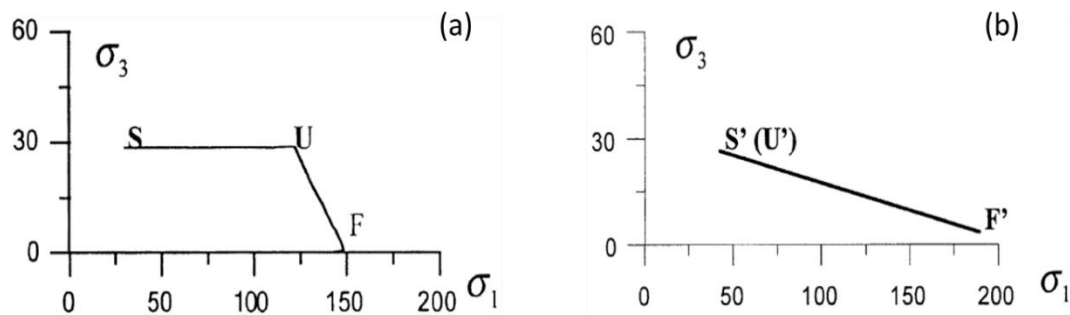


Figure 2.22: Stress-path (a) Displacement control, (b) Force control

This study concludes that irrespective of loading control, the failure characteristics of rock differ significantly under loading and unloading conditions. Elastic modulus of different rock types under loading conditions was higher than under unloading, indicating a reduction in rock material stiffness due to inelastic deformation in the post-peak regime.

Similarly, A. Hua and M. You (2000) performed unloading triaxial experiments on marble, sandstone, and siltstone (Hua and You 2001). Under this testing, a rock specimen is first triaxially loaded to acquire a pre-defined hydrostatic stress state. After that, deviatoric pressure increases in such a way that the maximum principal stress of the finalized state becomes higher than the uniaxial compressive strength but lower than the corresponding triaxial strength. After that, the confining pressure is reduced gradually while keeping the deviatoric magnitude constant. Under these conditions, a sample's

lateral deformation during unloading is so high that it results in frequent damage to the circumferential gauge. The majority of samples tested are reported to fail, not during loading when samples are absorbing strain energy, but during unloading due to rapid energy release. This mechanism of energy absorption/release is the conceptual material response under potential underground excavation.

Similarly, (Feng 2018) performed triaxial unloading tests on Jinping marble with the following detailed stress path (Feng 2018):

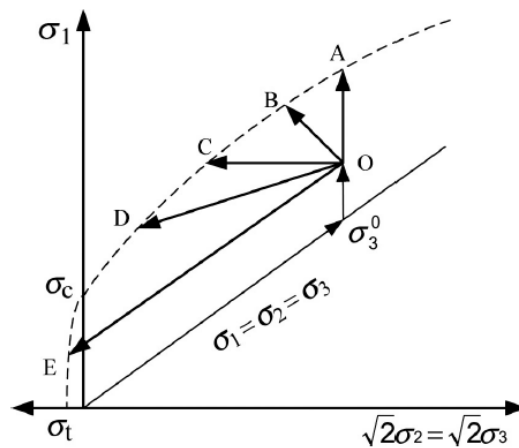


Figure 2.23: Different loading-unloading stress paths (Feng 2018)

The path OA represents the conventional triaxial compression. Due to practical difficulty and complications in the control system, OC is the most used stress-path, conducive to evaluate the effect of unloading on rock strength. This study also demonstrates a similar observation of very high circumferential deformation during unloading in comparison with the axial. The increase in confining pressure increases the strain energy absorbed before unloading, which eventually causes the brittle failure of samples with bulking and uncontrolled strain energy release.

D. Huang and Y. Li (2014) performed similar triaxial unloading tests on marble, where the mechanism of energy conversion during rock failure is the key focus (Huang and Li 2014). They evaluated the effect of the unloading rate and confining pressure. Figure 2.24 presents the typical time history results depicting the variation of strain energy conversion with unloading rates for a given confining pressure of 40 MPa.

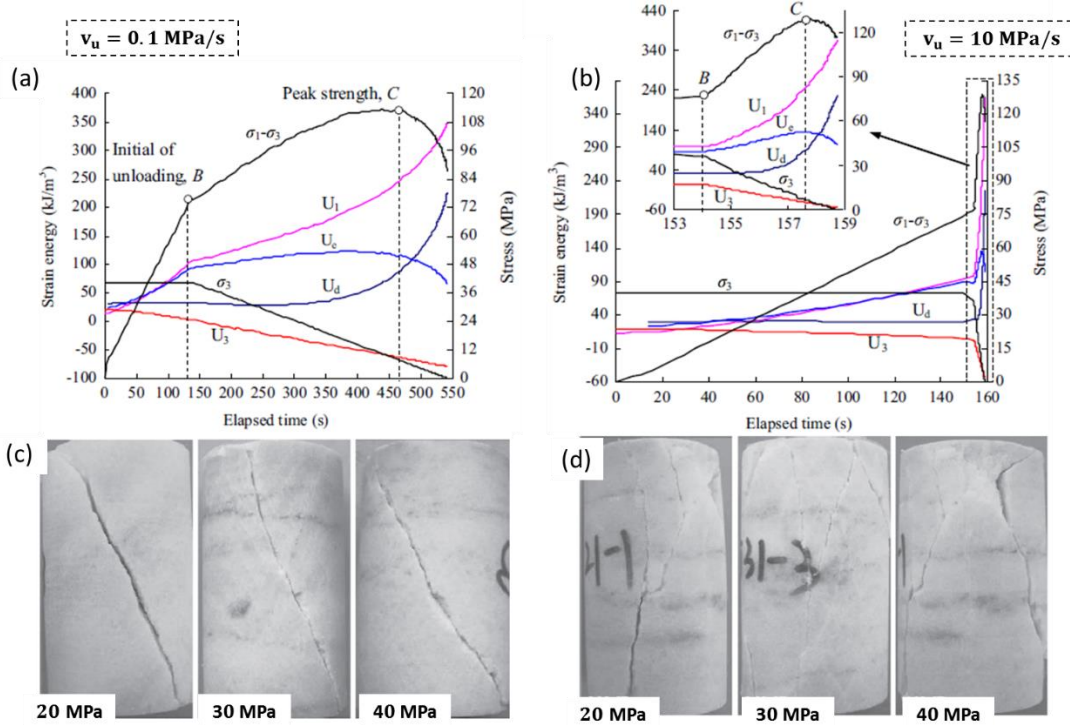


Figure 2.24: Time history for strain energy conversion under (a) 0.1, (b) 10 MPa/sec unloading rates. The fractured specimen in different confining pressure under (c) 0.1, (d) 10 MPa/sec unloading rates (Huang and Li 2014)

Figure 2.24, U_1 denotes the strain energy absorbed due to axial compression, U_3 the strain energy consumed by negative work done via radial dilation due to unloading (or σ_3 decrease). These energy parameters are obtained as the cumulative area under stress-strain response using the trapezoidal rule as follows:

$$U_1 = \int_0^{\varepsilon_1^t} \sigma_1 d\varepsilon_1 = \sum_{i=1}^n \frac{1}{2} (\sigma_1^i + \sigma_1^{i+1}) (\varepsilon_1^{i+1} - \varepsilon_1^i) \quad (2.17)$$

$$U_3 = 2 \int_0^{\varepsilon_3^t} \sigma_3 d\varepsilon_3 = \sum_{i=1}^n \frac{1}{2} (\sigma_3^i + \sigma_3^{i+1}) (\varepsilon_3^{i+1} - \varepsilon_3^i) \quad (2.18)$$

Here, n represents the total trapezoids on the stress-strain response, and i is the segmentation point. One can use the following expression to obtain elastic strain energy under triaxial compression:

$$U_e = \frac{1}{2E_u^t} [\sigma_1^2 + 2\sigma_3^2 - 2\nu_u^t (2\sigma_1\sigma_3 + \sigma_3^2)] \quad (2.19)$$

Where, ν_u^t and E_u^t are unloading Poisson's ratio and elastic modulus at time t while U_d indicates the strain energy responsible for plastic deformation. Point 'B' in figure 2.24 denotes the time of unloading while point 'A' indicates the peak strength.

One can observe here that inflection at point B shows that deviatoric stress increases significantly with the unloading (or decrease in σ_3). Consequently, stress starts increasing significantly after point 'B.' This unloading also results in rock material damage progression, followed by an increase in material damage corresponding to plastic deformation or energy component.

Additionally, this mechanism of strain energy accumulation, dissipation, and release becomes evident with an increase in the unloading rate from 0.1 to 10 MPa/s. This sudden change in energy conversion was considered responsible for the immediate release of stored strain energy, followed by violent fragmentation. Similarly, an increase in confining pressure also causes an increase in strain energy storing capacity, which eventually governs a comparatively violent rock failure mechanism. The governing failure mode in the highest unloading rate of 10MPa/s is of tensile or splitting nature, which eventually transforms to shear with the reduction in unloading rate to 0.1 MPa/s. It highlights the significance of tensile strength property in deep underground, bursting failure.

Li .et.al. (2017) performed similar true triaxial unloading experiments on granite rock with different initial confining pressures from 10 to 60 MPa with three different loading unloading conditions including conventional triaxial (i.e., group-I), unloading under constant (i.e., group-II) and increasing (i.e., group-III) axial stress (Li et al. 2017). This study demonstrates the evolution of key energy parameters, including total, elastic, and dissipative strain energy on rock deformation and failure with different stages of loading-unloading conditions. These energy parameters, including the total, elastic, and circumferential strain energies, increase with confining pressure. The dissipative strain energy component remained approximately invariable irrespective of confinement changes, shown in figure 2.25 below.

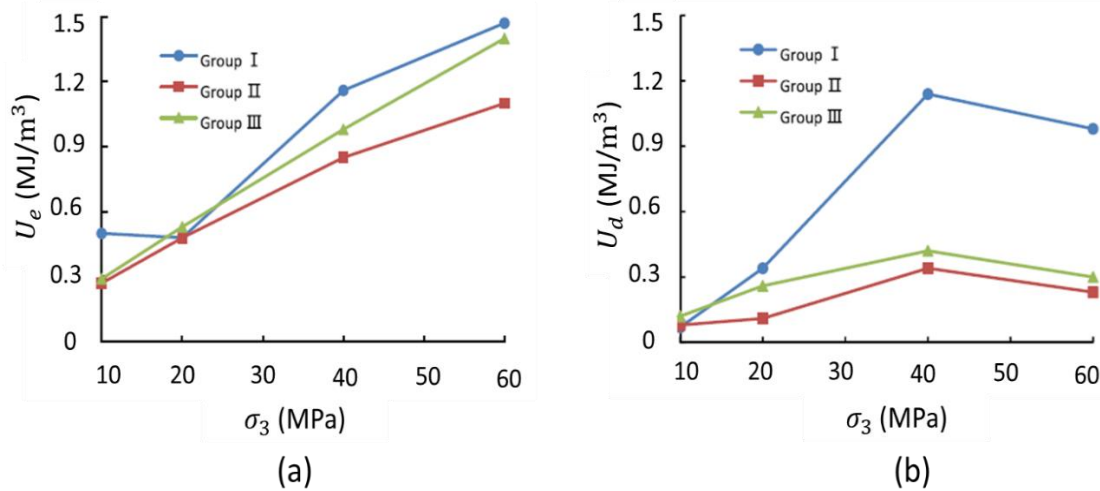


Figure 2.25: Variation in (a) elastic strain energy, (b) dissipative strain energy with confining (Li et al. 2017)

The above results re-iterates the observation of specimen failure in unloading cases due to the release of excess stored strain energy. This excess stored strain energy component in deep under-ground conditions with elevated confining pressure is significantly higher, and one cannot replicate it in conventional triaxial or uniaxial loading-based experimentations. Besides, these experiments cannot capture the polyaxial in-situ loading-unloading stress states, which differ significantly from the triaxial or uniaxial unloading conditions.

2.4.2 True-Triaxial Loading-Unloading

Before excavation, rock unit cells around potential underground openings are always under equilibrium in polyaxial stress state with three different principal stresses: major (σ_1), intermediate (σ_2) and minor (σ_3) components, as shown in figure 2.26(a) below.

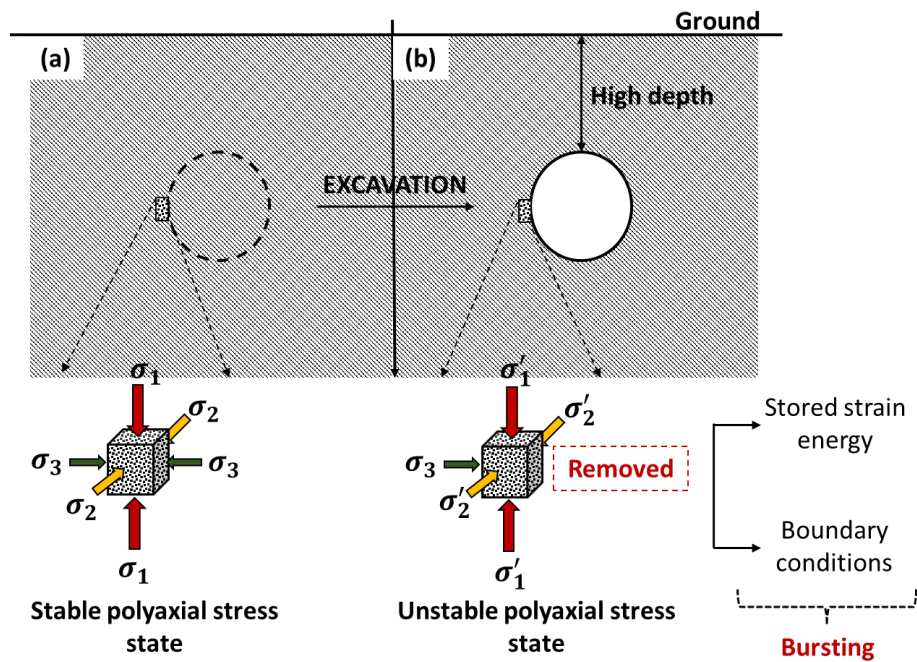


Figure 2.26: Change in boundary conditions (a) before, (b) after excavation

As excavation happens, it reduces the confinement from one face of the unit cell to zero, as shown in figure 2.26(b). This disturbance in polyaxial stress state's equilibrium, due to boundary condition changes, causes stress re-distribution where resultant σ_1 increases significantly and often exceed the yield strength of rock. As a result, it causes unstable and violent failure of rock constituting the bursting mechanism. Here, one can observe that two critical external factors are collaboratively influencing the overall bursting phenomenon: (a) the high magnitude of stored strain energy in rock before excavation and (b) effect of the sudden change in boundary conditions due to excavation. Prior factor has been the base of various attempts to rock-burst prediction study, as discussed in the previous sub-sections. The latter aspect required further attention; thus, the need for a polyaxial testing setup was evident.

Mogi (1971) developed one polyaxial testing setup to highlight the significance of intermediate principal stress (Mogi 1971). The leading inclusion in this new triaxial testing apparatus was the structural addition of lateral pistons for the independent application of intermediate principal stress (σ_2). Figure 2.27 below shows the schematic design of this polyaxial experimental setup.

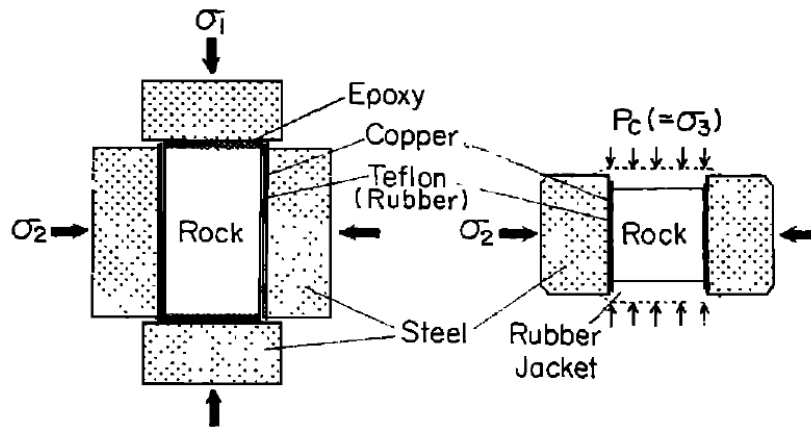


Figure 2.27: Testing setup with independent control over intermediate principle stress

Further, many researchers utilized this testing setup to explore the effect of intermediate principal stress on rock's yield strength, which was missing in the majorities of conventional failure criterion (Colmenares and Zoback 2002; Ramamurthy 2007; Cai 2008; Verma and Chandra 2020). However, the inability to imitate the stress path replicating the boundary conditions around an underground opening was still persistent.

Later, He et al. (2007 – 2015) in China University of Mining Technology Beijing developed a true triaxial experimental setup (He et al. 2007, He et al. 2010; He et al. 2012a; He et al. 2012b; He et al. 2015). They named it as Deep Underground Rockburst Analogue Machine (DUTM) (He et al. 2012b). This testing setup could control different loading rates in three different principal directions independently. It also allows achieving the sudden unloading on one face along minimum principal stress direction. To demonstrate its application, He. et al. (2010) used the above experimental setup to replicate the bursting phenomenon in limestone rock type (He et al. 2010). Figure 2.28 presents the graphical representation of the above testing setup. The maximum loading capacity of the testing frame is 450 kN with a fixed bottom plate. The movable top plate allows applying vertical compression loading via an in-built hydraulic pump. Besides, this setup contains four hydraulic pumps to apply loads in the remaining two principal directions. The horizontal piston movement and droppable loading bar facilitate the unloading mechanism. As evident, such a testing setup requires a rectangular testing sample. The size of the limestone rock sample used in this specific test was $150 \times 60 \times 30 \text{ mm}^3$, which adheres to the loading frame's physical limitation of specimen size to 65mm in σ_2 direction while 35mm in σ_3 direction. Figure 2.28(b) presents the three-dimensional schematic overview of the testing setup.

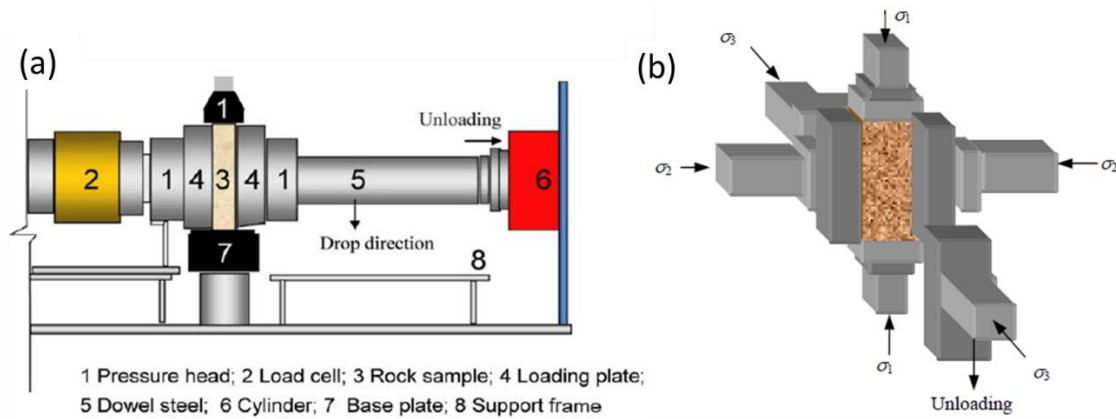


Figure 2.28: Change in boundary conditions (a) before (He et al. 2010), (b) after (He et al. 2012b) excavation

This experimental setup can be used to replicate the stress-path of in-situ dynamic unloading where the load in all three directions first increases to acquire expected in-situ confining pressure. After that, loads in two horizontal surfaces along the direction of the removable piston stays constant while loading on the remaining four directions increases to reach intermediate stress magnitude. Finally, the compression via top plate increases to the anticipated maximum principal stress while keeping the loads on remaining directions (i.e., σ_2 and σ_3) constant. After acquiring this applied in-situ stress state, one can remove the lateral confinement in minimum principal stress direction suddenly to replicates the in-situ excavation process.

The limestone rock sample was exposed to a similar testing schedule to observe laboratory-scale strain burst failure. If the sample did not fail within 30 minutes of unloading, the horizontal loading platen was placed again to resume the previously established minimum principal stress level. Now, the maximum principal stress increased to the pre-defined level, imparting more energy. After that, the minimum principal stress piston again gets removed to observe the potential bursting failure. This testing methodology recommends repeating the above loading-unloading cycles with continuously increasing maximum principal stress magnitudes until the sample failure. Figure 2.29 presents a brief outline of the results delineating the unique stress path for three different samples.

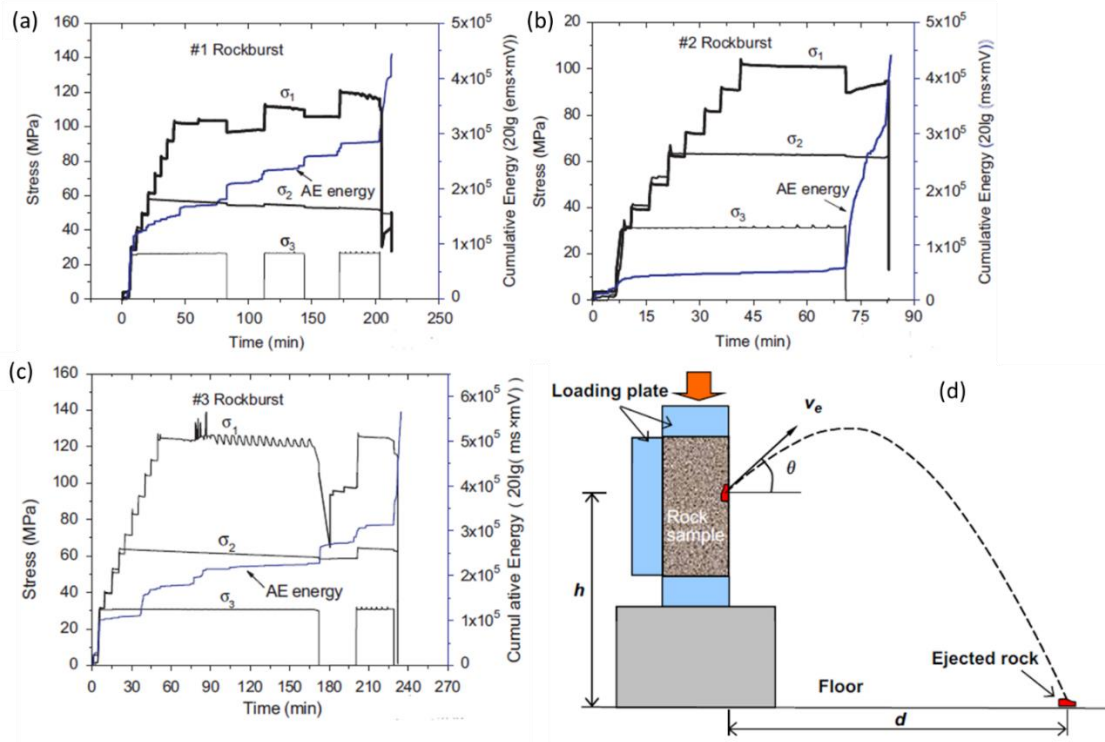


Figure 2.29: True-triaxial testing results using limestone rock type (He et al. 2010)

In the above experiment, the bursting failure of rock sample occurred in the range of σ_1 from 100 to 120 MPa. This σ_1 magnitude is close to the rock's uniaxial compressive strength (σ_c). However, it is not possible to generalize such observations as, in many cases, researchers witnessed the occurrence of strain-burst with in-situ maximum principal stress magnitudes much lower than the rock's uniaxial compression strength (Wu et al. 2010a). Besides, the bursting failure after the first unloading cycle was not evident in two out of three samples. The approach to re-loading with increased maximum principal stress appears to be an external effort to induce artificial bursting, which may or may not result in consistent, practical conclusions. Therefore, further investigation required to affirm its reliability.

The above experiment utilized the acoustic emission (AE) technique synchronized with stress-strain response to acquire a better insight into a sample's damage process. Also, a high-speed camera was used to record a sample's bursting observations where ejection velocity (v_e) of broken rock pieces was estimated as follows:

$$v_e = d \sqrt{\frac{g}{2h \cos^2 \theta + d \sin 2\theta}} \quad (2.20)$$

Where d is the ejection distance, g is the acceleration due to gravity, h is the height of ejection, and θ is the ejection angle assumed to be between 0° and 20° . The estimation of

this ejection velocity was more or less a qualitative add on to the observation of rock's bursting mechanism. The kinetic energy estimated from the above observations/calculations was still not enough to be linked with energy equilibrium formulations for quantitative analysis.

He. et al. (2012) attempted to explain the burst occurrence using stress concept with empirical Hoek-Brown failure criterion (Hoek and Brown 1980; Wawersik and Brace 1971; Czeczenska and Zuo 1986; He et al. 2012b). This study develops empirical criteria to determine rock mass strength and collaborates it with the stress-path of different bursting types to explain corresponding mechanisms. Figure 2.30 below presents a brief overview of strain-burst analysis.

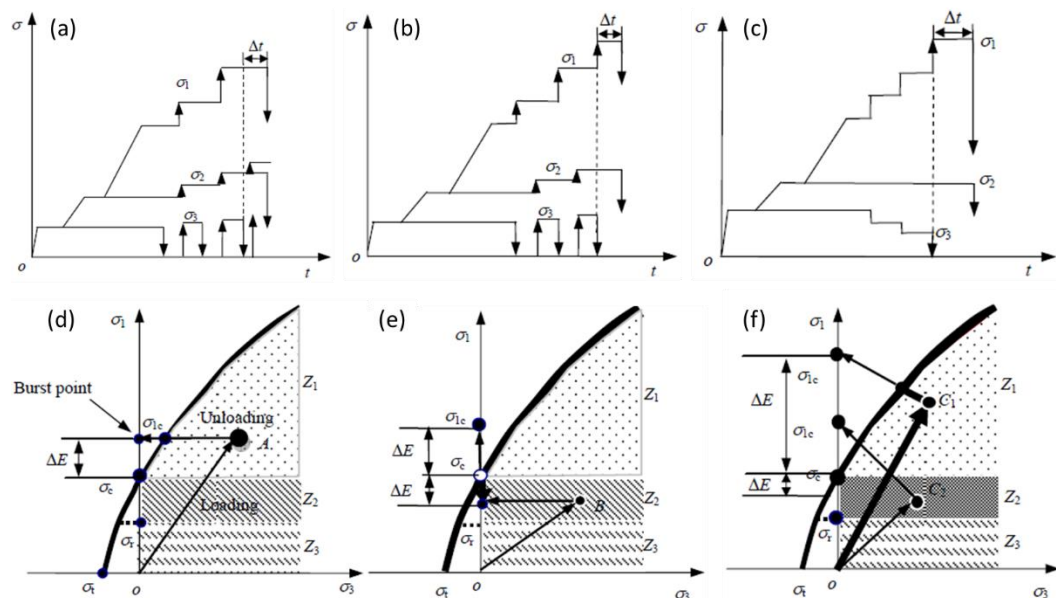


Figure 2.30: Summary of the bursting mechanism (He et al. 2012b)

Figure 2.30(a), (b) and (c) shows the loading-unloading path of instantaneous, delayed and pillar burst where figure 2.30(d), (e) and (f) presents the different stress paths using Hoek-Brown strength criterion. For instantaneous burst, one surface of the specimen was unloaded suddenly from the true-triaxial stress state to replicate the in-situ conditions immediately after excavation. Figure 2.30(d) uses the stress path to further explains this mechanism, where point A in the region Z_1 represents the initial stress state before excavation. Here, σ_c and σ_{1c} represents the uniaxial compressive strength of rock and maximum principal stress. It concludes that if in-situ maximum principal stress is greater than the uniaxial compressive strength before excavation, then unloading due to immediate excavation would cause bursting. However, one can contradict this conclusion

with several observations where strain burst occurred in stress-state with in-situ major principal stress below the σ_c of rock (Wu et al. 2010a).

On the other hand, vertically imposed load after the sudden removal of minimum principal stress characterizes the delayed burst loading-unloading path. Figure 2.30(e) shows the theoretical region encompassing that stress-state, which requires further loading after excavation to cause bursting. Physically, one can attribute this increase in vertically imposed stress to the increase in tangential stress and damage in the in-situ rock after excavation. In the event of pillar burst, excavation may result in a decrease in pillar size, lead by a gradual decrease in horizontal stresses (σ_2 and σ_3) while a significant increase in vertical stress (σ_1). Here, Z_1 and Z_2 are the potential burst prone regions with C_1 and C_2 as the initial stress state before excavation.

The above theoretical approach may provide a brief insight into the bursting mechanism up to a certain extent. However, there is no experimental, numerical, or any other evidence in support. Besides, the above approach is still dependent on the stress evolution changes, and it lacks a theoretical base to reasonably explain the bursting mechanism, which, in principle, is the energy-driven phenomenon. One can also question the representation of three-dimensional stress state evolution in two-dimensional space. There are many other limitations one could discern from the above approach. Primarily, the inability to address the following fundamental questions: which material parameters affect the bursting potential and how? Is it possible to link the material parameter with rock's bursting potential and eventually to real scale strain burst issue? Is the bursting phenomenon scale-dependent? If it is, then how can we derive the geometrical aspect of the bursting mechanism? There are many such key questions which the above presented experimental approaches could not answer.

Apart from above attempts, many researchers performed the true-triaxial experiments to explore the bursting behavior of rock (Jinli et al. 2011; Gong et al. 2013; Gong et al. 2015, 2014; Du et al. 2015; Zhao et al. 2014; Zhao and Cai 2015; He et al. 2015; Su et al. 2017; Wang et al. 2018; Dong et al. 2019a). The majority of these attempts could not contribute much beyond reporting the experimental observations despite collaborating the advanced instrumentation techniques AE and DIC. The prime reason behind this, as highlighted earlier, is the conventional approach based on stress-strain (or strength), is fundamentally incorrect and hence may not work well in the energy-driven phenomenon.

In particular, localized failure in the form of cracks or shear bands have been observed in these tests (e.g., figure 2.24), and as analyzed in my paper (Verma et al., 2019) the use of averaged stress-strain and specific energy as the area under the stress-strain curve is fundamentally incorrect or inappropriate. In this sense, one needs to analyze the energy storage and dissipation characteristics of a rock burst criterion considering the different scaling laws in energy storage (before localization, scaled with volume) and dissipation (scaled with the surface area). The theoretical framework for this difference has been established in (Nguyen et al. 2012, 2014, 2016; Nguyen and Bui 2019). It will be used and adapted for the theoretical development, experiments, analysis, and developments toward a size-dependent energy-based rockburst criterion in this thesis.

On the other hand, the other issues with these approaches are experimental limitations. For instance, the lack of visual access in true-triaxial testing methodology restrains the efficient application DIC techniques for capturing bursting images only. Few researchers attempted to utilize such fragmentation images to estimate the kinetic energy of flying fragments (He et al. 2010), which more or less are qualitative. One can always question the accuracy of such estimations considering the variations in fragmentation sizes and substantial dependability on the manual judgment. The other reason is the scarcity of useful experimental data, which could not only reveal the macroscopic/sample scale responses but could also provide insight into local scale behavior of rock material.

With this in mind, the one possible solution could be the use of numerical modeling approaches, which do provide flexibility in terms of performing rock's bursting analysis. The subsequent sub-section presents a detailed discussion on numerical modeling approaches in the field of rock's bursting analysis.

2.5 Numerical modeling base

The numerical modeling approach provides a better alternative, which has made it widely popular in the research community. Since the advent of advanced computing technologies, many numerical methods and modeling approaches developed, which one can broadly divide into two categories: continuum and discontinuum based. Continuum based approaches such as FEM, FDM, BEM, and corresponding numerical modeling techniques provide a computationally efficient platform to study the overall material response at a structural scale. However, frameworks of such numerical modeling techniques consider the assumption of continuity and homogeneity in the target domain,

which lacks the mechanism of automatic contact detection. They thus, cannot replicate discontinuities explicitly (Hammah et al. 2008). In advanced continuum numerical methods, researchers commonly use an interface material to simulate the discontinuities. Though, this logic also fails when the target domains have multiple intersecting discontinuities (Hammah et al. 2008; Lisjak and Grasselli 2014). The phenomenological approach via constitutive models could be the one way to capture the influence of discontinuities up to a certain extent. However, the majority of these phenomenological constitutive models are based on complicated constitutive equations designed to fit a given set of experimental data, which significantly lacks correlation with microstructural material response. It restrains the applications of such phenomenological approaches to the loading conditions inside the set of experimental data used for calibration. Thus, these approaches in literature have been mostly used to model field scale underground mining/tunneling projects with the intent to observe the in-situ deformation (Jiang et al. 2010; Manchao et al. 2012; Dong et al. 2018a; Dong et al. 2018b; Dong et al. 2019). It may provide a reasonable estimate to in-situ deformation, but the issue of bursting and the role of material scale parameters in causing burst is challenging to address.

To the contrary, dis-continuum based numerical modeling approaches utilize the explicit description of distinct elements. Such approaches have a natural ability to capture the discrete behavior of rock material explicitly, thus been widely used to study intact rock or rock mass behavior (Lisjak and Grasselli 2014; Lambert and Coll 2014; Kang et al. 2009; Jing and Hudson 2002). However, the realism of such numerical simulations to analyze intact rock behavior depends on two crucial factors: definition of material grains or grain aggregates and description of correct physics behind inter-granular interactions. In principle, rock material is an assembly of mineral grains of different shapes and sizes, interconnected via strong inter-granular cementitious bonds. However, incorporating the exact shape and sizes of various minerals in numerical simulation is an impossible task. Thus, every such numerical simulation requires certain assumptions to define material grains, which eventually endorse the extent of its practicality. For instance, the discrete element method (i.e., DEM) based numerical modeling technique, i.e., particle flow code (PFC), assumes material grains to be rigid blocks of round/disc shape (Potyondy and Cundall 2004; Lobo-Guerrero and Vallejo 2010; Bobet et al. 2009a). For any given dimension, round-shaped particles always have a minimum surface area. The assembly of such blocks will result in a higher void ratio comparatively. Such assumptions are

physically more appropriate for simulating soil, or weak rock material behavior, given that suitable inter-block interactions have been defined (Cheng et al. 2003; Yan et al. 2009; Nguyen et al. 2017; Schöpfer et al. 2009; Cho et al. 2007; Peng et al. 2017).

In the case of hard rock, geometrical features of material grains have a significant influence on overall structural stability, explained in terms of inter-granular locking and angularity (Potyondy and Cundall 2004). The use of round shaped particle assumptions in PFC most likely result in under-estimation of material strength as observed by many researchers (Potyondy and Cundall 2004; Bobet et al. 2009a; Peng et al. 2017). Researchers made several attempts to address this issue, which resulted in the development of Clumped Particle Logic (Peng et al. 2017), Smooth Joint Contact (Lambert and Coll 2014) and, Flat Joint Contact (Itasca 2008) treatments which are successful to a certain extent. However, all these attempts have increased the complexity in the existing DEM framework, giving rise to the use of several micro-parameters, which often lack physical significance and are difficult to calibrate (Mahabadi et al. 2010; Kazerani et al. 2010). Besides, the assumption of rigid particles in simulating intact rock material is efficient if the size of rigid particles in numerical simulation is of the order of actual grain size, which is computationally not feasible. In actuality, particle size in such simulations is decided based on computational efficiency, which eventually narrows down to the order of mineral aggregates size. Thus, rigid particles assumption in such simulations unconsciously neglects the deformational characteristics of grain aggregates, which has a significant contribution in actual rock deformation and fracture mechanism.

The two-dimensional hybrid numerical modeling tool, UDEC-Itasca (Itasca 2011), effectively addresses this issue. It idealizes the rock as an assembly of polygonal-shaped deformable particles without voids, which can efficiently produce zero initial porosity conditions commonly observed in hard rock (Bobet et al. 2009b; Y.M.Alshkane et al. 2016). Thus, in such conditions, the efficiency of numerical simulation predominantly depends on the theoretical description of correct physics behind inter-granular interactions. In reality, ahead of the actual crack tip, the strength of rock material at granular scale undergoes gradual decay, addressed in the '*cohesive zone model (CZM)*' concept proposed by Dugdale (1960) and Barrenblatt (1962) (Dugdale 1960; Barenblatt 1962). Competency of this concept to model uncracked material resulted in its wide popularity over conventional Linear Elastic Fracture Mechanics (LEFM) in continuum framework (Bažant and Yu 2004; Needleman 2013). Several discontinuum numerical

modeling frameworks incorporate this concept and consider to adopt a cohesive interface to capture the mechanism of inter-granular separation.

Consequently, many cohesive contact models for the discontinuum framework developed. The majority of earlier such models were either based on damage theory ignoring in-elasticity (explored in section 3.1 in details) or developed for mode-1 loading condition only (Needleman 2013; Elices et al. 2002). Kazerani et al. (2010) developed a cohesive fracture model for rock based on a damage-plasticity model with exponential elastic law (Kazerani 2013; Kazerani et al. 2010). However, the mechanism of plastic energy dissipation was not appropriate in the case of the stress-strain plot, where material resumes zero residual strain even after unloading from the inelastic regime. It also lacks the mechanism of capturing gradual de-cohesion in the shear loading case. Later, Gui et al. (2015) implemented a new cohesive fracture model UDEC to analyze soft rock behavior in-plane strain conditions, which efficiently incorporated the influence of irreversible plastic displacement. However, the computation of plastic displacement was not as per the theory of plasticity explicitly (Gui et al. 2015, 2016).

Based on earlier developments of thermodynamics-based coupled damage-plasticity approaches (Nguyen and Houlsby 2008; Nguyen and Korsunsky 2008; Guiamatsia and Nguyen 2012, 2014; Nguyen et al. 2015; Nguyen et al. 2017) also proposed a new and simpler cohesive model to address the above issue. However, it was developed for soft rock analysis and did not incorporate the influence of damage on material dilation (Nguyen et al. 2017). Despite all such attempts, the theoretical description of rock material's inter-granular interactions still requires further attention. Besides, the majority of the attempts mentioned above are restricted to two-dimensional cases. These are not competent to address the natural phenomenon like bursting, which operates under the polyaxial loading-unloading condition in three-dimensional space. Therefore, a three-dimensional robust numerical modeling approach is required to address critical issues like rock bursting.

Likewise, most such Hybrid/dis-continuum numerical modeling approaches are still being used to replicate field scale rock deformation via underground tunnel/mine simulations mainly (Jin-shan et al. 2007; Li et al. 2014). They lack the intent to address the fundamental issue of linking rock's bursting potential (significant for rock mass analysis as well) with its material properties. Even in the case of laboratory-scale numerical simulations, most attempts are limited to replicating the sample scale stress-

strain behavior under any given loading conditions. Not much effort put on exploring the bursting mechanism using numerical modeling approaches, which, in principle, would provide a sturdy base. The prime reason behind this could be the lack of competency to capture the rock material behavior outside the calibrated data set. A straightforward way to analyze this could be the double scale validation approach where numerical simulations intend to capture both sample and local scale rock material deformation from a single set of calibrated parameters. It further highlights the importance of enriched experimental data, which could provide both local and sample scale deformational response.

2.6 Summary and discussion

This literature review highlights the importance of the energy aspect to analyze the brittle fracturing and bursting behavior of rock. Consideration of the role played by material properties controlling strain energy storing and dissipation characteristics are paramount. There are different approaches to determining such vital properties. Experimental approaches in this direction could play an important role provided that enough control over the cracking mechanism is possible. For instance, controlled cracking in uniaxial compression enables us to capture the snap-back characteristics. It indicates the strain energy storing and releasing characteristics of rock under compression. Besides, most researches about rockburst analysis still focus on the empirical linkage of key energy parameters with bursting predictions. Such approaches may be easy to use but do not provide useful insight into rock bursting potential. The chief reason for this limitation is the explicit dependence on the conventional stress-strain response, which is not only scale-dependent but also fundamentally incorrect.

The other simple, but quite effective, experiment in terms of rock's material property evaluation is the Brazilian disc test. This experiment is widely popular for indirect tensile strength estimation, which often is not accurate in comparison with the direct tensile strength test. Scale dependency is the other aspect that again highlights the issue of conventional stress-strain dependency. Additionally, a noteworthy limitation of such experimentation is its uncontrolled dynamics associated with disc cracking, as in unstable cracking in a split-second time frame window. It does not allow the efficient application of advanced instrumentations, including DIC and AE. Require control in sample cracking in this experimental setup may add a new dimension. It may also allow the efficient application of advanced instrumentation towards material scale strength property

evaluation. This strength property will be scale-independent, accurate, and more reliable. Most importantly, it will allow us to evaluate rock material's energy characteristics, including fracture properties, relevant to burst potential evaluations.

In terms of boundary conditions, several unloading based experimental approaches (including triaxial and true-triaxial loading-unloading conditions based) are available. Majorities of these approaches are limited to reporting the experimental observation with little to no contribution towards the linkage of material properties with burst potential. There has not been any study or any theoretical framework available, to the best of my knowledge, which enables us to estimate the bursting potential of rock inside rock mass using critical factors including material scale energy parameters, geometrical characterization of rock blocks inside rock mass and the boundary or in-situ conditions. Such a framework requires the theoretical development and analysis of the correct fundamental of localized failure in rocks and similar materials. The importance and significance of such strength- and energy-based approach in analyzing data and formulating constitutive models that can bridge meso and macro scales have been addressed and illustrated in a series of recent papers (Nguyen et al. 2012, 2014, 2016; Nguyen and Bui 2019; Le et al. 2018; Le et al. 2019; Wang et al. 2019; Tran et al. 2019). The concept of combining strength and energy evolutions put forward in these papers will be adapted and used for the developments in this thesis.

We need to develop a methodology of systematically linking the strain energy-storing/releasing characteristics of rock material with its bursting potential. Based on that, we should also be able to test the above linkage using different loading-unloading induced boundary conditions changes. These two requirements require the combination of experimental, theoretical, and numerical modeling approaches to obtain essential strength and energy properties and to embed these properties in both theoretical and numerical developments for analyzing and predicting rock bursts. The following aims list the steps needed to pursue the proposed research direction.

2.7 Research aim and objectives

This research aims to develop a systematic approach to link rock material properties (which controls its strain energy characteristics) with its bursting potential, thus evaluate the bursting mechanism of rock inside rock mass around deep underground openings.

This task is quite challenging and requires the systematic collaboration of experimental, numerical, and theoretical approaches.

In this view, the first objective of this research is to determine the key parameters controlling strain characteristics of rock and utilize it to provide a preliminary basis for bursting potential analysis. For this purpose, this research develops an innovative methodology to control the dynamics associated with the sudden cracking of disc samples under diametrical compressive loading. Advanced instrumentation, including DIC and AE, are also used to demonstrate the significance of controlled cracking in evaluating material scale properties. This research also performs the uniaxial compression tests to obtain the required parameters relevant to the subsequent numerical development. Chapters 3 and 4 present a detailed discussion of the first objective of this thesis.

The second objective is to develop a robust numerical modeling framework that can not only capture the sample scale load-displacement response but also replicate the local-scale deformational behavior. For this purpose, this research improvises the hybrid numerical modeling based 3DEC-Itasca by developing and embedding a new cohesive contact model. This model is verified and validated under different loading modes. The experiments performed during the fulfillment of the first objective provide the base for the calibration of the developed numerical modeling suit. This calibrated suit is further validated with experiments, including uniaxial compression and conventional Brazilian disc tests. Validation at both local and global scale responses performed. Chapter 5 presents the details of the work done towards objective two.

The final objective of this research is to link the material properties with the bursting potential of rock and use this linkage for strain burst prediction analysis. For this purpose, this research develops a size-dependent energy-based theoretical framework to predict the bursting failure in the rock under true-triaxial loading-unloading conditions. Prediction of bursting failure of rock are made using the proposed theoretical framework, and the critical material properties obtained from objective 1. The numerical modeling tool developed in objective two is used to perform virtual strain burst experiments. These experiments facilitate the validation of the theoretical framework for rock's bursting potential evaluation. This research further utilizes the overall setup to study the influence of other important factors, including specimen size and in-situ stress/loading-unloading conditions on the overall bursting potential of rock. At last, this study presents a brief

discussion on the broader concept of strain burst occurrence in deep underground conditions using the proposed size-dependent energy-based strain burst criterion.

Chapter 3

A Novel Control Method for Brazilian Disc Test to Capture the Snap Back Behavior

3.1 Introduction

The use of circular-shaped disc samples is widespread, especially in the Brazilian disc testing approach, to obtain indirect tensile strength primarily. The ease in specimen preparation (i.e., because of simplistic circular shape) and low execution cost has made its applications popular in evaluating the strength parameter of rock, cement, concrete, ceramics, glass, and even tablets, i.e., pharmaceutical industry (Mazel et al. 2016; Nyonguè et al. 2016; Zhang et al. 2018; Candamano et al. 2019; Wang et al. 2019). However, all such experimental approaches based solely on diametrical compression of disc samples are very unstable where specimen cracks abruptly in a fraction of seconds. Consequently, load measurement drops suddenly immediately after peak load, which makes it practically impossible to capture the actual post-peak material response. A thorough search of existing technologies/methodologies, including patent and various research articles, shows the absence of attempts made to control the dynamics of the disc sample's instant failure. Table 3.1 below presents a summary of existing patents/technology.

Table 3.1: Patent search result

Sr. No.	Patent search engine	Country	Search result
1	Intellectual Property Australia	Australia	NA*
2	New Zealand Intellectual Property Office (NZ IPO)	New Zealand	NA
3	The United States Patent and Trademark Office (USPTO)	USA	NA
4	European patent office (EPO)	Europe	NA

5	Canadian Intellectual Property Office (CIPO)	Canada	NA
6	Korean Intellectual Property Office (KIPO)	Korea	NA
7	Intellectual Property China	China	NA
8	Intellectual Property Japan	Japan	NA

Keywords: Brazilian disc test, indirect tensile strength test, circular disc test, tensile strength of rock, rock tension, circular disc, fracture energy, fracture toughness, lateral strain-controlled Brazilian disc test, controlled circular disc, lateral control, disc, controlled fracture, controlled cracking.

Thus, it infers that the invented methodology is the first attempt of its kind and potentially is a crucial advancement in the broader range of brittle material-based research. It enables us to capture the possible snapback behavior of load-displacement response, which is essential for the measurement of energy-based parameters. It allows us to obtain both tensile strength and mode-I fracture energy using a simple testing setup. Additionally, one can also determine the critical material properties like fracture energy, fracture toughness, and material brittleness, i.e., all from one simple experiment. Furthermore, it also allows the applications of advanced experimental techniques like X-ray tomography and Digital Image Correlation (DIC) to obtain material property at the local scale, thanks to the controllable experiment. The measurement of direct tensile strength using a disc sample could be a potential outcome of the DIC collaboration with the invented methodology. It is a much-needed technical development in the field of rock mechanics where preparing complex-shaped samples for experimental evaluation has always been an unresolved issue.

3.2 Theoretical aspect: Brazilian disc test

3.2.1 Conventional (Axial strain controlled) Brazilian Disc test

In conventional Brazilian disc tests, deformation caused by diametrical compressive loading tends to accumulate the strain energy in the disc sample. Once this accumulated strain energy exceeds the limit, the material starts losing the additional energy components via dissipation and release forms. This evolution of stored strain energy, in principle, controls the fracture mechanism in the given rock sample. The load-displacement response is just the by-product of this strain energy evolution.

In this view, one can divide the possible responses from the conventional Brazilian disc tests into the following two categories: ductile (I) and brittle (II) type, as shown in figure 3.1. In case I, the energy required for central diametrical cracking (i.e., first crack) is higher than the accumulated strain energy under the elastic limit. Consequently, the additional energy demand to maintain a stable fracturing results in ductile post-peak behavior where one can easily control the strain energy supply from external loading.

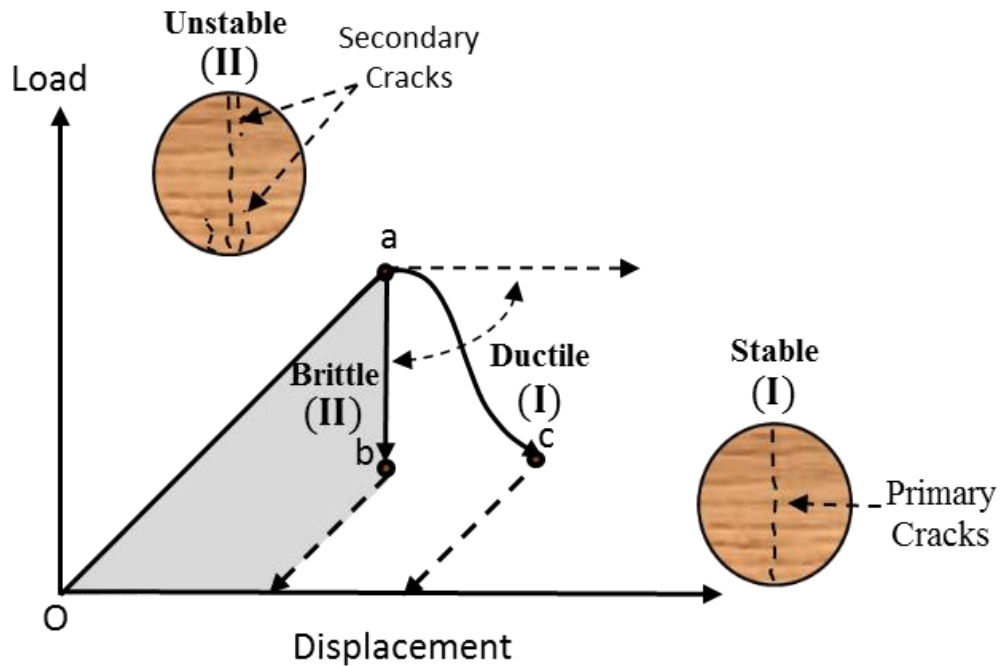


Figure 3.1: Conventional Brazilian disc test

As the dissipation capacity (i.e., the energy released per unit area) of material reduces in comparison with the stored elastic strain energy, the load-displacement response starts switching from case-I to II type. Under case-II type, sudden failure of disc specimen immediately after the peak is a common observation. The anticipated theory behind this instant failure is that: the constant vertical displacement of the loading platen at each step increases the overall lateral strain; thus, the increment in stored strain energy. At peak stage, load increment supplies energy added to the material's capacity to maintain overall structural stability. Consequently, it induces instability and stimulates energy dissipation causing material damage, thus immediate structural failure to release the stored (i.e., including unbalanced) energy component.

To further explore, this study conducts a conventional Brazilian disc test on sandstone rock type. Four disc-shaped samples with an aspect ratio of 1:2 (i.e., with 63 mm

diameter) utilized to conclude the results from this experiment. Three strain gauges attached on the front face of the sample to record the localized lateral strain variation throughout the test. Each sample diametrically compressed via flat loading plate (i.e., as per ASTM standards) with 0.5 mm/min (i.e., displacement control) as axial displacement rate, i.e., as per the quasi-static loading conditions. These experiments utilize Linear Variable Differential Transformers (LVDTs) to measure the vertical axial deformation of the specimen. Additionally, the front surface of samples sprayed with black and white paint to create random black speckle patterns on the white base. It enabled the application of the Digital Image Correlation technique (DIC) for the analysis of full-field strain evolution. The acoustic emission sensor also attached to the backside of the sample. Figure 3.2 below presents the preliminary results of the material's macroscopic response along with AE energy evolution.

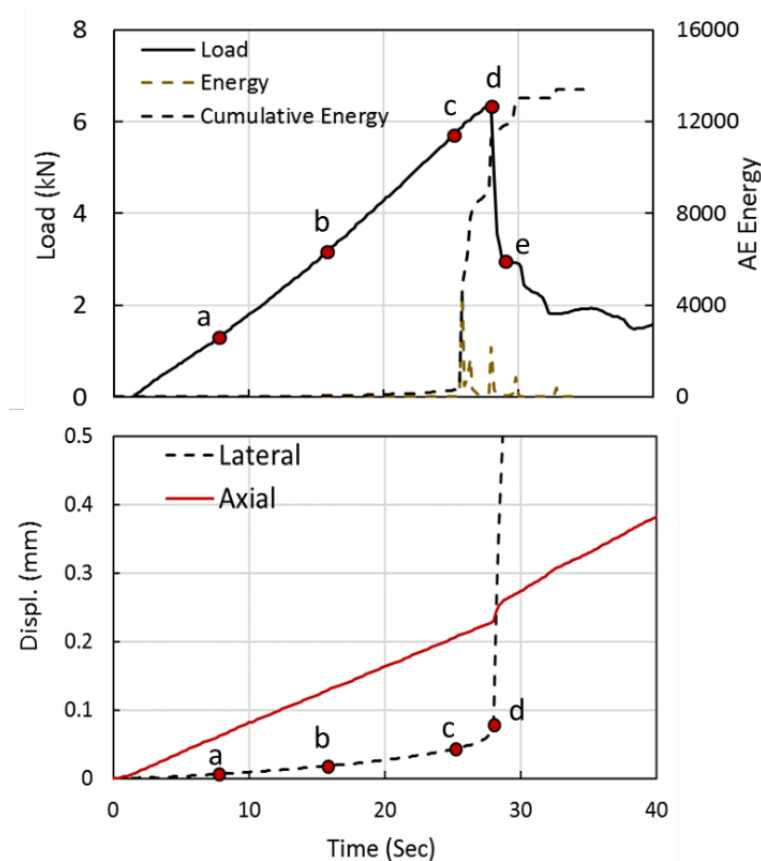


Figure 3.2: Brazilian disc test on Hawkesbury sandstone

Figure 3.2 shows the variation of load, axial, and lateral displacement along with AE energy evolution with time. These experiments utilize the proposed AUSBIT

instrumentation only to measure the lateral strain. Section 3.3 presents the detailed description and potential applications of the proposed AUSBIT approach.

Overall, the axial and lateral displacement of the disc sample increases uniformly from point ‘a’ to ‘c’ under constant axial displacement conditions. It results in a stable increase in load with insignificant AE activity to point ‘c.’ After that, the lateral displacement of the disc specimen deviates from linearity. It accompanies increased AE activity, indicating the advent of pre-peak material damage. At peak loading point ‘d,’ the sudden jump in the lateral displacement along with cumulative AE energy release rate occur while keeping the overall axial displacement rate constant. It indicates the localized inelasticity and rock material damage across the central diametrical axis. This localized inelasticity causes a sudden drop in observed load-displacement response, indicating the uncontrolled failure of disc specimen, as shown in figure 3.3 below.

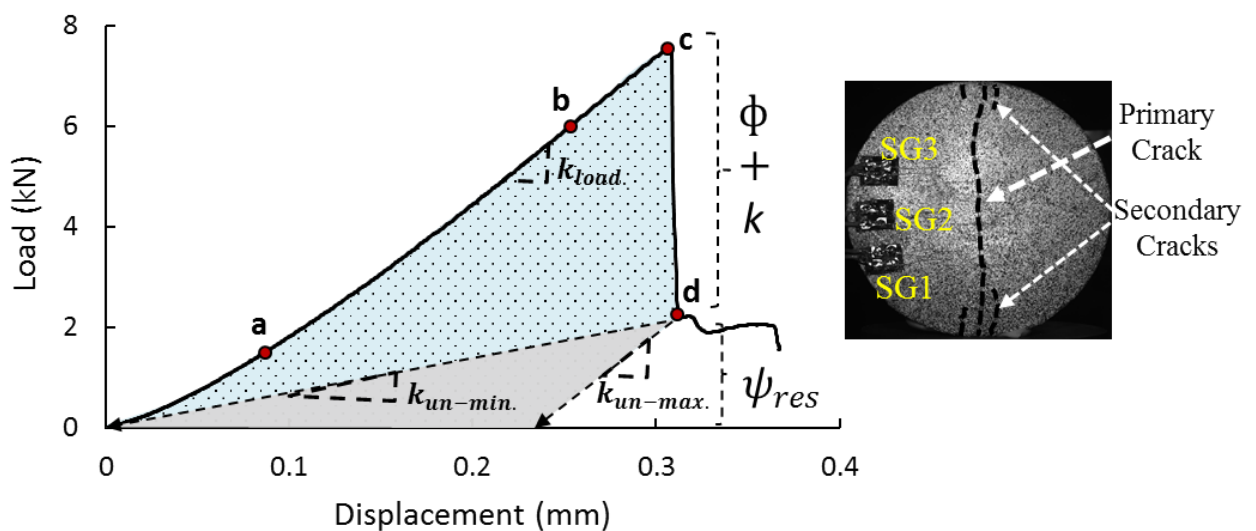


Figure 3.3: Conventional Brazilian disc test – load-displacement response

One can use the above load-displacement response of the disc sample in figure 3.3 for the evaluation of energy consumed in the process of diametrical disc sample cracking provided that a reasonable estimate of unloading modulus at point ‘d’ is known. Here, the shaded portion in the color blue indicates strain energy dissipated during material fracturing (ϕ) and energy additional to fracture requirement (k), i.e., elaborated in figure 3.5 as well. The latter induces dynamics to the cracking mechanism. The estimation of ϕ also requires unloading stiffness. One can consider two possible simplifications for unloading stiffness i.e. $k_{un-min.}$ and $k_{un-max.}$, as shown in figure 3.3 above. The first case (i.e., $k_{un-min.}$) physically implies zero residual strain after unloading, which

contradicts the practical observation of permanent deformation in disc sample at point 'd'. Therefore, this study adopts the second case simplification. Figure 3.3 also presents the cracked specimen after test completion, which shows the sign of several secondary cracks along with major vertical crack. It confirms that the energy available at peak load (i.e. Σ_{peak}) is higher than required for primary crack (i.e., ϕ) explaining the unstable fracturing of disc sample and abrupt release of strain energy components (i.e., AE energy jump) excluding residual (i.e. ψ_{res}) part. The overall energy balance condition explaining the observed uncontrolled mechanism summarises as below:

$$\Sigma_{peak} = \phi + k + \psi_{res} \quad (3.1)$$

Where,

$$\Sigma_{peak} \gg \phi \sim \text{Unstable Fracture} \quad (3.2)$$

Here, the residual strain energy component (i.e., k) represents the resistance of the broken rock sample to axial displacement, which does not have any physical significance in terms of material property evaluation. While ψ_{res} is the energy component additional to fracture requirement controlling the velocity and magnitude of sudden load drop. Higher k implies higher energy additional to fracture requirement. The ϕ component governs the material damage, and one can link it explicitly with fracture requirement provided that the disc sample fails stably. This energy component is a material property free from geometrical aspects and loading conditions. If known, it could reveal the material characteristics in terms of energy release rate, fracture toughness, strain energy storing capacity, and material brittleness. Nevertheless, it is impossible to determine ϕ under conventional Brazilian disc experimental setup where the k component of stored strain energy additional in the post-peak regime is difficult to control.

3.2.2 Proposed approach: Snapback factor ($\$$) – an Energy concept

In this view, the proposed experimental approach aims to control the instant diametrical cracking of the disc sample by systematically controlling the k strain energy component. From section 3.2.1, one can infer that lateral strain is the key to control the diametrical cracking in the disc sample. Therefore, this study proposes to use the loading frame's servo-control mechanism and maintain a constant lateral strain rate by continuously adjusting the axial loading rate, especially when approaching the peak load.

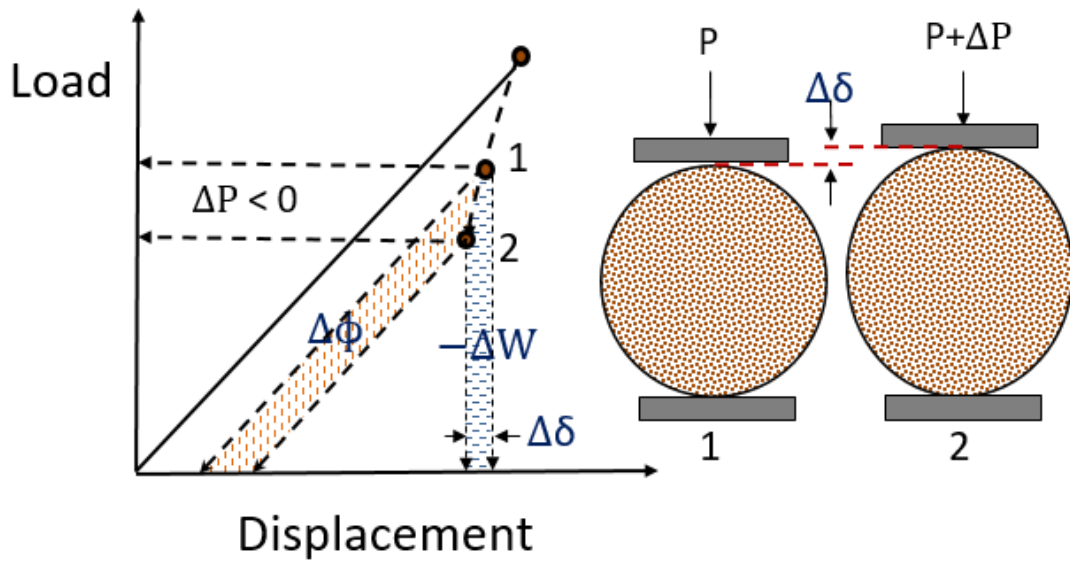


Figure 3.4: AUSBIT functioning

Figure 3.4 presents the functioning of the proposed approach using energy conservation principles, where the change in external work (ΔW) controls the change in the stored strain energy ($\Delta \Psi$) and dissipation ($\Delta \phi$) energy components. This ΔW change is further controlled by the external load (P), causing the compression ($\Delta \delta$) of the disc specimen, i.e., $\Delta W = P\Delta \delta$. Here, $\Delta \delta$ is considered positive under compression. Thus, when rock material starts yielding across the central diametrical axis, the servo-control mechanism of the loading frame reduces the $\Delta \delta$ by systematic unloading (i.e., negative $\Delta \delta$) to compensate for the additional lateral strain-induced due to material inelasticity in the lateral direction. Under these circumstances, the change in stored strain energy ($\Delta \Psi$) becomes negative i.e., considering the $\Delta \phi$ component positive always. Equation of 3.3 summarises the above functioning of AUSBIT in energy conservation principles as follows.

$$\Delta W = \Delta \phi + \Delta \Psi$$

$$\Delta \Psi = \Delta W - \Delta \phi \leq 0 \text{ (under systematic unloading)} \quad (3.3)$$

Where,

$$\Delta W \leq 0 \text{ as } P\Delta \delta \leq 0$$

The negative sign of $\Delta \Psi$ component indicates that the systematic unloading ($\Delta \delta < 0$) tends to extract the specimen's stored strain energy. Consequently, the target rock sample

consumes the only component of stored strain energy enough for primary vertical crack. This mechanism of systematic loading-unloading releases the additional strain energy (k) component to ensure the stable cracking of the disc sample. Under such conditions, one could reasonably anticipate the snapback characteristics of the load-displacement response similar to the class-II behavior of lateral strain-controlled uniaxial compression (UCS) tests, as shown in figure 3.5 below.

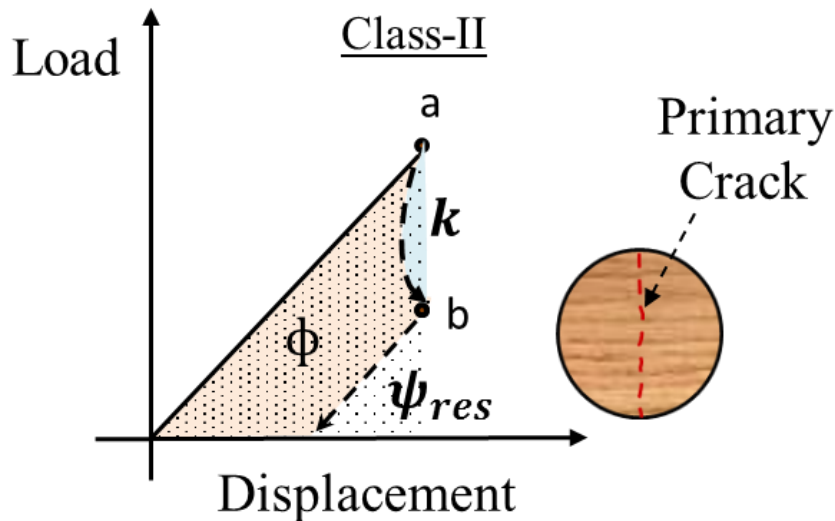


Figure 3.5: AUSBIT class-II load-displacement response

The key benefit of the proposed approach would be the accurate estimation of crack surface area, which is mostly diametrically vertical along the loading direction. It provides ease in fracture energy calculation (i.e., figure 3.5), which is not possible in conventional Brazilian disc tests and lateral strain-controlled UCS tests. Subsequently, it could reveal the contribution of ‘released’ (i.e. k), ‘residual’ (i.e. ψ_{res}) and ‘dissipated’ energy (i.e. ϕ) components in total stored strain energy at the peak loading stage.

Further, this chapter extends the above theoretical framework to predict the magnitude of potential snapping-back in the load-displacement response obtained from controlled indirect tensile strength tests. This snapback feature of load-displacement response is dependent on total strain energy stored at peak load (Σ_{peak}) and the energy required for the complete failure of the disc sample with single vertical crack, i.e., dissipation capacity (ϕ). The prior energy component can be computed from the following expression if the sample’s geometry (i.e., radius ‘ R ’ and thickness ‘ t ’), tensile strength (σ_t) and the elastic material property (i.e., elastic modulus ‘ E ’), are known.

$$\Sigma_{peak} = \alpha(\pi t R^2) \frac{\sigma_t^2}{2E} \quad (3.4)$$

This study utilizes factor α in the above expression (3.4) to incorporate the influence of non-uniformity in stress distribution across disc specimens. It can be determined using finite element or finite difference based numerical modeling tools, e.g., ABAQUS and 3DEC-ITASCA. Section 3.5.4 presents a brief example of α determination using a numerical modeling approach. Expression (3.5) presents the estimation of dissipation capacity.

$$\phi = 2tRG_f^1 \quad (3.5)$$

Here, G_f^1 is the mode-1 fracture energy. Using eq. (3.4) and (3.5), this chapter proposes the following parameter (\S) to quantify the magnitude of snapback.

$$\S = \frac{\Sigma_{peak}}{\phi} = \left(\frac{\alpha\pi R}{4}\right) \left(\frac{\sigma_t^2}{EG_F}\right) \geq 1 \sim \text{Class-II potential} \quad (3.6)$$

The \S is termed as the ‘*snapback*’ parameter. The higher magnitude of \S indicates a higher potential of snapping back of load-displacement response in the post-peak regime. One can anticipate this behavior in hard and brittle rock, e.g., granite, which can retain much higher elastic strain energy in the pre-peak regime as compared to the fracture requirement. It also indicates the higher bursting potential of rock on a preliminary basis; higher snapback indicates the relatively higher strain energy compared to rock’s fracture requirement. This typical trait of hard rock helps it in exhibiting class-II behavior in lateral strain-controlled UCS tests (Wawersik and Fairhurst 1970; Hudson et al. 1971; Wawersik and Brace 1971; Okubo and Nishimatsu 1985; Shimizu et al. 2010). Besides, expression (3.6) indicates the dependency of \S on two different factors: material property (i.e., E , σ_t and G_F) and sample geometry (i.e. R). Figure 3.6 presents the detailed description the \S variation with above parameters.

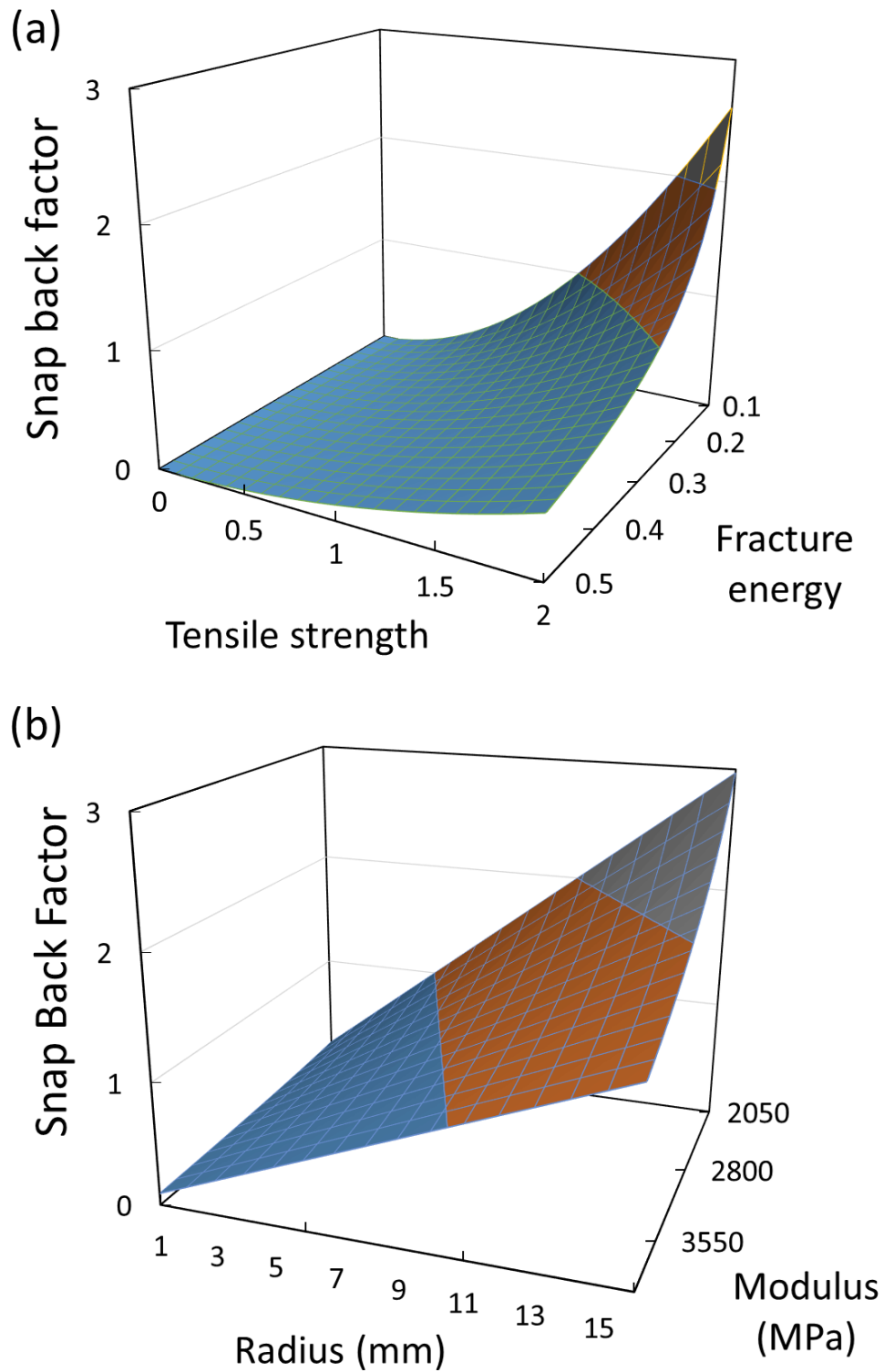


Figure 3.6: Variation of snapback factor with test specimen's (a) material aspect, (b) geometrical aspect

One can observe in figure 3.6(a) that for different materials with the same tensile strength and fracture energy, one with higher stiffness will have higher snapback potential.

Similarly, a material with the same stiffness and fracture energy, one with higher tensile strength, will have higher snapping back possibility, keeping the specimen geometry constant, i.e., figure 3.5(b). Additionally, potential snapping back will always increase with the increase in specimen geometry.

3.3 Proposed approach: Methodology

This section presents the experimental setup specifically developed to control the sudden cracking of disc samples and incorporate the above theoretical framework in the practical scenario.

3.3.1 Testing setup

Figure 3.7 presents a brief overview of the overall setup of the invented methodology. Here, the MTS loading frame (i.e., Model – LPS305) with a capacity of 300 kN, the sensitivity of 2.88 mV/V, was used to apply the vertical diametrical compressive load on the disc sample. The machine should have very high stiffness as compare to the rock specimen to ensure the negligible elastic energy stored during experiments. The loading plates are flat (i.e., figure 3.7g). At the same time, two vertical Linear Variable Differential Transformers (LVDTs) are used to record the vertical strain in the circular disc, as shown in figure 3.7(h). The loading machine has an inbuilt closed-loop servo-control system in the digitized form, which ensures flexibility in controlling load as per the pre-defined axial or lateral strain rate. This study also designs and develops a 3D printed plastic holder (or cap) to rigidly hold the LVDT across the horizontal diametrical axis of the disc sample. The feedback received in the form of lateral displacement will be used to control the axial loading rate via the servo-control mechanism. When the lateral strain rate across the central diametrical axis exceeds the pre-defined limit due to material inelasticity, the servo-control mechanism triggers the reduction (or even unloading if required) in the axial loading rate. Consequently, stress relaxation across the central diametrical axis accompanied by energy release takes place inducing snapping-back characteristics of the load-displacement response.

Table 3.2: Component description

Symbol	Detail	Symbol	Detail
a	MTS loading frame	h	DIC-camera
b	Top and bottom loading plates	i	DIC-light source

c	Holder	j	Sample front
d	AE sensor	k	AE sensor connection
e	Lateral LVDT	l	MTS-data acquisition
f	Cylinder for sample level (DIC)	m	DIC/AE
g	Axial LVDT		

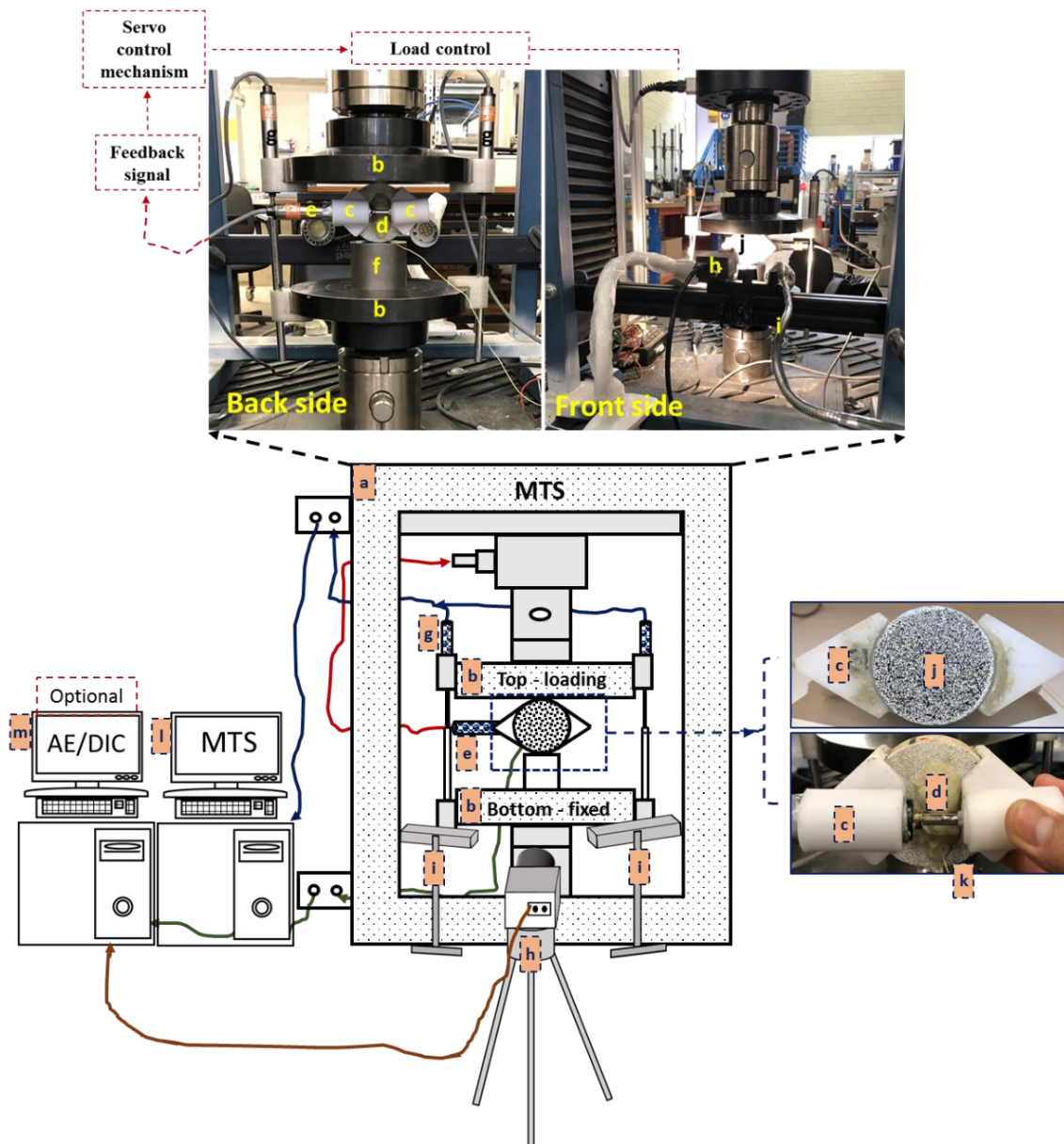


Figure 3.7: Detailed overview of the testing setup

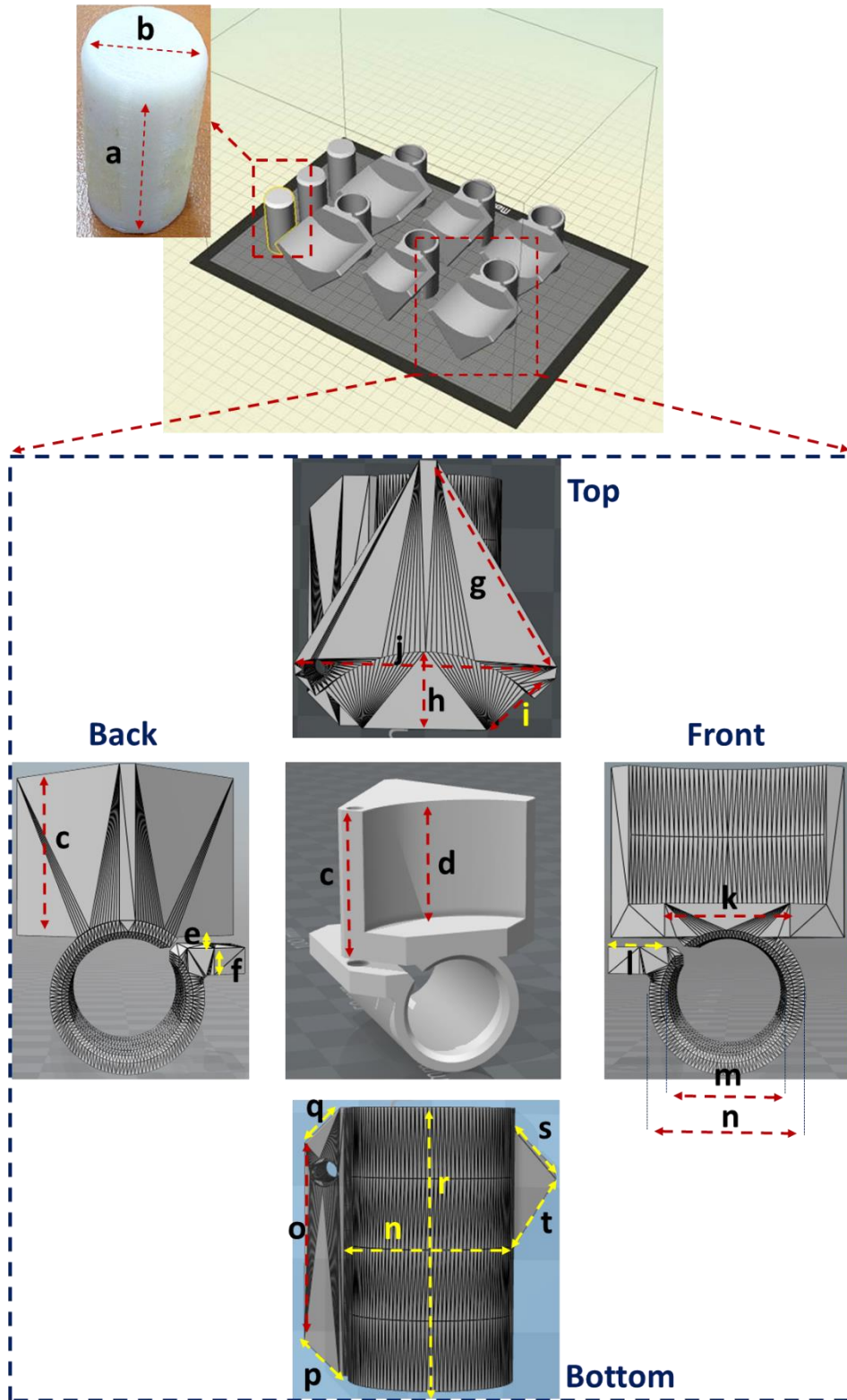
3.3.2 Technique for measuring lateral strain

In order to monitor the variation in the lateral strain rate, this study suggests the use of conventional LVDT. This LVDT is mounted laterally across the horizontal diametrical

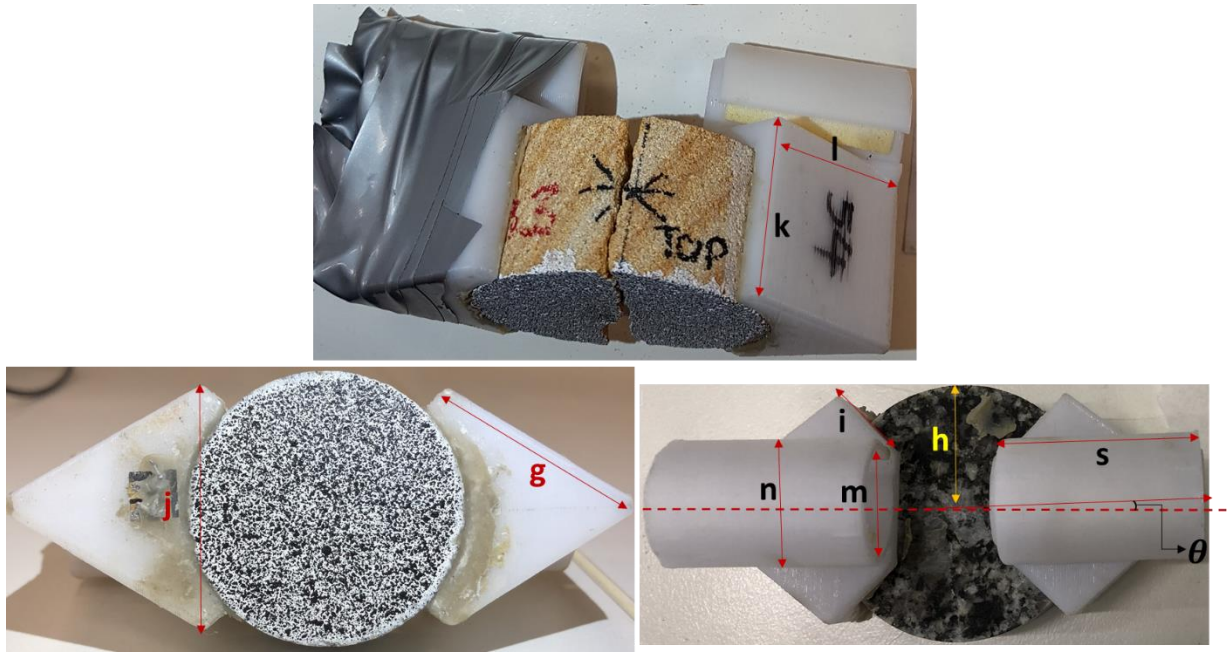
axis of a circular disc sample using the LVDT holder. The subsequent sub-section presents a detailed description of holder design and its practical application.

3.3.2.1 3D printed plastic cap

For recording the continuous variation of lateral strain throughout the test, this study designs the LVDT holder (or holder) and develops it using 3D printing technology. Figure 3.8 presents a detailed description of the holder design, along with the final sample setup after practical execution.



(i)



(ii)

Table 3.3: LVDT holder design

Symbol	Dimensions (mm)	Symbols	Dimensions
a	$D1 + 0.2$	l	20 mm
b	2a	m	a
c	$D3 + 5$	n	$\sim a + 5$
d	D3	o	$0.66 D2$
e	5	p	$0.17 D2$
f	5	q	$0.16 D2$
g	34 ± 2	r	38
h	$0.28 D2$	s	$0.2 D2$
i	$0.29 D2$	t	$0.38 D2$
j	$0.714 D2$	θ	± 20
k	$0.44 D2$		

Where,

D1 = LVDT diameter (in mm)

D2 = Sample diameter (in mm)

D3 = specimen thickness (in mm)

Figure 3.8: LVDT holder specifications (i) design details, (ii) practical applications

3.3.2.2 Bonding between the plastic cap and disc sample

The time frame window for triggering the servo-control response is concise, i.e., the fraction of a second. Thus, a stronger bond between holder and LVDT is required to ensure a swift response of the loading frame with a lateral strain signal. For this purpose, this study suggests the use of permanent glue named ‘Plasti-Bond Heavy-duty BOG,’ as shown in figure 3.9. It is a multi-purpose plastic putty, widely used for repair or building works where high bond strength is required. One can use this in a variety of brittle materials like concrete, rock, cement, glass, ceramic, fibers, tiles, and brick. The key characteristics of this multi-purpose putty, delineating its applicability on a broader range of engineering and non-engineering material types, are as follows:

- a) Appearance: Olive green.
- b) Working time: 5 to 8 minutes at 250C temperature.
- c) Set time: 20 minutes at 250C temperature. One can shorten this time, depending on the amount of hardener used. Usually, putty and hardener ratio is 1:3.
- d) Service temperature limit: -280C to + 1900C temperature.
- e) Lap shear, tensile adhesion strength on steel: 8 MPa.
- f) Shrinkage: Negligible.
- g) Chemical resistance: To acids, oils, alkalis, fresh, and saltwater.



Figure 3.9: Strong bonding between cap and disc sample

Further application sequence of above permanent glue is also essential for efficient sample preparation. Following is a brief overview of the above sequence:

- a) Clean the sample’s lateral surface properly and apply removable tape covering to provide temporary protection from dust particles.

- b) Clean the inner surface of the holder properly and apply removable tape temporarily to avoid the deposition of dust particles (figure 3.10).
- c) Insert plastic closure in one of the caps with as shown in the figure below.

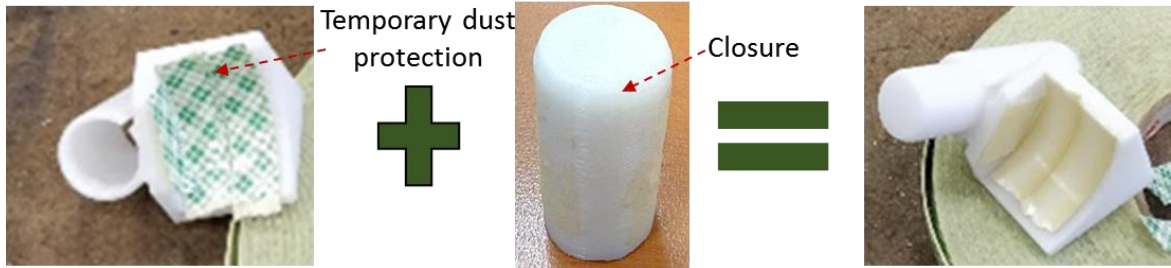


Figure 3.10: Dust protection

- d) Take approximately 2-3 gm of the plastic-bond putty on the strip along with hardener, as shown in figure 3.11. The ratio between the putty and hardener should be 1:3 approximately.



Figure 3.11: Plasti-bond putty

- e) Thoroughly mix the putty and hardener for not more than 5 minutes.
- f) Remove the temporary tape protection and apply the putty-hardener mixture uniformly on this inner surface of the holder.
- g) Quickly remove the tape on the outer surface of the sample and manually attach the above holder part with putty-hardener paste on the outer surface. Press the holder tightly across the sample to 2 minutes.
- h) Keep this attached part of the holder with the sample undisturbed for 25 minutes.



Figure 3.12: Specimen and holder bonding

g) Check the bond between the holder and the sample manually. If the bond is not permanently set, let it dry for a few 15 minutes more. One can also increase the hardener content slightly for the next cap to set the cap across the sample quickly.

h) Repeat the step ‘d’ to ‘h’ on the second part of the holder over the other lateral surface of the sample. The angle of inclination of the lateral holder axis with horizontal must not vary more than $\pm 2^{\circ}$. Figure 3.13 below presents the final attached sample along with the holder.



Figure 3.13: Finalised sample

h) Optional: Attach the AE sensor at the backside of the sample using attaching glue and AE gel.

i) Insert the LVDT in the second portion of the holder already attached to the sample. Make sure the firm hold of LVDT by the holder. One can also use a few layers of power tape over the LVDT surface to increase the friction between the holder and LVDT. Figure 3.13 presents the final sample ready for testing.

Note: It is important to note here that circular discs in the above description can be of different materials and shapes (with or without hole). It demonstrates the applicability of invented methodology on a broader range of material types and experimental approaches.

3.3.2.3 Other specifications

It is essential to ensure secure contact between LVDT (Linear Variable Differential Transformer) and the holder. This study suggests applying two to three layers of commercial tape on the LVDT surface, as shown in figure 3.14 below. It strengthens the hold of the cap on inserted LVDT.



Figure 3.14: Smooth contact between disc sample and loading plate

Further, contact between the sample surface (i.e., top and bottom) and the loading plate must be smooth, as shown in figure 3.14. It is because the potential unevenness of the specimen surface may influence its contact surface with the loading platen. It may further disturb the stress distribution to cause stress concentration or even buckling effect (i.e., instead of pure diametrical cracking). Thus, it may influence the feedback of lateral LVDT (i.e., inducing lateral compression instead of extension) placed at the rear face of the sample. As a result, it may trigger the increased loading rate instead of reduction, causing uncontrolled failure.

3.3.3 Loading mode and strain rate determination

Before starting the actual testings, this study ensures the viability and determine the suitable loading rate by performing dummy experiments on sandstone samples of 42mm diameter. It indicates the success of approximately 1.6×10^{-4} μ strain/sec lateral strain rate to facilitate the control over sample cracking mechanism. A higher lateral strain rate resulted in uncontrolled cracking while lower triggered unloading. The finalized rate of lateral strain-controlled loading could reduce the overall axial loading rate below the quasi-static loading conditions (i.e., approx. 1×10^{-4} strain/sec or below). It significantly increases the overall test duration. Thus, this study adopts the combination

of axial and lateral strain-controlled loading approach to optimize the overall test duration. For initial 0.6 times (i.e., approximately) of anticipated peak load is applied via conventional axial strain control approach with 2×10^{-5} strain/sec rate. After that, the lateral strain-controlled loading approach is adopted, which continues until the completion of the test. One can vary the point of switching loading approach (i.e., from axial to lateral strain-controlled) depending on the anticipated peak strength and material type.

3.3.4 Feasibility demonstration

This study uses three different rock types, i.e., Hawkesbury sandstone (Hon et al. 2018), Iranian granite, and Bluestone, to demonstrate the feasibility of the developed approach. For sandstone rock type, disc specimens with three different sample sizes tested (i.e., table 1) to comprehend the influence of specimen geometry on the potential snapping back characteristics. This study also evaluates the effect of the material property on snapback potential by varying the material types from weak (i.e., sandstone) to strong (i.e., Bluestone). Four samples for each specimen size and material type were taken, each with an aspect ratio (i.e., thickness/diameter) of 0.4 to 0.5, satisfying the ASTM/ISRM standards (ASTM 1994, 2000; ISRM 1978; ISRM 1988; ISRM 2007). Table 3.4 presents a brief description of experimental details and rock properties.

Table 3.4: Input parameters

Rock Type	Axial displ. Rate (mm/min)	Lateral displ. rate ($\mu\text{m}/\text{min}$)	UCS (MPa)	Tensile strength (MPa)	Brittleness (σ_c/σ_t)	Strength
Sandstone	0.2	0.6	40	2	25	Weak
Iranian granite	0.2	0.5	80	5	16	Intermediate
Bluestone	0.2	0.5	140	10	14	Strong

In table 3.4, the uniaxial compressive and tensile strength of the above three rock types shows Bluestone to be the strongest while sandstone to be the weakest. The strength-based Brittleness index i.e. $B_1 \sim \sigma_c/\sigma_t$ (Hucka & Das-1974) estimated using the above data indicates Bluestone to be the most brittle while sandstone to be the least. Overall, the above three rocks cover a broader range of rock types in terms of strength and brittleness. It ensures the feasibility and broader application of the proposed experimental approach. Figure 3.15 presents a summary of the experiment results.

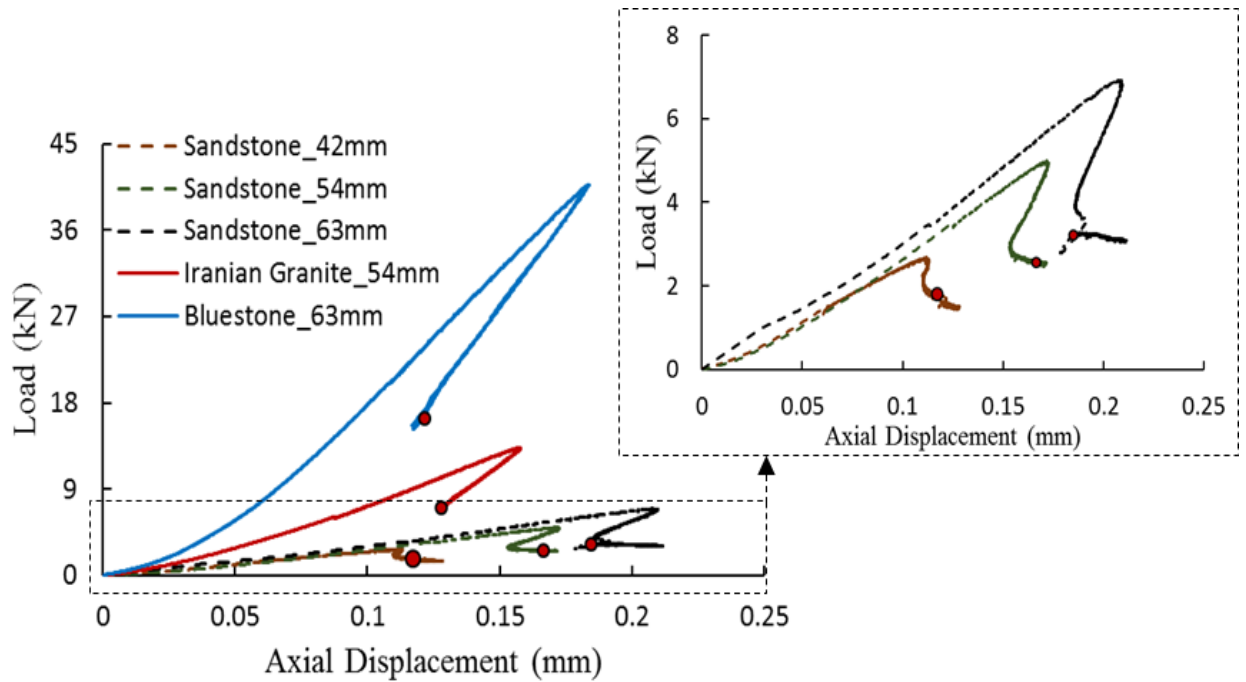


Figure 3.15: Feasibility demonstration

Figure 3.15 demonstrates that the proposed experimental approach is successful in controlling the instant cracking mechanism and capturing the snapback characteristics of load-displacement response for all three rock types. The above results also indicate the exact cracking point in each rock type. These snapback characteristics along with cracking point are promising in terms of ϕ and ψ_{res} energy component estimation. In qualitative terms, detailed results of sandstone rock types show that the energy release (k) component increases with an increase in specimen size. The higher magnitude of k theoretically indicates a higher and violent load drop occurrence in the conventional Brazilian disc test. Thus, it would be more challenging to control the instant cracking mechanism and may require a lower lateral strain rate. These observations are in accord with the theoretical consideration of the proposed experimental approach, i.e., section 3.2.2.

In this view, only larger sample dimensions have been chosen for hard rock types to optimize the overall effort, i.e., 63mm in Bluestone and 54mm in Iranian granite. Besides, figure 3.15 shows that sandstone exhibits the maximum axial strain with a minimum overall load, which indicates it to be the least brittle and weak rock type. It confirms the brittleness estimation from the proposed approach with table 3.4. These experimental data require an in-depth analysis to discuss the mechanism of energy evolution and the corresponding fracturing mechanism.

3.4 Result analysis

This section presents a comprehensive analysis of the energy evolution process in the proposed experimental approach using the detailed results of Hawkesbury sandstone’s disc sample, as shown in figure 3.16 below. The diameter of this disc sample is 54 mm. Here, figure 3.16 (a) shows the variation of load, axial and lateral strain along with total (Σ_{peak}), dissipated (ϕ), and released (k) energy components with time. This study considers the unloading modulus to be equal to the pre-peak elastic modulus to estimate the evolution of energy components. Figure 3.16 (a) also presents the evolution of acoustic emission (AE) hits energy and cumulative hits evolution with time. Figure 3.16(b) presents the variation of load with axial displacement.

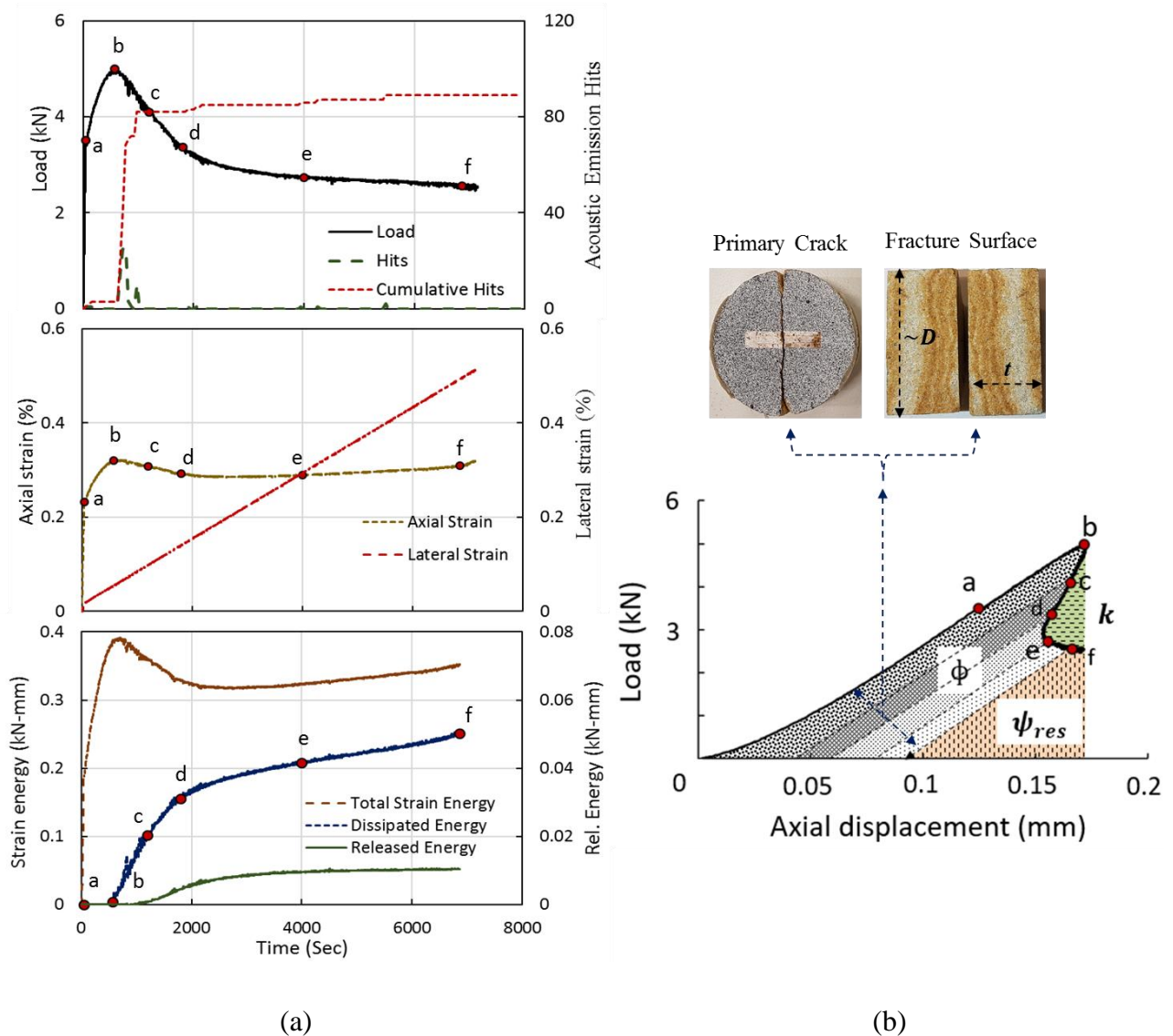


Figure 3.16: Experiment – 1: (a) Load, strain, strain energy with time, (b) load-displacement

The beginning of this discussion chooses five different points (i.e., from point ‘a’ to ‘f’) on the results in figure 3.16(b) to facilitate the description of the material cracking mechanism. Point ‘a’ denotes the sudden change in the slope of load variation with time, indicating the switch from axial to lateral strain controlled loading approach. For the remaining test duration, the axial strain rate is adjusted by the servo-control mechanism to maintain a constant lateral strain rate. The variation of load with time (i.e., figure 3.16a) and displacement (i.e., figure 3.16b) till point ‘b’ (i.e., peak load) is linear with the continuous increase in stored strain energy. Besides, there is no clear sign of energy dissipation, release, or acoustic emission activity in terms of energy consumption until the point ‘b.’

After reaching the peak, the axial strain rate becomes negative in ‘b-c’ section while maintaining a constant lateral strain rate, i.e., figure 3.16(a). The AE hits undergo jump, accompanied by an increase in the ϕ component. It indicates the material is utilizing already stored elastic strain energy to incur cracking. These alterations in the material’s internal structure result in permanent deformation causing material inelasticity and damage. It also gives rise to the AE events. Consequently, a significant drop in load-carrying capacity occurs in section ‘b-c,’ indicating significant degradation in material strength. During such experiments, the applied load causes tensile stress intensification localized across the central diametrical axis (Fairhurst 1964; Aliabadian et al. 2019a). It also indicates that the localization of inelastic deformation and material damage across the specimen’s central diametrical axis. Such degradation in material strength due to localized inelasticity causes the energy dissipation due to cracking and energy release (i.e., stress relaxation) in the region surrounding crack. This stress relaxation further explains the gradual increase in the rate of energy release (k) component, as shown in figure 3.16(a). One can observe here that the increase in the k is less intense in comparison with ϕ . It gets released instantly in the form of kinetic energy, thus controls the violent nature of disc sample failure in the conventional Brazilian disc test approach.

Further, above rock material strength degradation along with increased ϕ and k energy components continue in ‘c-d’ and ‘d-e’ sections. This material degradation occurs gradually over a long period in a controlled manner without any significant AE activity. Besides, the increment in strain energy components along with strength reduction rates decreases continuously in the above two sections. It indicates the approaching balance between the specimen’s load-carrying capacity and available elastic strain energy.

Consequently, the servo-control of the external loading source provides more energy to maintain a pre-defined lateral strain rate and continues the material cracking process in a gradual manner. It results in a stable increase in axial strain rate accompanied by a continuous increase in ϕ and k components, which lasts till the point 'f.' At point 'f,' vertical crack is visible, which assures the complete disc sample failure. The load recorded beyond this is the resistance of broken sample pieces (figure 3.16a) to the diametrical compression, which does not have any physical significance.

Overall, the rock sample in the suggested approach undergoes self-demolition under the influence of already stored strain energy, which gives rise to a swift snapback (i.e., section 'c'-'d'-'e'-'f') feature to the load-displacement response. The extent of this snapping back explicitly indicates the intensity of the catastrophic nature of disc specimen failure in the conventional approach. Here, systematic elimination of k energy component stabilizes the violent cracking mechanism of disc sample failure resulting in negligible AE activity in the post-peak regime. Additionally, it also offers an insight into the material's energy-storing and dissipation characteristics. Figure 3.16(b) presents the cracked sample with vertically diametrical crack. It enables us to estimate the fracture surface area reliably. All these observations are as per the theoretical formulation presented in section 3.2.2. To further validate the suggested theoretical background, figure 3.17 presents the brief results of load, strain, and strain energy variation of the other two rock types, i.e., Iranian granite and Bluestone. The legend of the plotted results are same as adopted in figure 3.16.

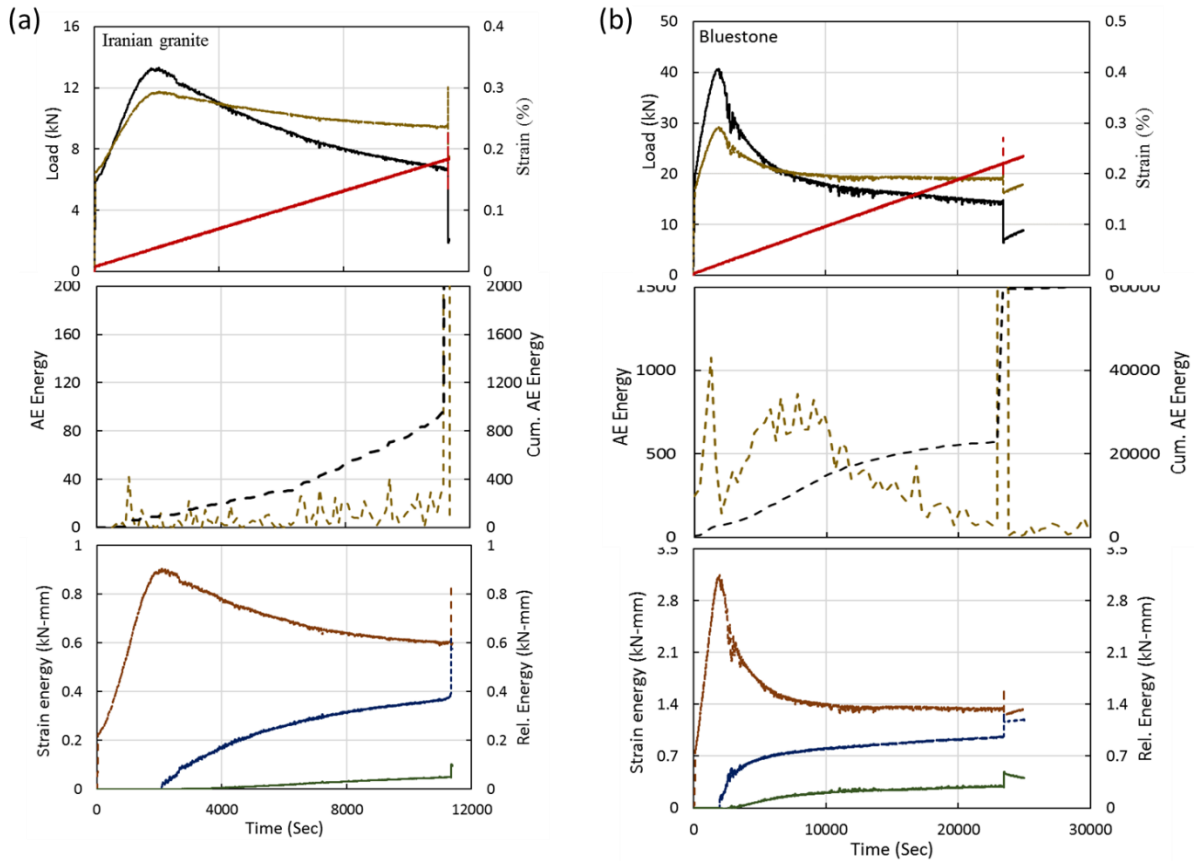


Figure 3.17: Result summary (a) Iranian granite, (b) Bluestone

In figure 3.17, one can observe that the trends of material damage, overall strain, and stored strain energy evolutions are similar to that of sandstone. The magnitude of AE energy release varies with material type, i.e., maximum for Bluestone while the minimum for sandstone. Besides, the overall magnitude of peak load, dissipation, and release energy components also vary with material types, which affects the corresponding load-displacement responses. Further comparison of these variables in relative terms could reveal the variation in failure characteristics with material type. Therefore, figure 3.18 presents the above results normalized with the corresponding parameters at the peak loading stage. This figure also contains the normalized results of the conventional Brazilian disc test to highlight the changes in the material response under the proposed experimental approach.

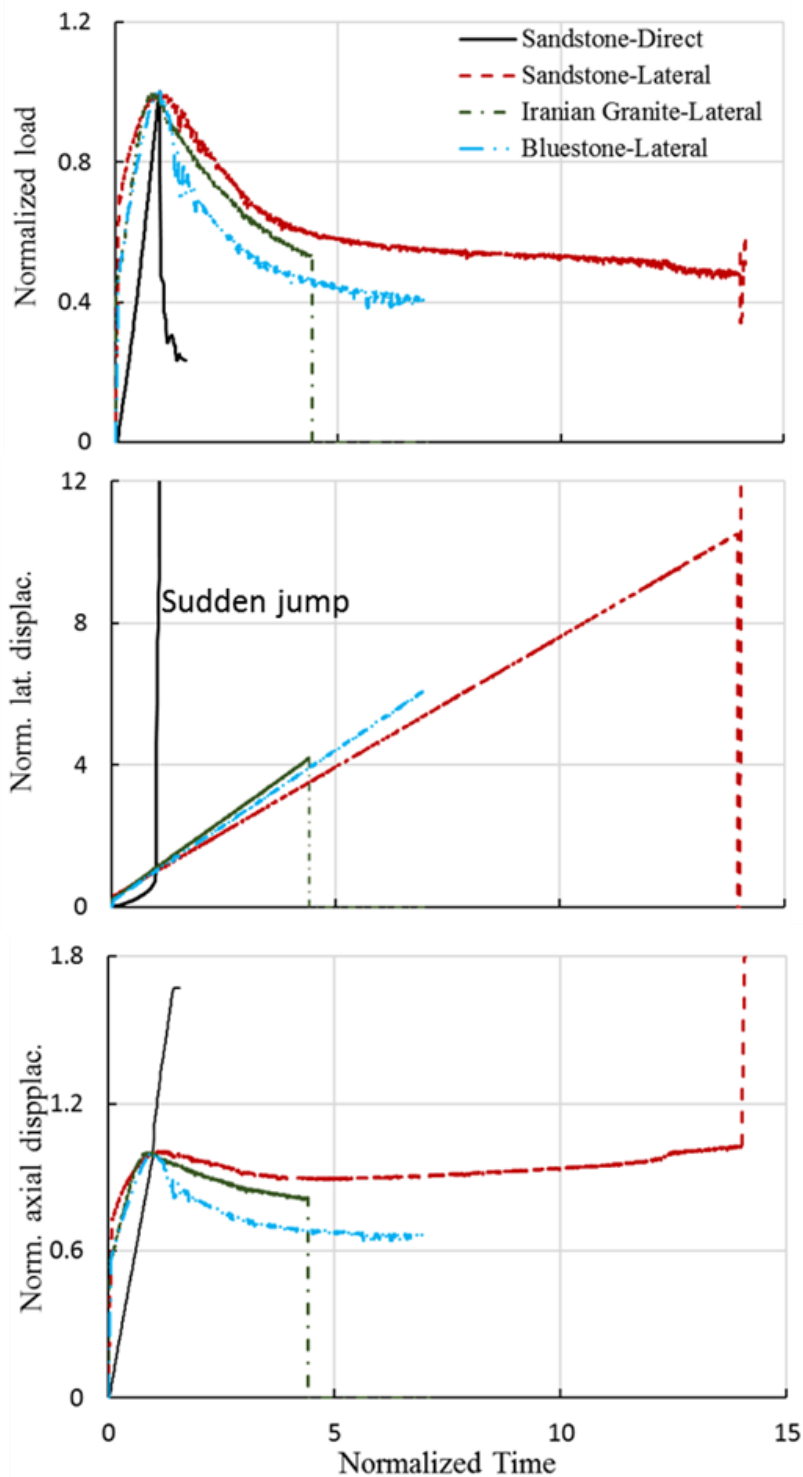


Figure 3.18: Result comparison – different rock types

Figure 3.18 shows that all three rock types undergo linear (i.e. with different slopes in axial and lateral strain-controlled regime) variation in applied load with time till peak. At the switching point, the diametrical compression rate reduces under the lateral strain control regime. At the peak loading stage, Brazilian disc response undergoes a sudden drop in load accompanied with an immediate jump in the lateral strain, indicating abrupt

failure of disc sample. On the contrary, the post-peak regime of results via the proposed experimental approach demonstrates gradual degradation over time while maintaining a constant lateral strain rate for all three rock types. It signifies the success of the proposed approach to control the disc sample's instant cracking.

In terms of loading conditions, the rate of axial displacement becomes negative in the post-peak regime, which in practical terms, implies unloading for all three rocks. However, the recorded load is continuously reducing while maintaining a constant lateral strain increment rate. It shows that disc specimens are always in the state of loading irrespective of global loading/unloading. The rate of global unloading varies with material types, i.e., maximum for Bluestone while the minimum for sandstone. One can observe a similar trend in the material damage rates (i.e., rate of load reduction) for all three rock types. Further, figure 3.19 presents the evolution of ϕ and ψ_{res} energy components in normalized forms (i.e., ϕ/Σ_{peak} and ψ_{res}/Σ_{peak}) for all three rock types along with normalized load-displacement.

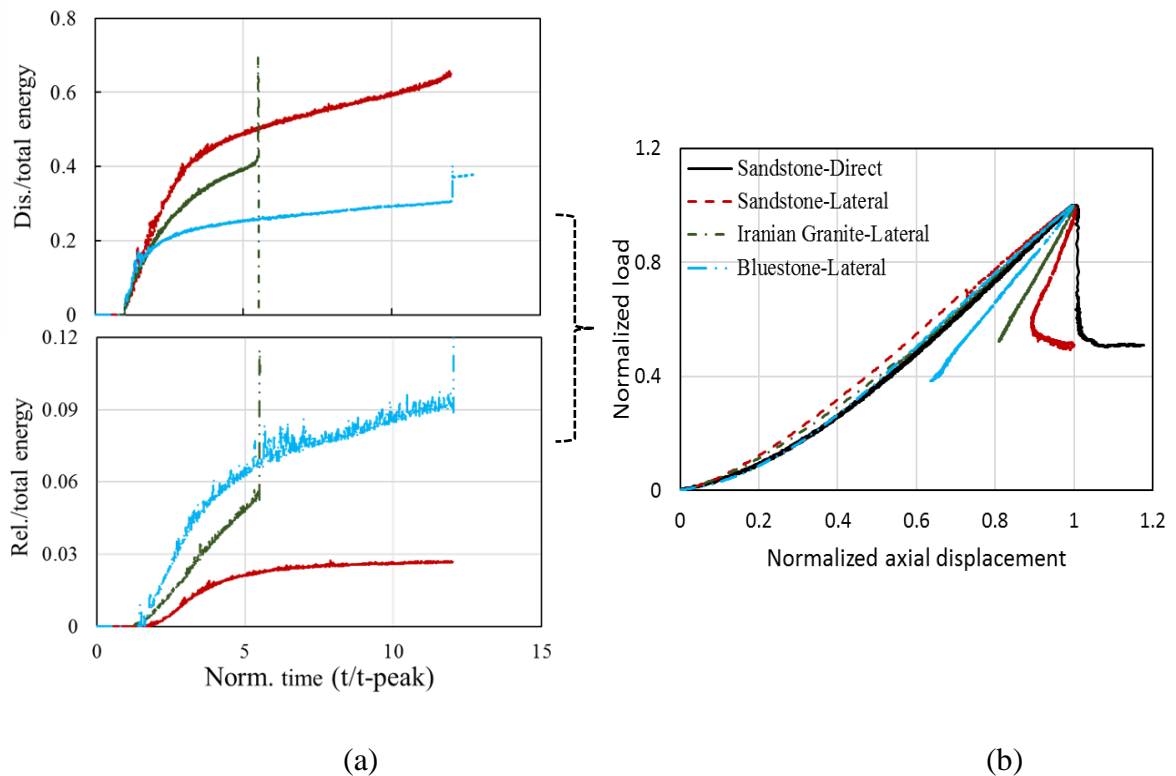


Figure 3.19: (a) Evolution of ϕ and ψ_{res} , (b) Overall comparison

The normalized energy components denote the fraction of total available strain energy get dissipated or released in the post-peak regime of load-displacement response. The fraction of total available energy, dissipated in material cracking, is minimum in

Bluestone and maximum in sandstone. On the contrary, released energy fraction is maximum in the case of Bluestone while minimum in sandstone. It indicates that the scale of violent and abrupt disc failure in the conventional Brazilian disc test approach would be maximum in Bluestone and minimum in sandstone. Additionally, despite having the highest strength in tension, Bluestone consumes the least fraction of the total energy for grain breakage and material degradation. These characteristics of rock material satisfy the typical definition of brittleness (Tarasov and Randolph 2011; Tarasov 2012; Tarasov and Potvin 2012, 2013) and show Bluestone to be the most brittle in tension among three rock type while sandstone to be the least.

In terms of energy evolution rate, all three rock types experience a higher energy dissipation rate immediately after the peak load, which reduces gradually to the minimum while keeping the overall lateral strain rate constant. It implies that maximum damage in all three rocks occurs immediately after peak load. This inelastic strain triggers immediate unloading to curtail the jump in the overall lateral strain rate commonly observed in the conventional Brazilian disc test approach. Besides, it also releases the strain energy component added to the material damage requirement, i.e., k . It induces snapping back characteristics to the load-displacement response. The magnitude of this snapback feature further reveals the material's brittleness level, which has also been compared in normalized form, as shown in figure 3.19(b). This result shows the lowest snapback to sandstone while highest to Bluestone, indicating latter rock type to be comparatively more brittle. Once the additional strain energy component gets released to acquire a balance between the available energy and material's energy-storing capacity, the rate of unloading and energy dissipation reduces significantly to maintain stability throughout the remaining test duration.

Overall, the entire experimental approach manages the energy component additional to fracture requirement in the post-peak regime for stabilizing the cracking process. The disc sample undergoes self-deterioration under the influence of already stored strain energy. This evolution of stored strain energy induces snapping-back feature to load-displacement response, which, in principle, reveals the material's brittleness characteristics and magnitude of kinetic energy released under the conventional Brazilian disc testing setup. It also enables the fracture energy calculations under an indirect tensile testing setup, which was not possible earlier. If the specimen dimensions increase then theoretically (i.e., figure 3.5 section 3.2.2), it also increases the k energy component in

comparison to ϕ , thus the snapback magnitude. Figure 3.20 below validates this inference by presenting the experimental observation of sandstone rock type with three different dimensions, i.e., 42, 54, and 63mm.

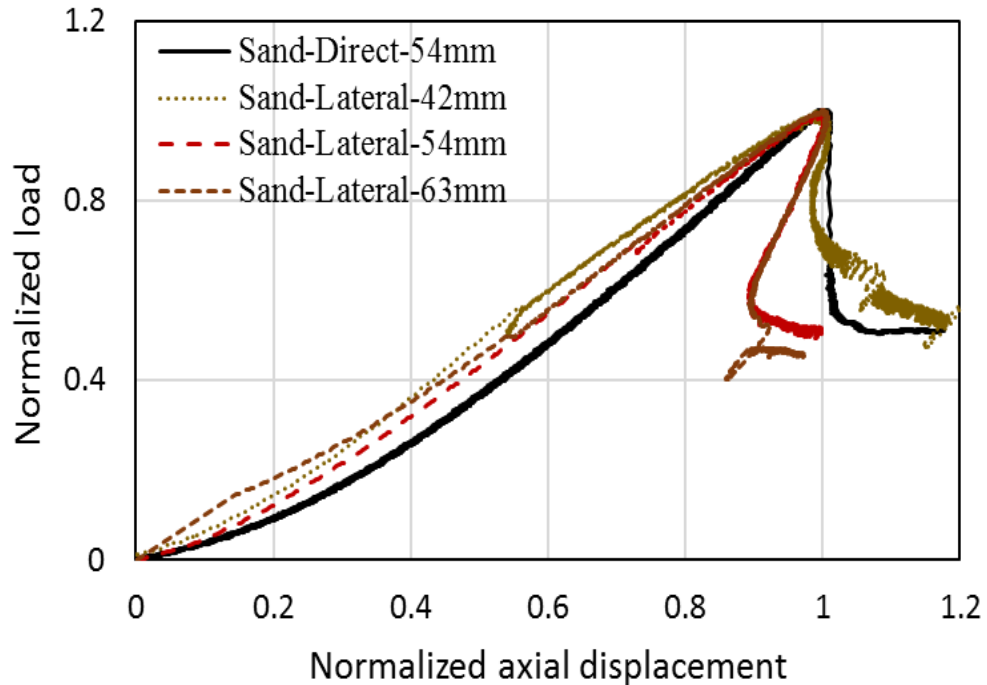


Figure 3.20: Effect of specimen dimension

3.5 Benefits

Following are the key benefits of the proposed experimental approach.

3.5.1 Tensile strength calculation:

Like the conventional approach, the proposed approach also uses the following empirical formulation for tensile strength (i.e. σ_t) calculation.

$$\sigma_t = \frac{2P}{\pi Dt} \quad (3.7)$$

Where P is the peak load (in newton) while D and t are specimen diameter and thickness (in millimeter). Material homogeneity and isotropy are the underlying assumptions of the above formulation. This study takes the actual tensile strength for each rock type as the average of all the tested specimens of different sizes. Figure 3.22 presents a summary of tensile strength estimation for all rock types.

3.5.2 Fracture energy calculation

Under the diametrical compressive loading, stresses across the central diametrical axis are tensile (Carneiro 1943; Goodman 1989; Piratheepan et al. 2012). This failure mode of disc sample offers ease for mode-1 fracture energy calculation provided that one should achieve stable cracking, as demonstrated in the proposed experimental approach. It enables us to estimate the total energy fraction dissipated to induce vertical diametrical cracking of the disc sample. All the points of actual cracking have also been visibly identified in each experiment, making sure to eliminate the residual energy fraction representing the strength of the broken disc sample. Therefore, one can estimate the overall ‘energy release rate’ or ‘fracture energy’ (i.e., in MPa-mm) as follows.

$$G_f^1 = \frac{\text{Area under load – displacement till fracture}}{\text{Fracture surface area}} = \frac{\int Pds}{A} \quad (3.8)$$

Where ‘ P ’ denotes the applied load in kN, and ‘ s ’ represents the overall displacement in ‘mm.’ The fracture surface area (A) is the area of the vertical diametrical crack. The potential error induced by this simplification is negligible, especially in case of stable diametrical cracking perpendicular to the loading direction. Figure 3.22 presents a summary of fracture energy estimation.

3.5.3 Fracture toughness calculation

Further, one can use the following expression based on plain stress conditions to estimate the fracture toughness (K_{I}):

$$K_{I} = \sqrt{E'G_f^1} \quad (3.9)$$

Where,

$$E' = \begin{cases} E, & \text{plane stress} \\ E(1 - \nu^2), & \text{plane strain} \end{cases}$$

Whereas the elastic modulus for each disc sample obtained by using a finite-difference based numerical modeling tool, i.e., 3DEC-ITASCA. In this approach, all the modeled blocks assigned an elastic constitutive model. The disc sample replicated as an intact cylindrical block with target material properties. Top and bottom steel blocks are assigned

elastic properties of steel. The Mohr-Coulomb model governs the contact between the disc sample and steel plates with very high contact stiffness and negligible friction angle ($\sim 5^\circ$). For load application, the bottom steel plate is fixed while the top plate is assigned downward velocity under the constraint of quasi-static strain rate conditions (i.e. $\dot{\epsilon} \leq 1 \times 10^{-4}$), which practically eliminates the influence of density (ρ) on overall response.

Additionally, all blocks in the above analysis are made deformable by discretizing it with a mesh size of 0.6 mm. This study performs mesh-sensitivity analysis to finalize the mesh size. Figure 3.21 presents the results of this analysis. The empirical equation in figure 3.21(a) summarizes the effect of mesh size on the stiffness. It also provides an ease to determine the stiffness of the disc sample corresponding to the ideal case of zero mesh size. Overall, figure 3.21(a) shows that the stiffness variation of load-displacement response diverges significantly from a mesh size of 1 and above. The reduction of mesh size to 1 mm and below diminishes its influence to negligible. Further, keeping this mesh size constant, the effect of poisson's ratio has also been evaluated, which shows its negligible influence on overall stiffness, i.e., figure 3.21(b).

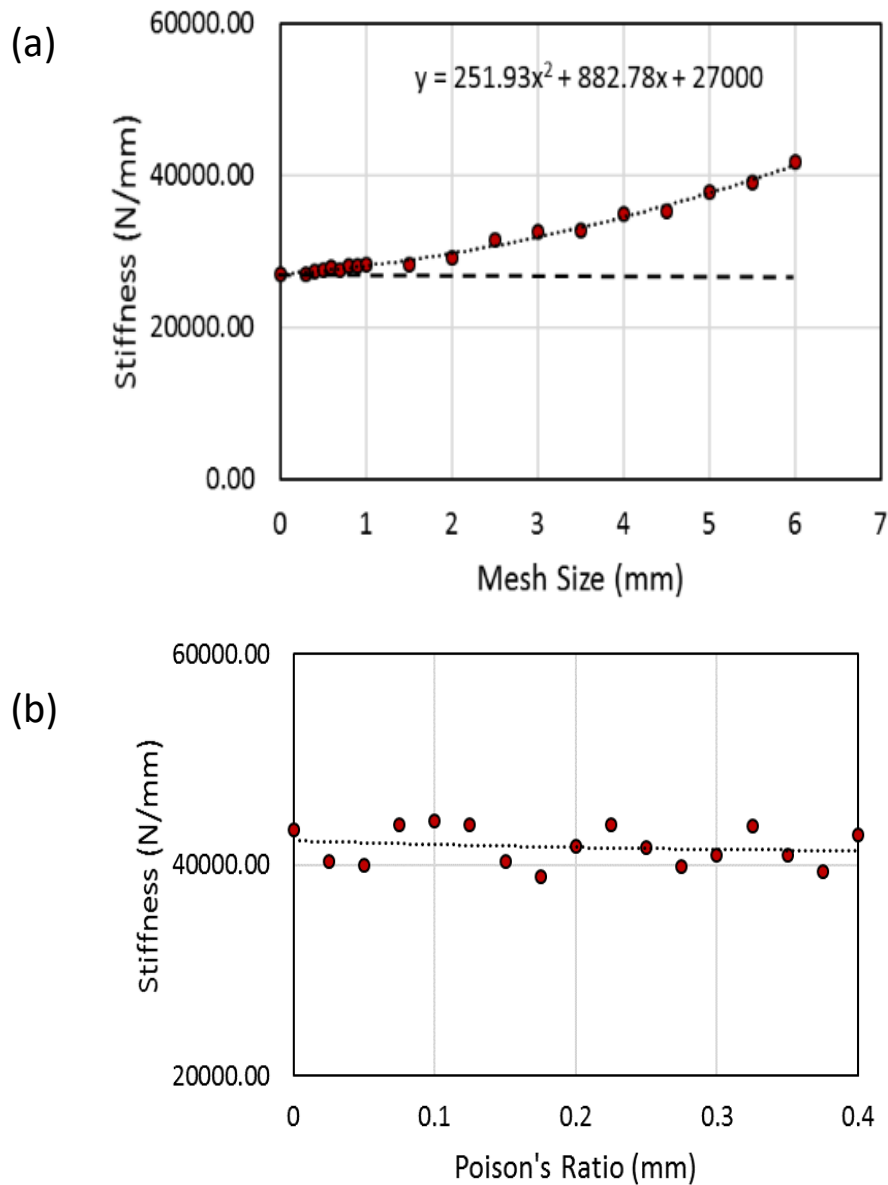


Figure 3.21: Effect of mesh sensitivity on (a) poisson's ratio, (b) stiffness

For further analysis, elastic material parameters (i.e., young's modulus or E) manipulated in the above numerical simulations to replicate the experimental observations of load-displacement response for each disc sample of different rock types. The finalized young's modulus is the actual material property representing the corresponding rock type. Table 3.5 presents a summary of the obtained young's modulus for each disc sample for different rock types. These elastic properties have been further used in expression 3.9 to compute the fracture toughness for each disc sample. Figure 3.22 presents the overall summary of the above analysis.

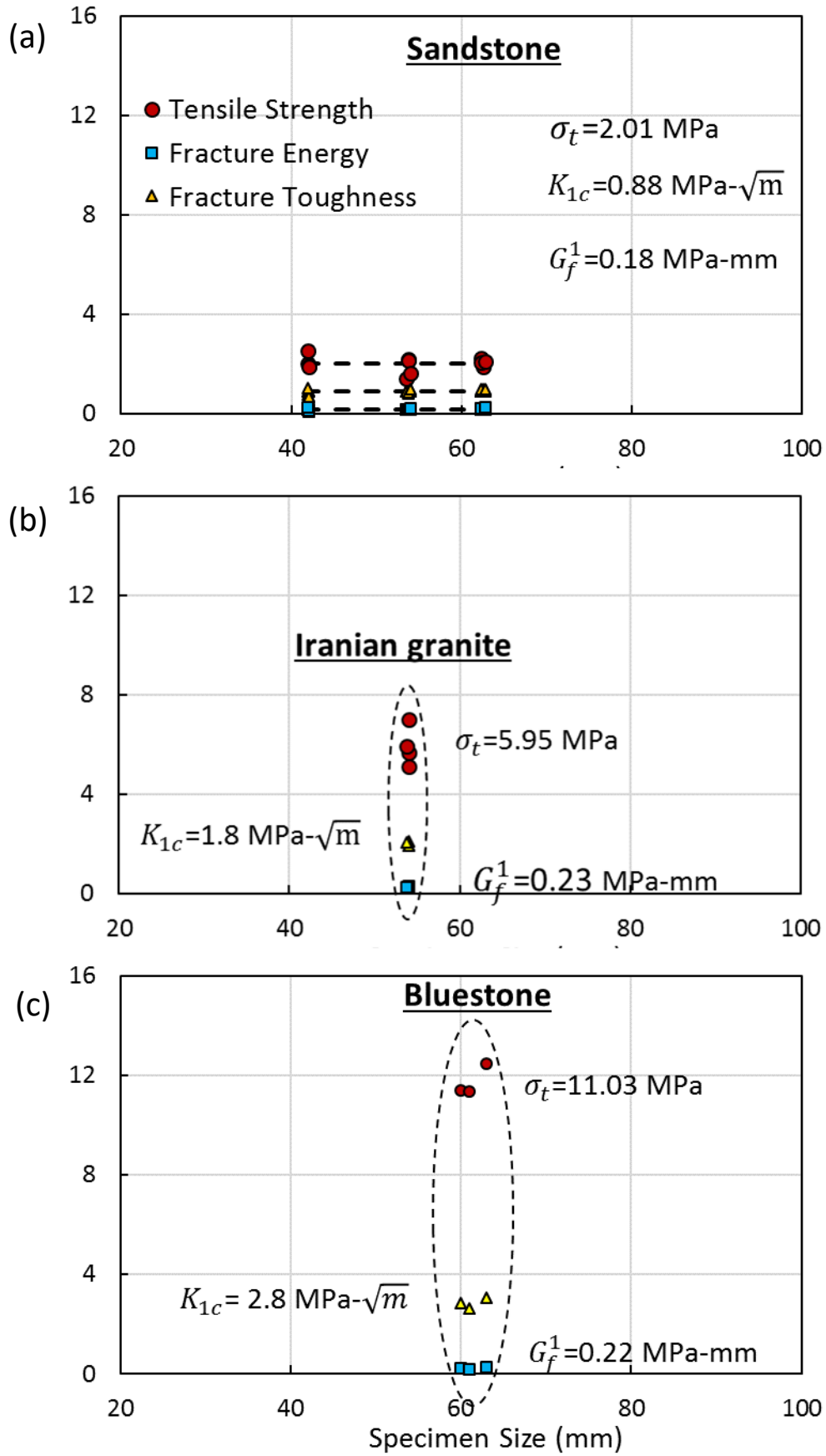


Figure 3.22: Result summary (a) Sandstone, (b) Iranian granite, (c) Bluestone

3.5.4. Snapback factor (\mathcal{S}) calculation and validation

The proposed experimental approach also provides an ease to analyze the material's brittleness characteristics via snapback factor (\mathcal{S}) using expression 3.6. Here, all the required parameters are available except non-uniformity constant(α). One can obtain this parameter by dividing the energy under the load-displacement curve (i.e., up to peak) of above numerical simulation by theoretical strain energy of the disc sample based on its material properties i.e. $(\pi t R^2) \frac{\sigma_t^2}{2E}$. It highlights the difference in energies between the actual responses and the idealized response. Table 3.5 below summarises the summary of all the obtained parameters for \mathcal{S} .

Table 3.5: Input parameters

	Sample	Dia. (mm)	Thick. (mm)	E (MPa)	ν	α	
Sandstone	i	41.99	21.13	3800	0.2	13.82	
	ii	42.1	20.8	4800	0.2	13.05	
	iii	42.02	21	3900	0.2	12.83	
	iv	42.01	23.01	4500	0.2	16.15	
	i	53.76	27.1	3900	0.2	11.40	
	ii	53.55	27.05	4300	0.2	11.40	
	iii	53.76	26.99	4400	0.2	13.93	
	iv	54	25	4450	0.2	18.98	
	i	62.5	31.43	5500	0.2	22.20	
	ii	62.33	31.52	3800	0.2	11.30	
	iii	62.32	31.53	4800	0.2	16.10	
	iv	62.84	25.5	3850	0.2	12.29	
	Iranian granite	i	54	22.13	15000	0.18	15.10
		ii	54.06	22.35	15000	0.18	12.50
		iii	54	21.97	13500	0.18	13.03
		iv	53.75	22.16	16500	0.18	11.66
Bluestone	i	63	33.01	36560	0.16	16.36	
	ii	60.2	30.6	36560	0.16	16.16	
	iii	62.5	31.66	36560	0.16	14.26	

One can compute the parameter \mathcal{S} for each rock type using the above parameters, fracture energy (G_f) and expression 6. Besides, the theoretical prediction of \mathcal{S} has also been made based on the basic material properties. The comparison between the theoretical prediction and experimental observation of the \mathcal{S} parameter provides the validity of the proposed theoretical formulation presented in section 3.2.2. Figure 3.22 presents the

overall results of this comparison. The experiments performed on sandstone rock with three sizes of sample geometry: 42, 54, 63 mm, demonstrate the effect of sample geometry on the ξ . In figure 3.23, one can observe that all the experimental observations are in close agreement with the predictions made by the corresponding theoretical formulation. These three rock types cover a broader range of rock types, which indicates the widespread applications of the proposed experimental approach along with its theoretical basis.

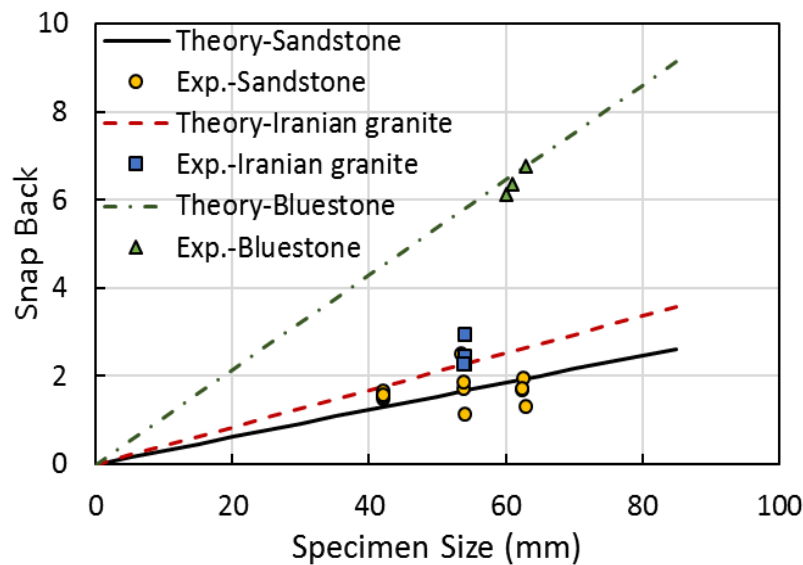


Figure 3.23: Validation: Snapback factor

Further, one can explicitly link the parameter ξ with the material's brittleness characteristics under tension, which was not possible in the conventional approaches. In this direction, figure 3.23 reveals the brittleness variation of three rock types in quantitative terms where Bluestone is 3.8 times higher than that of sandstone.

3.6 Discussion

The proposed experimental approach utilizes the Brazilian disc test's experimental framework, which is one of the most popular and widely used testing approaches for brittle material like a rock. It requires a simpler disc-shaped sample without any demanding specifications of different numbers, shape, size, and orientations of notches, commonly used in other fracture toughness testing approaches. Additionally, the experimental setup of the proposed approach requires LVDT for capturing the sample's lateral expansion, which, unlike the chain extensometer in lateral UCS tests, is

comparatively cheaper and commonly available experimental equipment. The remaining experimental setup is also standard and generally available in any geotechnical engineering laboratories.

Overall, the proposed approach provides an efficient technique to estimate various material properties, including tensile strength, elastic modulus, fracture energy, fracture toughness, and material brittleness via snap back parameter simultaneously with the single experimental setup. It also provides an insight into the material's energy storing and releasing characteristics under tension, which was not possible earlier. In collaboration with advanced experimental techniques, i.e., DIC and AE, its applications can be further extended to evaluate the uniaxial tensile strength of any given rock material using the Brazilian Disc test's experimental setup. In conclusion, the application of the proposed approach is not only time-efficient but also economically viable in terms of different sample demands and experimental setups, which enriches its feasibility and possibility of its more extensive application.

3.7 Conclusion

This chapter presents an innovative methodology to stabilize the instant cracking of circular disc samples under diametrical compression. It is a challenging task and has never been done before (to the best of author's knowledge), especially in simple circular shaped discs where cracking occurs abruptly in a split second-time frame window, e.g., Brazilian disc test. The proposed approach uses lateral deformation as feedback to control the overall axial loading rate. Pairs of the 3D printed plastic holder (or "holder") designed to carry the Linear Variable Differential Transformer (LVDT) laterally across the sample. Lateral strain feedback is coupled with servo-control of the MTS loading frame. This overall framework enables the efficient measurement of excess stored strain energy, which further has significant applications in a broader range of brittle materials. This study also conducts the proposed experiment on different rock types, and results were analyzed to prove the expected performance of the invented methodology. The proposed approach in this work is used to obtain the required material properties (i.e., tensile strength, poisson's ratio, elastic modulus, fracture energy, fracture toughness, and snapback characteristics) of our target rock type, i.e., Bluestone.

Chapter 4

Circular Disc under Diametrical Compression: Insights from DIC and AE based Analysis

4.1 Introduction

This chapter presents a detailed analysis of experimental data obtained from local-scale (\sim material) responses of rock material under circular disc splitting or Brazilian disc test. The intent here is to develop an approach for the tensile strength estimation of rock using local scale behavior rather than from empirical linkage with macroscopic observations. This entire process necessitates the collaboration of advanced experimental techniques, including Digital Image Correlation (i.e., DIC) and Acoustic Emission (AE) techniques, with the pre-defined experimental setup. Such a derived parameter, if determined, will be a better representative of material behavior.

This study has two key aspects: first and primarily, it would provide a crucial input parameter in the form of tensile strength for discrete numerical modeling simulations presented in the latter part of this research. Significance of this attempt could be better understood in the view that tensile strength estimation from indirect approaches focused on circular disc compression usually is not as accurate as obtained from direct approach, i.e., uniaxial tensile strength test. Still, indirect testing methodologies are popular because of their convenience in execution, especially in the case of hard and brittle rock types. Researchers suggested several possible modifications in indirect testing methodologies to address the issue of inaccuracies, which either compromise with the simplistic nature of the original circular disc compression setup or introduces empirical modifications in its theoretical formulation which itself is a matter of further discussion (Hudson et al. 1972a; Wang et al. 2004; Jianhong et al. 2009; Li and Wong 2013b; Perras and Diederichs 2014; Wang and Cao 2016; Masoumi et al. 2018). In this view, the presented work attempts to provide an efficient alternative that can overcome the above difficulties in obtaining a

reliable material strength property. It neither intends to introduce any empirical formulations nor alter the simple testing setup.

Secondly, this chapter presents an innovative approach to link local-scale behavior with sample scale responses using full-field strain evolution data obtained from Digital Image Correlation (DIC) technique. DIC is an efficient technique that uses a non-contact full-field kinematic measurement of planar or non-planar surfaces undergoing deformation (Nguyen et al. 2017b). It can measure full strain fields across the specimen surface and is much faster than other advanced techniques like X-ray. Despite such efficiency, it has not furnished well in revealing local scale material behavior and limited to adding more visual effects in majorities of the demonstrated applications (Fourmeau et al. 2014; Abshirini et al. 2016; Dong et al. 2017; He and Hayatdavoudi 2018b; Nath et al. 2018; Zhou et al. 2018b). Such quantifiable local-scale responses, if collaborated with sample scale behavior (i.e., from conventional load-displacement or AE responses or both), could provide us the insight into the cracking mechanism of brittle materials. It also has several allied applications additional to evaluating local scale strength parameters. For instance, to explore the phenomenon of crack induced localized dynamics. This phenomenon is widely observed in almost every brittle material cracking irrespective of sample scale loading conditions, e.g., quasi-static or dynamic. Nevertheless, not much has been done to explore this localized phenomenon. In this direction, this chapter demonstrates the effects and the significance of controlling these localized dynamics to assist the efficient applications of advanced experimental techniques, e.g., DIC and AE. It also presents the energy storing and releasing aspects of rock.

In addition to the above, the study reviews the role of AE damage mechanics in brittle material failure. Conventionally, researchers link AE signal observations with material damage, implying the consideration of material cracking as the actual reason for AE activity, which is not entirely correct (Wang et al. 2016; Rodríguez et al. 2016; Lacidogna et al. 2019; Rodríguez 2017). AE is an elastic wave generated due to the localized dynamics induced by material damage, not by material cracking explicitly. It implies that if one can control the localized dynamics, then it possible to acquire the physical conditions of sample cracking with no significant AE activity. This fundamental notion has been explored in this chapter using experimental illustrations based on conventional Brazilian disc and AUSBIT approach tests on the same rock type, i.e., sandstone. This

chapter also provides an added base for comprehensive numerical modeling validation, i.e., double scale validation. It is a much-needed advancement in conventional numerical modeling approaches, which mostly focuses on matching the numerical simulation with an experimental load-displacement response (i.e., sample scale).

The subsequent sub-section presents a brief overview of DIC and AE principles, followed by an analysis of DIC data obtained from the conventional Brazilian disc test in subsection 4.3. Such local analysis has collaborated with global/sample scale response from conventional loading frame (i.e., load-displacement responses) and allied AE setup. This sub-section also discusses the limitation of conventional Brazilian disc tests in terms of uncontrolled dynamics of sudden diametrical cracking. Sub-section 5.4 presented the analysis of DIC data obtained from lateral strain-controlled Brazilian disc test using the AUSBIT technique. It also describes the approach adopted to estimate the local scale tensile strength parameter.

4.2 Principle: Acoustic Emission (AE) and Digital Image Correlation (DIC) techniques

When any given structure/test specimen is subjected to continuous external loading, it causes material failure in the form of cracking to create new surfaces and stress relaxation in the form of energy release. This energy released, in principle, is the source for Acoustic Emission (or AE). As per the ASTM standards, one can define AE as time-dependent elastic waves generated by the rapid release of stored strain energy from a localized cracking source within the given specimen (Wisdom 1927; Stone and Dingwall 1977; Lockner 1993; He et al. 2010; Aggelis et al. 2011a, b; Farnam et al. 2015; Zhang et al. 2015; Sabri et al. 2016; Tsangouri et al. 2016). AE waves, once detected by AE sensors attached to the specimen surface, are converted into electrical signals and sent to the AE acquisition system for post-processing or further analysis. Silicon grease applied in between AE sensor face and specimen surface to ensure a reliable AE coupling. This overall arrangement for AE analysis comes under passive non-destructive testing methodology where the source of AE waves is inside the test specimen.

For post-processing, one can perform two types of analysis: signal-based and parameters-based. The present work conducts parameter-based analysis with the following critical parameters in focus: AE hits, amplitude (A), energy, and rise angle (RA). This study considers AE hit as the AE signals exceeding the threshold (i.e.,

minimum amplitude above which produced signal recorded). Amplitude is the peak signal voltage expressed in decibel (dB), AE energy is the area under signal over the duration, and 'rise angle' is the ratio of rise time (RT), i.e., time to reach the peak amplitude, to amplitude (i.e., $RA = RT/A$). Figure 4.1 presents the graphical representations of all the key AE parameters. In terms of physical interpretations, hits, amplitude, and energy parameters indicate the scale of damage accumulation. At the same time, rise angle and rise time help distinguish the source of crack, i.e., tension or shear-induced cracks. When tension induced material cracking occurs, it tends to move the sides of crack surfaces away, causing volumetric changes. Consequently, longitudinal wave types dominate in AE signals, which in general have shorter wave duration and rise time. On the other hand, in the case of shear cracking, localized material distorts without inducing any volumetric changes. As a result, shear (or secondary) waves dominate in the AE signal, which in general have a comparatively longer duration and rise time. The above parametric analysis, in collaboration with a typical load-displacement response, is efficient in understanding the sample scale material deterioration under any given loading conditions. The inclusion of additional AE parameter's analysis avoided duplicating the corroboration of standard macroscopic output from multiple sources. The present work utilizes the MISTRAS group Acoustic Emission testing technology for capturing and post-processing AE signals.

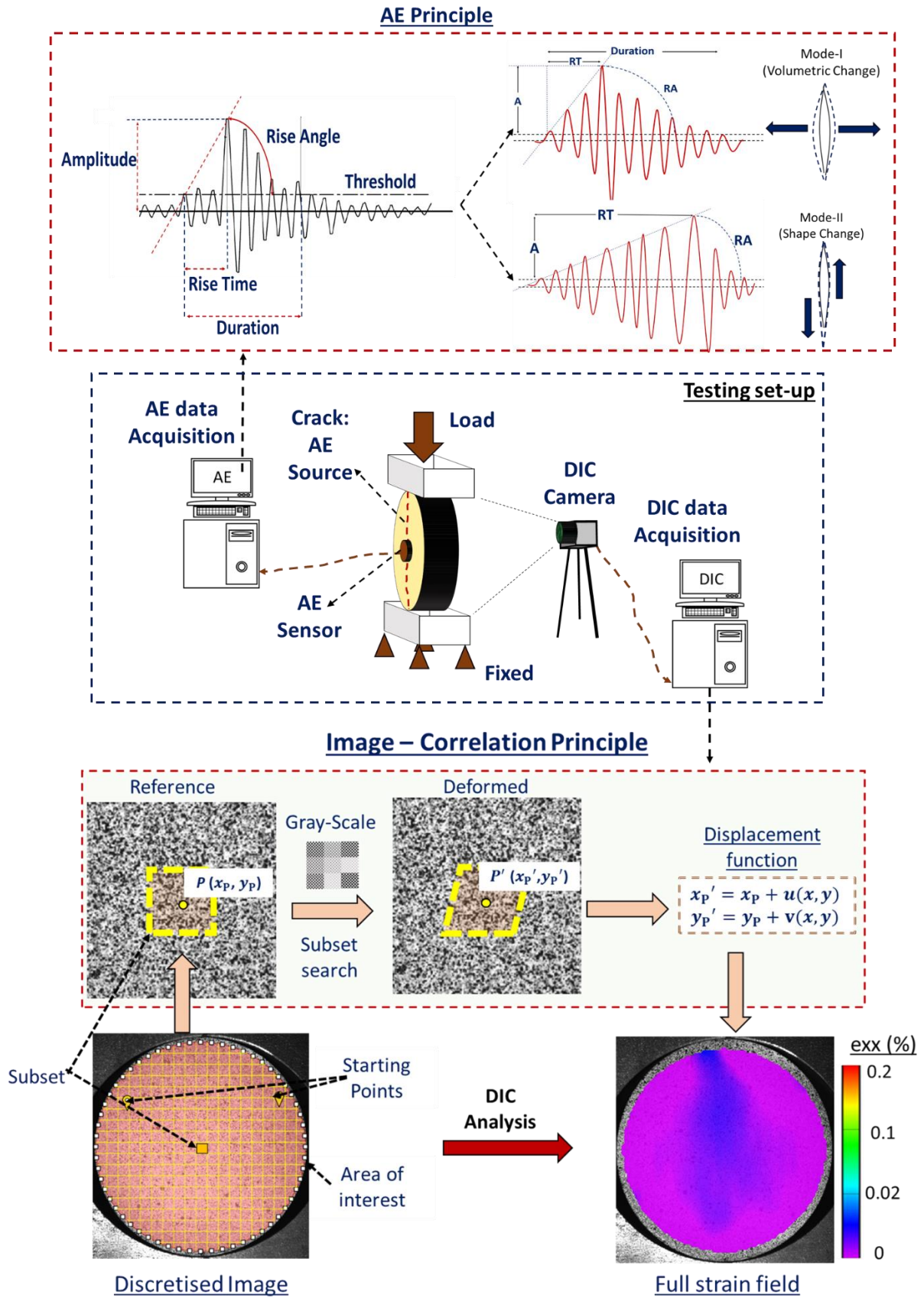


Figure 4.1: Fundamental principle behind AE and DIC functioning

One can link the sample scale behavior with local-scale responses across key locations to evaluate the contribution of localized material transformation in overall macroscopic behavior. In this direction, Digital Image Correlation (DIC) provides efficient experimental instrumentation. DIC, in principle, is a technique for correlating digital images of any object after deformation with the reference image (i.e., taken before deformation) to determine displacement and strain (i.e., after post-processing) fields across disc specimen. For this purpose, the front surface of the specimen exposed to black and white paints to create a random pattern of black speckles with a white background. The movement of randomly distributed speckles concerning its initial position in reference image had been tracked, which eventually forms the basis for deducing the full-field deformation over specimen surface. Therefore, images of a specimen have been captured continuously throughout the test at pre-defined intervals of 2 frames per second. For post-processing, the area of interest in an undeformed (or reference) image requires discretization. It results in the meshes of several sub-images termed as 'sub-sets.'

Each subset, thanks to stochastic speckle pattern, is identified by its grayscale estimation, which broadly defined as the number of bits per pixel (Solutions 2009; Tung and Sui 2010). This grayscale approximation helps in determining any subset's identification in deformed images based on the following correlation coefficient (*COF*) estimation.

$$COF = \frac{\sum g_{ij} \tilde{g}_{kl}}{\sqrt{\sum g_{ij}^2 \sum \tilde{g}_{kl}^2}} \quad (4.1)$$

Here, g_{ij} and \tilde{g}_{kl} are subset grayscales for reference and deformed image with (i, j) and (k, l) coordinates. The correlation coefficient acquiring maximum value confirms the location of the target subset in the deformed image. Tracking the movements of these subsets help in the determination of the functional relationship between point P shifting to P' . Figure 4.1 presents the corresponding expression where (x_p, y_p) and (x_p', y_p') are the coordinates of point P in reference and deformed images while $u(x, y)$ and $v(x, y)$ are the displacement functions. The present study uses the above setup to determine the displacement field and the corresponding gradient tensor (\mathbf{F}). The following expression summarizes the full-field strain estimation from the DIC technique.

$$\varepsilon_{xx} = \frac{\partial u_x}{\partial x} + \frac{1}{2} \left[\left(\frac{\partial u_x}{\partial x} \right)^2 + \left(\frac{\partial u_y}{\partial x} \right)^2 \right] \quad (4.2)$$

$$\varepsilon_{yy} = \frac{\partial u_y}{\partial x} + \frac{1}{2} \left[\left(\frac{\partial u_x}{\partial x} \right)^2 + \left(\frac{\partial u_y}{\partial x} \right)^2 \right] \quad (4.3)$$

$$\varepsilon_{xy} = \frac{1}{2} \left(\frac{\partial u_x}{\partial y} + \frac{\partial u_y}{\partial x} \right) + \frac{1}{2} \left[\frac{\partial u_x}{\partial x} \frac{\partial u_x}{\partial y} + \frac{\partial u_y}{\partial x} \frac{\partial u_y}{\partial y} \right] \quad (4.4)$$

The present work uses 'VIC-2D Correlation solutions commercial software where the subset size can be manually altered based on the required accuracy and processing time (i.e., a smaller subset requires higher processing time). Similarly, one can also control the number of points in each subset via an appropriate 'step' size (Solutions 2009). The software also analyses the attributes of digital images and suggests suitable subset and step size. It practically resolves the issue of identifying suitable DIC parameters for reliable strain estimation. Additionally, this analysis also requires two start points suggestions in the reference image (i.e., figure 4.1) to ensure correct strain field determination, especially after specimen cracking. These start points should be far from potential cracks. Furthermore, this study also utilizes different analyzing tools, including line section, virtual strain gauge, and inspection region of a square shape, to evaluate the local responses in quantitative terms.

4.3 Uncontrolled/Conventional Brazilian Disc Test

The present study conducts conventional Brazilian disc tests on Hawkesbury sandstone rock with different specimen sizes, including 42, 54, and 63 mm diameters and 0.4-0.5 aspect ratio. The axial displacement/compression rate of 0.2 mm/min is kept constant throughout the tests. One can estimate the indirect tensile strength (σ_t) in MPa using peak load (P) measure in Newton (N) as follows.

$$\sigma_t = \frac{2P}{\pi D t} \quad (4.5)$$

Here, D and t are specimen diameter and thickness in millimeter. Chapter-3 presented the macroscopic load-displacement response's analysis. The subsequent sub-sections present the in-depth DIC and AE data analysis using a 63mm diameter disc specimen for illustration.

4.3.1 DIC validation

Before starting an analysis, it is essential to validate the DIC strain estimation first. For this purpose, this study measures the overall lateral strain variations of the disc sample

using AUSBIT instrumentation. The VIC-Snap's in-built inspection tool, i.e., inspection extensometer (IE), is helpful to measure the sample's lateral deformation as a DIC estimate. It acts as a virtual strain gauge and measures engineering strain (i.e., $\Delta L/L$) along its alignment, where ΔL is the change in its original length (L). Three such virtual strain gauges (or IEs) have been considered across the central diametrical axis of the sample in the lateral direction, as shown in figure 4.2. The average elongation of these three IEs should be close to the disc specimen's overall lateral deformation estimation. It had been further compared with actual experimental observations, as shown in figure 4.2 below.

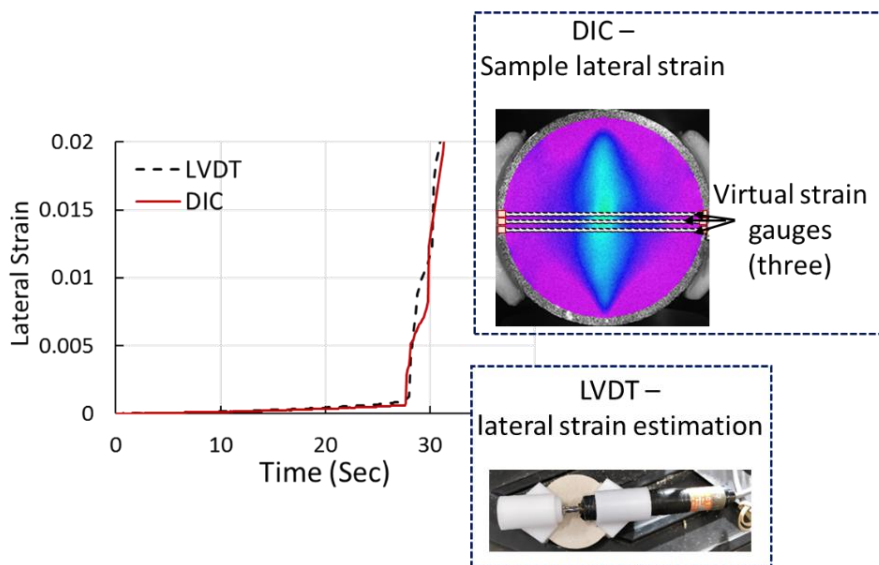


Figure 4.2: DIC validation

One can observe that the DIC estimation for strain calculations is in excellent agreement with the experimental observations. Minor variations in the result from these two sources (i.e., during/after strain jump) can be attributed to the dynamics associated with the specimen cracking. The slight difference between the area of interest in DIC analysis and the actual disc sample also contributes to the slight aberration. The other possible approach for the DIC validation could be the use of physical strain gauge attached over the front surface of the disc specimen, before applying the speckle pattern. This strain gauge could provide additional localized strain data for validation if it did not get dysfunctional during the experiment, which unfortunately is not the case often. This experiment also used one strain gauge of 10mm length, which got dysfunctional even before cracking.

4.3.2 Strain Contour Evolution

In biaxial loading conditions during indirect tensile strength testing, strain evolution in the transverse direction normal to vertical loading (i.e. ε_{xx}) is the key to unveil the material behavior responsible for tensile failure. Under such a scenario, the stress concentration at loading ends causes localized material shearing and has considerable influence on the overall sample failure mechanism. Therefore, the full field evolution of both key strain components (i.e. ε_{xx} and ε_{xy}) have been synchronized with a load-displacement response and presented in figure 4.3, where tensile strain is considered positive.

Further discussion divides the overall result in figure 4.3 into five main stages. Theoretically, an increase in the magnitude of ε_{xx} strain component across the center of the vertical diametrical axis demonstrates localization of tensile strain and, thus, tensile stresses. One can observe here that at point 'i' (i.e., 20% of peak load or 0.2P), distribution of ε_{xx} strain component is uniform. It starts localizing at point 'ii' (i.e., 0.4P), which got further intensified at point 'iii' (i.e., 0.9P) and 'iv' (i.e., peak load). Strain increment in the specimen's portion away from a central diametrical axis is insignificant during these stages. On the other hand, sample scale lateral strain variation demonstrates a steady increment till the peak, as shown in figure 4.2. It shows that tensile strain increment across the central diametrical axis controls the disc specimen's overall lateral deformation. At stage 'v' immediately after peak load, a clear sign of disturbed strain equilibrium with evident diametrical crack can be seen, i.e., figure 4.3, indicating sudden disc failure.

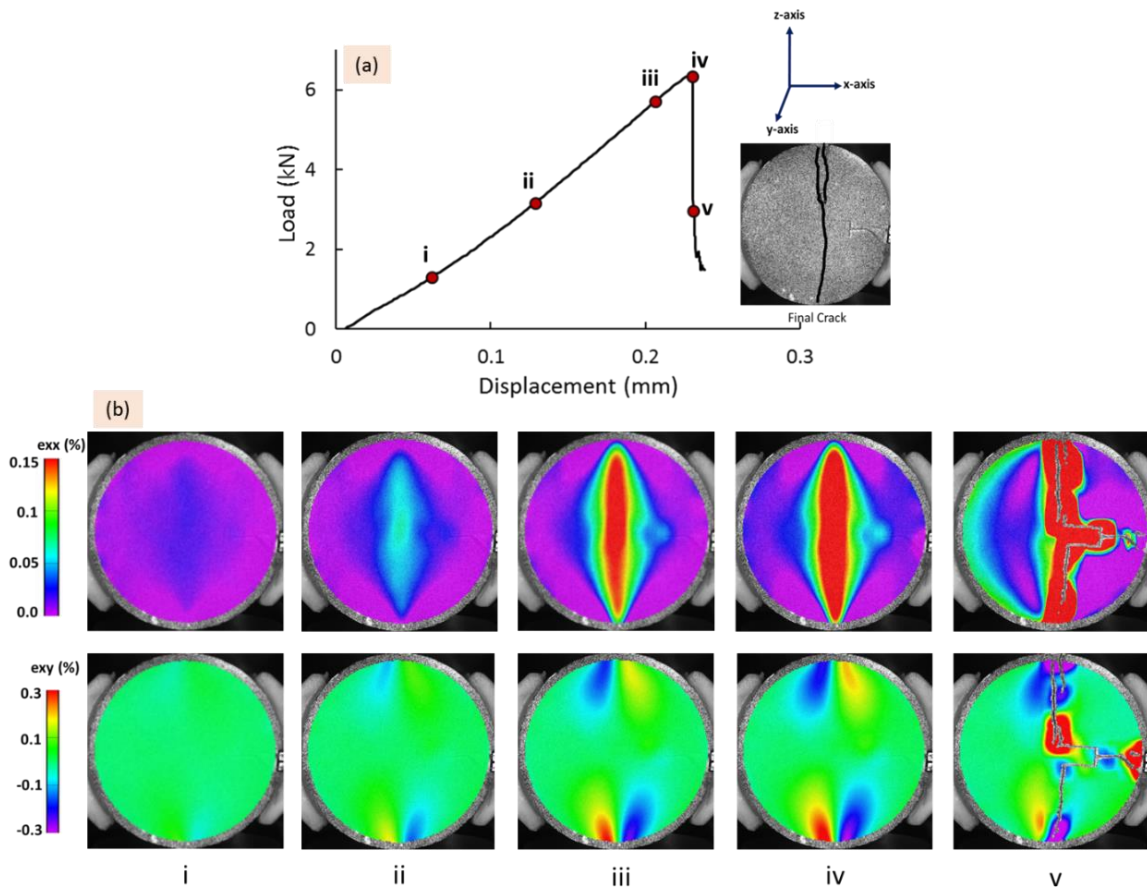


Figure 4.3: (a) load-displacement response, (b) strain evolution DIC data

Figure 4.3 also presents the evolution of shear strain component (i.e. ε_{xy}) with load demonstrating a similar trend of localized strain evolution from stage 'i' to 'v.' However, in this case, localization of ε_{xy} occurs at the top and bottom loading ends of the specimen mainly. It explains the common observation of crack initiation at loading ends due to shear first, not at the disc center due to tension. This aberration in the theoretical consideration affects the peak load magnitude and the tensile strength estimation; it is one of the critical reasons for Brazilian disc test results variation from uniaxial tensile strength test outcome (Perras and Diederichs 2014). To circumvent such issues, it becomes essential to evaluate the local scale material behavior in quantitative terms and derive corresponding strength parameters. The strength parameter derived from such analysis could be a better material representative, which in principle does not rely on the overall sample scale responses or sample dimensions. In this view, the above contour plots provide a qualitative overview of strain evolution, insufficient to perform quantitative analysis.

4.3.3 Acoustic Emission Analysis

This section presents a brief analysis of AE responses during the diametrical compression of a circular disc. Intend here is to derive critical information, including AE magnitude and source type (i.e., crack type), to characterize stress state inducing localized instability. Despite local origin, these events collaboratively provide a sequential summary of sample scale strength deterioration. For this purpose, this study considers parameter-based analysis with the following four key parameters, i.e., AE hits, amplitude, rise angle, and energy to characterize the crack type and corresponding instability magnitude. The AE hits, amplitude, and energy variations indicate the magnitude of localized dynamics. On the other hand, RA variation provides a qualitative characterization of stress state type (i.e., tensile or shear-induced), causing the above-localized dynamics during material cracking. Figure 4.4 presents the summary of AE results collaborated with the sample scale load-displacement response.

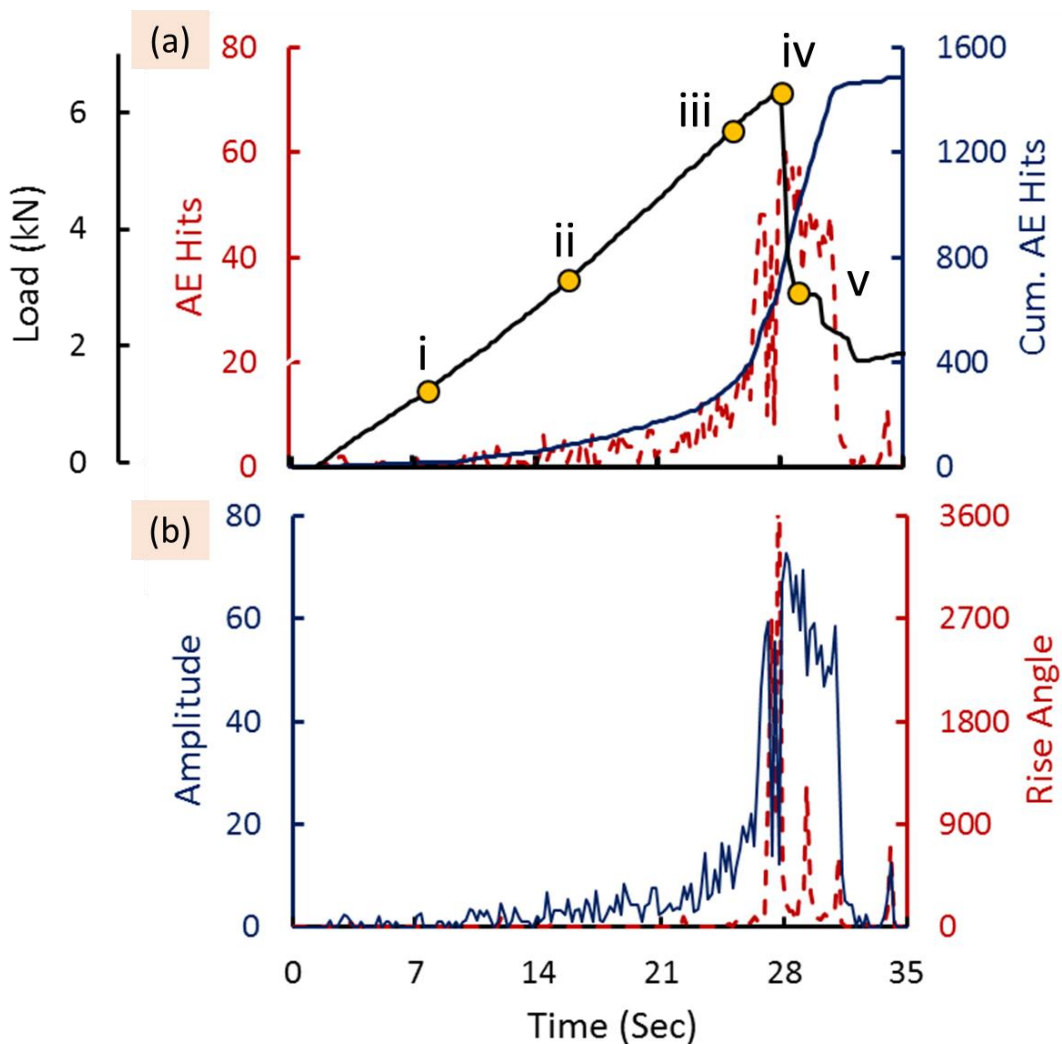


Figure 4.4: AE analysis: Conventional Brazilian disc test

Figure 4.4(a) presents the variation of load (MTS), AE hits, and cumulative hits, and figure 4.4(b) shows the variation of AE amplitude and rise angle with time. The magnitude of hits denotes the level of AE activity. Researchers often link it with the scale of material damage, i.e., micro-cracking or macro-cracking. On the other hand, cumulative AE hits variation with time indicates the cracking rate. In figure 4.4(a), one can observe insignificant AE hits increase in earlier loading conditions from stage i to iii. It indicates negligible dynamics at a local scale, thus stable elastic deformation. A consistent increase in cumulative hits during these stages shows the continuous accumulation of AE micro-events, which individually may not have much significance during these earlier stages. However, it collaboratively contributes to material deterioration, leading to peak load instability. Stage iii accompanies the sudden intensification in hits and jump in cumulative hits variation. It physically signifies the initiation of pre-peak material damage, which may not always be evident from the typical load-displacement response. This increase in AE hits further gets intensified into the immediate jump at peak and post-peak loading stages iv and v, indicating rapid energy release via macro-cracking or specimen failure. A sudden drop in the specimen's load-carrying capacity at iv and visible cracks at stage v further supports the above interpretation.

Further, figure 4.4(b) shows a negligible increase in RA as compared to the amplitude parameter during the first three stages. Immediately after stage iii before peak load, an increase in RA is insignificant as compared to the amplitude. It shows that the AE signals emitted during these stages have a shorter rise time (RT) in comparison to the amplitude, indicating the dominance of primary waves; thus, the occurrence of tension induced localized volumetric change. After that, a sudden jump in RA at time 28.1 sec (i.e., peak load) accompanies a drastic rise in amplitude. It indicates the overwhelming contribution of the shear wave with lower speed and high-rise time exhibiting a change in AE source from tension to shear type. Physically, these observations imply the dominance of tension induced micro-cracking throughout the significant proportion of loading from stage i till peak. These micro-cracks keep on accumulating. Eventually, at stage iv, these micro-cracks coalesce and start causing friction-induced shearing, which alters the AE source type from tension to shear, rightly captured by evolving RA characteristics. It denotes major cracking, which correspondingly enhanced the local scale dynamics causing a sudden jump in the AE amplitude and hits.

The above AE activity observations are in line with the conventional DIC data (i.e., figure 4.3), where one can ascertain the location of the localized instability using full-field strain contours. Despite the above analysis, it is still challenging to derive the localized material strength properties in quantitative terms.

4.3.4 Horizontal and vertical section

Given the previous discussion, it becomes inevitable to extract the localized strain data from different critical sections across the specimen. It could provide an insight into the localized strain evolution in quantitative terms. It could also help in the estimation of the localization zone where rock material is failing primarily in tension under the biaxial loading conditions. Therefore, this study extracts the ϵ_{xx} strain component at each point across the horizontal and vertical diametrical axis, and synchronize it with sample scale load-displacement response, as presented in figure 4.5. Here x-x and y-y denote horizontal and vertical sections. The tortuous crack trajectory, which does not coincide explicitly with vertical section y-y, has also been distinctly highlighted.

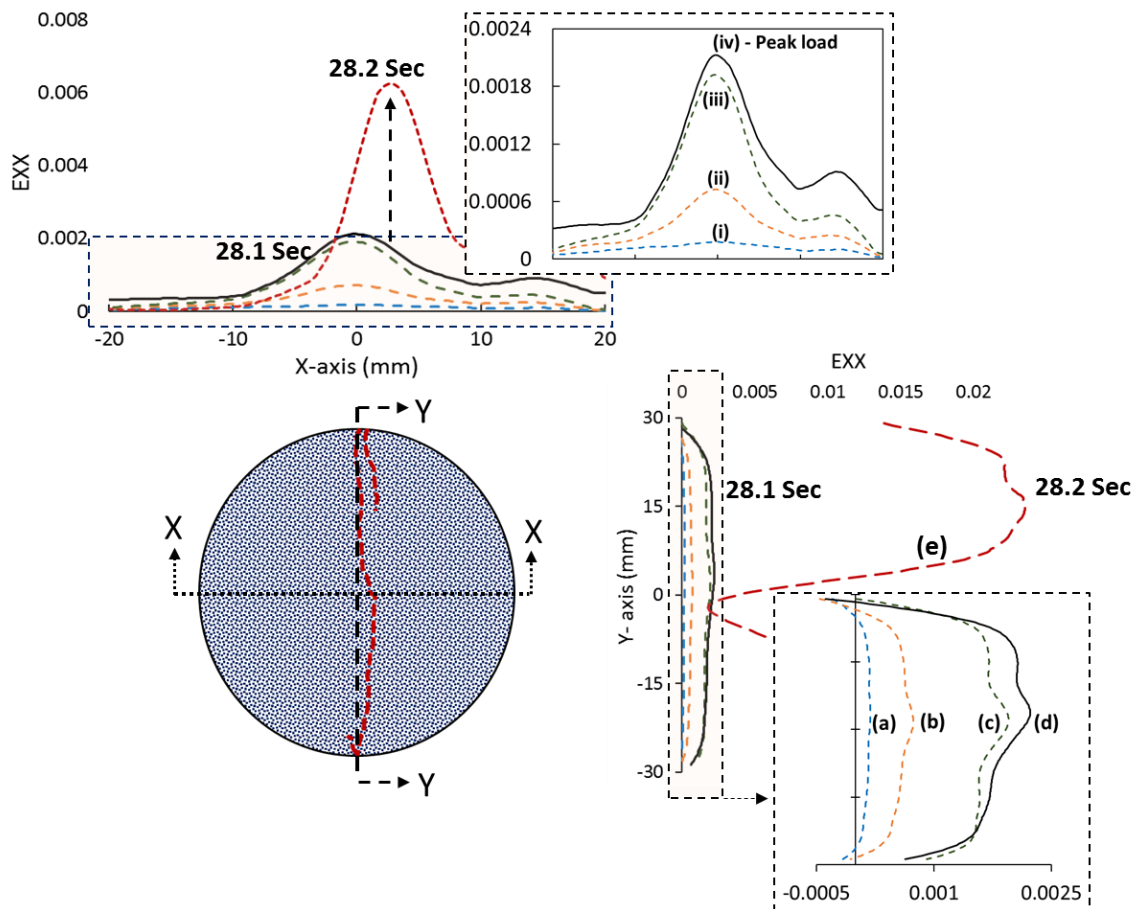


Figure 4.5: Strain evolution in conventional Brazilian disc test: horizontal and vertical sections

One can observe in figure 4.5 that strain variation across the horizontal section is quite uniform at stage i, which further intensifies from stage ii to iv in region ± 5 mm from the center of the specimen. Whereas, the remaining portion of the horizontal section, i.e., 10 mm away from disc center in both direction (i.e., left and right of center), demonstrate negligible strain intensification, thus, insignificant contribution in overall lateral deformation. The maximum strain (i.e. ϵ_{xx}) at peak load (i.e., 28.1 sec) has an approximate magnitude of 0.002 at the disc center. After that, ϵ_{xx} at stage 'v' at time 28.2 sec undergoes a significant jump of 300%. While the point of maximum strain gets shifts 3 mm approximate right from the disc center explaining the intersection of crack trajectory with the x-x axis. One can also observe the drop in ϵ_{xx} strain magnitude in the left portion of the x-x section (indicated by the 'red-dotted' line). Whereas, ϵ_{xx} in the right half of the specimen further intensifies. The above observations infer that the disc sample cracks at time 28.2 sec, i.e., immediately after peak load. Despite strain intensification at the disc center, the vertical diametrical crack passes through the horizontal axis at an offset of +3mm towards the right. It reflects the non-homogenous nature of rock material. This diametrical cracking causes a sudden release of stored strain energy, explaining the drop in strain magnitude due to stress relaxation immediately after peak across the left portion of the horizontal section. Whereas post-crack strain intensification in the right portion of the section signifies the load re-distribution, causing the increased compression of the right portion of broken disc specimen pieces. This uneven post-cracking resistance to diametrical compression is the response of broken rock pieces, which, in principle, does not have any physical significance.

Similarly, vertical inspection, i.e., y-y section, has also been taken, which shows uniformity in strain intensification throughout the vertical section with load application from stage i to peak loading point iv. Here, strain characteristics at a distance of ± 10 mm from loading ends are compressive. It shows that stress distribution is not uniformly tensile throughout the vertical diametrical section and has a significant shear component due to localized compression at loading ends. After point iv (i.e., peak load), one can observe an abrupt increase in strain throughout the entire vertical section, demonstrating a clear separation of two-disc portions. Whereas strain drop at the center of the vertical section is the response of rock portion near the actual crack due to strain relaxation. All jumps in strain variation are instant throughout the vertical diametrical crack indicating uncontrolled and abrupt disc cracking into two pieces. It shows that the magnitude of

elastic strain energy stored at the peak load in the disc sample was much higher than its diametrical cracking requirement or sample's fracture energy. Subsequently, disc specimen fails abruptly in a violent manner causing significant AE events during cracking, i.e., figure 4.4. The region of interest where tensile strain and thus tensile stress dominates is evident across the central diametrical axis along the crack trajectory. It excludes the stress localization region of 10 mm from the top and bottom loading ends.

4.3.5 Tensile strength determination

The above analysis provides a better insight into rock's local scale responses. Nevertheless, it requires further efforts to make a righteous judgment to derive local scale tensile strength as a material characteristic. For this purpose, this study considers different inspection rectangles (IR) across the crack trajectory to extract comprehensive data set reflecting localized strain evolution. These rectangles provide the strain components averaged over the area under consideration. The intent here is to capture the components of localized strain at which rock material did fail primarily under tension. Nonetheless, the question arises here are: what effect does the size of such IR have on its overall strain estimation, and what should be its appropriate size chosen to consider the output as a material response?

One basis for determining IR size could be similar to the mesh sensitivity analysis, where mesh size with the least effect on overall results is generally preferred. Therefore, this study considers different sizes of IR from R0 to R4 (where P0 is a point). It demonstrates the suitability of the R3 rectangle size below which size effect on overall strain response reduces to negligible before specimen cracking. After cracking, the size of IR does demonstrate a reasonable size effect, as shown in figure 4.6. The other reasonable explanation is to consider such rectangles to be a two-dimensional reflection of potential representative volume element (RVE). One should note here that the fundamental basis on which IR functions differ from any typical RVE where the latter is an explicit three-dimensional scaled-down version of the entire specimen, which can reflect specimen's overall mechanical characteristics. Whereas, the prior (i.e., IR) provides localized responses in terms of strain parameters in two-dimensional space. It individually could not represent the entire specimen, but collaboratively could deduce the rock specimen's mechanical characteristics. In this sense, again, R3 is the most suitable

option with maximum dimensions as ten times the average grain size of Hawkesbury sandstone rock type (i.e., 0.2mm), i.e., in line with RVE size selection (Lesley 1995).

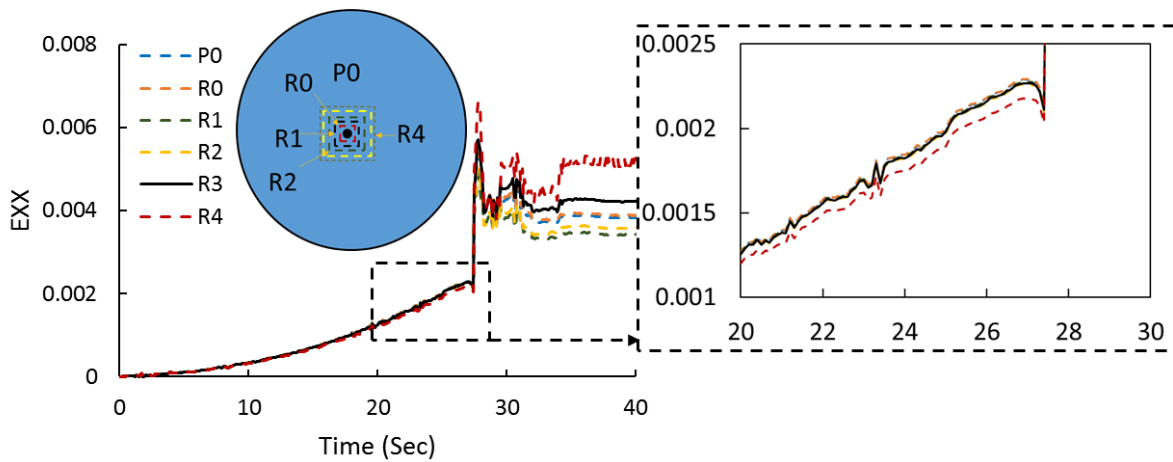


Figure 4.6: Effect of IR size on local scale response

After that, this study considers different IR (i.e., R0 to R7 in figure 4.7) of R3 size along the crack trajectory to extract the evolution of ε_{xx} and ε_{yy} strain components with sample scale load application across different localized regions along the crack trajectory. The region close to ± 10 mm from loading ends has not been taken into account considering the domination of the shear component. The IR aside crack trajectory (i.e., R7) is to capture the strain evolution in the localized region close to rock material cracking. It would provide insight into the undamaged localized rock specimen region close to the actual crack. Figure 4.7 summarises the above results.

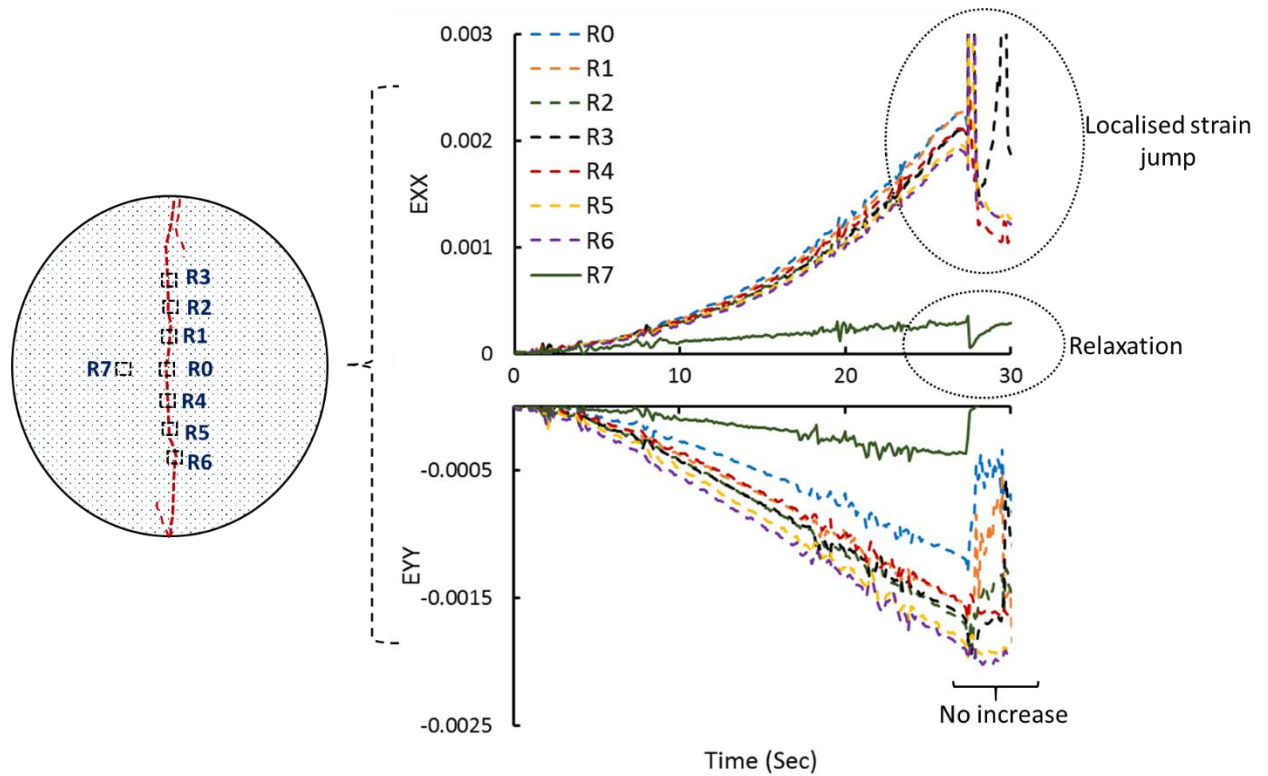


Figure 4.7: Conventional Brazilian disc test – local scale strain evolution

In figure 4.7, one can observe that rock material in localized regions across crack (i.e., R0 to R6) are undergoing a continuous increase in both, ϵ_{xx} and ϵ_{yy} strain components. The rate of tensile strain (i.e., ϵ_{xx}) increase is maximum in the localized region at the specimen center (i.e., R0). It further reduces as IR locations shift away from the center (i.e., R0) towards loading ends (i.e., R6). On the other hand, compression induced strain ϵ_{yy} variation demonstrate different responses with a minimum at specimen center, and maximum towards loading ends. The above observations of maximum tensile induced strain at the specimen center support the theoretical consideration of the Brazilian disc test. The non-uniformity in ϵ_{xx} magnitude and tortuous crack trajectory demonstrate the rock material non-homogeneity, which the theoretical consideration of conventional Brazilian disc test does not incorporate. Additionally, the magnitude of both ϵ_{xx} and ϵ_{yy} strain components at R7 (i.e., aside crack) throughout the loading scenario are less than 300% or more than the observations from IRs across crack trajectory. It shows that rock material across diametrical crack contributes maximum in overall specimen deformation. Whereas, the remaining sample portion behave more or less like a rigid body with negligible to no deformation.

Also, figure 4.7 shows that the lateral strain component (i.e. ε_{xx}) increases gradually in different IRs till peak load. After that, ε_{xx} undergoes sudden jump across all seven IRs from R0 to R6. These strain jumps occur at the same time (i.e., 28.1 sec) at peak loading stage 'iv.' On the other hand, despite localized dynamics due ε_{xx} jump, the magnitude of ε_{yy} either reduce or remain constant in all IRs. These observations demonstrate that the rock material under biaxial loading conditions fail primarily under tension resulting in ε_{xx} jump. While ε_{yy} reduces due to localized strain relaxation; ε_{xx} and ε_{yy} magnitude reduction in R7 denoting the elastic unloading due to nearby material cracking.

Further, figure 4.8 below presents the localized dynamic response (i.e. $\frac{d\varepsilon_{xx}}{dt}$ and $\frac{d\varepsilon_{yy}}{dt}$) in collaboration with the sample scale AE energy release.

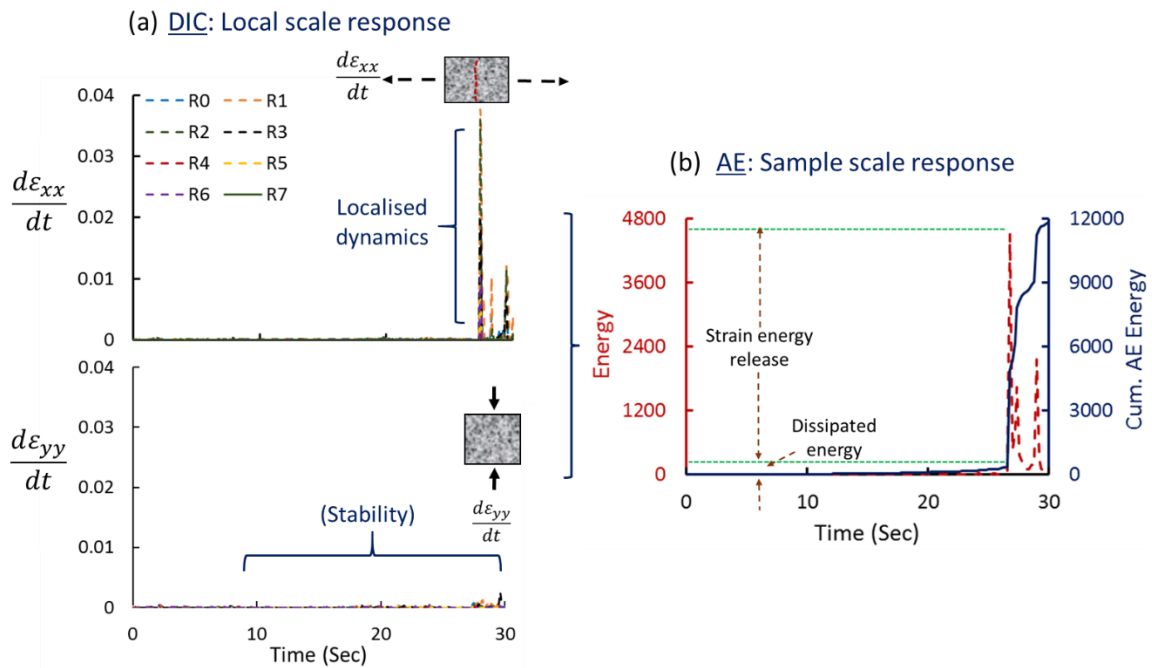


Figure 4.8: Cracking dynamics at local (DIC) and global (AE) scale

Figure 4.8 shows the sudden jump in the rate of ε_{xx} strain increment in all IRs along crack trajectory at global peak load. Whereas, the rate of ε_{yy} strain increment is always stable throughout the test. It shows that, despite global quasi-static loading conditions, rock material across above IRs undergoes dynamic failure primarily due to tension. It also forms the prime basis for the sample scale AE energy response, demonstrating a similar jump at peak loading stage iv. It shows that material cracking always induce localized dynamics. Before peak load, controlled dynamics indicate gradual or inconsequential strain energy dissipation due to localized micro-cracking. At peak load, these micro-

cracks coalesce to form major/sample scale crack releasing significant proportion of stored strain energy, causing localized strain jumps across crack trajectory and strain relaxation in surrounding intact rock material, i.e., figure 4.7.

Further, in terms of material strength analysis, one can observe that the region R0 acquires the maximum lateral strain of magnitude of 0.22% while R6 minimum of 0.16%. This variation in peak strain before failure is significant. The localized rock material in all IRs from R0 to R6 is undergoing cracking simultaneously almost at the same time fraction. Therefore, it is difficult or almost impossible to reliably determine the correct strain at which localized material undergoes tensile failure. An increase in frame rates (from 2 to 50 fps) did not yield much in this issue of direction but raised the DIC data storage demands.

4.4 Lateral Strain Controlled (Conventional) Brazilian Disc Test: Sandstone

This study presents a novel approach to control dynamics associated with the diametrical cracking of disc samples or also called 'AUSBIT.' It is an inevitable requirement and much-needed development to enable the efficient applications of advanced experimental techniques, including DIC. Chapter-3 demonstrated the feasibility and potential applications of the AUSBIT approach on various brittle materials like concrete and different rock types, including Hawkesbury sandstone and Bluestone. This chapter presents its benefits in terms of local scale rock material responses using Hawkesbury sandstone rock specimen with 42mm diameter. The experimental data from advanced instrumentation, including DIC and AE technique, have been used to unveil the linkage between localized controlled dynamics and sample scale damage characteristics.

In further our discussion on DIC applications, this section intends to present its validation first. For this purpose, a strain gauge of 10 mm length applied laterally across disc center over the front face of the sample. It was attached to the specimen surface before applying black speckles on the white base. The mechanism of controlled cracking enhances the usefulness of strain gauge by restraining the possibility of its dysfunctionality during/after specimen cracking and ensures a smooth outcome throughout. It is worth noting that the two terminologies, i.e., 'splitting' and 'failure,' have been used in different contexts where the latter denotes the rock material failure while the prior demonstrate complete separation of two cracked halves of disc specimen after

failure. Further, figure 4.9 presents the comparison between the strain (i.e., engineering strain) evolution from this localized strain gauge and the DIC's virtual strain gauge (i.e., inspection extensometer) of similar length (i.e., 10 mm) and alignment.

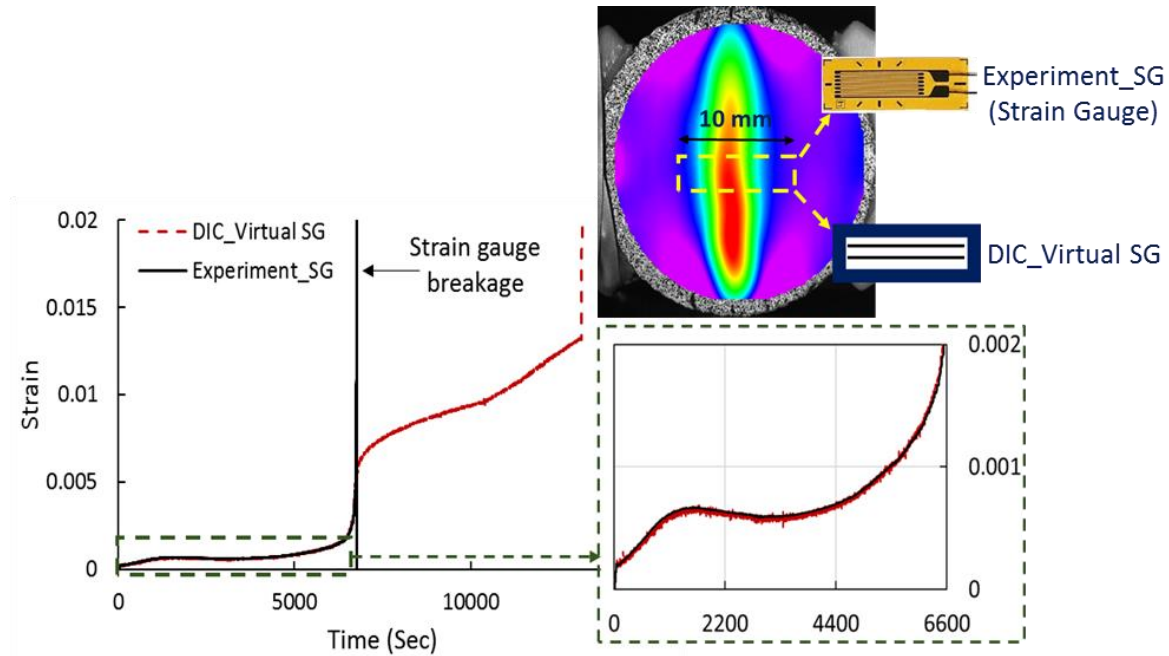


Figure 4.9: AUSBIT: DIC validation

One can observe here that the results obtained from the virtual strain gauge are in excellent agreement with the response from the actual strain gauge. These two responses can be seen inseparable till specimen failure indicated by lateral strain jump. After that, the actual strain gauge got dysfunctional. This key drawback of physical strain gauge has already mentioned in section 4.3.1. Nevertheless, the pre-crack results in this context are enough to demonstrate that the accurate calibration of DIC setup and reliability of obtained results.

4.4.1 Conventional Experimental Data

Figure 4.10 presents the conventional DIC full-field strain (i.e. ϵ_{xx} and ϵ_{xy} components) contours data obtained from lateral strain-controlled Brazilian disc tests in context with macroscopic sample behavior. One can observe here that the load-displacement response increases linearly with a gradual intensification of ϵ_{xx} and ϵ_{xy} strain fields from stage 'i' to 'ii' and then to stage 'iii' (i.e., peak). Where maximum intensification in ϵ_{xx} component occurs primarily in the region across central diametrical axis while ϵ_{xy} at loading ends. Stage 'i' indicates the switching of diametrical loading

from axial (with 0.2mm/sec axial displacement rate) to lateral (i.e. 0.2um/min lateral displacement rate) strain-controlled. The hint of unloading at this point shows the servo-control actions to adjust the loading pattern. Overall, it indicates that rock specimen at initial stages undergoes elastic deformation where tension induced strain (or stress) localizes across the loading axis. One can also observe that the position of maximum ε_{xx} intensity is not at the disc center, explaining the possibility of crack initiation away from the disc center (i.e., stage 'iii').

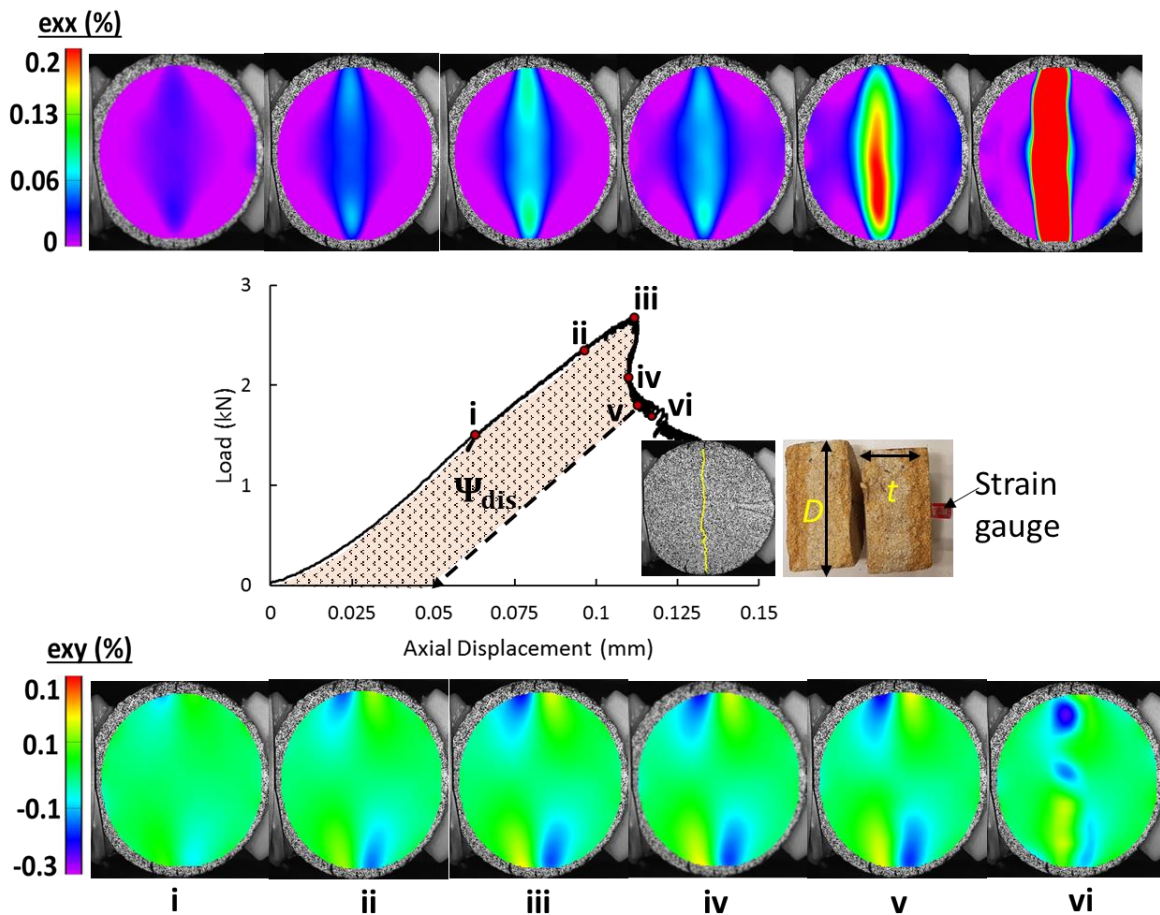


Figure 4.10: AUSBIT: full-field strain evolution.

Further, the load-carrying capacity of disc specimen decreases from stage 'iii' to 'iv' in the post-peak regime. Contrary to the conventional approach, this strength loss is accompanied by ε_{xx} intensity reduction without much variation in ε_{xy} component. The rate of axial compression of the disc specimen also reduces to induce 'snap-back' characteristics to sample scale load-displacement response. This loss of specimen strength occurs continuously in a gradual manner despite the reduction in axial compression rate (or even unloading at a specific time instant), i.e., the load-time response

in figure 4.11. It indicates the rock material undergoes significant damage immediately after stage 'iii' (or peak) in the post-peak regime. The specimen consumes the stored strain energy to govern the damage mechanism. Whereas, the servo-controlled loading-unloading cycles via constant lateral strain rate conditions remove the strain energy component additional to fracture requirement, thus stabilizes the overall cracking process. This sample scale effective unloading further explains the reduction in ε_{xx} strain intensity and the restrain in ε_{xy} component increments which play a significant role in localized material failure under conventional Brazilian disc test setup (i.e., figure 4.3).

The servo-controlled loading induced rock material damage continues to stage 'v' with a slight increase in axial compression. The ε_{xx} strain component also intensifies across the diametrical axis vertically around the disc center. It shows that the net energy available at stage 'iv' is insufficient to maintain a constant lateral strain rate. Consequently, the loading mechanism provides more energy to maintain a constant overall lateral strain rate. During this entire process, the localized tension induced by ε_{xx} strain across the central diametrical axis intensifies. It might even result in crack initiation too, which, due to the controlled nature of testing, is not visibly identifiable until stage 'vi.' One can affirm this via the change in ε_{xy} strain distribution pattern, which at stage 'vi' shifts from loading ends to disc sample's vertical diametrical axis. It shows that the disc specimen has failed, and now the two failed specimen portions are undergoing shearing.

4.4.2 Changes in global and local scale responses under servo-controlled loading

Before going into the quantitative analysis, it is essential to understand the influence of the servo-controlled loading system in the overall diametrical cracking mechanism of disc sample both at global (or sample) and local scales. For this purpose, figure 4.11 presents the overall AE results in collaboration with both MTS- load versus time (i.e., for global damage response) and DIC's inspections sections (both horizontal and vertical) responses.

This discussion divides the overall load-time response into six stages. Here, change in the slope of load versus time response along with initial AE hits observations at stage 'i' indicates the switching of loading applications from axial to lateral displacement-controlled type. After that, AE hits and amplitude observations stabilizes while approaching peak load from stage 'i' to 'iii.' This stability of AE continues in the post-peak

regime till stage 'v.' In the post-peak regime after stage iii, the sample scale load reduces gradually over a long period. These observations indicate that unlike the conventional approach, the servo-controlled mechanism has successfully controlled the dynamics associated with localized material damage. It consequently stabilized the overall AE activities. These overall observations demonstrate that rock material is undergoing stable cracking, thanks to a well-controlled experimental methodology. It is unlike the conventional approach where disc specimen undergoes sudden failure resulting in sudden release of stored strain energy. It causes increased localized dynamics; thus, the source for elastic waves recognized as AE.

One can perceive similar observations in the case of RA variation, which demonstrates stability throughout the test from stage 'i' to 'v.' It re-iterates the success of the adopted AUSBIT approach in controlling the dynamics, which consequently have converted the potential major crack at the peak loading stage to a series of continuous micro-cracking. Majorities of these micro-cracks are tension driven, resulting in a low RA magnitude. After that, in-between stage 'v' and 'vi,' significant rise in all the above three AE parameters, i.e., AE hits, amplitude, and RA, are observed, which indicate the possibility of shear-induced cracking. It illustrates the occurrence of diametrical cracking. Overall, the intensity of AE activities reduces to one-tenth of what observed in the conventional approach. It re-affirms the notion of AE linking with the dynamics associated with cracking, i.e., not with cracking itself.

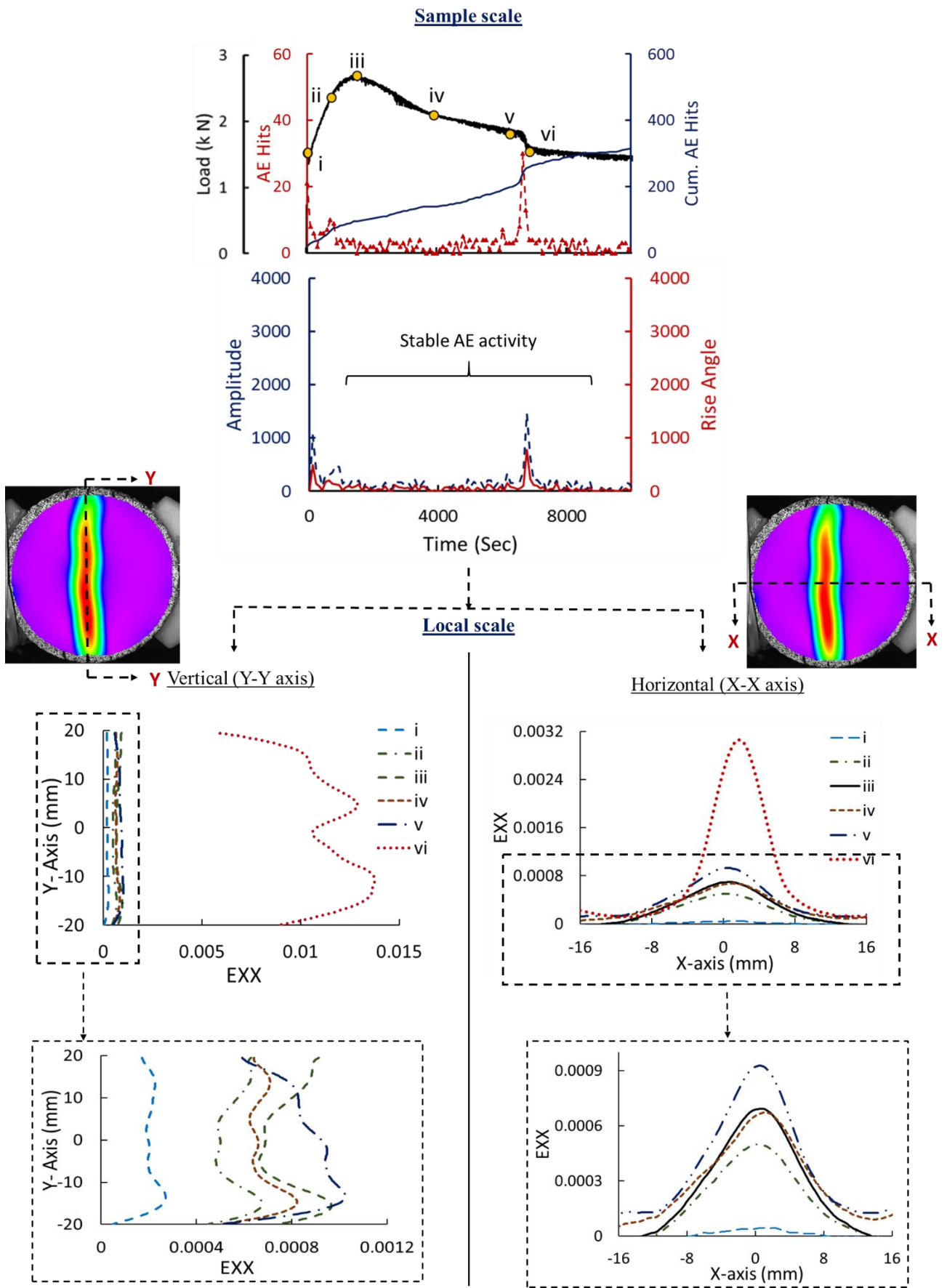


Figure 4.11: AUSBIT - sample (AE) and local scale (DIC) responses

Further in terms of local response via DIC analysis, figure 4.11 presents the ε_{xx} variation along a horizontal and vertical diametrical axis across disc specimen using two inspection lines, i.e., section x-x and section y-y. It demonstrates uniformity in the distribution of ε_{xx} strain across both sections at stage 'i' with less than 0.03% as maximum magnitude. These observations are in accord with the above AE early-stage analysis, indicating local scale elasticity. At stage 'ii,' loading approach switches to lateral strain-controlled where localization of ε_{xx} strain across the x-x section occurs within the effective range of ± 8 mm from the disc center. The maximum ε_{xx} recorded is approximately 0.05% across the disc center.

Further, ε_{xx} strain intensifies at stage 'iii' (i.e., global peak) throughout the x-x and y-y sections. Whereas, the rate of global-scale load increment decreases, indicating pre-peak damage initiation. At stage 'iv' in the post-peak regime, the disc sample's load-carrying capacity decreases significantly in a gradual manner. It demonstrates the success of the adopted AUSBIT approach to control the dynamics of the circular disc sample's instant cracking phenomenon. The sign of vibration in the loading plot (i.e., figure 4.10, 4.11) indicates the servo-mechanism induced loading-unloading cycles, which tends to remove the additional strain energy component and stabilize the cracking phenomenon. The above global loading conditions have a direct impact on disc sample's local behavior explaining the reduction in ε_{xx} strain magnitudes at stage 'iv' in comparison to stage 'iii' across both, x-x and y-y sections. This strain magnitude reduction (or strain relaxation) is quite uniform throughout the y-y section. Along the x-x section, strain relaxation is influential mostly in the localized region of ± 5 mm from the disc center. Strain in the remaining portion of this horizontal section, i.e. $[-16, -5] \cup [5, 16]$, intensifies comparative to previous stage 'iii.'

The physical interpretation of results in figure 4.11 is as follows: As the rock specimen undergoes diametrical compression, the localized region across the y-y axis get stressed the most but do not crack instantly. It continuously undergoes first elastic and then inelastic deformations. This highly stressed localized rock portion, in principle, controls the disc specimen's overall lateral deformation. Whereas, the surrounding regions mostly act as a rigid body up to a certain extent. The subsequent subsection further verifies this aspect of the region surrounding the potential crack. As the servo-controlled based global unloading happens, it induces localized unloading effect on the highly stressed centralized region. Consequently, this localized region observes strain relaxation causing recovery of

elastic component of localized deformation. This localized unloading caused strain (or deformation) intensification in the surrounding portion, as shown in figure 4.12. It further explains the ε_{xx} intensification in the surrounding region section i.e. $[-16, -5] \cup [5, 16]$ while strain relaxation in the centralised region (i.e. $\pm 8\text{mm}$ from disc centre) along x-x axis. In other words, the release of excess strain energy from this stressed localized portion adds-on to the deformation of the surrounding portion. Consequently, the specimen strength (or recorded load) reduces despite the systematic axial unloading.

As the damage process in rock material progresses, it practically becomes more challenging to maintain a pre-defined constant lateral strain rate without rock material failure. It further explains the extended time duration spent by the servo-controlled loading process to continue the controlled cracking from stage 'iii' to 'v' in the post-peak regime. At local-scale, significant strain intensification occurs at stage 'v' throughout the x-x section and from contour plots (i.e., figure 4.11). Where the point of the maximum strain of 0.09% still lies at the disc center. Section y-y at this stage demonstrates a similar pattern of strain intensification, but with significantly different distribution trends. Now, one can see that the strain intensification region across the vertical y-y axis has got re-distributed to be comparatively uniform along the center portion of the y-y section. It physically indicates that the servo-controlled loading-unloading cycles have brought the significant portions of the localized region across the y-y axis on the verge of failure. One should note that the work done by the external loading source during this entire process is negative (external work input < 0 , i.e., highlighted in eq. 3.3. in chapter-3).

At the final stage, both x-x and y-y axis observe a jump (i.e., from 0.09% to 0.32% approximately) in recorded strain. Along horizontal section x-x, this strain jump accompanies strain relaxations in the regions around the localization zone. The time duration of these evolutions is also in accord with AE hits observation, which further ascertains the cracking phenomenon across disc samples. Overall, the above analysis demonstrates the behavior of disc specimens at both global and local scales with a clear insight into the localization mechanism. Nevertheless, it is still difficult to estimate the reliable strain level at which the localized rock material fail under tension.

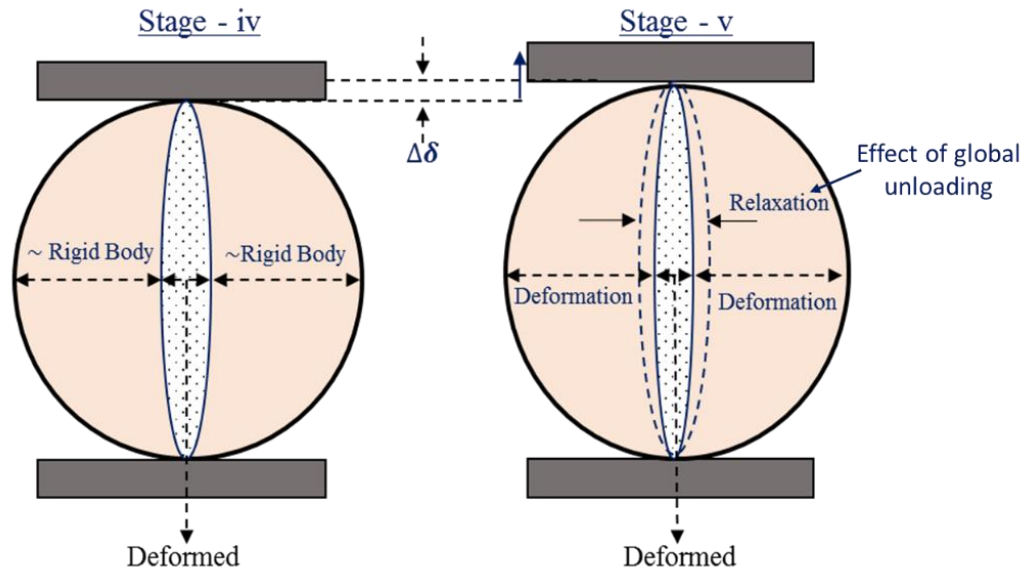


Figure 4.12: Mechanism of servo-controlled deformation

4.4.2 Tensile strength estimation

In order to further investigate the localized failure in quantitative terms, this study considers different inspection rectangles or IRs (i.e., 7 in numbers) across the crack trajectory. Approach delineated in section 4.3.5 utilized to finalize the size of such IRs. Such IRs are efficient to provide the complete strain description (i.e. ϵ_{xx} , ϵ_{yy} and ϵ_{xy}) as an average response over the area under consideration. Considering the biaxial stress state in diametrical compression of disc specimen, ϵ_{xx} and ϵ_{yy} strain components have been considered prime for this analysis. Figure 4.13 presents the details for strain evolution across the chosen IRs with time.

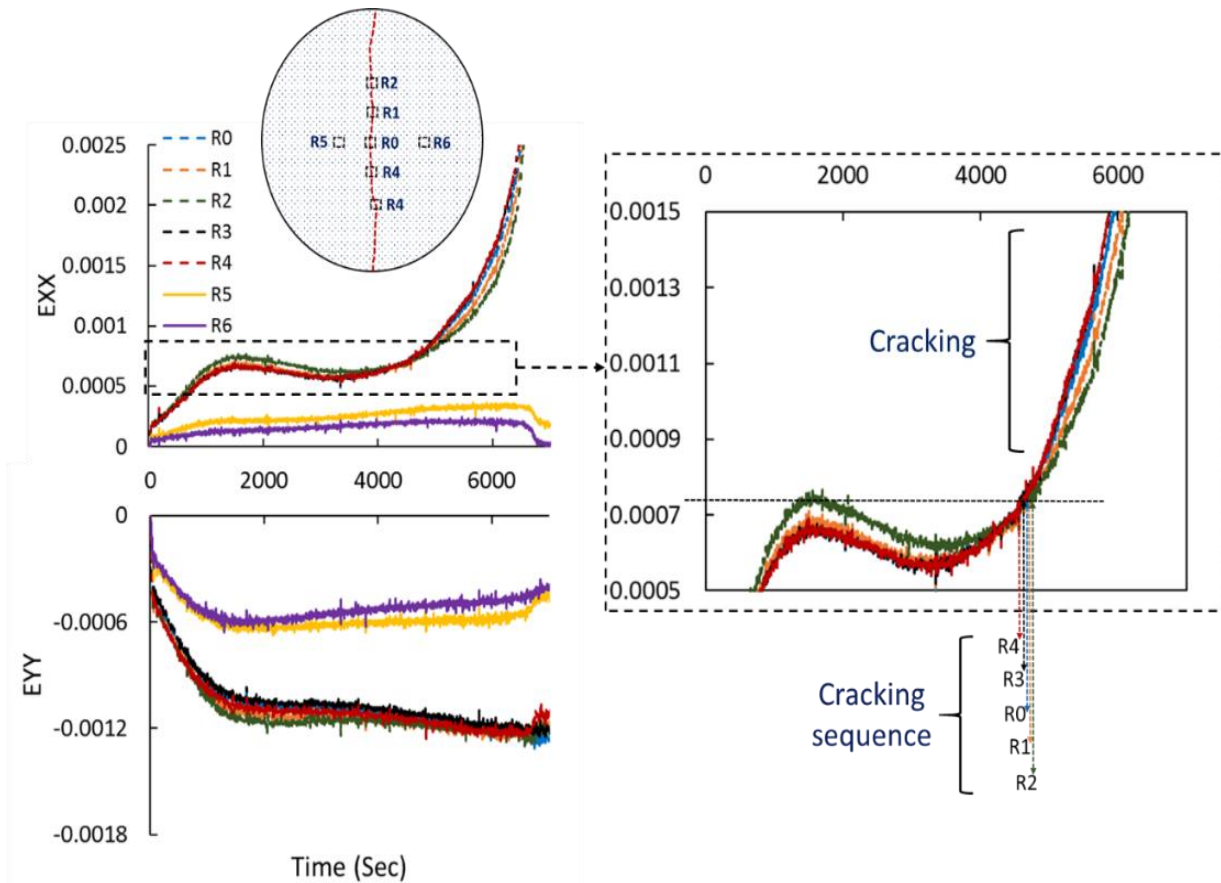


Figure 4.13: Cracking strain determination

In figure 4.13, both strain components (i.e. ε_{xx} and ε_{yy}) in all localized regions from R0 to R6 were continuously increase at initial loading stages. The magnitude of strain intensification in R5 and R6 is minimum because of its location, i.e., away from the centralized stressed region. It re-iterates the (almost) rigid body movement theory described in figure 4.12. After that, the rate of strain intensification changes in all IRs, indicating the effect of change in global loading technique (i.e., axial to lateral strain controlled) on local material response. At the global peak load stage 'iii,' the maximum strain level for above-localized areas are different. It shows that despite reaching a global peak load, many of these localized regions across the diametrical crack trajectory are still in its elastic regime, i.e., it demonstrates the influence of material heterogeneity. After this stage iii in the post-peak regime, the effect of the servo-controlled global loading-unloading cycle became more evident. In this regime, as the material started inelastic deformation, causing strength loss, it tends to increase the global lateral strain rate. Consequently, the axial loading rate reduces to compensate for this additional deformation and to maintain the pre-defined sample scale lateral strain rate. The reduction in global loading rate affects the local stress-state throughout the sample which further

explains the negligible increase in both ε_{xx} and ε_{yy} components in all IRs across crack trajectory, i.e., R0 to R4. It physically demonstrated the phenomenon of localized relaxation while maintaining a constant compression. Now the question arises that if the sample is undergoing servo-controlled global unloading, then how did it maintain a constant lateral strain rate?

To answer this, one should compare the response of R5 and R6 with remaining IRs, i.e., R1 to R4. One can observe the continuous intensification in ε_{xx} strain component while undergoing ε_{yy} (or axial compression) reduction. It shows that the strain relaxation in the central region driven by global unloading causes the deformation in the surrounding region (i.e., figure 4.11 and 4.13), which further re-affirms the deformation mechanism delineated in figure 4.12. At last, ε_{xx} strain component undergoes a sharp jump while maintaining constant ε_{yy} component across central IRs (R0 to R4). It indicates the localized cracking across the central diametrical axis. It further explains the drop-in ε_{xx} in surrounding R5 and R6 regions because of strain relaxation due to diametrical cracking. Here time fraction difference between ε_{xx} strain jumps would help identify the cracking sequence, from the lower half to the upper half of the sample, i.e., R6-R5-R0-R4-R1-R2-R3. One should also note here that the crack initiation point is again not at the specimen center. However, it would not be much relevant in the present approach, which does not rely on an empirical formulation for tensile strength estimation.

Further, to evaluate the effect of controlled dynamics, figure 4.14 presents the strain rate ($\frac{d\varepsilon_{xx}}{dt}$ and $\frac{d\varepsilon_{yy}}{dt}$) variation across R0 to R4, in collaboration with sample scale AE energy observations. Overall, figure 4.14 demonstrates a significant reduction in localized dynamics under the AUSBIT approach. The maximum rate of ε_{xx} change is under 2×10^{-3} which itself is quite close to generalized quasi-static conditions of 10^{-4} to 10^{-3} i.e., approximately. Such control over localized dynamics is significant especially considering the conventional approach where strain rate jump is around 4×10^{-2} . In terms of AE observation, the AUSBIT's controlled cracking approach results in a 94% lower AE energy magnitude in comparison with the conventional approach. This significant difference in AE energy release between conventional and AUSBIT approach re-iterates the importance of localized dynamics associated with the cracking (i.e., not the cracking itself) as the prime source for AE events. Besides, AE energy variation in figure 4.14 indicates that majorities of stored strain energy are now dissipating to create new

crack rather than releasing due to uncontrolled splitting (not cracking) in a conventional approach. One should note here that the AE events occurring, in this case, are again due to localized dynamics (but relatively controlled in the present case) associated with material cracking.

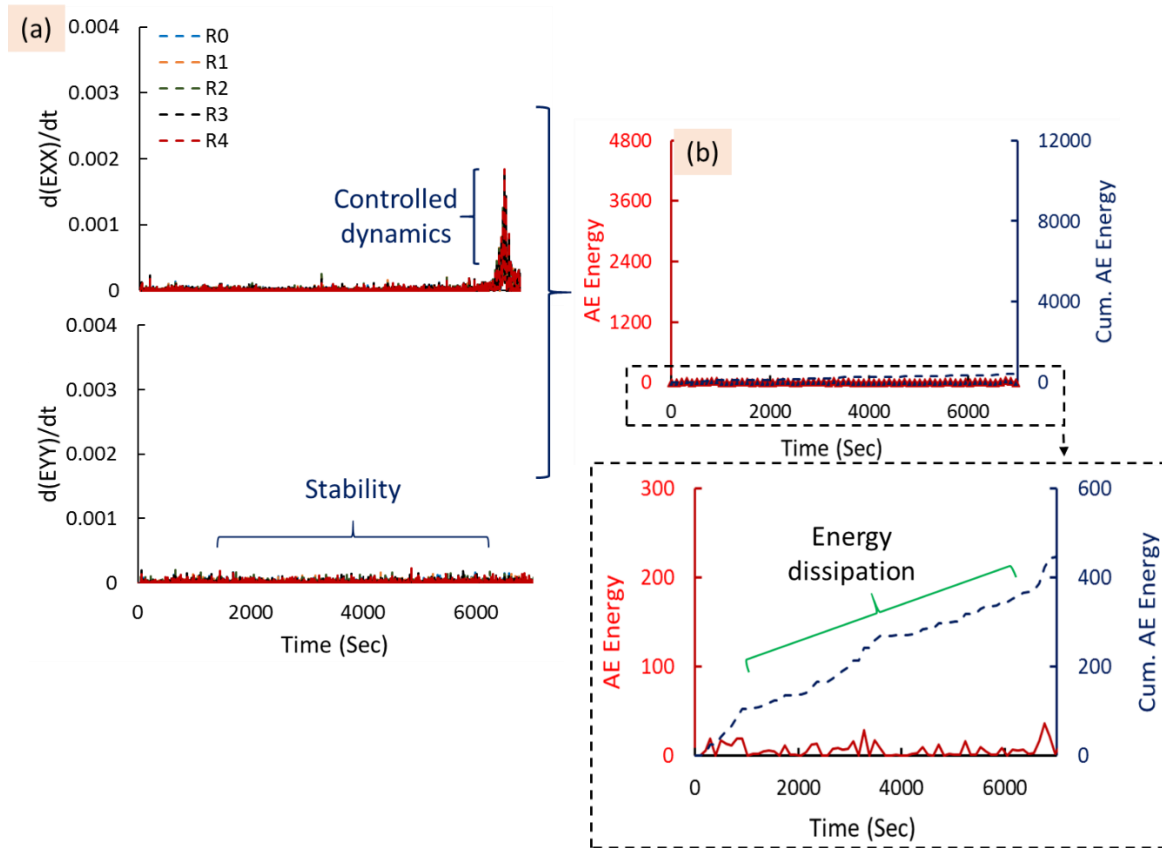


Figure 4.14: Effect of localized dynamics on AE energy

The prime benefit of the above-controlled dynamics is the reliability of localized response to estimate the tensile strength parameter. It reduces the variation in the peak ε_{xx} strain levels before jump across the central diametrical axis, i.e., R0 to R4. This study considers complete strain-description at each IRs to evaluate the localized stress state. The 2D frame of DIC strain evaluation has been considered compatible to evaluate biaxial plane stress conditions across specimen to evaluate stress from a given strain state using the following formulation:

$$[\sigma] = [C][\varepsilon] \quad (4.6)$$

Where,

$$[\sigma] = \begin{bmatrix} \sigma_{xx} \\ \sigma_{yy} \\ \tau_{xy} \end{bmatrix}; [\varepsilon] = \begin{bmatrix} \varepsilon_{xx} \\ \varepsilon_{yy} \\ \gamma_{xy} \end{bmatrix}; [C] = \frac{E}{1-\nu^2} \begin{bmatrix} 1 & \nu & 0 \\ \nu & 1 & 0 \\ 0 & 0 & (1-\nu)/2 \end{bmatrix}$$

Here E and ν are elastic modulus (i.e., 4800 MPa) and poisson's (0.2) ratio for Hawkesbury sandstone, i.e., chapter 3. While C is elastic constitutive matrix considering the Brazilian disc's isotropy and linear elasticity assumptions. This study further utilizes the obtained stress state to compute principal components (i.e. σ_1 and σ_2).

Figure 4.15 presents the stress paths for each IR in principle stress space to identify the location of potential failure envelope and thus the actual tensile strength (σ_t). Stress-path of all IRs along the crack trajectory (i.e., R0 to R4) clearly shows jump after elastic regime demonstrating in-elastic response. Whereas, stress paths of IRs in located in intact part (i.e., R5 and R6) rock specimen demonstrates elastic loading (and unloading after crack initiation) response. Though its unloading responses are affected by localized dynamics induced after diametrical cracking, thus showing significant instability. One should note here that the constitutive matrix in in-elastic regime should be corrected to incorporate in-elasticity induced damage to identify the corrected yield surface. However, one can avoid the entire process at this stage as the prime focus here is only to estimate the tensile (σ_t) of material by identifying the intersection of initial failure envelope with the x-axis (i.e. σ_1 axis).

At last, as the ratio of compressive to tensile strength (i.e. σ_c/σ_t) of rock generally varies from 10 to 20 times; this study considers the σ_c of Hawkesbury, sandstone rock to be in the range of 40 – 60 MPa. This information in collaboration with an average of the point (i.e. σ_1) of switching from elastic to the in-elastic regime have been used to draw the potential failure envelope. In a typical scenario, the average of all the switching points should be sufficient to evaluate tensile. It is because in case of biaxial loading conditions where tensile induced stress dominates, the stress path of such localized region always side close to principle stress (σ_1) axis. Although, the presence of potential failure envelopes would be visually better informed in terms of stress state for present or other loading conditions (e.g., uniaxial compression, shear). The present study observes the intersection of the potential envelope with the x-axis (i.e., the tensile strength of given rock) to be at 2.24 MPa approximately. This estimation of tensile strength from localized sources is roughly 20% higher than what estimated Brazilian disc's empirical estimation (i.e., 1.92 MPa). Such variation in tensile strength is in line with the commonly observed

differences between the direct and indirect approaches (Fairhurst 1964; Yu et al. 2009; Li and Wong 2013b; Perras and Diederichs 2014).

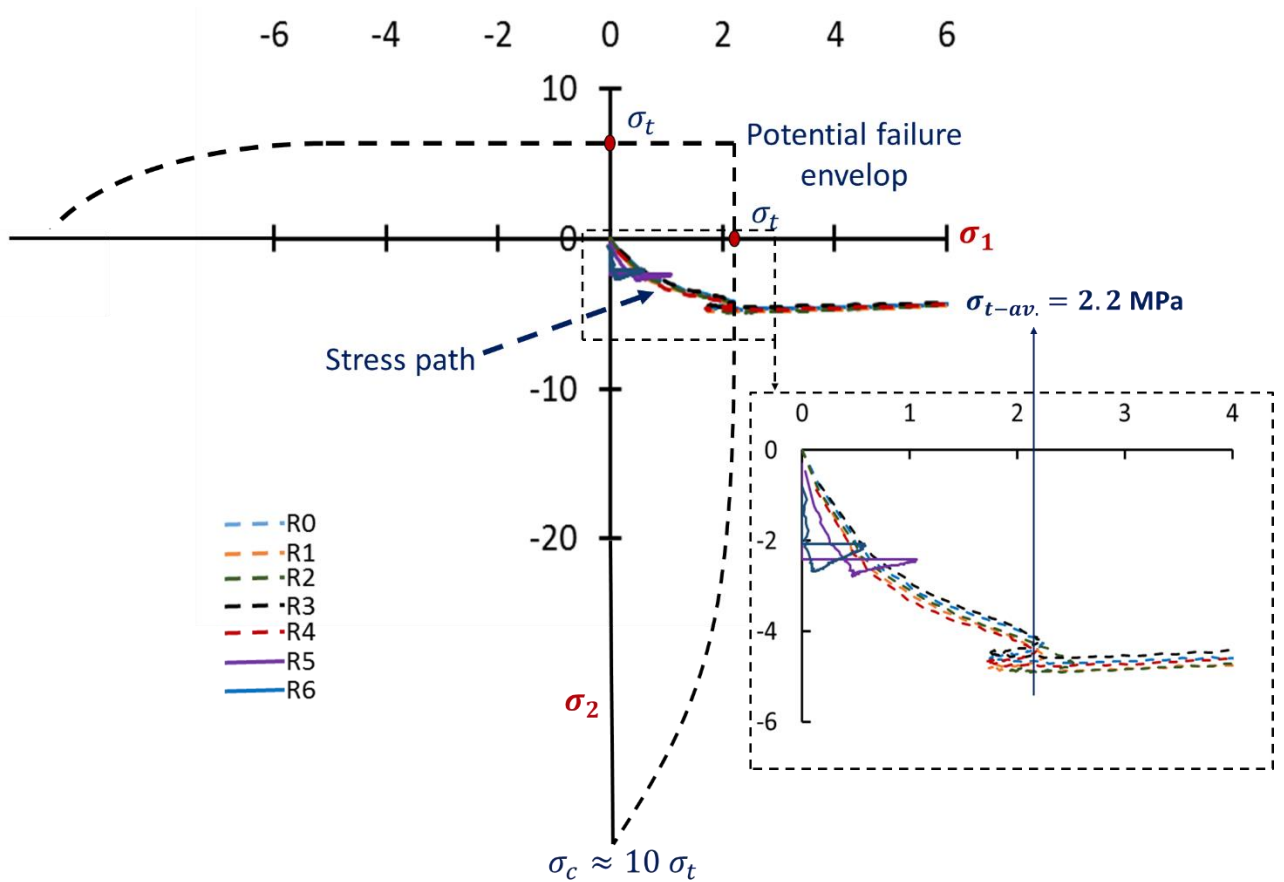


Figure 4.15: Failure envelope: tensile strength estimation

4.7 Conclusions

This work presents an innovative approach to derive the tensile strength parameter (i.e., close to uniaxial tensile strength) of rock material using diametrical compression of disc sample, commonly recognized as an indirect testing approach. The presented approach does not require any empirical formulation to link the macroscopic observation with material tensile strength property. This study gathered and analyzed local scale material responses using an advanced experimental approach, i.e., DIC, to derive the target property, which, in principle, is a true representative of overall rock material. Therefore, irrespective of material heterogeneity, one can always acquire a reliable estimate of the tensile strength material property via an indirect circular disc test. Such estimation would provide a better insight into the material property and, thus, will be comparable to direct tensile strength test results as well. In this sense, it becomes possible to circumvent the need of validating the following assumption of the conventional

Brazilian disc test; (a) crack must initiate at the disc center, (b) rock sample is homogenous, (c) stress across disc's diametrical axis are tensile without incorporating the effect of shear at loading ends.

This chapter also presents a novel approach of DIC data analysis, which enables us to derive material properties in quantitative terms. It provides an approach to utilize the DIC test data effectively and perform quantitative analysis to determine material property in quantitative terms. Such rigorous analysis of experimental data is missing in the majority of DIC's applications available in the literature. The presented data analysis approach has a significant potential to be used in other engineering and non-engineering fields as well.

At last, this chapter explores the role of local dynamics associated with cracking and its link with AE events. It highlights the significance of dynamics associated with the material cracking, which, in principle, is the source AE activity, i.e., not the crack itself explicitly. In a controlled environment, the same rock type sample with similar fracture energy would produce the AE events with significantly lower magnitudes as compared to what generated in an uncontrolled (or conventional) Brazilian disc test approach. This mechanism of delayed mechanism also enhances the efficiency of the DIC applications. The present approach of controlled cracking in indirect tensile testing has potential applications in different engineering and non-engineering materials, including concrete, ceramic, tablets (Pharmacy), and magnets. The techniques discussed in this chapter have been further applied to the Bluestone rock type to evaluate its fracture and strength parameters useful for numerical simulations in the subsequent chapters

Chapter 5

A 3D Dis-continuum Approach to Analyse Fracture Initiation and Propagation Mechanism in Hard Rock

5.1 Introduction

A numerical modeling approach is a robust tool that provides a great deal of flexibility and enables us to acquire a good insight into material behavior that is hard or impossible with actual laboratory experiments. Therefore, it is essential to develop the numerical modeling suits which can mimic the actual physics behind the material interactions, rather than just matching stress-strain curves. The resulting response at different scales under diverse loading conditions should then be the by default outcome. In the case of rock, which inherently is a discrete geo-material, preference of dis-continuum framework over continuum is quite apparent (Jing 2003; Johnson et al. 2009). Nevertheless, modeling rock as a collection of rigid circles (i.e., in 2D) or sphere (i.e., in 3D), i.e., in case of conventional DEM frameworks (Schöpfer et al. 2009; Tomac and Gutierrez 2012; Scholtès and Donzé 2013; Cao et al. 2018b; Dinç and Scholtès 2018; Ma and Huang 2018), is not appropriate, if not wholly incorrect. The prime reason behind this could be the nature of mineral or mineral aggregates constituting rock, which in actual, are not ideally rigid but deformable controlling the overall sample scale deformation under the elastic regime.

This study adopts the hybrid numerical modeling approach by collaborating continuum and dis-continuum frameworks together. It idealizes rock samples as the group of mineral aggregates represented by deformable continuum blocks. Specific elastic properties assigned to these continuum elements are obtained from laboratory experiments. It means that the deformable blocks in the adopted approach do not require actual calibration required to match the elastic response. This chapter directly uses the experimentally determined elastic properties from chapters 3 and 4 as input. Overall sample scale elastic deformation would be the collective response of continuum

tetrahedral blocks (or mineral aggregates in this case). At the same time, inter-block contact properties control the peak strength, post-peak behavior, and cracking mechanism. Section 5.2 presents a brief description of the adopted numerical modeling framework (i.e., 3DEC-Itasca). One essential improvement such a framework requires is the use of an efficient contact constitutive model, which could capture the mechanism of inter-granular micro-cracking realistically. It becomes more critical considering the in-built contact models, which are quite elementary in this context (Itasca 2016).

This study develops a new cohesive contact model that not only overcomes the limitations of inbuilt contact models and other existing cohesive models (i.e., as also highlighted in literature review sections) but also provides the base to capture the fracture mechanism of any given rock type realistically. This model utilizes the generic conceptual framework developed based on (Guimatsia and Nguyen 2012, 2014). The developed cohesive contact model has further been implemented in 3DEC as a DLL file via the C++ programming language subroutine. A detailed description of the proposed model, along with its stress-return algorithm, is presented in sections 5.3. Subsequently, verification of the proposed cohesive model is presented in section 5.4, followed by model implementation and validation in section 5.5.

This study further explores the potential applications of the developed numerical modeling suit by conducting virtual experiments, including Uniaxial compression (UCS) and conventional Brazilian disc (BD) experiments. These sets of experiments have also been conducted in the laboratory using advanced experimental techniques, including *Digital Image Correlation* (DIC). The use of DIC enables us to capture the local scale response, along with the standard sample scale stress-strain curve. Sub-section 5.6.1 presents a brief overview of performed experiments. The above experimental data set obtained from advanced instrumentation enables us to conduct the double scale validation (i.e., both at a sample and local scales) which itself is a much-needed improvement in the conventional approaches (Einav and Collins 2009; Nguyen et al. 2012b, 2014a, 2016c; Nguyen and Amon 2016; Le et al. 2017, 2018b).

The developed numerical modeling tool is further used to explore the cracking mechanism under UCS (i.e., leading to shear band formation before sample failure) and BD (i.e., sudden splitting failure) tests. Sub-section 5.6.2 and 5.6.3 present the detailed description of virtual UCS and BD experiments. Overall, the above exercises demonstrate

the robustness and reliability of developed numerical modeling suit in exploring the behavior of given rock type under any given loading conditions. It forms a strong base to explore further the bursting potential of the given rock type under complex loading conditions.

5.2 Dis-continuum modeling of intact rock: Numerical background

This study defines minerals aggregates as elastic deformable tetrahedral blocks formed by discretization of rigid blocks into tetrahedral finite difference meshes. Vertices of these finite difference meshes are the grid-points which comply with the following equation of motion based on Newton's second law of motion (Itasca 2016):

$$\frac{\dot{\mathbf{u}}_i^{(t+\frac{\Delta t}{2})} - \dot{\mathbf{u}}_i^{(t-\frac{\Delta t}{2})}}{\Delta t} = \frac{\sum \mathbf{F}_i}{m} \quad (5.1)$$

where for i^{th} grid-point, \mathbf{u}_i denotes grid-point displacement, ' t ' denotes the time at which the above variables are evaluated, ' m ' is the lumped mass at grid points enclosing the surface ' s ' and \mathbf{F}_i is the resultant nodal force vector calculated at each grid point. Here nodal force vector is the result of external applied load (\mathbf{F}_i^l), sub-contact forces (\mathbf{F}_i^c), forces due to internal stress in the zones neighboring grid-points (\mathbf{F}_i^z) and force due to gravity (\mathbf{F}_i^g). Expressions (5.2) and (5.3) present the rotation ($\dot{\boldsymbol{\theta}}_{ij}$) and strain ($\dot{\boldsymbol{\epsilon}}_{ij}$) corresponding to nodal displacements as follows:

$$\dot{\boldsymbol{\theta}}_{ij} = \frac{1}{2} (\dot{\mathbf{u}}_{i,j} - \dot{\mathbf{u}}_{j,i}) \quad (5.2)$$

$$\dot{\boldsymbol{\epsilon}}_{ij} = \frac{1}{2} (\dot{\mathbf{u}}_{i,j} + \dot{\mathbf{u}}_{j,i}) \quad (5.3)$$

The nodal displacement at each time step results in sub-contact relative displacement increment which leads to the following sub-contact force (\mathbf{F}_i^c) components in normal (F^n) and shear direction (F^s):

$$\Delta F^n = k_n \Delta u^n A_c \quad (5.4)$$

$$\Delta F^s = k_s \Delta u^s A_c \quad (5.5)$$

where, u^n and u^s are relative displacements while k_n and k_s are contact stiffness in normal and shear directions and A_c is the sub-contact area. After that, the next time-step applies these sub-contact forces to blocks.

As the 3DEC-Itasca is based on a dynamic algorithm, it results in the accumulation of kinetic energy at each time step, which is problematic in the case of static/quasi-static analysis. To avoid this problem, the simulations in this study adopt *local damping* (Cundall 1987) option in which damping force of magnitude proportional to the unbalanced nodal force is applied at each nodal point in the direction opposite to the unbalance force to acquire force equilibrium at earliest (Cundall 1987; Itasca 2016). It modifies the equation of motion as follows:

$$\dot{\mathbf{u}}_i^{(t+\frac{\Delta t}{2})} - \dot{\mathbf{u}}_i^{(t-\frac{\Delta t}{2})} = (\sum \mathbf{F}_i^t - (\mathbf{F}_d)_i) \frac{\Delta t}{m_n} \quad (5.6)$$

where,

$$(\mathbf{F}_d)_i = \alpha |\sum \mathbf{F}_i^t| \text{sgn}(\dot{\mathbf{u}}_i)^{(t-\frac{\Delta t}{2})} \quad (5.7)$$

In the above equations, $\alpha = 0.8$ is a constant and m_n is the nodal mass. The key benefit of the above damping treatment is the efficient handling of body force to achieve a steady-state with a steady damping constant (i.e., dimensionless), which is independent of material properties or boundary conditions. Besides, it adopts the numerical servo-control mechanism to control the damping amount from point to point, which is crucial for anticipating localized behavior in given numerical modeling. As the solution scheme of proposed numerical modeling technique is conditionally stable, it is inevitable to determine the limiting time step (Δt) before every numerical simulation to satisfy the following stability criterion for both, block deformation (Δt_n) and inter-block relative displacement (Δt_b) calculation:

$$\Delta t = \min(\Delta t_n, \Delta t_b) \quad (5.8)$$

Further, at each time step, the interface element (i.e., joint constitutive model) controls the relative inter-block displacement. Thus, for a realistic simulation of rock material cracking mechanism, the assigned joint constitutive model should have the competency to replicate the realistic inter-granular interactions.

5.3 Crack initiation mechanism and model description

The efficiency of the contact model to capture the mechanics of inter-granular interactions plays a vital role in the realism of performed numerical simulations. In this view, one approach could be to represent the inter-granular cementitious bonding via cohesive resistance to inter-block relative displacement, which degrades with damage

resulting in contact loss, physically signifying crack opening mechanism (Lisjak and Grasselli 2014; Bobet et al. 2009a; Needleman 2013). Such damage-based models neglect the contribution of inter-granular in-elastic relative displacement, which in physical terms, could be similar to smooth/clean crack surfaces, as shown in figure 5.1(a). Here, D and ΔD denote material damage and its increment at any loading stage. Nevertheless, crack surfaces in the actual rock are rough and unclean, as shown in figure 5.1(b), which indicates the significance of frictional component in inter-granular cementitious forces causing irreversible deformation in inter-granular relative displacement (Nguyen and Bui 2018; Bažant 1996).

The roughness of crack surfaces also governs the dilation behavior of the contact under shearing, given the two sides of the crack cannot smoothly slide against each other. Thus, it is inevitable to incorporate the influence of inter-granular friction along with cohesion and couple material damage with irreversible deformation to capture the realistic inter-granular interaction mechanism, as shown in figure 5.1(c). The coupling of damage with plasticity in constitutive modeling of geo-materials, including both continuum and cohesive-frictional models, becomes essential to reflect the underlying nature of failure that includes a considerable fraction of frictional dissipation, as addressed in a series of papers (Nguyen and Houlsby 2008; Nguyen and Korsunsky 2008; Nguyen et al. 2012, 2014; Guiamatsia and Nguyen 2012, 2014; Nguyen and Bui 2019). It forms a steady basis and physical justifications for the development of a cohesive-frictional model based on coupling damage mechanics with plasticity theory in this thesis. The subsequent subsection presents the constitutive formulation for the proposed cohesive model to incorporate the above discussed physical characteristics of inter-granular interactions.

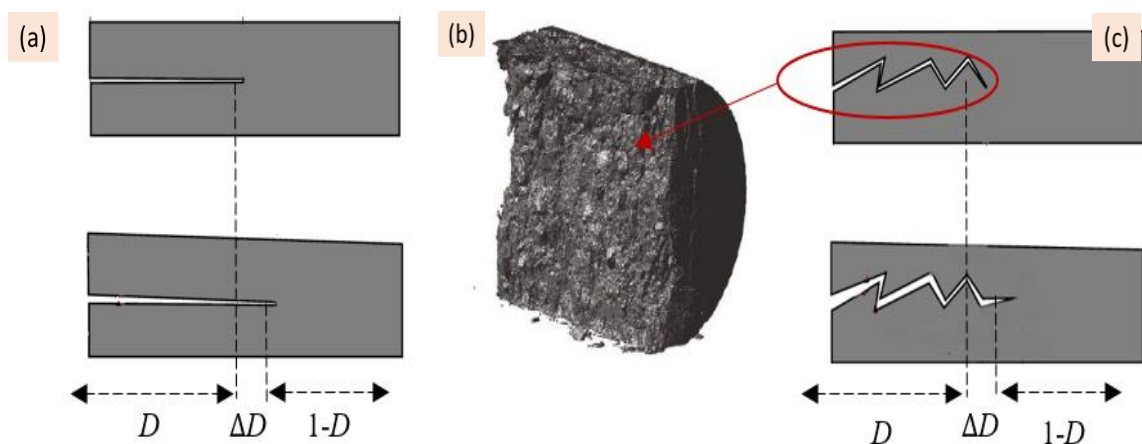


Figure 5.1:(a) Damage, (b) rough and unclean fracture surface, (c) damage-plasticity

5.3.1 Constitutive formulation

To incorporate the influence of material's grain-scale in-elasticity, the proposed cohesive model aims to couple damage with plasticity where relative displacement at contact level, i.e., \mathbf{u} (u_n, u_s), is sub-divided into elastic (\mathbf{u}^e) and plastic (\mathbf{u}^p) components as follows:

$$\mathbf{u} = \mathbf{u}^e + \mathbf{u}^p \quad (5.9)$$

where,

$$\mathbf{u} = u_n \mathbf{n} + u_s \mathbf{s} \quad (5.10)$$

$$\mathbf{u}^p = u_n^p \mathbf{n} + u_s^p \mathbf{s} \quad (5.11)$$

Here, \mathbf{n} and \mathbf{s} are unit vectors in normal and shear (i.e., in-plane) directions of any contact plane, u_n and u_s are coefficients of total inter-block relative displacements and u_n^p and u_s^p are coefficients of in-elastic (or plastic) inter-block relative displacement components in normal and shear directions. One can obtain the elastic component of inter-block relative displacement from equation (5.9), (5.10) and (5.11) as follows:

$$\mathbf{u}^e = \begin{bmatrix} u_n^e \\ u_{s1}^e \\ u_{s2}^e \end{bmatrix} = \begin{bmatrix} u_n - u_n^p \\ u_{s1} - u_{s1}^p \\ u_{s2} - u_{s2}^p \end{bmatrix} \quad (5.12)$$

These elastic components of inter-block relative displacement, i.e. ($u_n - u_n^p$) or u_n^e and ($u_s - u_s^p$) or u_s^p , are further used to determine the normal (t_n) and shear (t_s) traction components of contact stress state ($\boldsymbol{\sigma}$) as follows:

$$\mathbf{t} = \begin{bmatrix} t_n \\ t_{s1} \\ t_{s2} \end{bmatrix} = \begin{bmatrix} 1 - DH(u_n^e) & 0 & 0 \\ 0 & 1 - D & 0 \\ 0 & 0 & 1 - D \end{bmatrix} \begin{bmatrix} k_n^0 & 0 & 0 \\ 0 & k_s^0 & 0 \\ 0 & 0 & k_s^0 \end{bmatrix} \begin{bmatrix} u_n^e \\ u_{s1}^e \\ u_{s2}^e \end{bmatrix} \quad (5.13)$$

$$= \mathbf{K}^{\text{sec.}} \cdot \mathbf{u}^e$$

where,

$$t_n = \begin{cases} (1 - D)k_n^0 u_n^e, & \text{Tension} \\ k_n^0 u_n^e, & \text{Compression} \end{cases} \quad (5.14)$$

Here, k_n^0 and k_s^0 are contact stiffness in normal and shear directions, D denotes scalar damage parameter with maximum value 1 indicating the complete separation of contact resulting in the full crack opening. Whereas, $D = 0$ indicates the intact contact condition. Figure 5.2(a) presents a detailed schematic description of the above constitutive

formulation. It shows that contact undergoes irreversible plastic deformation and thus degradation in the post-peak regime of traction-displacement variations. Consequently, damaged inter-block (i.e., replicating inter-grain aggregate) contact stiffness i.e. $(1 - D) k_n^0$ and $(1 - D) k_s^0$ governs the loading-unloading path in the plastic regime under tensile/shear/combination loading conditions. The Heaviside function ensures complete recovery of contact stiffness in compression (i.e., no stiffness k_n^0 , degradation), which physically represents the crack closure phenomenon in actual rock material under compression. It also highlights that the effect of asperity degradation due to compressive stresses on inter-grain aggregate interactions may not be incorporated, i.e., a limitation that the present research acknowledges and considers to address in the future work.

It is essential to note here that the presented 3-dimensional dis-continuum approach describes the normal traction component (i.e. t_n) as a scalar parameter while shearing traction component as a vector (i.e. t_s). The magnitude of this shear traction vector is a scalar coefficient i.e. $t_s = \sqrt{t_{s1}^2 + t_{s2}^2}$, utilized by the stress return algorithm, as shown in figure 5.2(b). The essential advantage of this approach is that no coordinate transformation in three-dimensional virtual space is required to perform while computing traction components at a local scale induced by load increments at a global scale. In short, the implemented cohesive contact model acts at the local scale taking contact's relative displacement as input and providing contact stresses as an output. The stress transformation of these stresses from local to the global coordinate system is taken care of by 3DEC-Itasca functioning.

Further, to define the damage evolution law, this study utilizes the following exponential function in terms of inter-block relative plastic displacement in the proposed constitutive formulation as follows.

$$D = 1 - e^{-\frac{u^p}{\delta_0}} \quad (5.15)$$

Here, u^p is the total contribution of contact's relative plastic displacement in damage which at each loading step increases as per the following expression:

$$\Delta u^p = \sqrt{A (\Delta u_n^p)^2 + B (\Delta u_s^p)^2} \quad (5.16)$$

where, Δu_n^p and Δu_s^p are the components of relative plastic displacement increments in normal and shear direction of any contact plane, δ_0 is the relative displacement of unit magnitude utilized to normalize total plastic displacement u^p and make the overall

damage parameter unitless. ‘A’ and ‘B’ are model parameters which signify the contribution of Δu_n^p and Δu_s^p (i.e. $\Delta u_s^p = \sqrt{\Delta u_{s1}^p + \Delta u_{s2}^p}$) in total plastic displacement (i.e. u^p) controlling damage. These parameters control the damage mechanism at inter-grain aggregate contact. Thus, one can correlate these explicitly with the fracture energies and calibrate it using mode-I (i.e. G_f^I for calibration of ‘A’) and mode-II (i.e. G_f^{II} for calibration of ‘B’) fracture energies. A higher value of constant parameters ‘A’ denotes low G_f^I , i.e., more susceptibility to contact failure in tension. Similarly, a higher value of parameter ‘B’ comparatively signifies low G_f^{II} which signifies weak shear strength of inter-granular cementitious bonding in actual rock material. As the magnitudes of input damage parameters (i.e., ‘A,’ ‘B’) increase, it results in a sharp peak with high rates of post-peak softening, indicating brittle characteristics of the target material.

The advantage of the above scalar damage parameter (i.e., D) and its evolution is its simplicity, which makes its numerical implementation user-friendly and enhances the efficiency of numerical computation. The orthotropic formulation of the proposed cohesive model, along with randomly oriented inter-block contact surfaces, helps to capture the effect of material heterogeneity and anisotropy. Thus, it eliminates the requirement of complex damage evolution laws, i.e., vector or tensorial format. Besides, the exponential format of above scalar damage evolution law efficiently controls the role of cohesion and friction via total energy dissipation and smoothen out the cohesion to friction transition which has been the critical issue with linear, bi-linear damage evolution laws (Nguyen et al. 2017; Pouya and Bemani Yazdi 2015). Also, it obeys the experimental observation of ultimate damage at tremendous strain, especially in case of shearing under compression.

5.3.2. Yield criterion and plastic potential

This study proposes a unique yield loading function to define the initiation of inter-block plastic displacement along with damage. The proposed function could ensure smooth transition among different loading modes, thus could also take mixed mode loading conditions into account. In this view, this study acknowledges the efficiency of hyperbolic shaped yield surfaces (Eekelen 1980; Carol et. al. 1997; HAM 1980) over conventional yield criteria, e.g., Mohr-Columb, Hoek Brown, and proposes following unified yield-failure criterion expression.

$$f = t_{s1}^2 + t_{s2}^2 + t_n (c - t_n \tan^2 \Phi) - \sigma_t (c - \sigma_t \tan^2 \Phi) \quad (5.17)$$

where, c , Φ and σ_t are the strength parameters of the proposed cohesive model, which numerically represent cohesion, friction, and tensile strength components of intergranular cementitious bonding. As the stress state at any contact reaches the above yield surface (i.e., $f = 0$) it results in plastic displacement and evokes damage to cause inter-grain aggregate strength degradation, i.e., $c = c^0 (1 - D)$ and $\sigma_t = \sigma_t^0 (1 - D)$, where c^0 and σ_t^0 denotes initial cohesion and tensile strength of contact strength in a pre-peak regime of stress-displacement response (i.e., $f < 0$ and $D = 0$). The parameter Φ incorporates the influence of contact roughness, which also undergoes degradation with damage. One can achieve this by defining the model's friction parameters as follows.

$$\Phi = \Phi_{\text{res}} + (\Phi^0 - \Phi_{\text{res}})(1 - D) \quad (5.18)$$

Here, Φ_{res} is friction angle at residual state when two distinct surfaces forms due to material cracking and Φ^0 is an initial friction angle (i.e., in the pre-peak regime). It is often difficult to obtain the above two friction parameters distinctly. Therefore, it is convenient to adopt a residual value for the above two parameters i.e. $\Phi^0 = \Phi_{\text{res}}$, which replaces the friction variable in eq. (5.18) with constant parameters, i.e., $\Phi = \Phi_{\text{res}}$. This degradation in contact strength parameters results in shrinking of proposed yield criterion to acquires residual state, schematically shown in figure 5.2(a).

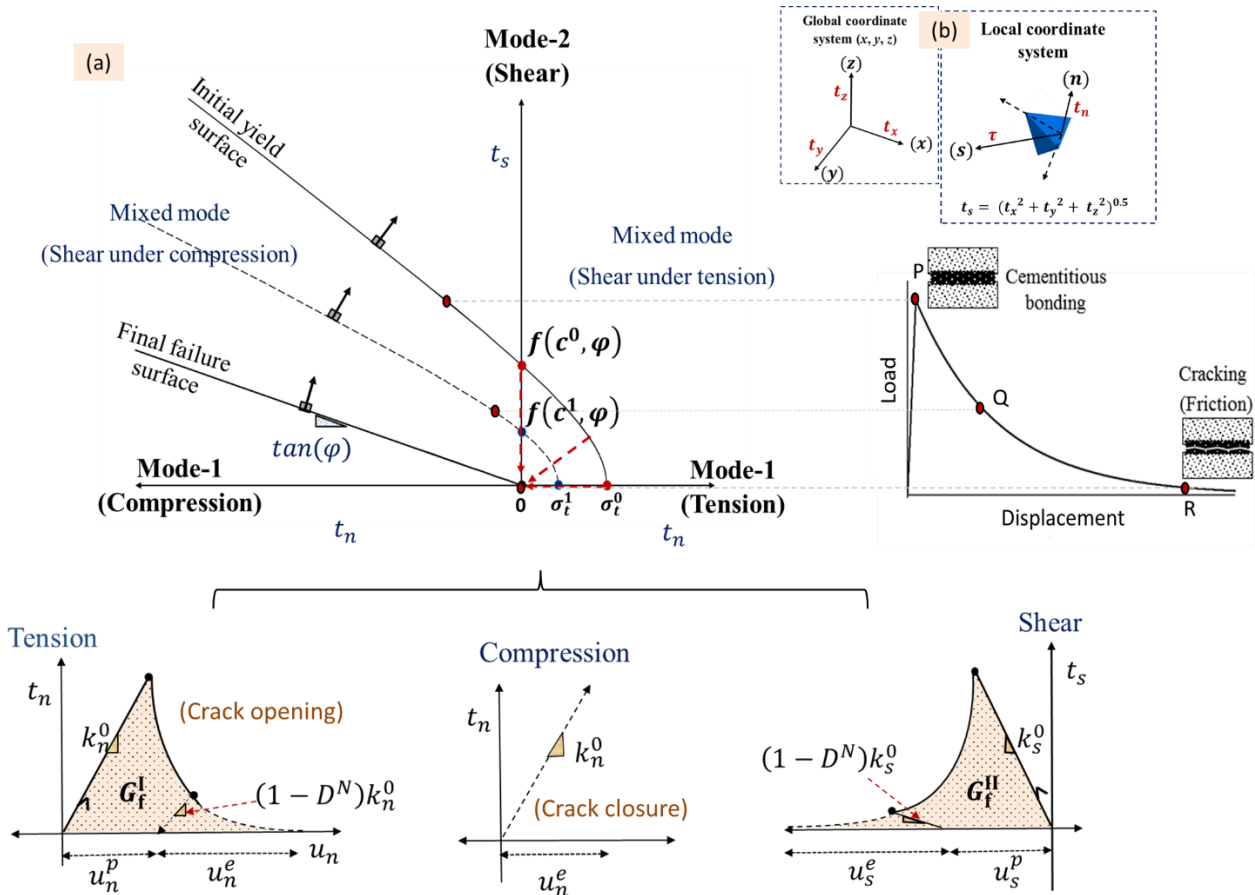


Figure 5.2: (a) Yield surface and constitutive behavior under pure tension, compression and shear, (b) Coordinate system

In figure 5.2(a), the horizontal axis represents normal traction component variation (i.e., mode-1; tension takes positive sign), at contact level with maximum value defined by model’s initial tensile strength parameter (i.e. σ_t^0). The vertical axis shows the shear traction component, i.e., mode-2 (shear) loading conditions, with maximum value controlled by the model’s initial cohesion parameter (i.e. c_0). The region in between these axes signifies mixed mode loading conditions with a positive quadrant representing shearing under tension and negative quadrant as shearing under compression. Thus, under any given loading conditions, when the contact stresses reach its peak strength, i.e., point ‘P,’ yielding of inter-granular cementitious bonding starts taking place (or $f=0$). It invokes inelasticity represented in the model by plasticity and damage, causing degradation of contact strength parameters and resulting in the shrinking of yield envelope from initial yield (i.e., $D=0$) to residual or final failure surface (i.e., $D=1$). Such a response of the constitutive model demonstrates the gradual de-cohesion of inter-block cohesive traction. It indicates the decay of inter-granular cementitious forces in actual

rock material. This gradual de-cohesion eventually results in the formation of two distinct crack surfaces. The residual yield surface expression, which is the classical Mohr-Columb criterion, i.e., $t_s = t_n \tan(\Phi_{\text{res}})$, controls the interaction of these distinct crack surfaces, thus highlights the significance of confinement (i.e. t_n) and residual friction angle (i.e. Φ_{res}) in a residual stress state. It implies that in the absence of any external confinement (i.e., positive quadrant of figure 5.2a or $t_n \geq 0$), ultimate strength at contact level acquires zero residual value, which can capture the physical mechanism of grain aggregate separation, causing a crack opening in the actual rock. Overall, the above mechanisms illustrate the ability of the proposed model to acquire a smooth transition from cohesion to a frictional mode of energy dissipation with damage as commonly observed in actual rock material (Nguyen and Bui 2018).

At last, to define the magnitude and direction of plastic displacement, which is the principal factor controlling the dilation, the proposed cohesive model adopts non-associated flow rule with the following plastic potential (g) expression:

$$g = t_{s1}^2 + t_{s2}^2 + t_n(c - t_n \tan^2 \Phi_d) - \sigma_t(c - \sigma_t \tan^2 \Phi_d) = 0 \quad (5.19)$$

Here, Φ_d controls the material dilation parameter. Using non-associated flow rule conditions (i.e., $d\mathbf{u}^p = \Delta\lambda \frac{\partial g}{\partial \mathbf{t}}$) and above plastic potential expression, i.e., eq. 5.19, one can estimate the total plastic increment at each step as follows.

$$d\mathbf{u}^p = \Delta\lambda \begin{bmatrix} du_n^p \\ du_s^p \end{bmatrix} = \Delta\lambda \begin{bmatrix} \frac{\partial g}{\partial t_n} \\ \frac{\partial g}{\partial t_s} \end{bmatrix} = \Delta\lambda \begin{bmatrix} c - 2 t_n \tan^2 \Phi_d \\ 2 t_s \end{bmatrix} = \Delta\lambda \mathbf{S} \quad (5.20)$$

where, $\Delta\lambda \frac{\partial g}{\partial t_n}$ and $\Delta\lambda \frac{\partial g}{\partial t_s}$ are plastic displacements increments in normal (i.e., du_n^p) and shear direction (i.e., $du_s^p = \sqrt{(du_{s1}^p)^2 + (du_{s2}^p)^2}$), t_n and t_s (i.e., $t_s = \sqrt{t_{s1}^2 + t_{s2}^2}$) are the normal and shear traction components. The $\Delta\lambda$ indicates scalar plastic multiplier. Equation (5.20) shows that the dilation angle parameter could affect the normal component of plastic displacement. In fact, from the definition of the plastic multiplier (i.e., $\Delta\lambda \geq 0$) and negative sign of compression, one can perceive that under shear or shearing-compression, an increase in dilation parameter (Φ_d) always increases the normal component of plastic displacement, i.e., irreversible expansion or dilation. The use of the dilation parameter in the proposed constitutive formulation indicates the phenomenological attempt to incorporate the influence of surface unevenness/roughness

characteristics. These surface characteristics are commonly known as *asperities*. The proposed model also incorporates the influence of dilation parameter degradation with damage i.e. $\Phi_d = \Phi_d^0(1 - D)$, which shows the physical mechanism of complete asperities degradation under shearing resulting in the gradual decay of material's dilatational characteristics. Figure 5.3 summarizes the physical mechanism of material dilation evolution with the stress-path mentioned above.

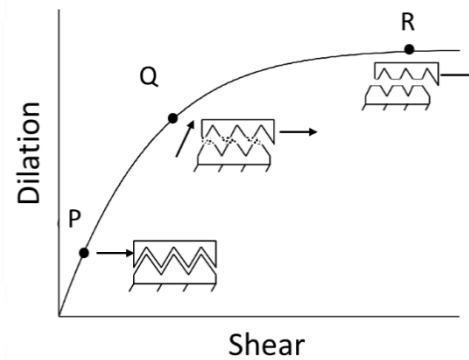


Figure 5.3: Evolution of dilation angle with damage

5.3.3. Model parameter determination

The proposed model's micro-parameters control the behavior of the cohesive contact and require proper calibration. It not only adjusts the cohesive model to the given rock material type but also acquires practical relevance in terms of physical significance. Therefore, a systematic approach to detection and calibration is essential to replicate the given rock or any other brittle material type.

In this view, the first set model parameters are contact stiffness in normal (k_n) and shear (k_s) direction, which indicates the contact's elastic stiffness and controls the slope of stress-displacement responses under different modes of loading conditions. The calibration procedure for these parameters depends upon the type of numerical simulations. The prime intent of the proposed cohesive model in this research is to replicate the inter-grain aggregate behavior of any given rock specimen. Here, the cohesive model intends to replicate the microcracking mechanics. While the deformable continuum blocks may capture the rock's elastic deformation response. Under such a scenario, it is essential to assign very high values to these contact stiffnesses (i.e., k_n , k_s) in such a way that further increases in their magnitudes may not influence the overall elastic response. This will nullify the contribution of inter-granular relative displacement

in overall elastic deformation. It ensures that the elastic response of the given rock sample would be purely due to block's (or mineral aggregates) elastic deformation collaboratively. The inter-granular (grain aggregate) relative displacement comes into picture only when the contact stiffness starts deteriorating due to the activation of damage parameter (D) in case of material fracturing. Whereas, in the case of rock's joint replication in association with rigid blocks, the k_n stiffness parameters should be adjusted to replicate the overall elastic modulus (E) while k_s is tuned to simulate the Poisson's ratio effect of the overall rock sample.

The remaining micro-parameters of the proposed cohesive model can be classified into two main categories: peak strength and post-peak behavior controlling parameters. The prior category includes tensile strength (σ_t), cohesion (c), and friction (Φ), while the latter includes damage parameters A and B . The σ_t parameter indicates the tensile strength of the given contact. One can adopt material tensile strength obtained from laboratory experiments explicitly as the cohesive model's σ_t parameter. The cohesion (c) parameter indicates contact's cohesion controlling its peak strength under shear or shear-compression. These two parameters in the proposed model act as contact properties controlling the peak strength of the entire sample under compression or tension. Provided the known value of σ_t , the cohesion (c) should be tuned to capture peak strength magnitude under tension and compression. The friction (Φ) parameter, on the other hand, intends to capture the friction properties of the given rock or rock-joint type. For a rock joint, one can calibrate it explicitly by matching the post-peak residual strength in shear under constant normal loading conditions. In case of rock specimen where cohesive model controls the contact behavior, the Φ should be calibrated to capture correct post-peak crack pattern.

The parameters A and B control the evolution of damage variable D . Thus, these parameters are explicitly linked with the fracture properties of rock and requires fracture energies in mode-I (i.e. G_f^I) and mode-II (i.e. G_f^{II}) loading conditions for proper calibration. The explicit determination of parameter A can be achieved via the analytical solution for the proposed cohesive contact model under pure tension (i.e., mode-I) loading condition, as presented in section 5.4.1. Once parameter A is calibrated, the next step is to calibrate the parameter B , which requires mode-II fracture energy, can also be achieved by utilizing the analytical solution for pure shear loading conditions, as presented in

section 5.4.2. In the absence of required experimental data, parameter B can be calibrated by fine-tuning the post-peak response of numerical simulation. At last, the parameter (Φ_d) controls the magnitudes, direction, and ratio of contact's plastic normal and shear displacement (i.e., eq. 5.19 and 5.20). It shows that Φ_d controls the dilation angle (ψ), i.e., $\tan \psi = \frac{\Delta u_n^p}{\Delta u_s^p}$. Therefore, it requires fine-tuning with the rock's dilation response commonly observed in shear under constant normal loading conditions, mixed-mode tests, and triaxial experiments. One example of Φ_d calibration is presented in section 5.5 as well.

5.3.4. Stress return algorithm

This section presents the implicit calculations for the stress-return in the proposed cohesive contact model. The adopted implicit calculations enable the model to produce good results even with relatively larger incremental steps. This approach is quite practical, especially when compared with explicit calculations based on tangent stiffness estimation. Figure 5.4 presents the notion of the adopted stress-return algorithm, where point 'A' indicates the present, point 'B' is the trial, and point 'C' is the corrected/new stress state. f^n is the current yield surface while f^{n+1} is the yield surfaces at point 'C,' i.e., at $n+1^{\text{th}}$ step. At each step, the stress return algorithm initially estimates the stress increment using expression 5.13. If the resultant stress state (i.e., $\mathbf{t}^{\text{Trial}} = \mathbf{t}^n + d\mathbf{t}^{\text{Trial}}$) satisfies the yield criterion (i.e., $f^{\text{Trial}} < 0$), then it considers the contact to be in the elastic regime, thus applies no damage to the contact strength parameters. However, if the trial stress states violate the yield criterion indicating its position at point 'B' outside the yield surface, then it tends to estimate the corrective stresses increment ($d\mathbf{t}^c$) to bring the resultant stress state at the new yield surface (i.e., f^{n+1}), obtained from the damaged strength parameters of the cohesive model, as shown in figure 5.4. One can express the new yield function using the First Taylor expansion approximation, as follows.

$$f^{n+1} = f^{\text{trial}} + \frac{\partial f}{\partial \mathbf{t}^c} \cdot d\mathbf{t}^c + \frac{\partial f}{\partial D} dD \quad (5.21)$$

The corrective stress increment can be estimated as follows.

$$d\mathbf{t}^c = \frac{\partial \mathbf{t}}{\partial \mathbf{u}^p} \cdot d\mathbf{u}^p + \frac{\partial \mathbf{t}}{\partial D} dD \quad (5.22)$$

The plastic increment at each step is estimated by Eq. 5.20. The damage evolution estimation utilizes the following expression.

$$dD = \frac{\partial D}{\partial u_n^p} du_n^p + \frac{\partial D}{\partial u_s^p} du_s^p = \Delta\lambda \left(\frac{\partial D}{\partial u_n^p} \frac{\partial g}{\partial t_n} + \frac{\partial D}{\partial u_s^p} \frac{\partial g}{\partial t_s} \right) = \Delta\lambda R \quad (5.23)$$

Here, t_n and t_s (i.e., $t_s = \sqrt{t_{s1}^2 + t_{s2}^2}$) are the normal and shear traction components, du_n^p and du_s^p are the plastic displacements in normal and shear directions.

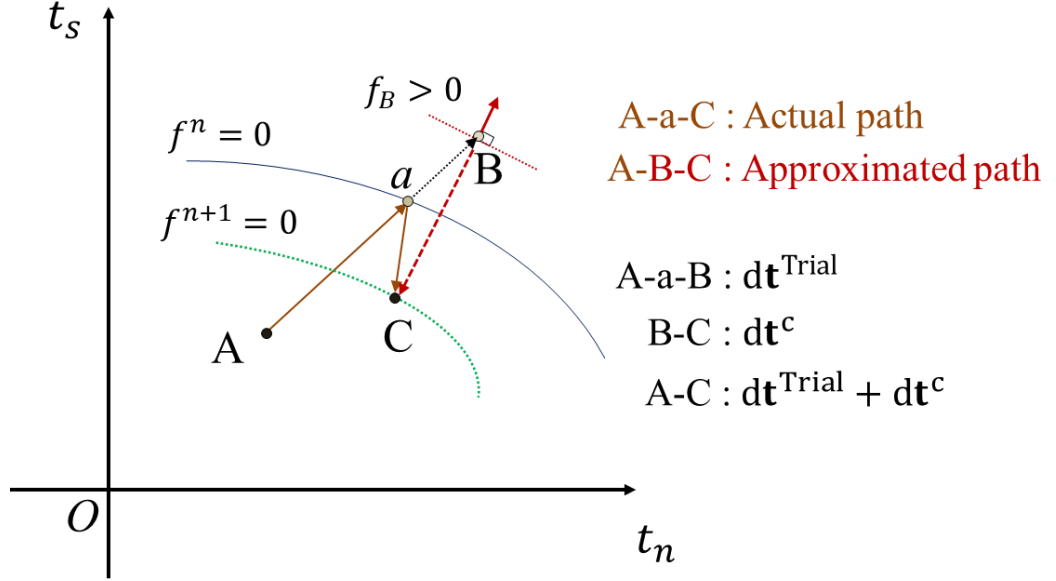


Figure 5.4: Stress-return algorithm.

Now, using expressions 5.23 in 5.22 and after that replacing the resultant 5.22 in 5.21 to enforce the new yield surface to zero, one can obtain the $\Delta\lambda$ scalar multiplies, as follows.

$$d\lambda = -\frac{f^{trial}}{\frac{df}{dt} \frac{dt}{du^p} \cdot \mathbf{S} + \left(\frac{df}{dt} \frac{dt}{dD} + \frac{df}{dD} \right) R} \quad (5.24)$$

The above scalar factor helps in the computation of corrective stresses to bring the trial stress state at point 'B' to point 'C' at the correct yield surface at the $n+1^{\text{th}}$ step. One should note here that the elastic component is zero while moving from 'B' to 'C.' It is because the elastic component was already taken into account while moving from 'A' to 'B.' The above plastic multiplier helps in updating the stress components and damage variable D , which consequentially updates all the model parameters for the next (i.e., $n+2^{\text{nd}}$) stage estimations. Table 5.1 below summarizes the above stress-return algorithm sequentially.

Table 5.1: Description of cohesive model's stress return algorithm

Stress Return Algorithm	
1.	At any N step, the input displacement given to the loading will be Δu_n^N and Δu_s^N .
2.	Incremental traction components in normal (Δt_n^N) and shear (Δt_s^N) direction will be as follows. $\Delta t_n^{\text{Trial}} = k_n^N \Delta u_n^N \quad ; \quad \Delta t_s^{\text{Trial}} = k_s^N \Delta u_s^N$
3.	Thus, trial stress at step N is as follows. $t_n^{\text{Trial}} = t_n^{N-1} + \Delta t_n^{\text{Trial}} \quad ; \quad t_s^{\text{Trial}} = t_s^{N-1} + \Delta t_s^{\text{Trial}}$
4.	These traction components describing the trial stress state at given contact inserted in yield surface expression to check the yield state of contact as follows. $f^{\text{Trial}} = (t_s^{\text{Trial}})^2 + t_n^{\text{Trial}} (c^N - t_n^{\text{Trial}} \tan^2 \Phi^N) - \sigma_t^N (c^N - \sigma_t^N \tan^2 \Phi^N)$
5.	If $f^{\text{Trial}} < 0$, contact stress state is in the elastic state. Thus no damage in contact material strength, which results in the following updates. <ul style="list-style-type: none"> a) Update the stress state at the Nth step: $t_n^N = t_n^{\text{Trial}} \quad ; \quad t_s^N = t_s^{\text{Trial}}$ b) Update the contact strength parameters for the N+1th step: $k_n^{N+1} = k_n^N \quad ; \quad k_s^{N+1} = k_s^N$ $c^{N+1} = c^N \quad ; \quad \sigma_t^{N+1} = \sigma_t^N \quad ; \quad \Phi^{N+1} = \Phi^N \quad ; \quad \Phi_d^{N+1} = \Phi_d^N$
6.	Else ($f^{\text{Trial}} \geq 0$), it signifies that the current stress state has reached the failure envelope and has evoked plastic relative displacement at the inter-block contact level. Thus, the trial stress state needs to be corrected to bring it on yield surface as follows. <ul style="list-style-type: none"> a) Compute the plastic multiplies ($\Delta \lambda$). $\Delta \lambda = - \frac{f^{\text{trial}}}{\frac{df}{dt_n}(\alpha) + \frac{df}{dt_s}(\beta)}$ <p>Where,</p> $\alpha = k_n^N \left(\frac{\partial g}{\partial t_n} \right) + t_n^{\text{Trial}} \sqrt{A \left(\frac{\partial g}{\partial t_n} \right)^2 + B \left(\frac{\partial g}{\partial t_s} \right)^2}$ $\beta = k_s^N \left(\frac{\partial g}{\partial t_s} \right) + t_s^{\text{Trial}} \sqrt{A \left(\frac{\partial g}{\partial t_n} \right)^2 + B \left(\frac{\partial g}{\partial t_s} \right)^2}$ b) Compute the corrective traction increments in normal and shear direction. $\Delta t_n^{\text{Corrective}} = \Delta \lambda (\alpha)$ $\Delta t_s^{\text{Corrective}} = \Delta \lambda (\beta)$ c) Update the traction increments. $\Delta t_n = \Delta t_n^{\text{Trial}} + \Delta t_n^{\text{Corrective}}$ $\Delta t_s = \Delta t_s^{\text{Trial}} + \Delta t_s^{\text{Corrective}}$ d) Update total traction components at the damage parameter. $t_n^N = t_n^{N-1} + \Delta t_n$ $t_s^N = t_s^{N-1} + \Delta t_s$

e) Update the damage parameter.

$$\Delta u_n^p = \Delta \lambda \frac{\partial g}{\partial t_n} = \Delta \lambda (c^N - 2t_n^N \tan \Phi_d^N)$$

$$\Delta u_s^p = \Delta \lambda \frac{\partial g}{\partial t_s} = \Delta \lambda (2t_s^N)$$

$$(\Delta u^p)^N = \sqrt{A(\Delta u_n^p)^2 + B(\Delta u_s^p)^2}$$

$$(u^p)^N = (u^p)^{N-1} + (\Delta u^p)^N$$

$$D^N = 1 - e^{-(u^p)^N}$$

f) Update the contact strength parameters for the N+1th step:

$$k_n^{N+1} = (1 - D^N) k_n^0 \text{ (Tension)}$$

$$k_n^{N+1} = k_n^0 \text{ (Compression)}$$

$$k_s^{N+1} = (1 - D^N) k_s^0$$

$$c^{N+1} = (1 - D^N) c^0; \sigma_t^{N+1} = (1 - D^N) \sigma_t^0$$

$$\Phi^{N+1} = \Phi_{res} + (\Phi^0 - \Phi_{res}) (1 - D^N)$$

$$\Phi_d^{N+1} = (1 - D^N) \Phi_d^0$$

5.4 Constitutive model implementation and verification

Table 5.1 presented the subroutine written in C++ programming language and uploaded as a DLL file, to implement the above stress-return algorithm in the discontinuum based three-dimensional numerical modeling tool, i.e., 3DEC-Itasca. The following sub-section presents the analytical solutions for the proposed cohesive model's behavior under different loading conditions, i.e., mode-I, mode-II, and mixed-mode (schematically shown in figure 5.2). Additionally, this study performs simple numerical experiments (i.e., using two tetrahedral blocks) at the constitutive level under different loading conditions. The comparison between the numerical experiments with the analytical solution helps in the analysis and verification of the constitutive behavior of the proposed cohesive model. This sub-section also highlights the effect of damage parameters (i.e., A and B), and the dilation parameter (Φ_d) at the constitutive level. Table 5.2 presents the properties of the contact model and corresponding tetrahedral blocks.

Table 5.2: Cohesive contact model parameters

k_n^0 (MPa/mm)	10000	φ	30
k_s^0 (MPa/mm)	5000	Φ_d	20
c^0 (MPa)	1	A	10, 100, 1000
σ_t^0 (MPa)	1	B	10, 100, 1000

5.4.1 Mode-I loading (Tension)

This study derives the analytical solution delineating the behavior of the cohesive contact model under uniaxial tensile loading conditions. It uses damage increments as an input to evaluate the contact's normal traction (t_n) and relative normal displacement, including inelastic (u^p) and total normal displacements (u_n) components.

In the beginning, this analytical solution determines the cohesive model parameters based on the input damage variable (i.e., D), as highlighted in step 6.(f) in table 5.1. One should note here that there shall not be any inter-contact shear displacement and contact shear stress under uniaxial tensile loading conditions (i.e. $u_s = 0$; $t_s = 0$; $u_s^p = \Delta\lambda 2t_s = 0$). Consequently, it transforms the resultant loading functions as follows.

$$f = t_n(c - t_n \tan^2 \Phi) - \sigma_t (c - \sigma_t \tan^2 \Phi) \quad (5.25)$$

The resultant plastic potential expression is same as 5.25 with Φ replaced by Φ_d . The above expression with loading function forced to zero (i.e., $f = 0$) along with the modified model parameters (i.e., step 6.f in table 5.1) results in the following expression of contact's relative normal traction in the inelastic regime.

$$t_n = \frac{c - \sqrt{c^2 - 4\sigma_t \tan^2 \Phi (c - \sigma_t \tan^2 \Phi)}}{2 \tan^2 \Phi} \quad (5.26)$$

Next, the analytical solution uses the definition of damage (i.e., eq. 5.15 and 5.16) along with uniaxial loading conditions (i.e. $u_s = u_s^p = 0$) to express the contact's normal displacement (i.e. u_n^p), in terms of D as follows.

$$u_n^p = \frac{u^p}{\sqrt{A}} = \frac{1}{\sqrt{A}} \ln \frac{1}{1 - D} \quad (5.27)$$

One should note here that this analytical solution implicitly considers the inclusion of unit displacement parameter δ_0 (i.e., in eq. 5.15) for normalization purposes. The expressions 5.26 and 5.27 along with 5.13 results in the estimation of contact's total normal displacement (i.e. u_n), as follows.

$$u_n = \frac{c - \sqrt{c^2 - 4\sigma_t \tan^2 \Phi (c - \sigma_t \tan^2 \Phi)}}{2 \tan^2 \Phi (1 - D) k_n^0} + u_n^p \quad (5.28)$$

The above expression completes the essential details to estimate contact's normal displacement and traction components in the inelastic regime using damage as an input.

In the elastic regime, this analytical solution utilizes the 5.13 along with u^e as input to estimate contact's normal traction component t_n .

Further, this study uses the micro-parameters presented in table 5.2 to illustrate the functioning of the above analytical solution and corresponding numerical simulations. Figure 5.5 (a) demonstrates an excellent agreement of the results from the 3DEC simulation of the uniaxial tensile strength test at the constitutive level (i.e., damage parameter $A=10$) with the above derived analytical solution. It also illustrates an increased softening rate of post-peak behavior at the constitutive level under uniaxial loading conditions, with an increase in the damage parameter A from 10 to 1000, keeping parameter $B=1$ as constant. It shows the expected results of increased post-peak softening with the decrease in mode-I fracture energy (i.e., G_f^I).

5.4.2. Mode-2 loading (Pure shear)

In the case of mode-2 (i.e., shear) loading condition in 3DEC simulations, the lower block is fixed while the upper block sheared under two different boundary conditions: the upper boundary is free (i.e., $t_n = 0$) and the upper boundary fixed (i.e., $t_n < 0$, considering tension as positive).

5.4.2.1 Pure shear: free upper boundary

In this case, the free upper boundary allows the unrestricted movement of the upper block under dilation, thus, no t_n traction component. Therefore, one can perceive it as a particular case of constant normal conditions (CNL) with zero as the applied normal stress component (i.e., $t_n = 0$).

One can start this analytical solution derivation in the way similar to 5.4.1 with the determination of the cohesive model's micro-parameters using D as an input. This analytical solution applies to the inelastic regime. The elastic response can be obtained from eq. 5.13 with elastic shear displacement increments (i.e., du_s^e) as input. In the inelastic regime, one can obtain the following expression for contact's shear traction (i.e., t_s) by enforcing yield surface to zero with $t_n = 0$ boundary conditions.

$$t_s = \sqrt{\sigma_t (c - \sigma_t \tan^2 \Phi)} \quad (5.29)$$

Additionally, one can obtain the resultant inelastic displacement (i.e., u^p) with from eq. 5.15 as follows.

$$u^p = \delta_0 \ln \left(\frac{1}{1-D} \right) \quad (5.30)$$

Using the above resultant inelastic displacement at each step, one can further estimate the change in the total elastic displacement at each step [i.e., $(du^p)^{n+1} = (u^p)^{n+1} - (u^p)^n$]. This du^p at each step along with eq. 5.15, 5.16, and 5.20 result in the following expressions for the inelastic displacement in normal and shear directions.

$$du_n^p = \frac{P}{\sqrt{A(P^2)+B}} du^p ; du_s^p = \frac{1}{\sqrt{A(P^2)+B}} du^p \quad (5.31)$$

where,

$$P = \frac{(c - 2 t_n \tan^2 \phi_d)}{2\sqrt{\sigma_t (c - \sigma_t \tan^2 \phi) - t_n (c - t_n \tan^2 \phi)}}$$

At last, from eq. 5.13 and 5.31, one can derive the following expression for the total shear displacement (u_s).

$$u_s = \frac{\sqrt{\sigma_t (c - \sigma_t \tan^2 \phi) - t_n (c - t_n \tan^2 \phi)}}{(1-D) k_s^0} + u_s^p \quad (5.32)$$

Additionally, this study performs a parametric study to evaluate the influence of the damage parameter B on the overall post-peak response, which shows an increased softening rate with an increase in parameter B from 10 to 1000, keeping parameter $A=1$ as constant. Overall, figure 5.5 (b) verifies the excellent functioning of the implemented model under mode-II loading conditions.

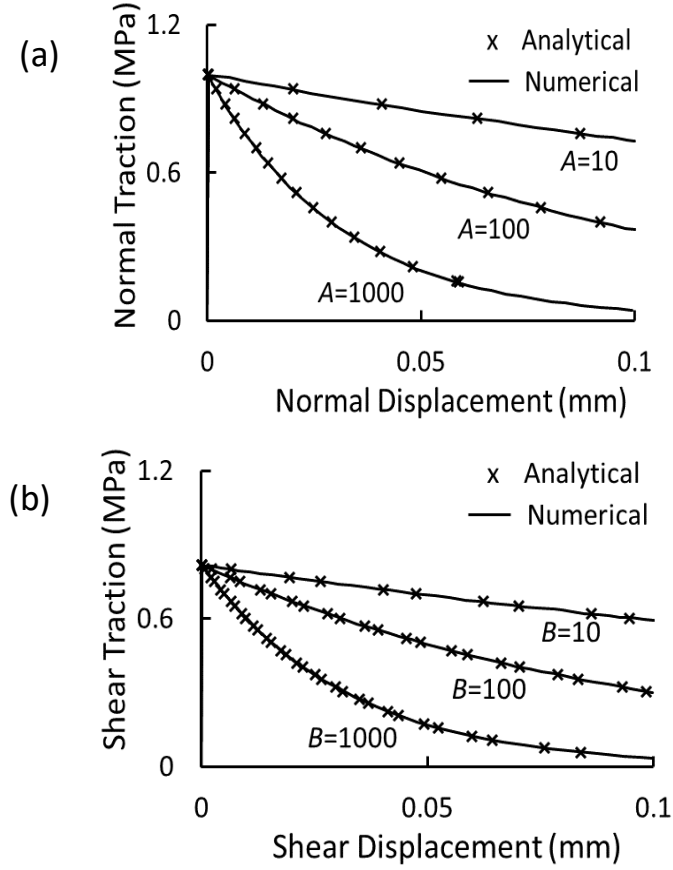


Figure 5.5: (a) Yield function shrinking with damage evolution, (b) Corresponding softening in the stress-displacement plot

5.4.2.2 Pure shear: fixed upper boundary

Similarly, one can also derive the analytical solution for the shear under both (i.e., upper and lower) block's vertical displacement fixed. Under such a scenario, the fixed boundary conditions restrain the dilation of the top block. Consequently, it generates the additional compression at contact [i.e. $dt_n = -k_n^0 (1 - D) du_n^p$] in the inelastic regime. Therefore, one can obtain the total shear traction (t_s) in the inelastic regime using damage as an input and forcing yield surface to zero, as follows.

$$t_s = \sqrt{\sigma_t (c - \sigma_t \tan^2 \Phi) - t_n (c - t_n \tan^2 \Phi)} \quad (5.33)$$

The remaining expression for the plastic displacement increment in normal (i.e., du_n^p) and shear (i.e., du_s^p) along with the total shear displacement (i.e., u_s) will be the same as described in eq. 5.31 and 5.32 in the previous section.

5.4.3 Mixed mode loading (Shear under CNL/Shear under Tension)

In order to verify the model's performance under mixed-mode loading conditions, this study assigns a constant horizontal velocity at the top block under constant normal tensile loading of 0.1 MPa, i.e., stress path will lie in the right quadrant of figure 5.2(a). Similarly, the developed constitutive model had also been exposed to shear under compression (i.e., the constant vertical compressive stress of 1 MPa) loading condition. Stress path under this loading conditions would lie in the left quadrant under yield surface, i.e., in figure 5.2(a). The model's damage parameter, i.e., B , was taken 100 in both simulations.

In terms of analytical solution, this particular case of loading conditions ensures normal confining stress of constant magnitude applied over the top block throughout the test. It dictates contact's normal displacements under elastic conditions to be zero (i.e., $\Delta u_n^e = 0$). Whereas, under the inelastic regime, the damage mechanism at the asperity level tends to dilate the top block. As highlighted in the previous sub-section, this dilation may affect the normal stress conditions in case of fixed boundary conditions, i.e., top and bottom block's normal displacement fixed. Therefore, to maintain and constant normal loading (i.e., CNL) conditions during contact shearing in the plastic regime, the top block adjusts continuously in normal direction to incorporate the dilation effect and maintain constant normal stress (i.e., $= \sigma_{CNL}$) conditions throughout the test. Consequently, this analytical solution enforces the following boundary conditions.

$$dt_n = \frac{\partial t_n}{\partial u_n} du_n + \frac{\partial t_n}{\partial u_n^p} du_n^p + \frac{\partial t_n}{\partial D} dD = 0 \quad (5.34)$$

Using the constant normal conditions (i.e., $t_n = \sigma_{CNL}$) and eq. 5.13, one can obtain the following expression for the change in contact's normal displacement (du_n).

$$du_n = du_n^p + \frac{\sigma_{CNL}}{(1-D)} \frac{\partial D}{k_n} \quad (5.35)$$

where,

$$k_n = [1 - DH(u_n^e)]k_n^0$$

Further, one can estimate the resultant shear traction (i.e., $t_s = \sqrt{t_{s1}^2 + t_{s2}^2}$) in the elastic regime using eq. 5.13 with zero damage and change in shear displacement ($du_s^e = \sqrt{(du_{s1}^e)^2 + (du_{s2}^e)^2}$) as input. In the inelastic regime, the resultant shear traction can be obtained by enforcing the yield conditions (i.e., $f = 0$) as follows.

$$t_s = \sqrt{\sigma_t (c - \sigma_t \tan^2 \Phi) - t_n (c - t_n \tan^2 \Phi)} \quad (5.36)$$

The subsequent derivation of the plastic shear displacement increments in normal (i.e., du_n^p) and shear (i.e., du_s^p) directions along with total shear displacement have already presented in sub-section 5.4.2.1.

Further, figure 5.6 (a) and (b) shows the comparison of results obtained from the analytical solution with the numerical simulation output for the above two cases of mixed-mode loading conditions.

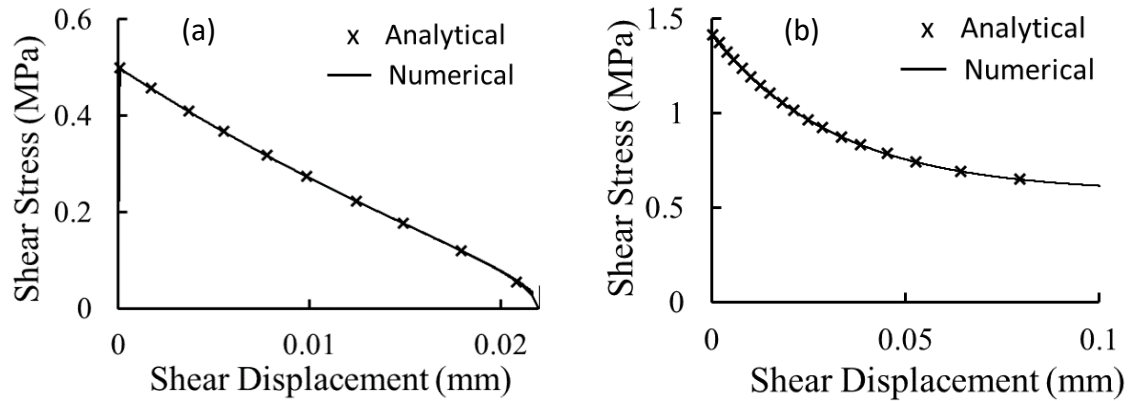


Figure 5.6: (a) Tension-Shear, (b) Compression-Shear

In the above figure, one can observe that the numerical simulation results are in excellent agreement with analytical solutions. This study also investigates the model's mechanism to incorporate realistic dilation characteristics. In this view, figure 5.7(a) presents the variation of the model's dilatational response with dilation parameter i.e. Φ_d , while figure 5.7(b) shows the variation of the model's dilation with confinement.

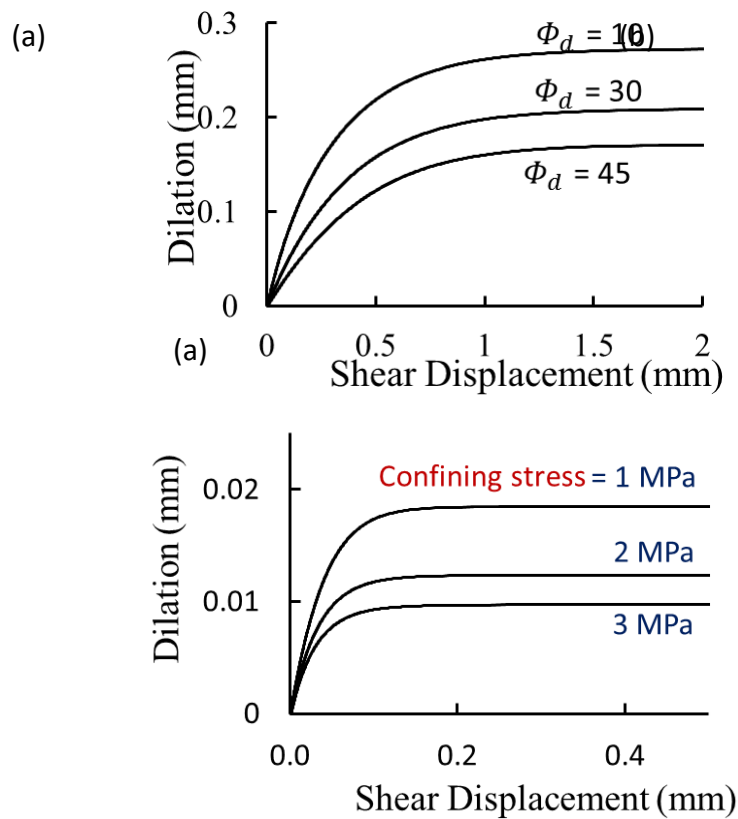


Figure 5.7: (a) Variation of dilation with dilation parameter (Φ_d), (b) variation of dilation with confinement

This parameter provides an ease to implicitly capture the roughness characteristics of inter-granular interaction in numerical modeling. The section 5.3.2 already briefed the mathematical functioning of this parameter. Further figure 5.7 (b) shows the reduction of the model's dilatational response with an increase in confining pressure. These characteristics of the model capture the mechanism of asperity's wearing and tearing under increased confinement. It also captures the crack closing phenomenon with increase confinement, which increases in material shear strength.

5.5 Constitutive model validation

This section presents the validation of the model's performance in comparison with actual experimental data obtained from literature under mixed-mode loading conditions. For this purpose, numerical simulation of the direct shear test under constant normal pressure ($t_n = 7, 14, 21$ MPa) conditions on Granite mortar replicas performed (Gentier et al. 2000). The proposed cohesive model is used to capture the evolution of the joint responses. The actual rock sample is cylindrical with a circular joint of 90mm diameter. Figures 5.8(a) and 5.8(b) presents roughness and unevenness of the actual surface of the

rock joint along with its three-dimensional schematic view. Figure 5.8(a) presents the test geometry of 3DEC simulation with the fixed bottom block and the top block moving laterally under constant normal loading (CNL) boundary conditions.

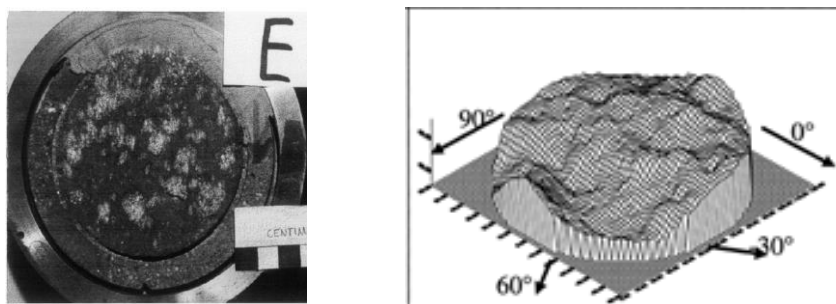


Figure 5.8: (a) sample's lower surface, (b) 3D presentation of surface (Gentier et al. 2000)

The primary purpose of this simulation is to validate the cohesive model's competency to capture the realistic rock dis-continuity (i.e., rock joint in this simulation) behavior. Here, the cohesive model is explicitly representing the actual rock joint's characteristics on the macro-scale. Therefore, all the parameters obtained from experiments, i.e., young's modulus, poison's ratio, joint stiffness, friction angle, assigned as it is to the cohesive model in numerical simulation as block and joint parameters. Parameters that are not available from experimental data, i.e., joint cohesion, tensile strength, and damage parameters, were calibrated with experiment result of one confinement set, i.e., 14 MPa. Here, deformable blocks were assigned elastic zone constitutive model where elastic parameters were explicitly taken from experiments, as summarized in table 5.3 below. Whereas, joint constitutive model parameters were adjusted to match stress-strain and dilation responses from experiments in pre- and post-peak regime at 14 MPa confinement pressure. The summary of the calibrated parameter is presented in table 5.3 as follows.

Table 5.3: Calibrated parameters

Block-parameters		Source
E_{block} (GPa)	30.8	Experiment
ν_{block}	0.2	Experiment
Joint parameters		
k_n^0 (MPa)	1000	Experiment
k_s^0 (MPa)	39	Experiment
c (MPa)	12	Calibrated

σ_t (MPa)	6.6	Calibrated
Φ	38.66 ⁰	Experiment
A	1	Calibrated
B	6.5	Calibrated
Φ_d	14	Calibrated

Now, using these calibrated parameters, the direct shear test under different confinements, i.e., 7 and 21 MPa, are performed. Figure 5.9(b) presents the shear stress-displacement results obtained from numerical simulation and its comparison with an experimental output. One can divide it into four sections; elastic hardening, peak strength detection, post-peak softening, and residual stress state. The overall model's response is in good agreement with experimental observations. The initial elastic hardening predicted by the model's response is similar to experimental observations. In terms of peak strength prediction, the proposed model's estimation at different confinements is accurate in comparison with experimental observations, which indicates the efficiency of hyperbolic yield surface expression in the constitutive formulation.

Further, on comparing the post-peak softening response, the model's predictions for material softening are in excellent agreement with experimental observations for all sets of confinements throughout the test. It shows the suitability of adopted non-associated flow rule and plastic potential in capturing material's gradual strength degradation characteristics via gradual de-cohesion and yield surface shrinking mechanism (i.e., section 5.3). It also indicates the accuracy of stress return algorithm and damage increments controlled by plastic displacements at each time step. Besides, the prediction of residual strength of rock joint at each confinement highlights the appropriateness of residual yield surface expression.

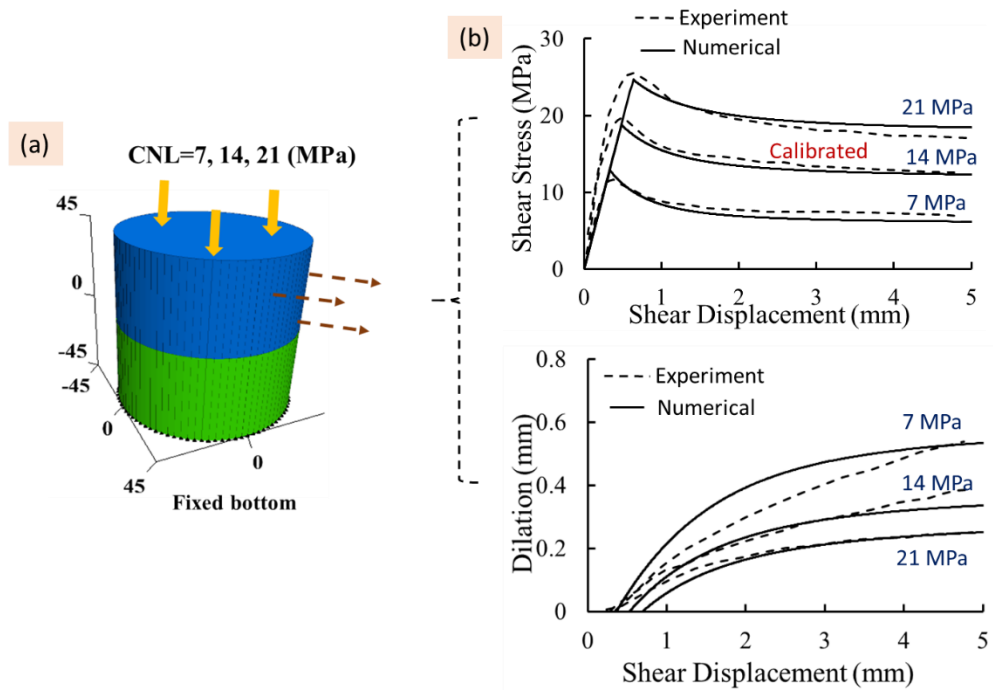


Figure 5.9: (a) 3DEC test geometry, (b) validation

Figure 5.9 (b) also presents the model's prediction of a rock joint's dilatational behavior. In the beginning, the point of dilation initiation in the model's response varies with an increase in confinement, which agrees with theoretical consideration but shows slight variation from experimental observation. However, later trends show that overall prediction from the model is quite convincing and is in good agreement with experimental observations. One should also note here that the actual joint surface is very rough and uneven as compared to the idealized sample. Additionally, the proposed model does not include any additional parameters to explicitly describe the joint roughness features, which is often difficult to obtain. The proposed constitutive formulation takes these characteristics implicitly to capture the effect of joint unevenness in a phenomenological manner. It also captures the degradation of material dilation with increased confining pressure, which indicates that the mechanism of increased asperity breakage due to increased confinement. These additional features enhance the capability of the proposed model to capture the effect of the material cracking mechanism.

5.6 Applications: 3D numerical simulations of Uniaxial compression and Brazilian disc tests

Further to demonstrate the efficiency of the developed numerical modeling framework to realistically capture the cracking mechanism in complex scenarios, virtual experiments,

including uniaxial compression (UCS) and conventional Brazilian disc tests, are conducted using the above developed numerical modeling framework. This study also performs the actual laboratory experiments to acquire a useful dataset for calibration and rigorous validation purposes. The target rock types chosen for the above exercise and further bursting potential analysis were Bluestone, i.e., hard rock type. Advanced experimental techniques, including *digital image correlation* (DIC), used to obtain the local scale responses. It enabled us to validate the results obtained from the above numerical simulations at both sample and local scales.

5.6.1 Experimental specifications

This study performed the uniaxial compression test using a large INSTRON (i.e., INSTRON 1282) testing frame with a maximum loading capacity of 1000 kN on cylindrical samples of bluestone rock type. The sample dimension was 42mm diameter with a ~ 2.4 aspect ratio. The lateral strain-controlled approach (i.e., using chain extensometer around the specimen periphery) controlled the axial loading rate to capture the potential snap back response of the given rock type. The lateral strain rate was 8×10^{-6} m/min (i.e., $1.3 \mu\epsilon/\text{sec}$). The complete stress-strain response from the above experiment demonstrates practically insignificant snap-back magnitude. Therefore, to optimize the overall computational cost and time, conventional axial strain-controlled uniaxial compression tests were conducted numerically.

This study also performed the conventional Brazilian disc (BD) tests on the same rock type. It provides additional experimental data set for the validation of the developed numerical modeling framework. These experiments used disc-shaped samples of ~ 60 mm diameter and 30mm thickness. Three samples were considered for each test. During experiments, axial displacement-controlled approach with 1.2×10^{-4} m/min (i.e., $4.8 \times 10^{-4}\mu\epsilon/\text{sec}$) loading rate was adopted. The front face of all samples, including cylindrical for UCS and disc-shaped for BD test, were exposed to random speckle patterns (i.e., black speckles on white base) to enable the application of DIC technique. These speckle patterns were non-repetitive with high contrast in nature, inevitable for efficient image post-processing. Commercial image processing software packages, i.e., Correlation solutions VIC-2D for disc (i.e., BD) and VIC-3D for cylindrical (i.e., UCS), were used. In both experiments, images captured with a speed of 5 frames per second. In UCS, two cameras used at an angle of $\sim 170^\circ$ with the specimen axis. On the other hand,

the Brazilian disc test utilized a single camera along the specimen axis. Figure 5.10 presents a brief overview of the above experimental setup.

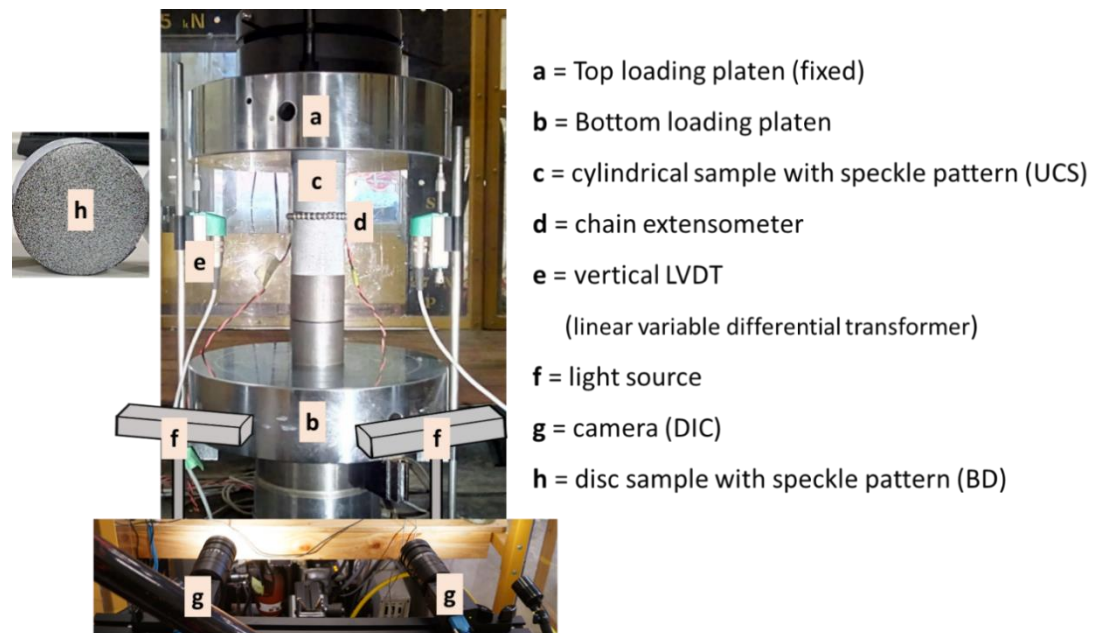


Figure 5.10: Experimental setup

Table 5.4 summarizes rock sample parameters obtained from the above experiments, where fracture properties were acquired from newly developed and patented AUSBIT technique (Verma et al. 2019a), as presented in chapter 3.

5.6.2 Numerical simulation: Uniaxial compression test

This study utilizes the developed numerical modeling suite to simulate the uniaxial compression test. The dimensions of the cylindrical specimens are 42 mm diameter with 100 mm height, i.e., in line with the experimental data. Figure 5.11(a) presents the three-dimensional virtual specimen formed by the randomly generated tetrahedral deformable blocks. This study also performs the mesh-sensitivity analysis to evaluate the effect of deformable tetrahedral block sizes on the overall sample response. Figure 5.11(b) presents the results of this sensitivity analysis, demonstrating the inconsequential influence of block size on the overall sample response. Though the pattern of the specimen cracking and overall computational cost does depend on the block size, i.e., smaller block size results comparatively natural cracking pattern but with the increased computational cost. Therefore, one can optimize the block size aspect to acquire the required computation cost without affecting the overall mechanism responsible for imitating the actual physics behind rock material cracking. Based on the above

consideration, the size of the block finalized is 4 mm (i.e., grain/specimen's minimum dimension $<1/10$), which is in line with (Mahabadi 2012; Kazerani 2013; Liu and Deng 2019).

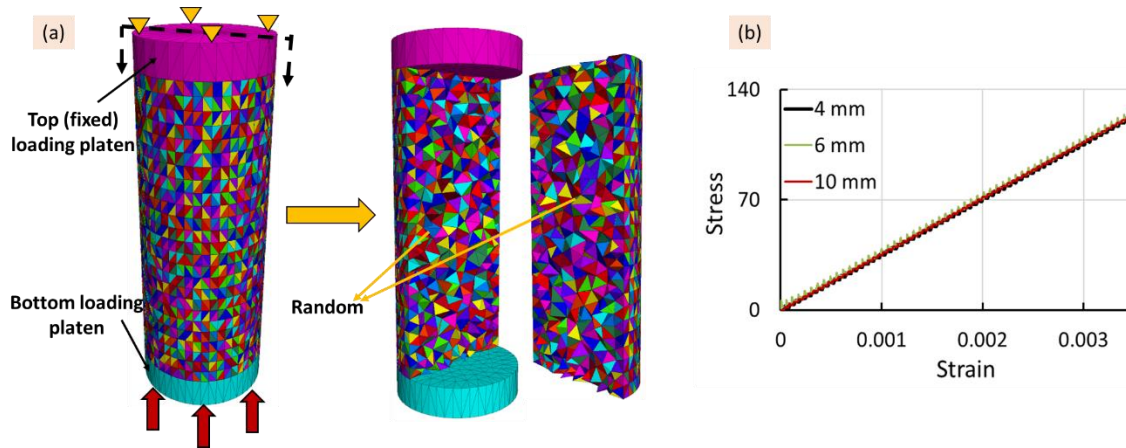


Figure 5.11: (a) UCS testing setup, (b) sensitivity analysis (i.e. block size effect)

The top and bottom intact blocks represent the loading platens. The uniaxial compression load on the specimen is applied by the bottom platen while keeping the top platen fixed, i.e., similar to the experimental conditions. All these tetrahedral blocks (i.e., representing mineral aggregates and loading platens) are coarsely discretized to optimize the overall computational cost further.

5.6.2a Calibration

The developed numerical approach simplifies the overall calibration process, where the elastic zone constitutive model assigned to the continuum elements while cohesive contact model to the dis-continuum (i.e., contacts) elements. One can directly assign elastic properties of rock, including young's modulus (E), poisson's ratio (ν), and density (ρ), as the macro-parameters for the continuum elements. It implies that, unlike the conventional DEM based approaches which require adjustment of contact stiffness parameters artificially to match the slope of elastic stress-strain curve (Potyondy and Cundall 2004; Cho et al. 2007; Bobet et al. 2009a; Schöpfer et al. 2009; Yan et al. 2009; Nguyen et al. 2017a), the proposed approach does not require any such calibrations and captures the overall elastic response naturally using laboratory parameters explicitly as an input. It justifies the conceptual framework for imitating correct physics behind rock material deformation.

On the other hand, the micro-parameters controlling the behavior of the cohesive contact model, require proper calibration. In this view, the contact stiffness in normal (k_n) and shear (k_s) direction are assigned very high values in such a way that further increase in the above magnitudes does not influence the overall elastic response. The intent here is to nullify the contribution of inter-granular relative displacement in overall elastic deformation. It ensures that the elastic response of the given rock sample would be purely due to block's (or mineral aggregates) elastic deformation collaboratively. The inter-granular (grain aggregate) relative displacement comes into picture only when the contact stiffness starts deteriorating due to the activation of damage parameter (D) in case of material fracturing.

One can classify the remaining micro-parameters into two categories: peak strength and post-peak behavior controlling parameters. The prior category includes inter-granular contact's cohesion (c), tensile strength (σ_t) and friction (Φ), while the latter includes damage parameters A and B . The tensile strength (σ_t) is explicitly taken from DIC analysis of the AUSBIT technique based indirect testing approach (i.e., detailed description in chapter 4). The determination of damage parameters requires calibration using fracture energies in mode-I (i.e. G_f^I) and mode-II (i.e. G_f^{II}) loading conditions. The mode-I fracture energy is estimated again from the AUSBIT technique, while mode-II is considered roughly double of mode-I. The remaining parameters, including cohesion (c) and friction (Φ), are calibrated to capture peak strength. The dilation parameter (Φ_d) is assigned a smaller value considering the hard and brittle nature of Bluestone rock type. The entire calibration process, along with finalized parameters, is summarised in table 5.4.

Table 5.4: Calibrated Parameters

Experiments		Numerical		
Properties		Micro-parameters		Source
ρ_{rock} (g/mm ³)	2.72×10^{-3}	ρ_{block} (g/mm ³)	2.72×10^{-3}	experiment
E_{rock} (GPa)	36.6	E_{block} (GPa)	36.6	experiment
ν_{rock}	0.16	ν_{block}	0.16	experiment
-	-	Micro-parameters		
-	-	k_n^0 (MPa)	8×10^6	very high
-	-	k_s^0 (MPa)	6.89×10^6	very high
-	-	c (MPa)	55	calibrated
σ_t (MPa)	~ 11	σ_t (MPa)	10	experiment
UCS (MPa)	~ 140	Φ	25^0	calibrated
G_f^I (MPa-mm)	0.22	A	2.02×10^3	calibrated

G_f^{II} (MPa-mm)	0.44	B	1.01×10^3	calibrated
		Φ_d	10^0	calibrated

5.6.2b Validation

Figure 5.12 presents the comparison of overall results obtained from numerical simulation with experimental observation. Here, figure 5.12(a) presents the sample scale validation via conventional stress-strain responses, and figure 5.12(b) demonstrates the local scale validation of numerical simulations using full-field displacement contours obtained from the DIC experimental technique.

Figure 5.12(a) shows that the overall stress-strain response from numerical simulations, including pre-peak elastic hardening, agrees well with the experimental observations. It also depicts the peak loading point correctly. Capturing the elastic response with such an accuracy using raw elastic properties data, taken directly from experiments, is commendable. After that, one can observe an immediate strain-softening response from the numerical simulation. This response is minutely different from the experimental observations due to the difference in the loading style, i.e., axial strain-controlled in numerical while lateral strain-controlled in an experiment. In principle, we cannot make a direct comparison with two tests with different loading styles. However, we can still compare the elastic response and peak strength. The observed similarity in post-peak is something that this study does not intend to. The prime intention here is to acquire material parameters to prepare the base strain burst experiments in the later stage of this research. The acquired resemblance with experimental data boosts up our confidence in the performed simulations. To further ensure the reliability, this study uses the same numerical modeling set to perform a conventional (axial strain controlled) Brazilian disc test. In this experiment, we adopt similar boundary conditions and loading styles as of the experiment. The results validation at multiple scales (local and global) will ensure the reliability of the developed numerical modeling tool.

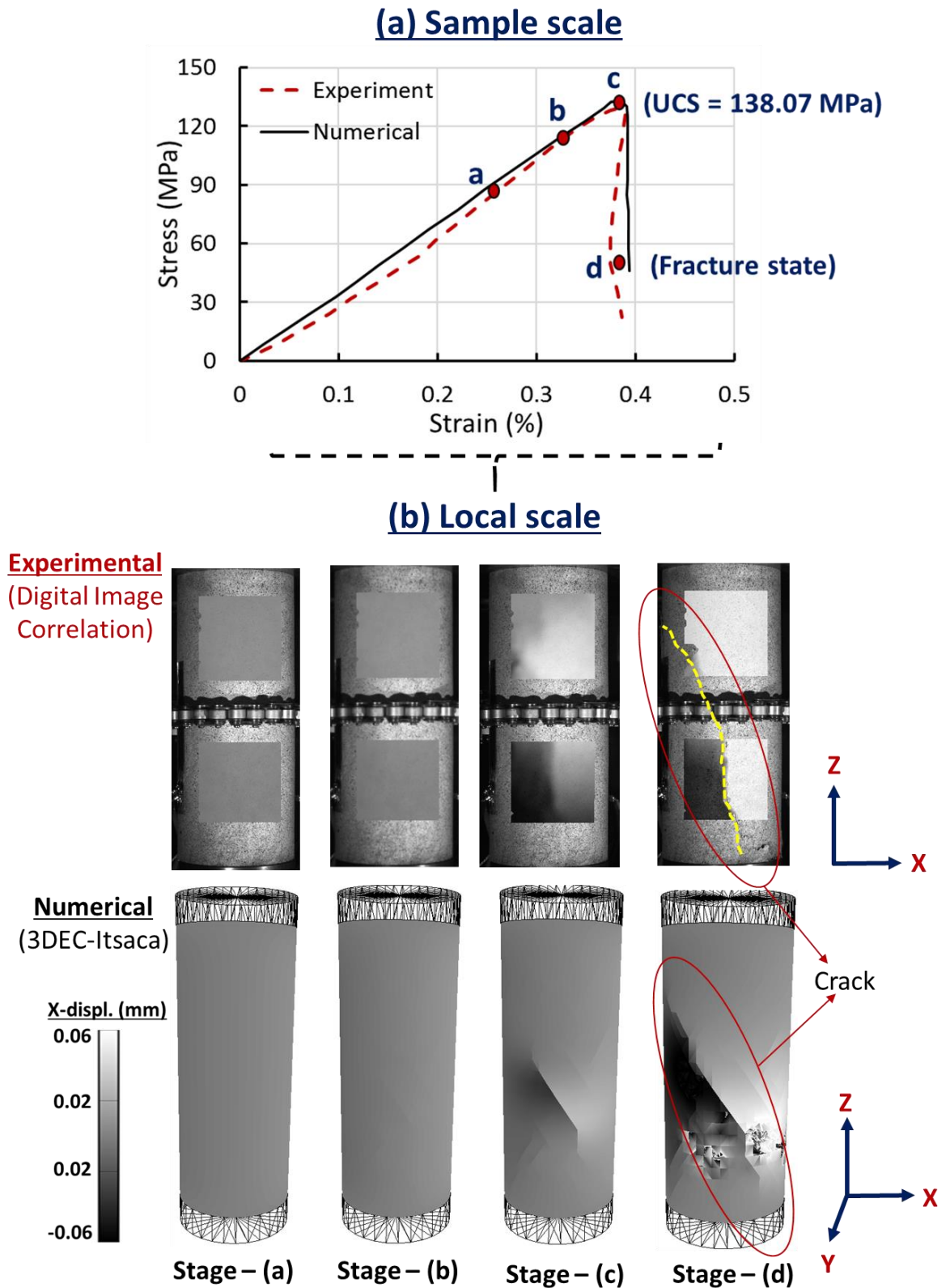


Figure 5.12: Uniaxial compression test (a) sample scale, (b) local scale validation

Figure 5.12 (b) presents the comparison of the full-field displacement contours obtained from experiments using DIC techniques with the numerical simulation responses. The overall stress-strain plot is divided into four stages, i.e., ‘a’ (60% peak), ‘b’ (85% peak), ‘c’ (peak) and ‘d’ (~35% peak). This comparison shows the homogenous distribution of local scale deformation in the x-direction at stage ‘a’ and ‘b,’ demonstrating local scale elasticity. The global response (i.e., stress-strain) is also in accord with the local scale elasticity. After that, as the load approaches its peak, i.e., stage c, the full field deformation contours start deviating from homogeneity to induce localization. It indicates the onset of pre-peak material damage. This observation of localization with deformation magnitude (i.e., in quantitative terms) in numerical simulation agrees well with the experiments. At stage ‘d,’ rock sample’s structural failure becomes visibly evident at both global (i.e., clear drop in stress-strain response) and local (visible shear zone extreme displacement magnitude in both experimental and numerical observations) scales. The magnitude (i.e., maximum lateral displacement of $\pm 0.06\text{mm}$) and position of localized displacement increase in the numerical simulation are close to the experimental observations. It further explains this close resemblance of the cracking pattern of the experimental rock sample with the presented numerical simulation. Overall, one can observe that the numerical simulation outcome is in good agreement with the experiments at both local and global scales.

5.6.2c Damage based shear localization analysis

This study further explores the applications of the developed numerical modeling suite to investigate the mechanism of strain localization and shear band formation in the rock under uniaxial compression. Figure 5.13(a) and (b) presents the sequence of tensile (i.e., positive major principle stress) and shear stress evolution with load application. It also presents the damage evolution in context with the above stress changes. For this purpose, figure 5.13(c) also dissects the transparent virtual sample demonstrating damage evolution to acquire a better inside look in three-dimensional space.

At stage ‘a’ (i.e., 0.65 % peak), one can observe the uniform distribution of the tension and shear-induced stresses throughout the sample without any sign of material damage. It indicates the elastic deformation of the cylindrical sample under quasi-static loading conditions, which also agrees well with global scale elasticity, i.e., linearity in the stress-strain curve. As the load approaches to stage ‘b,’ shear stresses intensify uniformly

throughout the sample. On the contrary, the tensile stresses intensify locally, i.e., ± 10 mm across the central diametrical axis, as shown in figure 5.13a. It explains the initiation of localized material damage, which eventually causes material micro-cracking. These insights reverberate natural characteristics of brittle material like a rock (i.e., weak in tension and strong in compression) and the role of localized material deformation and damage mechanism in the material micro-cracking and strength degradation. Although the overall global scale response is still linear under the elastic regime, it explicitly indicates the difference between rock behavior at different scales, i.e., elastic at global and inelastic and local. The onset of localized material damage creates weak zones inside the specimen, which further intensifies the stress concentration crucial for further localization.

At stage 'c,' i.e., peak load, localized stress distribution undergoes significant changes marked with uneven diffusion of tensile stresses. Whereas, the shear stresses start localizing across the inclined region (i.e., figure 5.13b) where tension induced damage occurred in the previous stage. Shear stresses outside this inclined localized band of shear domination are practically constant as compare to the previous stage 'b.' In contrast, shear stresses insider the localized zone has significant variation from nill as a minimum and almost 140 MPa as a maximum. The region of minimum shear stress is wholly damaged (i.e., damage approached to its maximum magnitude ~ 1), indicating the mechanism of localized stress-relaxation due to material cracking (Johnson et al. 2009; Ma et al. 2016; Dinç and Scholtès 2018). Exact replication of grain crushing typically observed in actual experiments may not be feasible in such optimized numerical modeling techniques. Such maximum damage in a localized portion is a conceptual imitation of a completely damaged/crushed localized zone. The region of maximum localized shear stress follows the region of maximum damage, which indicates the mechanism of crack propagation and extension of the above-localized zone to form a major crack. One can perceive this crack propagation occurred due to damage accumulation as the mechanism of micro-crack coalesces to form a major crack. The rock material outside this localized band is least affected in terms of the overall stress and damage magnitude.

After that, tensile stresses got diffused across the sample. Nevertheless, the stresses in the localized zone are primarily shearing in nature, which further expanded the localized zone in the form of the major crack across the sample. One can further affirm this by damage evolution, which shows that the increase in material damage across the localized

shear band is significantly higher than the material outside this shear band. The crack propagation via shear localization causes the continuous relaxation of shear stresses in the regions outside the localized band. The imitated rock material outside this localized portion is mostly intact with zero to negligible (i.e., $D < 0.2$) material damage. It becomes evident at stage 'd' that the shear band induced localization at previous stages is the prime cause of the cylindrical specimen's structural failure, which also causes the immediate sudden drop in load in the post-peak regime.

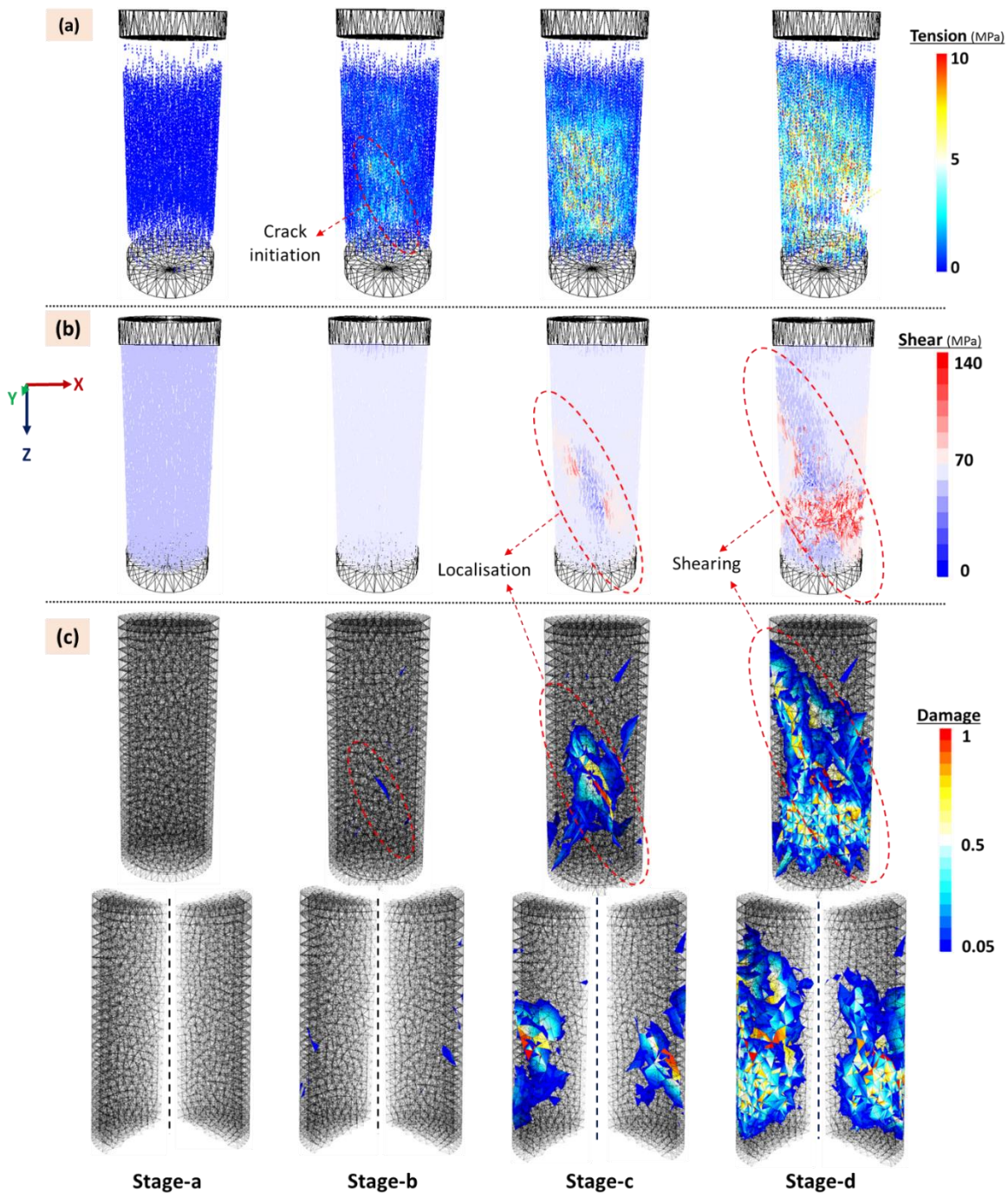


Figure 5.13: (a) Tensile stress, (b) shear stress, (c) damage

Figure 5.14 presents the finalized damaged distribution with a modified scale (from 0.3 to 1, i.e., for better visualization of the shear band). This three-dimensional image of damage distribution shows the localized shear band region in the performed numerical simulation also agrees well with the experimental observation. The obtained results from optimized deformable block size provide a good insight into the localization mechanism, which is not convenient to acquire in conventional (or in many advanced) experimental approaches. One can further improve these results with reduced block sizes, if possible.

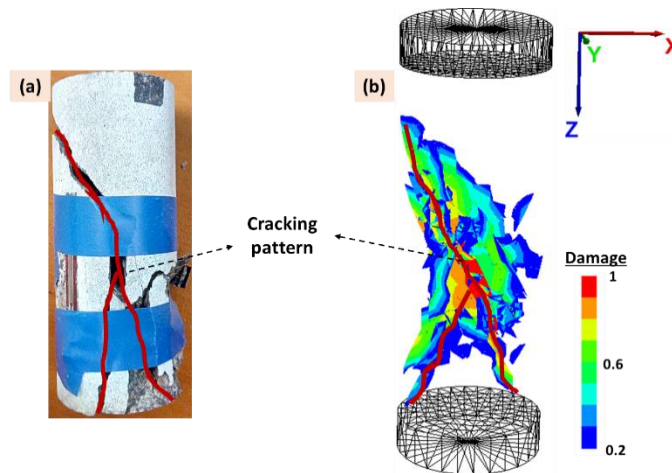


Figure 5.14: (a) Experimental observation, (b) numerical: final stage damage distribution

Overall, the above analysis demonstrates the mechanism of localized material cracking, where tension induced localized stresses to cause the initiation of localized micro-cracking. Subsequently, shear localization occurs, which eventually leads to complete structural failure under uniaxial compression. One can further add the comparison between local response contours comparison between numerical and experimental observations to strengthen the claims of the performed numerical simulations. The sample scale stress-strain response, along with the final cracking pattern from the above two sources, is also in excellent agreement. Overall, the above analysis demonstrates the robustness of the adopted hybrid numerical modeling approach in capturing the realistic rock material behavior in three-dimensional space.

5.6.3 Numerical simulation: Brazilian disc test

This study further performs the conventional Brazilian disc test using the above calibrated numerical setup. In this indirect tensile testing approach, the disc specimen undergoes splitting failure under bi-axial loading conditions (Jianhong et al. 2009; Tomac

and Gutierrez 2012; Li and Wong 2013; Saksala et al. 2013; Aliabadian et al. 2017, 2019a, b). The present idealization utilizes the plane strain conditions and reduces the thickness of the virtual disc sample to 2mm with restrained out of the plane movement. This simplification allows us to attain the required computational efficiency without compromising the reliability of the obtained results. The virtual disc sample of 60 mm diameter (~experimental sample diameter) is compressed diametrically by keeping the bottom loading plate fixed and the top platen moving downward, maintaining quasi-static loading conditions throughout the test. The overall results of this numerical simulation along with double scale validation and damage evolution is presented in figure 5.15.

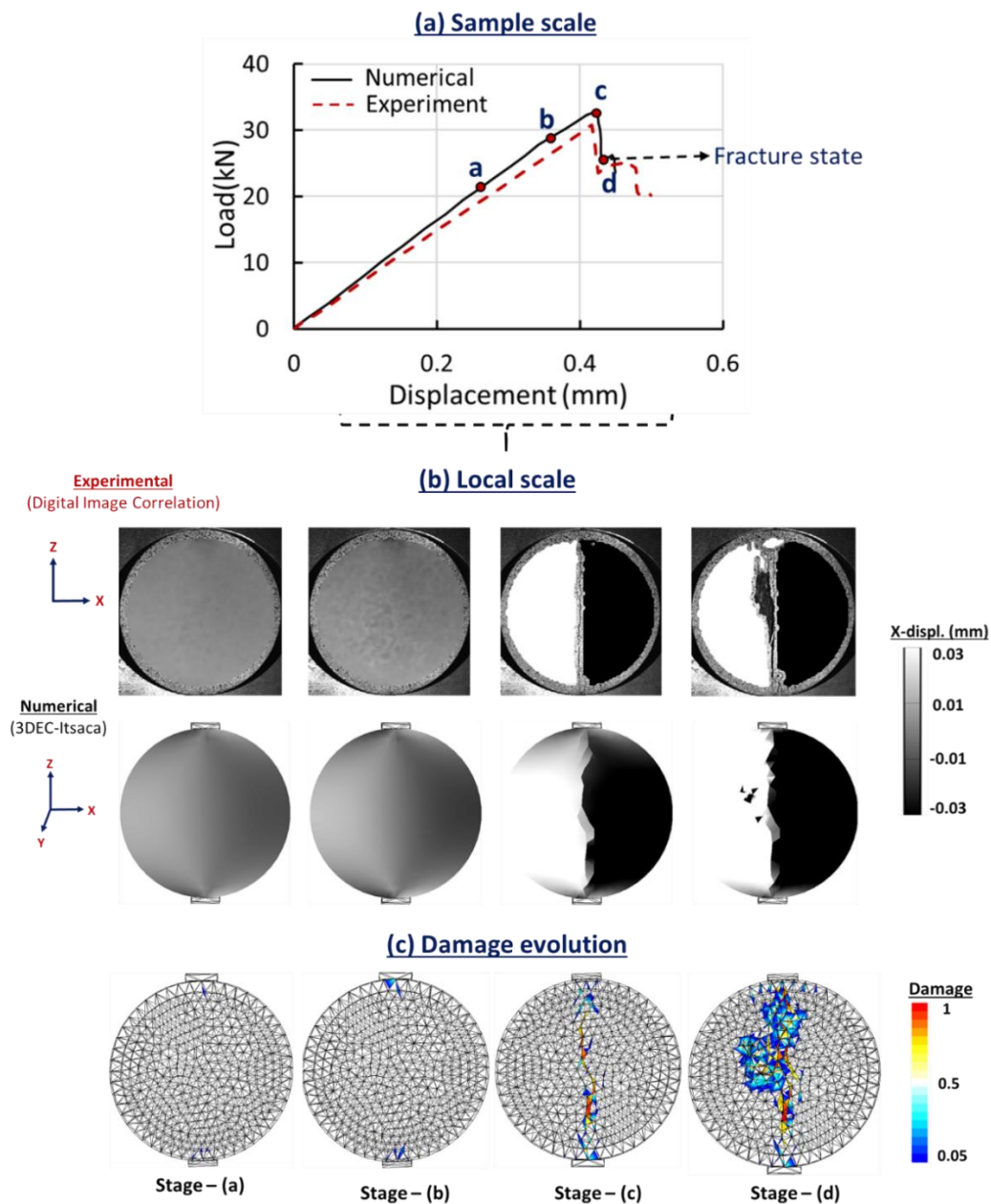


Figure 5.15: Conventional Brazilian disc test validation (a) Sample, (b) local scale, (c) damage evolution

The responses obtained from numerical simulations are compared with the experimental observations at both sample and local scales. After removing the initial non-linear part (Kazerani 2013; Gui et al. 2015b), the overall load-displacement response is divided into four main stages (i.e., stage ‘a,’ ‘b’ as 60%, 85% of peak load, while ‘c’ and ‘d’ are peak and $\sim 80\%$ of the peak in post-peak regime), as shown in figure 5.15(a). Figure 5.15 (b) presents the evolution of full-field displacement contours at the above four stages. Displacement in the positive x-direction has assigned a positive sign. This figure also compares the local scale deformations from numerical simulations with experimental observations. Figure 5.15(c) presents the damage evolution across the specimen at above mentioned four stages of global scale load-displacement response.

Figure 5.15 (a) shows that, despite minor differences, the overall sample scale load-displacement response is in good agreement with the experimental observation. The predicted peak load in numerical simulation is slightly on the higher side comparatively. In contrast, the elastic and post-peak sudden load drop in numerical simulations is in accord with the experiment. In terms of local-scale responses, overall displacement field at stages ‘a’ and ‘b’ are in acceptable agreement with the corresponding numerical simulation where the overall deformation magnitude varies within $\pm 0.01\text{mm}$ range throughout the sample. At these earlier stages, one can observe the negligible damage across the disc sample, i.e., almost zero at stage ‘a’ while ≤ 0.1 at stage ‘b,’ indicating elastic behavior throughout the sample. This local-scale observation further supports the sample scale load-displacement elasticity.

Damage evolution at stage ‘b’ also indicates the crack initiation mechanism at loading ends, not at the specimen center. This behavior of given rock type is not as per the theoretical consideration of the Brazilian disc test yet common in such indirect testing approach, raising questions over its validity (Fairhurst 1964; Yu et al. 2009; Li and Wong 2013; Perras and Diederichs 2014; Verma et al. 2018). At peak loading stage ‘c,’ a significant increase in the damage (i.e., from 0 at stage ‘b’ to \sim one at stage ‘c’) across the central diametrical axis occurs. Subsequently, one can perceive a visible diametrical crack via displacement contours in both numerical and experimental observations. The damage at loading ends is still under 0.25. It shows that despite crack initiation at loading ends, the tension induced stresses across the central diametrical axis, controls the structural failure of disc specimen. The stresses at loading ends, which governs the crack initiation due to induced stress concentration via loading platens, are mixed-mode in

nature (Yu et al. 2009; Perras and Diederichs 2014). The overall local scale deformation distribution from the numerical simulation are in good agreement with the experimental observations.

In the post-peak regime, the disc specimen undergoes complete failure, i.e., evident from overall damage distributions in figure 5.15(c) where non-uniformity in overall material damage indicates the unbalanced stress distribution due to specimen cracking. The final cracking pattern from numerical simulation demonstrates a considerable resemblance to the experimental observations. Additionally, the above observations can be further reinforced with more stress and strain evolution data from numerical modeling setup to further evaluate the failure mechanism of disc specimen under diametrical compressive loading conditions. Appendix A presents a brief example of such evaluation using the Hawkesbury sandstone rock type.

Overall, the above results demonstrate the capability of the developed numerical modeling framework to predict realistic material behavior at different scales. Such rigorous validation under uniaxial (i.e., in UCS test) and diametrical compressive (i.e., in Brazilian disc test) loading conditions with a single set of input parameters ensures the reliability of developed numerical modeling framework. It forms the basis for numerical experiments under other loading conditions different from the calibration data set, i.e., crucial for the evaluation of rockburst potential.

5.7 Conclusions

This chapter presents the development of a hybrid numerical modeling approach (i.e., 3DEC-Itsaca), which utilizes both continuum and dis-continuum frameworks collaboratively to capture the realistic behavior of hard and brittle rocks. The continuum components (i.e., deformable tetrahedral blocks) control the elastic deformation while inherent dis-continuum mimics the inter-granular interactions and cracking mechanism. This chapter also develops a new cohesive contact model based on the elastoplastic-damage coupling to capture inter-granular deterioration due to microcracking and friction. The model has been implemented in 3DEC-Itasca, followed by its verification under different loading conditions, including mode-I (or tension), mode-II (or shear) and mixed-mode, and validation with experimental data available in the literature.

This study also performs laboratory experiments to obtain good experimental data set for calibration and rigorous validation purposes. These laboratory experiments include uniaxial compression (UCS) and conventional Brazilian disc test on Bluestone rock type using advanced experimental techniques, including Digital Image Correlation (DIC). The data set from the UCS test utilized to calibrate the above numerical modeling framework. The experimentally determined elastic parameters were directly taken as input macro-parameters. The calibrated model is used to perform UCS and BD tests to demonstrate its capability in capturing the experimental responses under different loading conditions. The sample scale stress-strain responses from both virtual experiments are in excellent agreement with laboratory observations. At the same time, local scale deformation evolution across the sample also demonstrates a good agreement with the full field deformation evolution obtained from DIC data. This additional layer of validation at a lower scale enhances the confidence in the reliability of the performed numerical simulations. It also provides a good insight into the fracturing mechanism of brittle rock under different loading conditions. The developed and calibrated numerical modeling framework is now ready to be further used to evaluate the bursting characteristics of Bluestone rock type. Chapter 6 presents a detailed discussion on the applications of the above developed numerical modeling framework to evaluate the bursting potential analysis of the given rock type.

Chapter 6

A Size-Dependent Energy-Based Strain Burst Criterion

6.1 Introduction

In deep underground conditions, rock around underground openings face a true triaxial stress state and often fail due to unloading caused by excavation (Cook 1963; Dong et al. 2018a, 2019b; Zhou et al. 2018a). This sudden change in boundary conditions under high in-situ confining pressure, in principle, governs the bursting failure of rock, commonly known as 'strain burst,' i.e., a rockburst type. It highlights the importance of strain energy storing and dissipation characteristics of rock in context with bursting potential analysis. In this direction, literature review pertaining rock-burst studies illustrates the availability of several approaches ranging from rock-burst classification, numerous empirical burst factors, triaxial unloading experiments and recently developed true-triaxial experimentation based rockburst studies (Zhou et al. 2018a; MOGI 1971; Hua and You 2001; He et al. 2010, 2012c, 2015a; Zhao et al. 2014; Du et al. 2015; Yang 2016; Li et al. 2017; Liang et al. 2017). Researchers mostly use numerical modeling approaches to simulate rock mass failure without incorporating the bursting potential of rock as its material property (Dong et al. 2018b, 2019a).

Among all, bursting analysis using true-triaxial experimentations have been the key highlight of rock-burst studies. It enables the application of polyaxial loading conditions (i.e., which has always been the critical limitation of the conventional uniaxial and triaxial testing setups) and rock sample failure due to sudden unloading in minor principal stress direction mimicking the unloading effect caused by underground excavation. Many researchers performed such experiments in collaboration with advanced experimentation techniques (i.e., AE and DIC) and reported different stress levels for rock's bursting failure depending upon rock type and polyaxial confining pressures (He et al. 2010, 2015a; Zhao et al. 2014; Du et al. 2015; Su et al. 2017; Dong et al. 2019a). The application of the AE technique has been useful in acquiring information about energy

dissipation and sample damage. The DIC technique has mostly been used to capture the rock fragmentation after unloading. Few researchers used this fragmentation images to estimate the kinetic energy of flying fragments to indicate the bursting scale (He et al. 2010). Such estimations are mostly qualitative, where the accuracy of results could always be debatable considering the different forms of energy dissipation, fragmentation sizes, and substantial dependability on a manual judgment.

The issue of improved access to the specimen's mechanical response under polyaxial loading-unloading condition can be addressed using the developed numerical modeling framework presented in the previous chapter. It also provides an ease to vary the specimen dimension and loading conditions with a wide range of flexibility, which may not be possible in actual laboratory experiments. Nonetheless, there are many unresolved issues regarding bursting failure observed in such experiments that are yet unaddressed and need further attention. For instance, is it possible to determine beforehand the stress-state at which unloading in σ_3 direction cause burst in the given rock sample? Is it possible to estimate the bursting scale? What happens if one changes the unloading directions? What are the factors which, in principle, control the bursting mechanism? What role do the specimen's geometric properties play in observed bursting, and why? How can we correlate these observations with actual in-situ bursting possibilities? Majorities of available approaches in rockburst studies, to the best of the author's knowledge, did not address these fundamental questions and were primarily focused on reporting or interpreting the observed results from laboratory experiments.

In this view, one should understand that true-triaxial experiments (or any experiments for the sake of discussion) in the laboratory or numerical analysis alone cannot address such fundamental questions. The need for a systematic framework based on the fundamentals of rock failure is inevitable to address such questions, explain the laboratory observations, and improve our understanding of bursting failure. One can realize its importance from the brief overview of the enormous studies evaluating the failure mechanism in the rock, thus, resulted in numerous phenomenological (Ouyang and Elsworth 1991; Zhou et al. 2001; Hoek et al. 2002; Al-ajmi and Zimmerman 2005; Wu et al. 2010b; Labuz and Zang 2012) and few mechanisms based approaches and explanation (Chang 1990, 1993; Chang and Liao 1990; Chang et al. 1993; Brocca and Bazant 2000; Bažant et al. 2005; Yin and Chang 2009; Yin et al. 2010, 2014; Le et al. 2018c). Such approaches clearly define the theoretical conditions for material failure,

either with the help of yield surfaces (i.e., in phenomenological approaches) or via addressing the cracking mechanism at the local scale (i.e., mechanism-based approaches). It not only explains the laboratory observations but also enables us to make reliable predictions beforehand.

Unfortunately, this is often not the case with strain-burst studies. Majorities of approaches, as mentioned earlier, did focus on reporting the laboratory observations and, thus, end up developing empirical factors to utilize such observation, which may be useful for preliminary analysis purposes but lacks the capability of revealing the bursting mechanism. The other aspect of the laboratory-scale bursting analysis is the effect of specimen size and aspect ratio. Researchers attempted to demonstrate the effect of specimen dimension on overall bursting observations (Zhao and Cai 2015); however, a clear link between this aspect ratio and overall bursting potential with sufficient reasoning behind such possible links is yet not available. Besides, a robust link of material properties' effect on bursting potential does require further attention.

In this view, this chapter proposes a theoretical framework based on elastic strain energy storing and dissipation characteristics to analyze the bursting potential of rock. It is because the failure of rocks and similar geomaterials usually localize with the appearance of cracks (or shear bands) where inelastic behavior and hence dissipation takes place (Nguyen et al. 2012a; Nguyen et al. 2014b; Nguyen et al. 2016b; Nguyen and Bui 2019). The dissipation capacity in such case scales with the surface area created due to cracking. This localized mode of failure precedes the homogenous stage of (usually) elastic deformation where the energy stored in the whole volume area scales with the volume. The difference in scaling rules (energy storage scaling with volume, while energy dissipation scaling with the surface area) (Nguyen et al. 2012a; Nguyen et al. 2014b; Nguyen et al. 2016b; Nguyen and Bui 2019) leads to the excess strain energy storage before the activation of localized failure, which often releases via kinetic energy of rock fragments. Subsequent section 6.2 presents the details of the proposed development. After that, a hybrid numerical modeling tool, developed in previous chapter 5, is used to examine the functioning and effectiveness of the proposed framework. Laboratory experiments, including lateral strain-controlled uniaxial compression tests and in-house AUSBIT-indirect tensile strength testing methodology (i.e. recently patented) were also proved effective and resourceful in this process. These experiments provide the required strength and fracture parameters, which this study subsequently use to illustrate and

analyze the strain-burst mechanism with Bluestone rock type as an example. Section 6.3 presents the details of this illustration and thus validation of proposed framework. At last, section 6.4 demonstrates the eventual applications of proposed development in analysing different types of bursting failure, understanding the influence of geometric properties of test specimen and material properties of given rock type on overall bursting potential.

6.2 An energy-based strain burst criterion

In order to derive such a theoretical framework for bursting failure analysis, it is important to start with the basics of geo-material failure and derive the conditions for bursting accordingly. This study utilizes the concept of yield surface, which is quite common in classical continuum mechanics (or dis-continuum analysis as well) to identify and predict brittle material failure (Chen and Han 1988). Also, this study considers that yielding (onset of inelastic behavior) and failure coincides in rock. Therefore, these terms are interchangeable in the further discussion. One can plot the yield surface governed by yield criterion in three-dimensional stress space, which defines the limit of elasticity under the combination of different possible stress states. Figure 6.1(a) presents an imaginary open-ended yield surface where stress tensor σ_{ij} represents the pre-defined stress state $P(\sigma_1, \sigma_2, \sigma_3)$, in principal stress space. The hydrostatic axis is inclined equally to the three principal stresses where the first stress invariant indicates the hydrostatic stress magnitude ($\sim I_1/3$). The plane perpendicular to this hydrostatic axis is the deviatoric (or octahedral or π) plane. The shape of such a yield surface indicates different possible stress combinations that can fail the given rock material. Therefore, a wide range of laboratory experiments under different loading conditions is required to obtain failure points, which eventually one can join smoothly to determine the actual shape of the yield surface.

For instance, uniaxial compressive strength tests (i.e. $\sigma_1 > \sigma_2 = \sigma_3 = 0$) at which rock sample is compressed under zero confining pressure, could provide point 'a' on yield surface in figure 6.1. One illustration of sample failure with shear band localization under uniaxial compression using Bluestone rock type as an example has already presented in chapter 5. The inclination of this shear band concerning the loading axis increases with increase in confining pressure under conventional triaxial loading conditions (i.e. $\sigma_1 > \sigma_2 = \sigma_3 > 0$) (Le et al. 2018b; Le, 2019). In these scenarios, sample scale response indicates rock material behavior switching from brittle to ductile (Byerlee 1968; Yu et al.

2019) and provides different loci on yield surface, i.e., point 'b,' 'c' and 'd' under different confining pressures. In principle, true-triaxial experiments are also required to determine the correct shape of yield surface in an octahedral plane, which further evolves with confining pressure. For instance, F. Descamps reported such evolution of yield surface from the almost triangular shape (i.e., close to Lode-type criterion) at low mean stress of 90 MPa to hexagon (i.e., similar to Mohr-Coulomb criterion) at 130 MPa mean stress, and finally to circular at high mean stress around 210 MPa, i.e., similar to Griffith-Murrell or Drucker Prager model (Descamps and Tshibangu 2007). Interested readers can refer to the following articles to view the practical illustration of the above approach for yield surface determination in three-dimensional principal stress space (Descamps and Tshibangu 2007; Labuz and Zang 2012; Guo 2014; Wu et al. 2017).

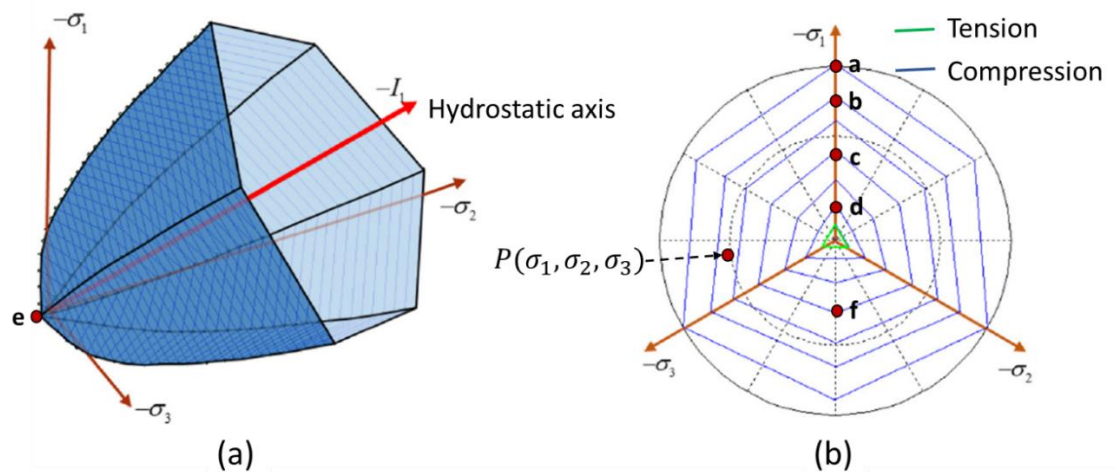


Figure 6.1: (a) Initial yield surface in principle stress plane, (b) in octahedral (or π -plane) (Le et al. 2018a; Le 2019)

Once experimentally determined, the yield surface obtained will form the base to predict failure of given rock specimen, i.e., any stress state hitting this yield surface will fail but may or may not burst. One can observe here that the above discussion of failure (i.e., conventionally used) is primarily from a stress evolution point of view, which may not be helpful to analyze the burst phenomenon. Failure of rocks and similar geo-materials is usually localized, with intensive deformation in a tiny band. The zone outside this band usually undergoes significantly smaller deformation (Nguyen et al. 2012a; Nguyen et al. 2014b; Nguyen et al. 2016b; Nguyen and Bui 2019). Therefore, the use of strength only based on conventional stress-strain responses is not entirely correct once localized cracking occurs (Le et al. 2018a). For instance, it is an undeniable fact that the

mechanical behavior of rock is scale-dependent (Tuncay and Hasancebi 2009; Xie et al. 2009; Zhao and Cai 2015). Based on uniaxial compression tests, many researchers reported the variation in compressive strength with specimen aspect ratio. Mogi (1966) reported the decrease in uniaxial compressive strength of different rock type including Westerly granite, Dunham dolomite and Mizuho trachyte with increase in slenderness ratio from 1 to 4 (Mogi 1966; Zhao and Cai 2015). Li et al. (2011) demonstrated the change in failure mode under uniaxial compression from axial splitting to shear with a decrease in specimen's aspect ratio (Li et al. 2011). In-fact, observing different failure modes in different rock types with the same specimen dimension and almost similar stress-strain response is also quite common. Variation in stress in the same specimen at a different scale of analysis (i.e., local and global scale) is another aspect of this conversation regarding the conventional stress-strain based approach which has already presented in-depth in chapter-2. One can also utilize the statistical view-point to explain the size-dependent behavior and properties: large specimens are likely to contain more defects. From the mechanic's view-point, one can reason that the localized failure modes induce the deterministic size effects as the responses inside the localization band govern the overall sample scale inelastic behavior. Whereas, the bulk material outside this localized zone undergoes elastic unloading (Nguyen et al., 2012, 2014, 2016; Nguyen & Bui, 2019). This deterministic size effect is related to localized failure and requires interpretation of experimental data and analysis based on the energy concept, in addition to the classical strength concept. In simple terms, the strain energy before failure initiation scales with specimen volume, dissipation due to localized failure in the form of cracks (or thin shear bands) scales with a surface area of the cracks. They are following different scaling rules, and therefore changing the specimen size leads to a "mismatch" between energy storage and dissipation capacities leading to stable or unstable (self-sustainable) failure processes. One can find further details in (Nguyen et al. 2012, 2014, 2016; Nguyen and Bui 2019; Le et al. 2018, 2019).

As a result, it becomes inevitable to account for energy storage and dissipation capacities in addition to strength-based criteria, especially in case of bursting analysis. In this view, this chapter proposes to explore the fundamental of strain energy evolution for the dissipation characteristics of rock in collaboration with the conventional yield surface concept. The intention here is to determine the possibility of failure and identification of its type (i.e., bursting or non-bursting), all depending upon the strain energy storing and

dissipation status derived from the current stress-state and eventual stress path in three-dimensional principal stress space. For illustration, figure 6.2 presents a rectangular prismatic rock sample of thickness ' B ,' width ' W ' and height ' H .'

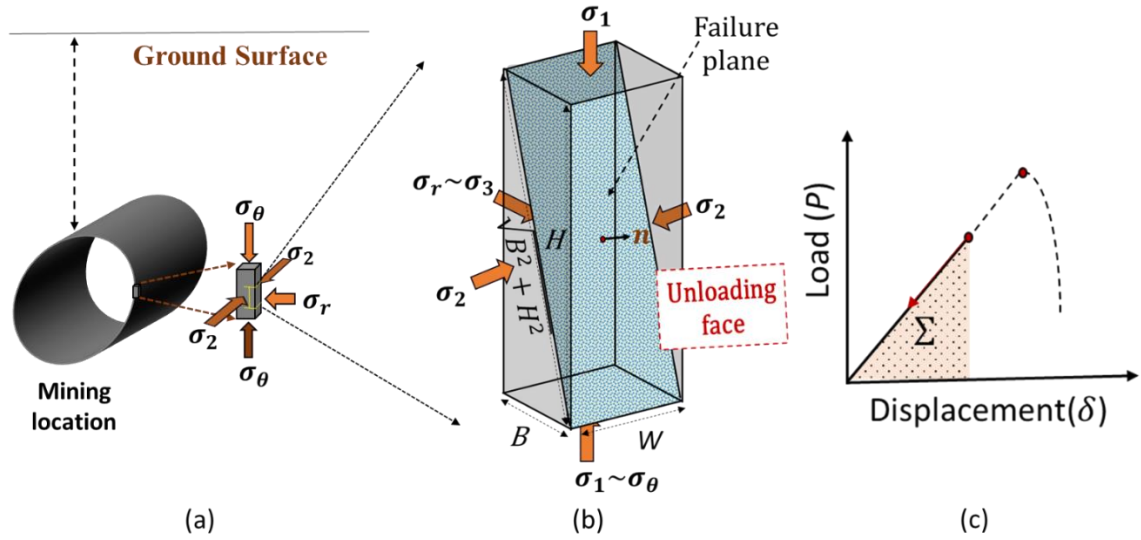


Figure 6.2: (a) Deep underground mine location, (b) rectangular prismatic sample, (c) strain energy in uniaxial case

Subscript 1,2,3 denotes major, intermediate, and minor principal stress components. Under true-triaxial compression similar to the in-situ conditions at the periphery of underground opening before excavation (i.e., figure 6.2a), the above rock sample deforms elastically. It may not fail considering the position of stress state inside the yield surface. In terms of energy conversion, the work done by external loading source via polyaxial loading transforms and stores inside the specimen in the form of elastic strain energy (Σ). In the more straightforward uniaxial condition, one can estimate it from the load (P) versus displacement (δ) or stress versus strain response and the volume, assuming a homogeneous distribution of strain energy density (i.e., figure 6.2c) as follows:

$$\Sigma = \frac{1}{2} p \delta = \frac{1}{2} \sigma_1 \varepsilon_1 V \quad (6.1)$$

Where, V is the specimen volume (i.e., $\sim WBH$ in case of the prismatic specimen). Under above three-dimensional true-triaxial loading conditions (i.e. $\sigma_1 > \sigma_2 > \sigma_3$), one can further simplify the expression 6.1 as follows.

$$\Sigma = \frac{1}{2} \sigma_i \varepsilon_i WBH \quad (6.2)$$

where, $i = 1,2,3$ and ε_i is:

$$\varepsilon_i = \frac{1}{E} \sigma_i + \frac{2\nu}{E} (\sigma_j + \sigma_k) \quad (6.3)$$

Here, σ_i , ε_i are principal stresses and strains while E and ν are elastic parameters, i.e., young's modulus and poison's ratio. Using expressions 6.2 and 6.3, one can obtain the total Σ estimate, as follows (Xie et al. 2009).

$$\Sigma = \frac{1}{2E} [\sigma_1^2 + \sigma_2^2 + \sigma_3^2 - 2\nu(\sigma_1\sigma_2 + \sigma_2\sigma_3 + \sigma_3\sigma_1)] WBH \quad (6.4)$$

Under the confined condition, the subsequent increase in polyaxial stress state will cause the increase in stored elastic strain energy until the present stress state hits the yield surface, i.e., commonly observed in conventional triaxial experiments. Nevertheless, if one removes the confinement from minor principal stress direction (i.e., similar to the stress state around the underground opening after excavation), it changes the boundary conditions. It provides a free surface to dilate and thus release the stored elastic strain energy. This release of strain energy often causes the failure of rock around underground openings. Now, the magnitude of elastic strain energy available for release to fracture requirement for overall structural failure will determine the possibility and scale of bursting. If the stored strain energy is higher than the overall energy requirement for structural failure, then the above change in boundary conditions will cause bursting. Otherwise, the specimen may (in case of stress state hitting yield surface) or may not fail, or even if it fails, it may not cause bursting.

Now, the question arises: how can one determine the energy requirement for structural failure, especially in such complex loading conditions? The concept of fracture energy (i.e., energy consumed to create new surface via fracturing) will form the base to address this issue. Still, one requires to estimate the area of new surfaces created under the assumed quasi-static loading condition, which is not straightforward. It depends upon the applied stress state and geometries besides other inherent material heterogeneity. Therefore, this study suggests a conservative approach to consider maximum possible and estimable fracture surface area with the potential to cause structural failure under quasi-static condition, i.e., represented by normal vector \mathbf{n} as shown in figure 6.2(b). This link between mechanical behavior and mechanism of localized failure (cracks or shear bands) follows earlier work in Nguyen et al. (2012, 2014, 2016); Nguyen & Bui, 2019; Le et al. (2018, 2019) in which the dissipation and inelastic behavior of a volume element are governed by what happens inside the localization zone. This assumption provides us

with ease to estimate the total energy requirement for structural failure via fracturing, i.e., derived in eq. 6.5 as follows:

$$\phi = FG_fNW\sqrt{B^2 + H^2} \quad (6.5)$$

where, G_f ($\frac{N-mm}{mm^2}$) is fracture energy, N number of fracture planes (i.e., considered one with maximum possible) and factor 'F' is introduced to correct the mode I fracture energy G_f , taking into account the fact that the assumed failure plane in true triaxial condition (Fig. 6.2b) is under mixed-mode conditions, which possess higher energy dissipation capacities. Section 6.3 discusses the detailed approach to estimate this parameter. In this sense, this study assumes that the fracture energy is invariant with the stress state, which may not be entirely accurate. For example, energy dissipation per unit area is different in pure tension (mode I), pure shear (mode II), and combined shear-tension (mixed mode). However, this difference is generally not significant (e.g., shear fracture energy can be assumed to be equal to tensile fracture energy). Hence, it justifies the above simplification assumption and allows us to arrive at a simple bursting criterion, as a first-order approximation. A brief discussion about this is also presented in chapter-2, section 2.4.1. The further enhancement of this criterion considering the dependence of fracture energy on stress state will be considered in the future.

Overall, the above formulation leads to the proposal that bursting failure may occur only if the available strain energy at a stress state during unloading is higher than the above fracture energy requirement to cause structural instability, and the yield condition also met. The high strain energy storage is necessary, but not enough condition to trigger burst. The yield condition is needed to trigger inelastic behavior. An example to illustrate this is a hydrostatic condition. Rocks under sufficiently high hydrostatic pressure may not burst as it does not violate the yield criterion. It requires the release/unloading from one stress principle stress direction to induce yielding and potentially bursting. Higher strain energy will scale up the bursting magnitude, and thus enhance the kinetic energy proportions of bursting fragments. This study utilizes the above principle and proposes the following Strain-Burst Potential (\mathbb{P}) index.

$$\mathbb{P} = \frac{\Sigma}{\phi} = \frac{[\sigma_1^2 + \sigma_2^2 + \sigma_3^2 - 2\vartheta(\sigma_1\sigma_2 + \sigma_2\sigma_3 + \sigma_3\sigma_1)]BH}{2E NG_fF \sqrt{B^2 + H^2}} \quad (6.6)$$

It can further be simplified as follows:

$$\mathbb{P} \geq 1 \rightarrow \text{Bursting failure with } \Sigma - \phi \text{ as the kinetic energy of fragments} \quad (6.7)$$

Considering the above burst conditions, i.e., eq. 6.7, the following bursting criterion for a prismatic specimen (Fig. 6.2b) under true triaxial loading-unloading conditions can be derived:

$$(\sigma_1, \sigma_2, \sigma_3) = \sigma_1^2 - 2\vartheta(\sigma_2 + \sigma_3)\sigma_1 + (\sigma_2^2 + \sigma_3^2 - 2\vartheta\sigma_2\sigma_3 - 2FNG_f E \frac{\sqrt{B^2+H^2}}{BH}) \leq 0 \quad (6.8)$$

where $b(\sigma_1, \sigma_2, \sigma_3) = 0$ is the "burst surface," and any stress state outside this surface indicates bursting. It shares similarities with yield criterion usually used in classical plasticity. Figure 6.3 presents the proposed burst criterion in collaboration with the potential yield surface. This study uses it to demonstrate and differentiate between the mechanism of conventional and burst failure under different possible stress-path in three-dimensional stress space.

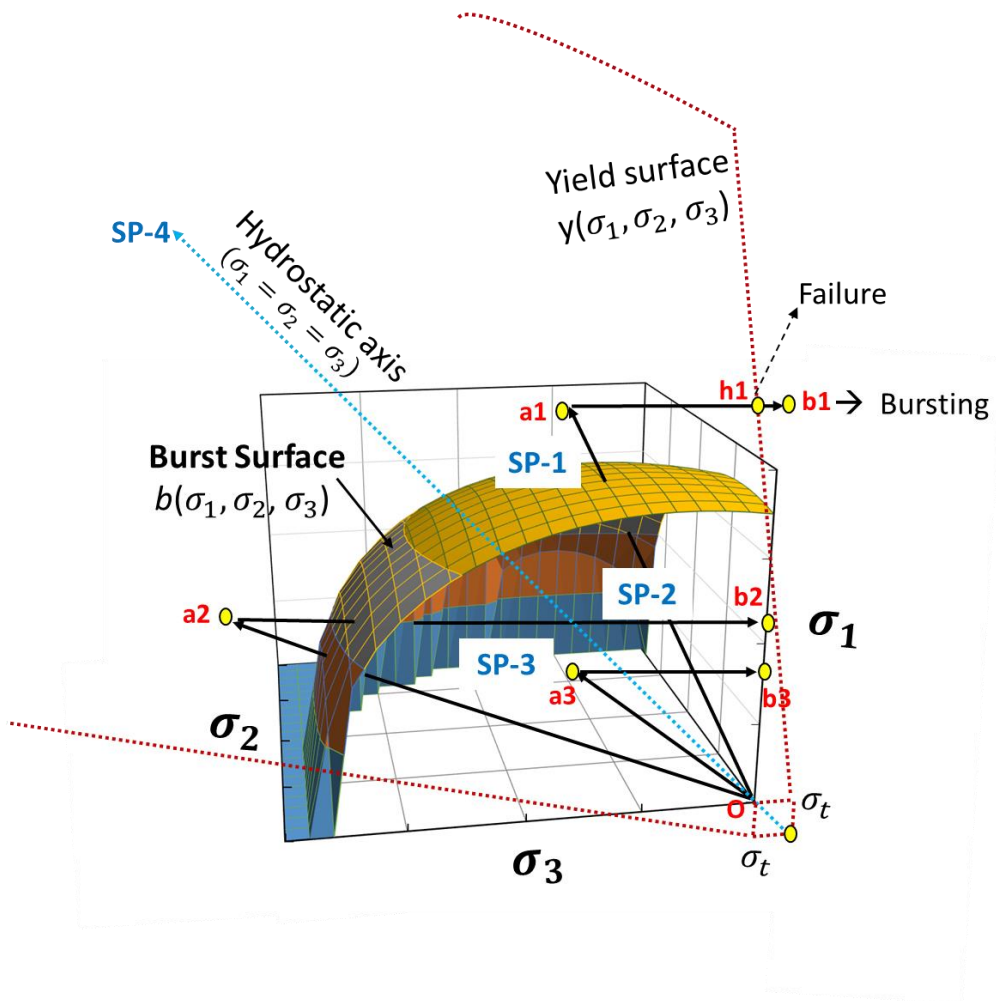


Figure 6.3: Energy-based strain-burst envelope

Given the true triaxial stress state with three stresses (assuming inside the yield envelope), removing one stress may lead to burst if the unloading stress path intersects the yield surface, and this intersection is outside the burst envelope. The intersection with the yield surface indicates in-elastic behavior. On the other hand, the intersection with the bursting envelope reveals the relationship between strain energy storage at the intersection and the energy dissipation capacity of the specimen. It requires details on the yield envelope in principal stress space, which is not an easy task given the complex shape with the effects of the Lode angle (Le et al. 2018, 2019). Instead, a conservative approach is used in this study by projecting the unloading stress path on the $\sigma_1 - \sigma_3$ plane and using the position of this 2D stress state in relation to the 2D bursting envelope in the 2D $\sigma_1 - \sigma_3$ space to indicate bursting potential. The 2D stress state is associated with a lower strain energy storage and if bursting happens under this stress state, it should happen under a 3D stress state at the intersection between the unloading path and the initial yield envelope.

Figure 6.3 considers four stress paths based on true-triaxial loading-unloading conditions to illustrate the above bursting mechanism. Each stress path denotes true-triaxial loading conditions and unloading in σ_3 direction. The detailed discussion on the bursting prediction for each stress path is as follows:

- **Stress-path 1 (SP1):** In the first case, the applied load brings the resultant stress-state before unloading outside the burst envelope, i.e., for instance, the stress path o-a1 in figure 6.3. Upon unloading in σ_3 direction at point a3, the consequential stress-path hits the initial yield surface first, resulting in specimen failure and then acquire residual stress state located outside the burst envelope. As a result, excess stored strain energy releases violently in fractions of a second, causing burst failure. The magnitude of this burst is proportional to the distance of residual stress state after unloading from the burst envelope, i.e., \sim kinetic energies of bursting fragments.
- **Stress-path 2 (SP2):** In this case, true triaxial loading brings the corresponding stress state outside the burst envelope but inside the yield surface again. At point a2, despite being in an elastic state, the elastic strain energy stored in the specimen is higher than the fracture energy requirement for structural failure (with the assumed fracture plane in Fig. 6.2). This stress state is still inside the initial yield; consequently, inelastic behavior does not trigger. Unloading in minor principal

stress direction brings this stress state back inside the burst envelope, indicating finalized strain energy magnitude lower than the overall fracture requirement. In such conditions, minor damage due to excess energy dissipation could be possible, as the unloading path intersects with the initial yield envelope; however, burst failure may not occur.

- **Stress-path 3 (SP3):** In this loading-unloading case, point a1 at which unloading occurs is inside both burst envelope and the yield surface. Consequently, the final stress state after sudden unloading at point b1 also falls inside the burst envelope. It indicates that the strain energy available at both a1 and b1 is lower than the energy required to cause failure. Thus, the rock sample responds elastically, resulting in the complete recovery of the stored strain energy by external work done without dissipation after unloading. As a result, no bursting or even sample failure will occur.
- **Stress-path 4 (SP4):** In this case, the specimen loaded hydrostatically (i.e. $\sigma_1 = \sigma_2 = \sigma_3$) to a very high-stress level. The removal of any stress component will result in the residual stress state outside the burst surface, thus lead to burst failure.

In conclusion, the burst failure occurs if the residual stress state after excavation (i.e., after unloading) locates outside the proposed burst envelope and the initial yield surface. The present derivation is currently in generalized form for a simplified version of "presumably intact" rock samples. It is suitable for any type of rock (or more generally, brittle materials), given the appearance of rock properties (yield strength envelope and fracture energy) in the expressions. It can be further modified to account for other geotechnical factors contributing to in-situ strain energy dissipation by altering the expression for energy dissipation (ϕ).

6.3 Illustration and validation: An energy-based strain burst criterion

This section presents the illustration and validation of the proposed energy-based strain burst criterion using the Bluestone rock type as an example. The intent here is to analyze the behavior of given rock type under true triaxial loading conditions and utilize these results to validate the accuracy of the developed energy-based theoretical framework. The first step in this direction is to obtain the required strength, elastic, and fracture properties from laboratory experiments. These parameters will further lead to the determination of

yield surface, and the burst envelope of any target rock type. In order to efficiently obtain the required material properties, this study utilizes the following two unconventional experiments: lateral strain-controlled uniaxial compression test (figure 6.4a) and AUSBIT-indirect tensile strength test (figure 6.4b). An in-depth discussion about experimental details results from the analysis, AUSBIT-methodology-inception, and proposal has already presented in chapters 3, 4, and 5.

6.3.1 Laboratory experiments: burst envelope and yield surface determination

The first set of experiments, i.e., UCS provides compressive strength (σ_c) and elastic properties, i.e., E and ν , i.e., figure 6.4(a), (b), whereas, parameters including tensile strength (σ_t) and mode-I fracture energy (G_f^I) obtained from AUSBIT indirect tensile strength experiments. In the AUSBIT experiment, the diametrical compressive load was continuously adjusted to maintain a constant lateral strain rate (i.e., 2.1 $\mu\text{m}/\text{min}$) of disc specimen. Chapter-3 presented a detailed discussion regarding the below experiments. The complete diametrical crack in the AUSBIT experiment occurred at point 'a,' as shown in figure 6.4(b). It was confirmed via DIC analysis, whereas the area under triangle 'abc' is the energy stored in the broken rock pieces after diametrical cracking. Therefore, it does not contribute to the fracture surface creation thus, excluded from G_f^I calculations. Strength parameters (i.e. σ_c , σ_t) were used to determine the yield surface, presented in figure 6.4c in conventional p - q space where p indicates hydrostatic (i.e., $p = \frac{I_1}{3} = \frac{\sigma_1 + \sigma_2 + \sigma_3}{3}$) and q denotes deviatoric stress components as follow:

$$q = \sqrt{\frac{(\sigma_1 - \sigma_2)^2 + (\sigma_2 - \sigma_3)^2 + (\sigma_3 - \sigma_1)^2}{3}} = \sqrt{3} J_2 \quad (6.9)$$

Here, I_1 is the first invariant of stress tensor while J_2 is the second invariant of the deviatoric stress tensor.

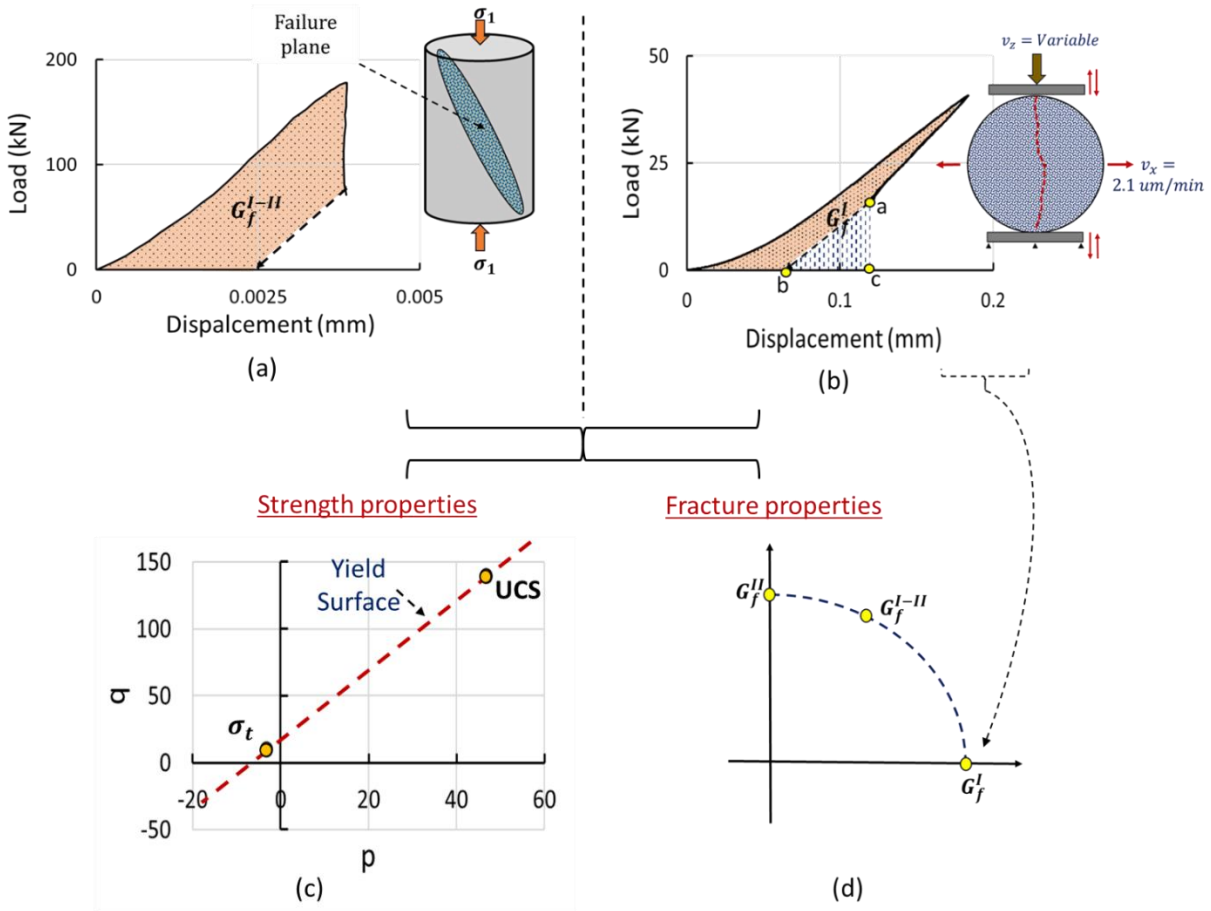


Figure 6.4: (a) Uniaxial compression test, (b) AUSBIT indirect tensile strength test, (c) determination of yield surface, (d) fracture locus

We also require several other laboratory experiments to test the rock's material strength in biaxial, triaxial, and polyaxial loading conditions. It would help to determine the actual shape of yield surface in three-dimensional principal stress space. Nevertheless, performing that many experiments are not feasible currently. In this view, this study adopts a more straightforward but reliable Mohr-Coulomb failure criterion, suitable for geo-material like a rock (Schreyer 2007; Labuz and Zang 2012). It provides a preliminary basis, good enough to illustrate the functioning of the proposed theoretical framework. Equation 6.10 presents its definition in three-dimensional principal stress space with no order implied:

$$\pm \frac{\sigma_1 - \sigma_2}{2} = a \frac{\sigma_1 + \sigma_2}{2} + b; \pm \frac{\sigma_2 - \sigma_3}{2} = a \frac{\sigma_2 + \sigma_3}{2} + b; \pm \frac{\sigma_3 - \sigma_1}{2} = a \frac{\sigma_3 + \sigma_1}{2} + b \quad (6.10)$$

Where, $a = \frac{m-1}{m+1}$, $b = \frac{1}{m+1}$, $m = \frac{\sigma_{ucs}}{\sigma_t} = \frac{1+\sin \varphi}{1-\sin \varphi}$. Here, σ_{ucs} and σ_t are uniaxial and tensile strength parameters obtained from UCS and AUSBIT experiments and used to develop the yield surface, as shown in figure 6.5.

The next step is to describe a burst envelope for Bluestone rock with pre-defined elastic, strength, and fracture properties. Parameter F , as shown in equation 6.8, is also required, which is currently unknown. For this purpose, the proposed energy-based criterion applied to the cylindrical sample in UCS test scenario, i.e., considering $\sigma_1 > 0, \sigma_1 = \sigma_2 = 0$ loading conditions. It resulted in the following expression:

$$b(\sigma_1, \sigma_2, \sigma_3) = \sigma_1^2 - 2\vartheta(\sigma_2 + \sigma_3) \sigma_1 + \left(\sigma_2^2 + \sigma_3^2 - 2\vartheta\sigma_2\sigma_3 - \right. \quad (6.11)$$

$$\left. 2FNG_f E \frac{\sqrt{D^2+H^2}}{DH} \right) = 0$$

Where D and H are diameter and height (in mm) of a cylindrical specimen. The above expression helps in the determination of the parameter F . After that, this study further extends the above setup to determine the burst envelope for the rectangular prismatic specimen with $125 \times 50 \times 25$ mm dimension. The determined burst envelope, along with a pre-defined failure criterion, forms the base to conduct burst predictions in strain burst experiments using rock specimens with dimensions.

One should note here that the fracture mode in specimen failure under UCS is entirely different from failure mode in strain burst experiments. During strain burst experiments, stress-state throughout the sample varies significantly with change in loading-unloading conditions. Determination of such fracture mode variation and thus estimating fracture parameters in fracture loci (i.e., figure 6.4b) is practically not feasible. In this view, the introduction of calibration parameter (F) based on uniaxial compression data and considering G_f^I as invariant input generalized for polyaxial loading unloading would provide a reasonable approximation. Where parameter (F) diminishes the potential error and average out the collaborative influence of fracture mode difference in UCS and strain-burst experiments and variations in strain-burst experiment alone.

Further, this study conducts virtual strain burst experiments using the numerical modeling setup developed in chapter-5 to illustrate and validate the functioning of the above developed energy-based framework for strain burst prediction. The specimen is compressed independently in all three directions, as shown in figure 6.5(a). Figure 6.5(b) presents the summary of the applied loading (or the stress path) in three-dimensional principal stress space, where, σ_2^c and σ_3^c denotes the planes in which intermediate (σ_2) and minor (σ_3) principle stresses are kept constant. Figure 6.5(c) presents the proposed

theoretical framework for burst prediction using the burst envelope and Mohr-Coulomb yield criterion. In this setup, the specimen undergoes hydrostatic compression to reach stage i first, as shown in figure 6.5(a),(b). After that, σ_3 is kept constant to keep stress state on σ_3^c plane while increasing the other two stress components further with the same rate to reach σ_2^c plane at stage ii. At this stage, σ_2 is also kept constant while increasing σ_1 with the same loading rate. It consequently increases strain energy stored in the sample. Now, thanks to the proposed framework, one can utilize the pre-defined burst envelope in three-dimensional principal stress space, i.e., figure 6.5(c), and determine the burst possibility depending upon the stress-state location at unloading (in σ_3 direction) stage. For illustration, this study chooses three levels of major principle stress (i.e. $\sigma_1 = 180, 140$ and 80 MPa) to induce in σ_3 direction. Subsequent sub-section will demonstrate the sample failure mode upon unloading via virtual strain burst experiments. Stress variations in three-dimensional space (i.e., figure 6.5b) will be used in collaboration with a two-dimensional theoretical framework to facilitate the theoretical predictions for burst occurrence.

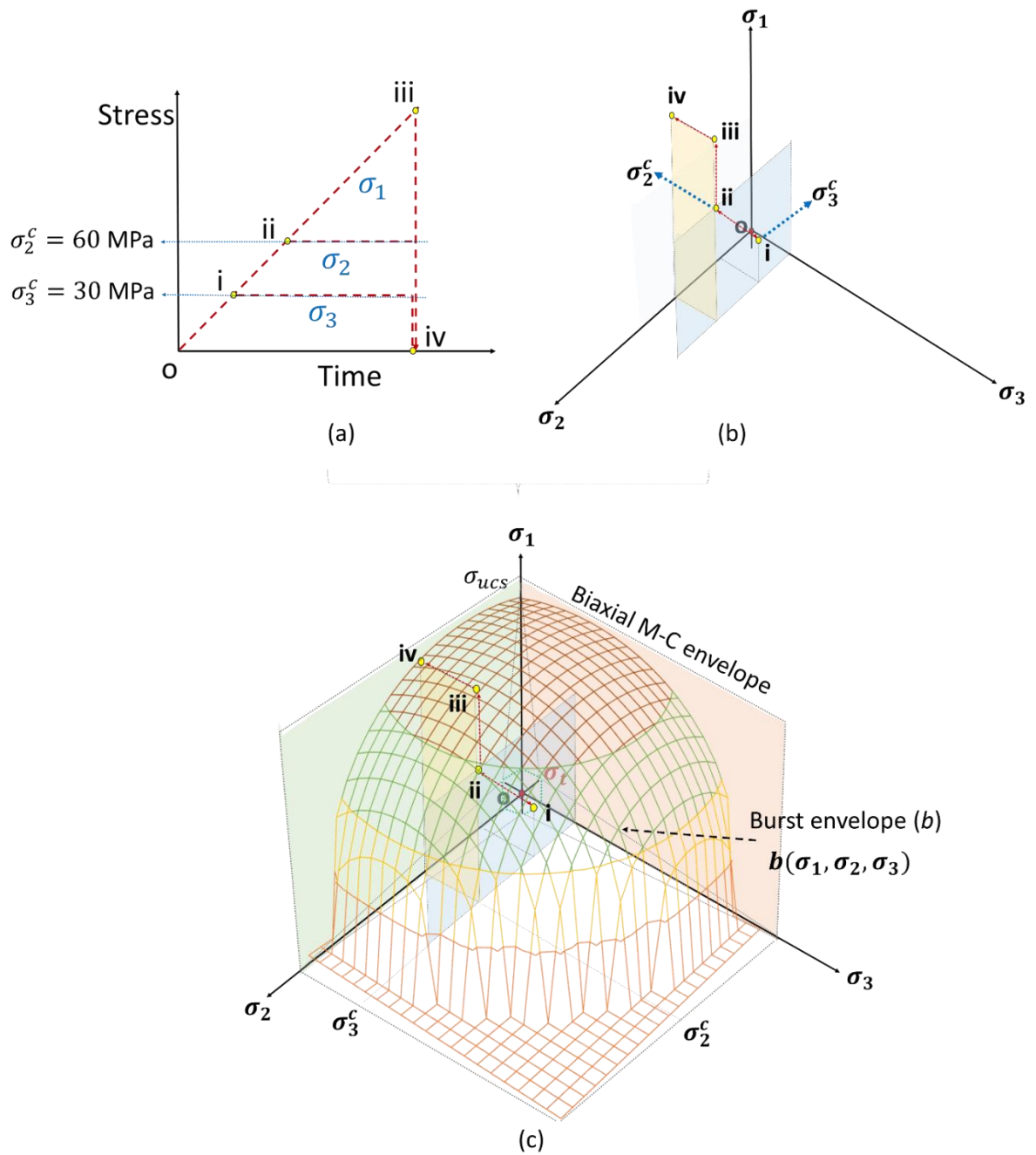


Figure 6.5: (a) True-triaxial stress variations, (b) three-dimensional stress path, (c) proposed energy-based theoretical framework for burst prediction

6.3.2 Numerical simulations: Strain burst virtual experiments

This study utilizes the numerical modeling framework presented in chapter-5 to conduct virtual strain burst experiments. It not only provides an ease to adopt different stress paths and specimen dimensions based on our requirements but also enables us to acquire better insights into material damage evolution in three-dimensional space. The

brief overview of numerical modeling setup adjustments for performing virtual strain burst experiments is presented in the subsequent section as follows.

6.3.2.1 Strain burst virtual experiments: test setup

This study chooses a rectangular prismatic specimen for numerical strain burst experiments (i.e., a combination of deformable tetrahedral blocks) with $125 \times 50 \times 25$ mm (i.e., $H \times W \times B$) dimension with the prime intent to analyze the bursting potential, ignoring the minor details of fracture pattern and cracking mechanism. The tetrahedral block size considered was relatively coarse (i.e., grain/specimen's minimum dimension ~ 0.4) to acquire better computational efficiency. Rock type chosen for these virtual experiments was Bluestone. Chapter-5 presents the details of the mesh sensitivity analysis, model calibration, and finalized model parameters.

Further, six intact loading platen (i.e., steel properties assigned) devised to apply independent loading in all three principal directions. Table 5.4 presents a summary of all calibrated parameters. Figure 6.5 below shows the testing arrangements before and after unloading in σ_3 direction. This arrangement requires fixing the steel platen located at the bottom in z, right in x, and back in y-directions. Whereas, constant velocities (i.e., displacement controlled) assign to the platens in opposite directions to compress the specimen in all three directions under all times quasi-static loading conditions. In later stages, the servo-controlled displacement approach, devised using in-built programming language FISH, to maintain a constant stress level in lateral (i.e., in σ_2 and σ_3) directions. Once the pre-defined stress level in respective principal directions achieved, the loading platen in positive x-direction deleted to induce the abrupt unloading effect. Table 6.1 presents a brief overview of loading schemes and overall test summary of the strain burst experiments.

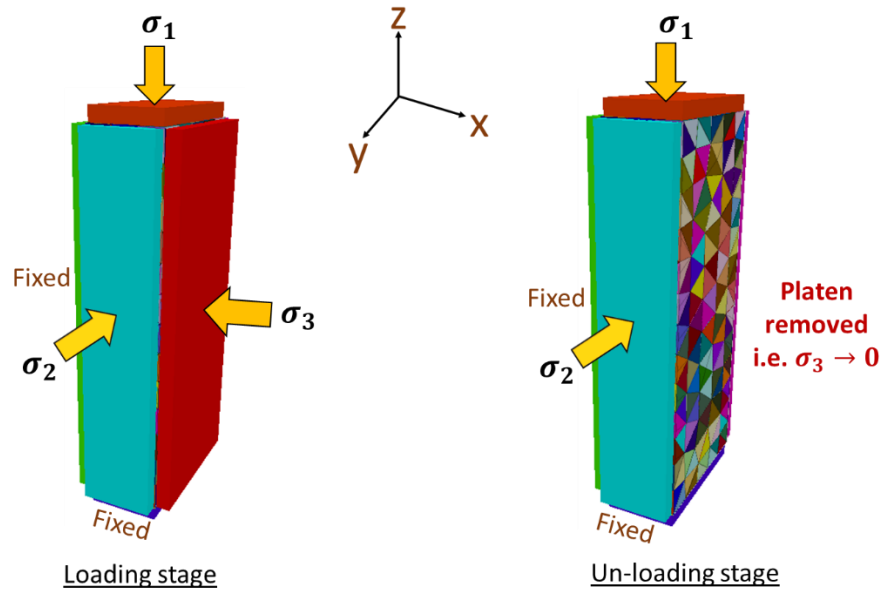


Figure 6.6: Strain-burst experiments

Table 6.1: Strainburst numerical experiments

Sr. No	Dimension (mm) $B \times W \times H$	Initial loading (MPa)			Unloading ($\sigma_3 \rightarrow 0$)		Bursting at unloading	Failure state (MPa)		
		σ_3	σ_2	σ_3	σ_1	σ_3		σ_2	σ_3	
1	$25 \times 50 \times 125$	30	60	80	180	Yes	0	60	180	
2	$25 \times 50 \times 125$	30	60	80	140	Yes	0	60	140	
3	$25 \times 50 \times 125$	30	60	80	80	No	0	60	139	
4	$25 \times 50 \times 75$	30	60	80	80	No	0	60	158	
5	$25 \times 50 \times 100$	30	60	80	80	No	0	60	146	
6	$25 \times 50 \times 150$	30	60	80	80	No	0	60	141	

First three cases in table 6.1 use specimens with the same dimensions but with different in-situ stress state before unloading in σ_3 direction. This study uses virtual experiments with the first three samples to verify the proposed theoretical framework and analyze the effect of stress path changes on overall bursting potential. It also uses the burst indicator in 3DEC simulations (or other such numerical simulations for discussion sake) to ensure and predict the bursting failure.

Majorities of available research studies in this direction suggest qualitative approaches and may not work in numerical simulation. For instance, laboratory experiments based researches mostly adopted visual inspection of flying fragments after bursting using digital images and considering the audible crunching noises during violent bursting as the basis to ensure bursting failure (He et al. 2010, 2015a; Zhao et al. 2014; Su et al. 2017). Therefore, this study adopts a simple indicator based on maximum displacement, i.e., $\max(|u_x|, |u_y|, |u_z|)$, of tetrahedral blocks estimated from full-field displacement contours, i.e., bursting is real if the maximum displacement of nodal points exceeds 10% of the minimum dimension of the specimen. This indicator, in collaboration with damage evolution, provides an adequate indication of bursting failure.

6.3.2.2 Validation: stress-path 1

The first stress path and corresponding loading scheme analysis for bursting failure is sr. no.1 in table 6.1. In this case, the numerical setup applies the compressive load to the prismatic specimen independently in three principal stress directions to acquire initial polyaxial stress state of $\sigma_1 \sim 80$, $\sigma_2 \sim 60$ and $\sigma_3 \sim 30$ MPa. After that, it keeps σ_3 and σ_2 principle stress components constant while σ_1 increasing until the limit of 180 MPa. Figure 6.7(a) presents the two dimensional $\sigma_1 - \sigma_3$ plane with Biaxial Mohr-Coulomb envelope estimated from experimental strength parameters (i.e. σ_{ucs} and σ_t). Figure 6.7(a) presents the proposed burst envelope, i.e., $b(\sigma_1, \sigma_2, \sigma_3)$, derived from elastic strain energy storing and dissipation characteristics. It also contains the insight of three-dimensional stress-path variation similar to figure 6.5(b) for better visualization of overall stress variations. An outline of the present stress-path illustrates that increase in σ_1 brings the resultant stress state outside the burst envelope, i.e., stage iv, as shown in figure 6.7(a). It indicates that the magnitude of elastic strain energy stored in the specimen is higher than the structural failure requirement. Therefore, the resultant stress path after unloading in σ_3 the direction theoretically hits the yield surface. It causes specimen failure first, followed by the release of stored strain energy in the form of burst.

To verify the above theoretical prediction, figure 6.7(b) presented the sample scale stress and stored strain energy variations with the loading time step. Figure 6.7(c) presents full field (including local scale) damage evolution, figure in 6.7(d), and 6.7(e) indicate the specimen configuration evolution for visual inspection of bursting failure, and the burst indicator in the form of displacement in the x-direction (u_x) contours as described

in sub-section 6.3.2.1. Overall results from the above virtual experiment demonstrate that at stage iii, the rock material is in stable conditions with negligible to zero damage (i.e., figure 6.7c). Distribution of u_x is quite uniform depending upon the local stress in minor principle (or x) direction, with a smaller magnitude as compared with the burst indicator, i.e., 10% of minimum specimen dimension. It shows that the rock material is behaving elastically even after reaching a very high-stress state under confined conditions. These observations agree well with the proposed bursting theory showing that rock under the confined stress state could mostly locate inside the yield surface irrespective of its position to the burst envelope. Consequently, the rock may not fail, and the applied external work via loading will increase the stored elastic strain energy, as shown in figure 6.7(b).

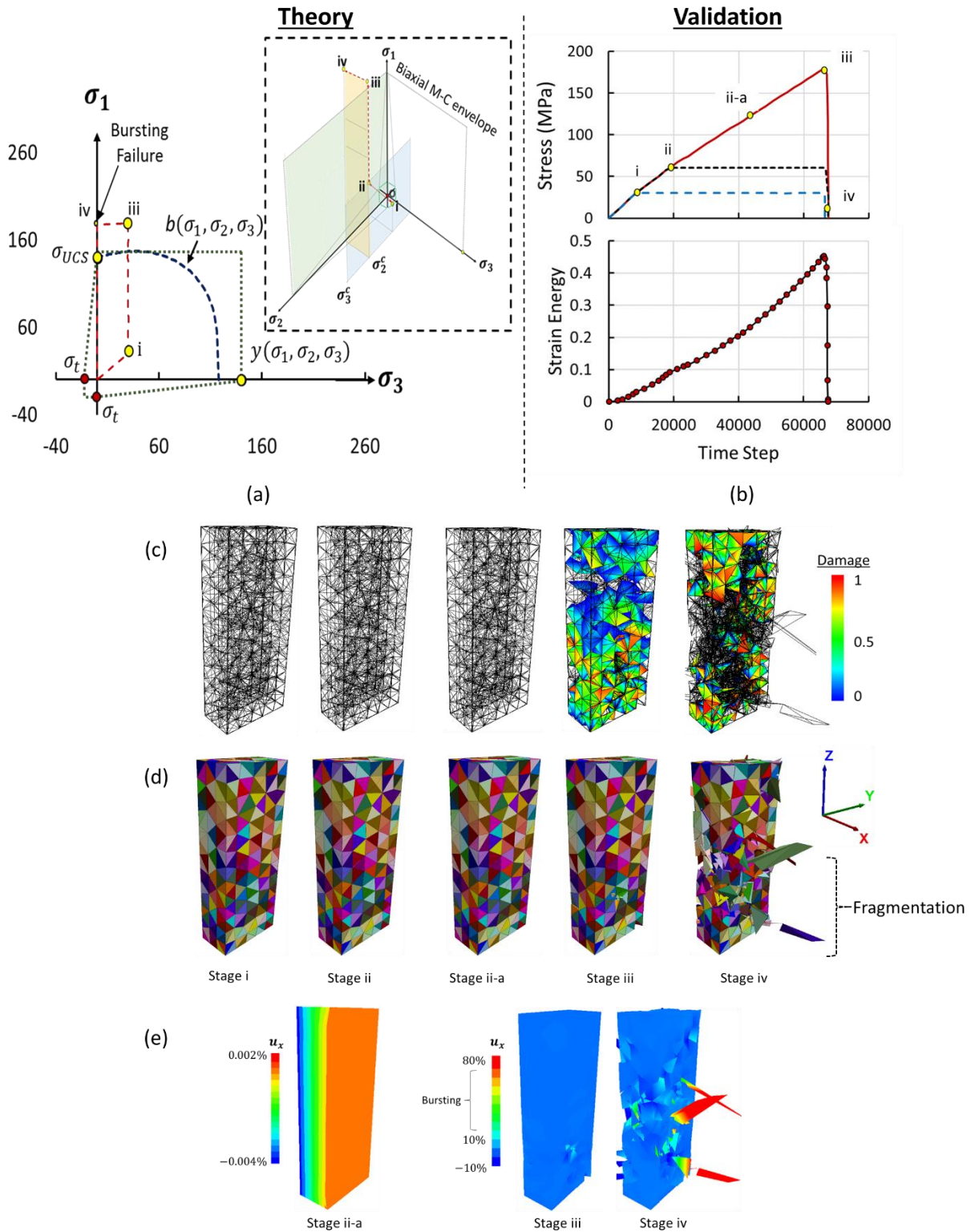


Figure 6.7: Stress-path 1 (a) Theoretical prediction, (b) sample scale stress and strain energy evolution, (c) damage evolution, (d) rock specimen bursting, (e) burst indicator

The occurrence of unloading at stage iv (i.e. $\sigma_1 \sim 180$ MPa at which the overall stress state detects inside the yield surface but outside the burst envelope), the entire stress state drastically changes at both global and local scales. The sample scale stresses in the

remaining two directions (i.e. σ_1, σ_2) and elastic strain energy stored in the specimen instantly reduces to zero. The damage magnitude across the sample jumps from to maximum, i.e., close to 1, at stage v. The u_x displacement, i.e., $\max(|u_x|, |u_y|, |u_z|)$, also jumps from 0.002% to more than 10% of the minimum specimen dimension followed by flying fragments, as shown in figure 6.7(d),(e). It demonstrates the mechanism of uncontrolled and violent failure of the specimen, i.e., under strain-burst characterization. These observations validate the predictions of bursting failure made by the proposed energy-based strain-burst criterion.

In terms of practical significance, the above case of bursting failure is typical in hard and brittle rock types in deep underground conditions. Under such conditions, rock deforms elastically (i.e., stress state inside yield surface) before excavation and stores enormous elastic strain energy certainly much higher than its energy dissipation characteristics (i.e., stress state outside the burst envelope). Consequently, when unloading in the radial (or σ_3) direction occurs via excavation, a sudden, uncontrolled, and violent release of stored strain energy follows in the form of burst failure, known as *instantaneous strain-burst*.

6.3.2.3 Strain burst virtual experiments: stress-path 2

In the second case of loading condition (i.e., SP-2 or Sr. No.2 in table 6.1), the unloading in σ_3 the direction occurs when the stress state is close to the burst envelope, as shown in figure 6.8(a). Theoretically, the unloading at this stage should cause the resultant stress state located on or just outside the burst envelope, indicating the available elastic strain energy just sufficient to cause burst failure.

Figure 6.8(b), (c), and (d) presents the results from virtual true-triaxial experiments replicating the above stress path. It shows that prismatic sample under confined state undergoes negligible damage, limited u_x displacement (i.e., <0.002%) with continuous increase in elastic strain energy stored. At stage iv when unloading in σ_3 the direction occurs, it subsequently causes stress drop in other principal stress directions followed by elastic strain energy release and jumps in material damage along with u_x displacement (>10%). It indicates bursting failure. The stress drop, in this case, is not as abrupt as observed in the previous case of SP-1. It is because the strain energy available in this case for causing overall failure is 60% smaller than the previous case, which, as per the proposed theory, is just sufficient to cause the bursting failure. In other words, a sample

under these loading conditions underwent burst failure but with a smaller magnitude relatively. Overall, the above results from virtual experiments are again in good agreement with theoretical predictions validating its applications in strain burst studies.

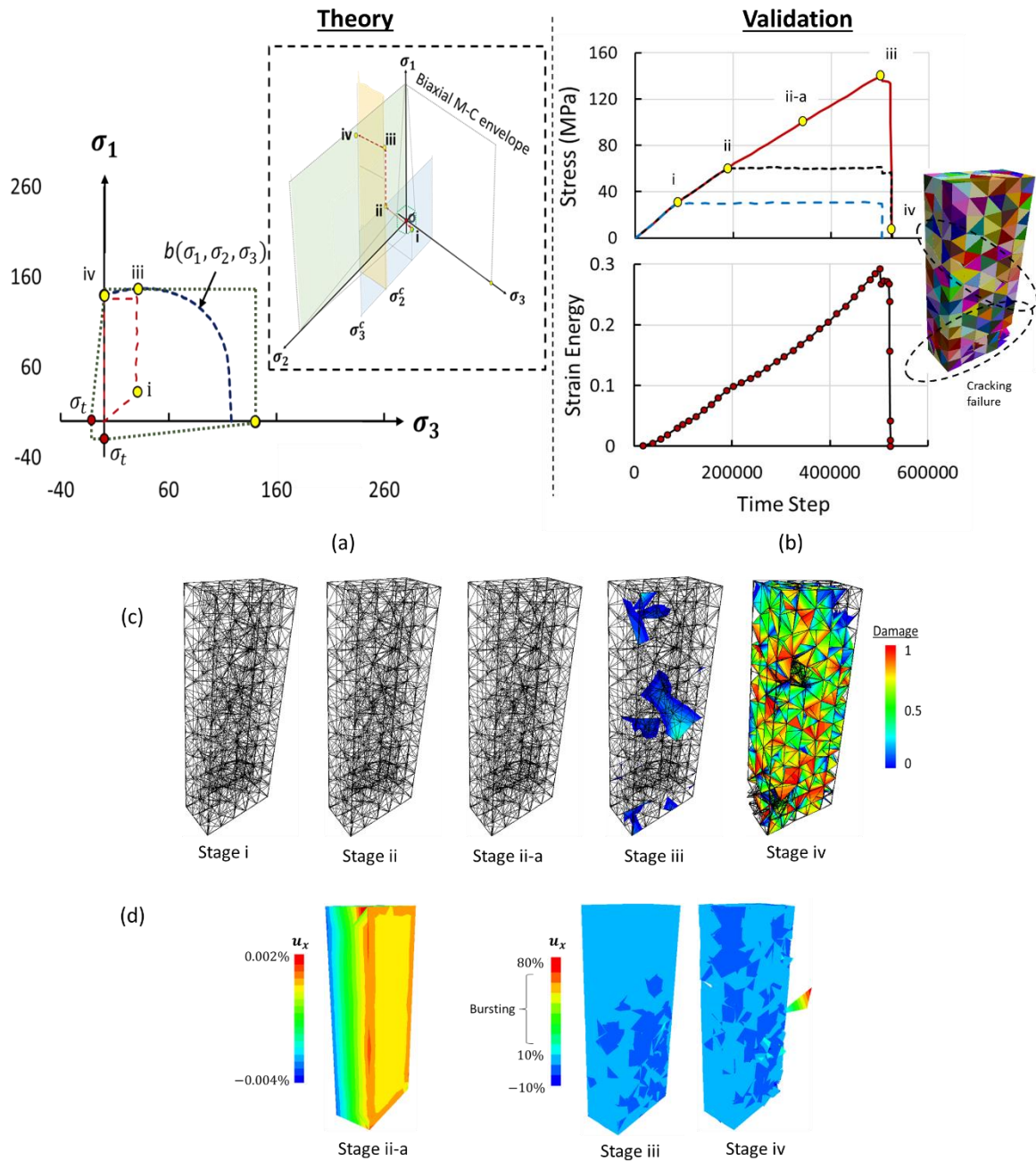


Figure 6.8: Stress-path 2 (a) Theoretical prediction, (b) sample scale stress and energy evolution response, (c) damage evolution, (d) burst indicator

6.3.2.4 Strain burst virtual experiments: stress-path 3

In the last case of SP-3 stress path, unloading in σ_3 direction occurs at stage iii, i.e., within yield surface and burst envelope. Theoretically, at this stage, elastic strain energy

stored in the specimen is much lower than the energy required to cause burst or even controlled failure. Consequently, the specimen should not even fail, left alone the burst occurrence. Observations from virtual experiments are also in accord with these theoretical predictions where specimen unloading at stage iii induces a slight drop in stresses in the remaining two directions. Nevertheless, there is no sign of material damage along with u_x displacement $<0.07\%$ (i.e. no bursting). It shows the specimen might have gone elastic unloading at the time of σ_3 removal; however, neither bursting nor failure happens in the specimen. In the deep underground scenario also, the rock under such in-situ conditions with insufficient stored elastic strain energy stored in comparison with the rock's dissipation characteristics are less likely to face strain-burst accidents.

In most of the available researches pertaining strain burst experiments, specimen under such scenario often continued to load in σ_1 the direction while keeping the σ_2 constant to artificially induce bursting. The proposed framework can also explain the mechanism behind such bursting. Here, further loading results in an increase in stored elastic strain energy. The moment when the resultant stress state crosses the burst envelope and touches the yield surface, the specimen fails with burst characteristics. Uniaxial compression tests that exhibit class II failure are some key examples of such scenarios. One can also illustrate this artificial bursting via the presented virtual strain burst experiments by unloading the specimen in σ_3 direction at stage iii and then continue to load in σ_1 direction till stage v. Such type of strain burst experiments is not realistic to derive the bursting potential of rock. It is because the specimen under such a scenario forced to undergo bursting failure artificially. Many researchers did try to link this type of failure with delayed bursting type. The argument presented is that after unloading in σ_3 direction, stresses in the other two principle directions increases gradually to cause bursting. However, the rate of loading in the other two directions after unloading is not easy to determine. It may or may not be quasi-static, commonly adopted in laboratory experiments. Additionally, in majorities of true-triaxial experiments, loading in σ_2 the direction is constant (similar to SP-3 in this study), which is not the case with the in-situ loading conditions after excavation.

Overall, the above three cases demonstrate that the proposed theoretical framework is capable of predicting the burst occurrence under different loading conditions reliably. The subsequent section presents the key benefits and further applications of the energy-based proposed strain burst criterion.

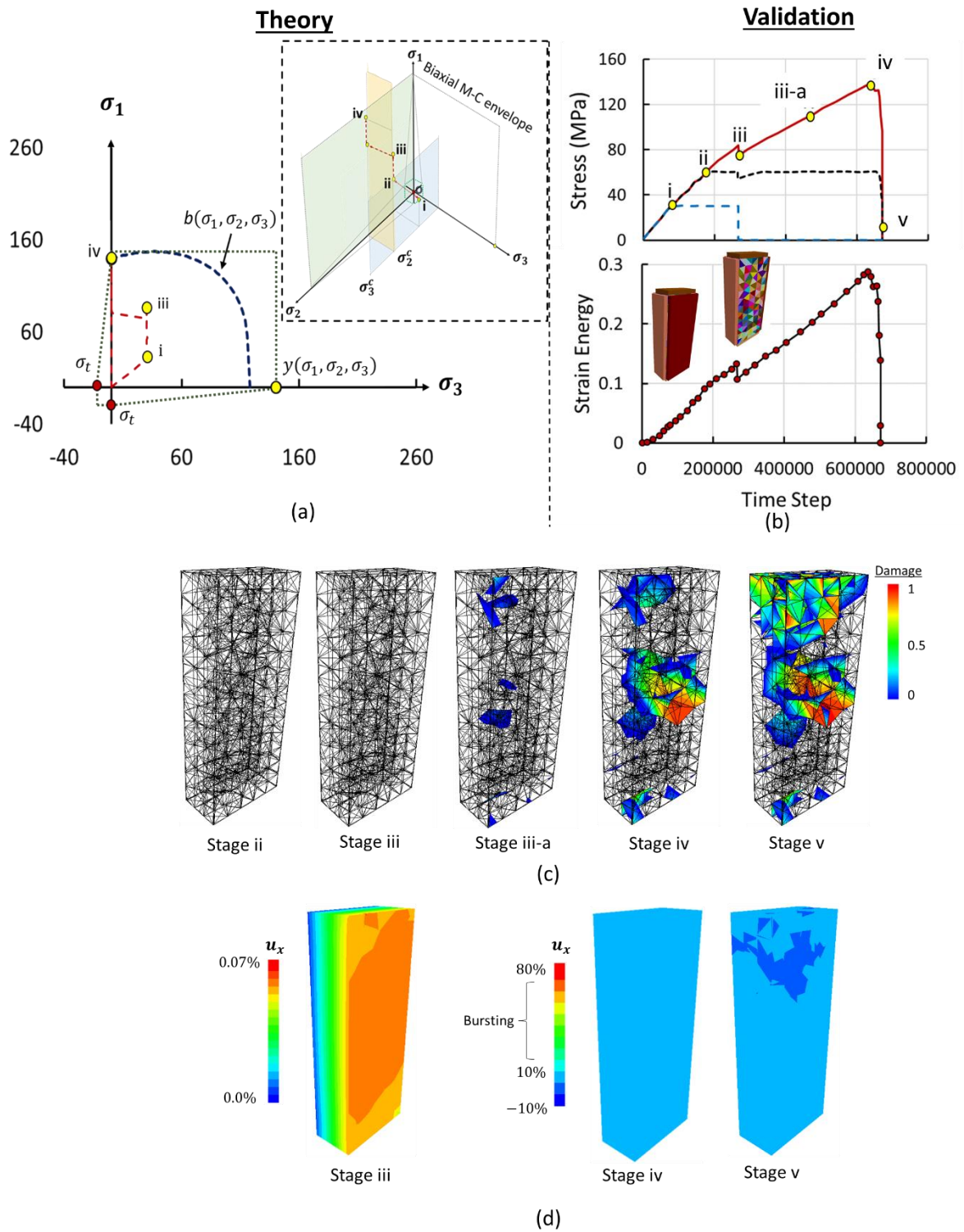


Figure 6.9: Stress-path 3 (a) Theoretical prediction, (b) sample scale stress and energy evolution response, (c) damage evolution, (d) burst indicator

6.4 Bursting potential quantification: Strain burst index (\mathbb{P})

The other aspect of burst prediction is the scale, i.e., the magnitude of the burst. At present, majorities of approaches in this direction utilize strength-based empirical

formulations, which take the strength ratio into account to predict the burst scale. Few experimental approaches attempted to analyze the burst potential based on strain energy evolution in which lateral strain-controlled uniaxial compression test is among the most useful ones. The lateral strain-controlled loading enabled to capture of the snap-back post-peak behavior (i.e., figure 6.10), which provides a reasonable estimation of total strain energy stored at the peak load and energy dissipated in the post-peak regime. However, this approach is still somehow qualitative as far as analyzing snap-back response and linking it with the rock's burst potential is concerned.

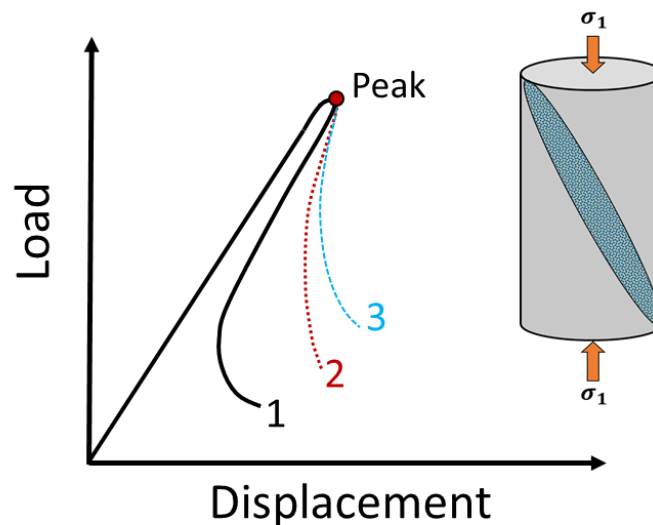


Figure 6.10: Burst estimation: lateral strain-controlled UCS test (snap-back)

For instance, figure 6.10 presents three different cases of post-peak behavior where rock type-1 demonstrates the maximum snap-back, while rock type-3 the minimum. Thus, it would be easier to differentiate the burst potential between rock types 1 and 3, however, not in 2 and 3 or even more close cases. It highlights the requirement of a reliable scale to measure the magnitude of snap-back in quantitative terms and differentiate between burst potentials of different rocks in a precise manner.

In this view, chapter-3 provides an efficient basis for snap-back quantification via the snap-back factor ($\$$) using energy principles. This chapter presented its application using AUSBIT experimentation. Figure 6.11 illustrates the application of AUSBIT and the estimation of $\$$ in three rock types, including sandstone, Iranian granite, and Bluestone. It shows that Bluestone rock is the most brittle and hard rock type with the highest $\$$ magnitude. Table 3.4 in chapter-3 validates these indications. Thus, $\$$ made it possible to quantify any possible snap-back response and differentiate between the close cases with

similar trends, i.e., sandstone and Iranian rock in figure 6.11 or cases 2 and 3 in figure 6.10. However, linking this snap-back magnitude with burst potential in quantitative terms requires further attention. The prime reason behind this is loading conditions, which in the above sets of experiments (i.e., lateral strain-controlled uniaxial compression and AUSBIT) are nowhere close to the actual in-situ conditions where strain burst occurs.

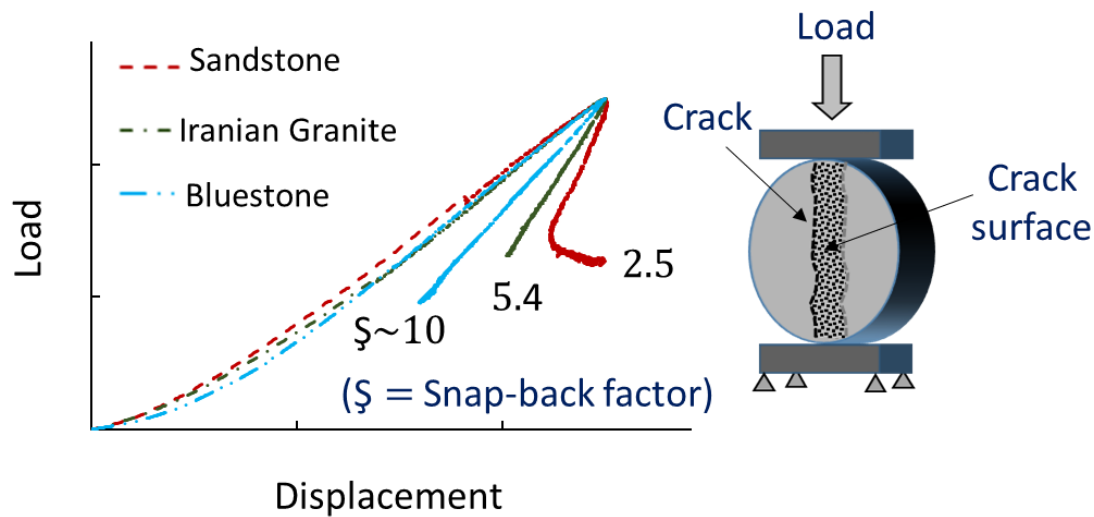


Figure 6.11: AUSBIT - Snap back estimation

In this view, the proposed approach in this chapter provides a theoretical basis using strain energy evolution principles to depict not only the possibility but also the scale of bursting via strain burst potential index (\mathcal{P}), i.e., eq.6.6. This study obtains the proposed strain burst index (\mathcal{P}) by collaborating the critical material parameters (i.e., including elastic, strength, and fracture properties) with the in-situ stress conditions via a well-defined theoretical framework. It is a much-needed development in the strain burst studies. It ensures the prediction reliability in different rock types under any given loading conditions. Figure 6.11 illustrates this aspect and presents the variation in the burst potential for the three loading cases used in section 6.3.

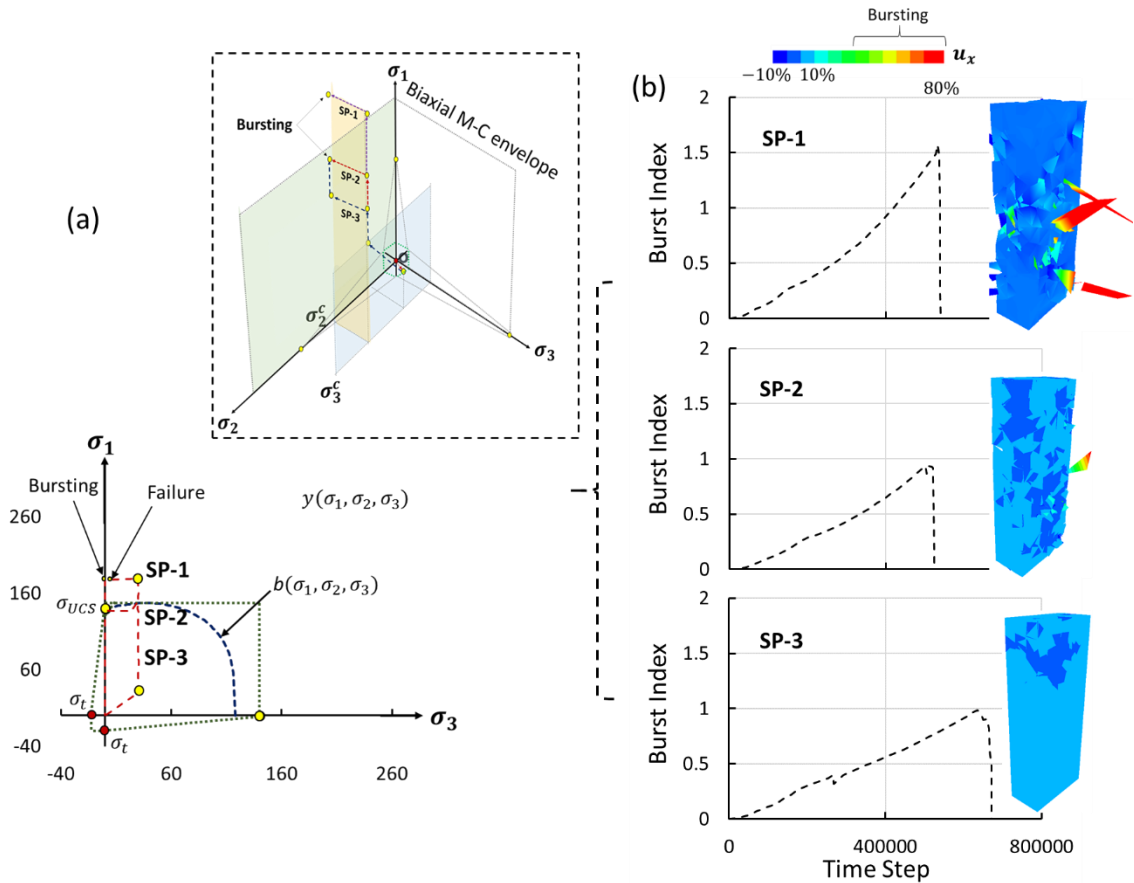


Figure 6.12: Strain burst index (\mathbb{P})

In figure 6.12, the stress path-1 acquires the maximum burst tendency of burst index $\sim 1.5 \mathbb{P}$, whereas $\sim 1 \mathbb{P}$ for the remaining two cases. It demonstrates that the bursting magnitude in the case of stress-path-1 is 50% higher than the remaining two cases, which can be cross-verified from the fragmentation patterns of the above three cases. The displacement contours also show that the number of blocks undergoing bursting deformation with u_x displacement ($>10\%$) is relatively higher than the case-I. The proposed framework also allows us to evaluate the bursting potential under any given loading-unloading conditions, thus has applicability to study other strain burst types. For instance, stress-path-1, along with the proposed framework, can be used to test the possibility of instantaneous strain burst. Similarly, one can analyze the occurrence of pillar burst by inducing a gradual increase in σ_1 stress along with a reduction in σ_3 i.e., like the formation of pillar during the excavation in deep underground mining. For delayed burst, one needs to incorporated loading unloading condition changes of increasing both σ_1 and σ_2 components with a reduction in σ_3 component over time.

Furthermore, one can estimate the burst scale using the \mathbb{P} index in each case of strain burst type. It provides a reliable quantitative basis to measure the magnitude of the burst.

6.5 Effect of material properties and confining pressure on burst potential

Several factors affect the burst potential of rock. In this view, figure 6.13 presents the influence of crucial material properties including fracture energy (G_f) and elastic modulus (E) on the rock's burst potential (\mathbb{P}) at different peak stress levels in quantitative terms. It incorporates the effect of peak in-situ maximum stress (i.e., σ_1), keeping the other stress components constant (i.e., $\sigma_2 \sim 60, \sigma_3 \sim 30$), on the overall burst potential variations. The geometrical aspects of the test specimen are also kept constant in this illustration. Here, elastic modulus indicates the effects of rock's stiffness (under any given stress level) on the overall strain energy storing capacity. The G_f indicates the strain energy dissipation property of rock. One should note here that this study considers mode-1 fracture energy into consideration, which is a reasonable simplification to overcome the requirement of a wide range of experimental data from rock testing under different modes of loading conditions, as described in section 6.3.1 as well.

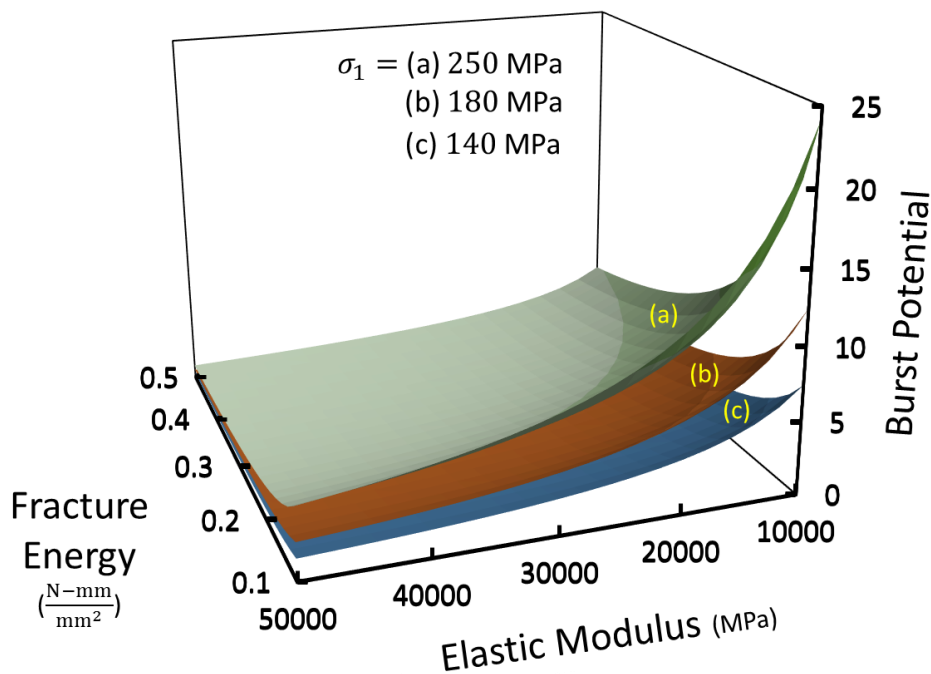


Figure 6.13: Effect of material properties on the Burst potential

Figure 6.13 illustrates that for any fixed magnitude of E , the overall \mathbb{P} reduces with increase in G_f . It shows that the increase in G_f enhances the strain energy dissipation ability of rock, thus, reduces the stored strain energy component available to cause burst failure. Consequently, the burst potential of rock measured via \mathbb{P} index reduces. One can observe the similar trend of \mathbb{P} reduction with increase in E for the fixed magnitude of peak in-situ stress (σ_1). It is because at any give stress level, stiffer rock with higher E deforms less, thus stores relatively smaller elastic strain energy, as shown in eq. 6.4 as well, consequently reduces the \mathbb{P} magnitude. Additionally, the increase in maximum in-situ stress (i.e., σ_1) for the given rock indicates increased deformation; thus, higher elastic strain energy storage to increase possibility and scale of burst failure. One can quantify this burst tendency and corresponding scale via \mathbb{P} magnitude. Nevertheless, this effect of σ_1 on the \mathbb{P} also varies with material type, i.e., rock with smaller G_f experience a significantly higher increase in \mathbb{P} with the increase in σ_1 . Whereas, the rock with very high G_f experience negligible increase in \mathbb{P} with the increase in σ_1 . It shows that the rock's fracture properties are relatively more significant to govern rock's burst potential in comparison to the in-situ stress conditions.

6.6 Effect of geometrical aspect on burst potential

Apart from the material properties and in-situ stress-state, the geometrical aspect of the test specimen also influences the rock's burst potential. The specimen geometry has two key facets: aspect ratio (i.e., H/B) and specimen size.

6.6.1 Effect of aspect ratio on burst potential

The behavior of rock varies with the aspect ratio of the test specimen. It is a common observation in the uniaxial compression test. Few researchers reported such observations in strain burst experiments as well, where specimen's height/width (H/W) ratio affects the burst characteristics of rock (Tuncay and Hasancebi 2009; Li et al. 2011; Zhao and Cai 2015). In this view, the proposed conceptual framework is competent in not only demonstrating but also explaining such observations, thanks to its energy-based formulations. To further elaborate on this, figure 6.14 presents the evolution of burst surface in two dimensional ($\sigma_1 - \sigma_3$) stress space with the specimen aspect ratio (or H/W) for Bluestone rock type.

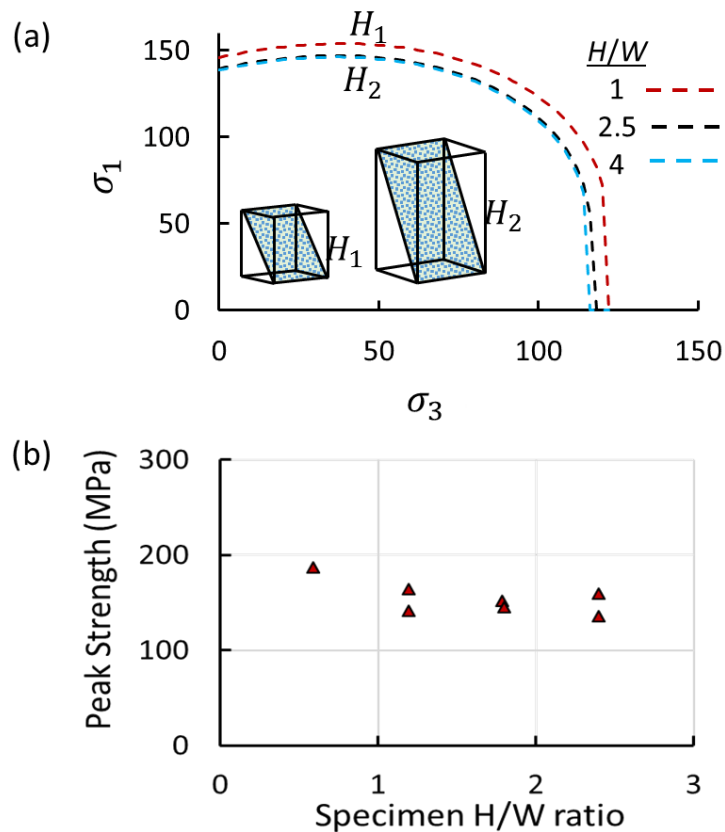


Figure 6.14: Effect of specimen dimension on burst envelope size, (b) size effect on Tianhu granite (Zhao and Cai 2015)

The proposed burst envelope shrinks with an increase in aspect ratio (H/W). It indicates that specimens with a smaller aspect ratio require relatively higher strain energy via external work done to undergo burst failure. In order to validate the above observations, this study performs a few more virtual strain burst experiments on test specimens with different heights. Loading scheme is similar to the section 6.2.2.4 (i.e., sr. no. 3 in table 6.1). Figure 6.15 presents a summary of the above results.

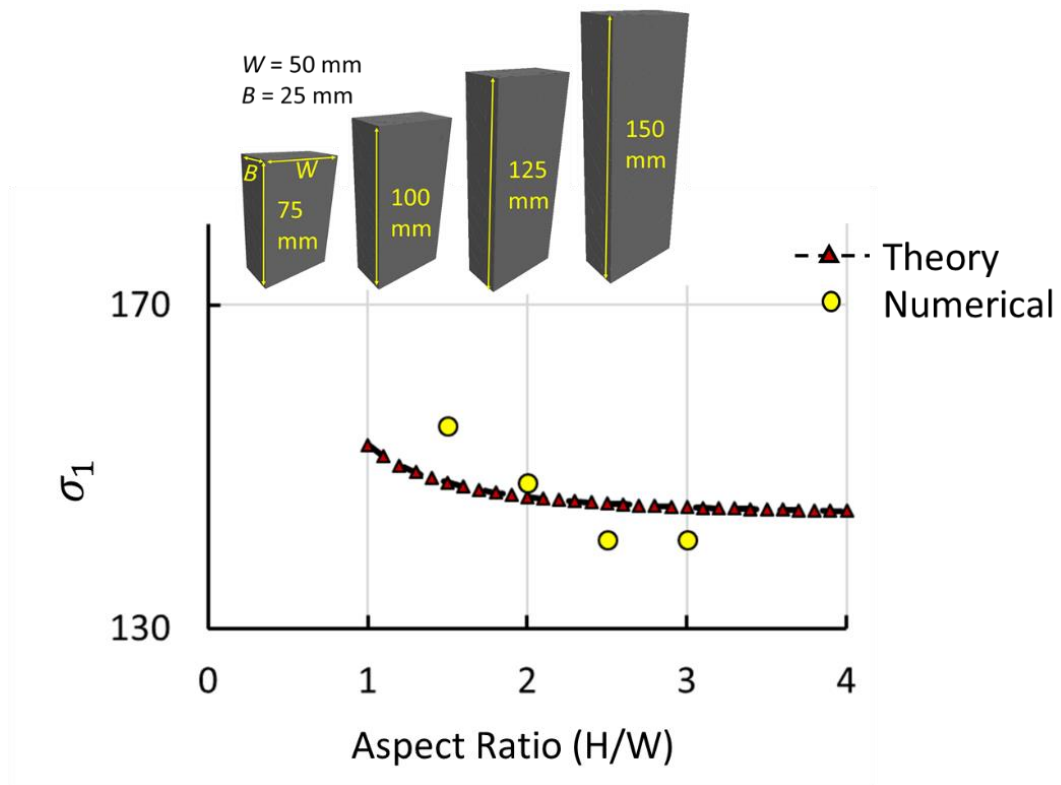


Figure 6.15: Aspect ratio effect: Validation

Figure 6.15, demonstrates a reasonable agreement between the results from the virtual strain burst experiments and the theoretical predictions. It shows that the peak load required to cause burst failure gradually decreases with an aspect ratio (H/W) varying from 1 to 2. It eventually diminishes to negligible with further increment in aspect ratio to 2 or 2.5 onwards.

One can attribute these above observations to the end effect phenomenon induced by infinitely stiff loading platens. It is challenging to eliminate irrespective of what measure one could take in the laboratory (for instance, using lubricant in between loading platen and specimen etcetera.) or in virtual/numerical experiments. In fact, in all the presented virtual experiments, friction between loading platens and virtual samples is zero. Despite this, it was not possible to eliminate the end effect in the specimen with a smaller aspect ratio ($H/W < 2$). This end effect is a well-accepted phenomenon in uniaxial compression tests, which eventually became one of the prime reasons for ISRM and ASTM to recommend specimen aspect ratio (i.e., H/D in the cylindrical specimen) in the range between 2 to 3 (ASTM 1994, 2000; ISRM 2007). It further explains the common observation of higher load requirement to cause bursting in a specimen with a smaller dimension, as shown in figure 6.13 (b) (Tuncay and Hasancebi 2009; Li et al. 2011; Zhao

and Cai 2015). It also explains the common observation of more violent strain burst in a specimen with a smaller H/W ratio comparatively (Zhao and Cai 2015).

Similarly, one can also evaluate the effect of the H/B ratio on the overall burst potential. In this view, figure 6.16 presents the evolution of burst potential with a variety of factors including peak stress (σ_1) and fracture energy along with the specimen aspect ratio (H/B) ratio.

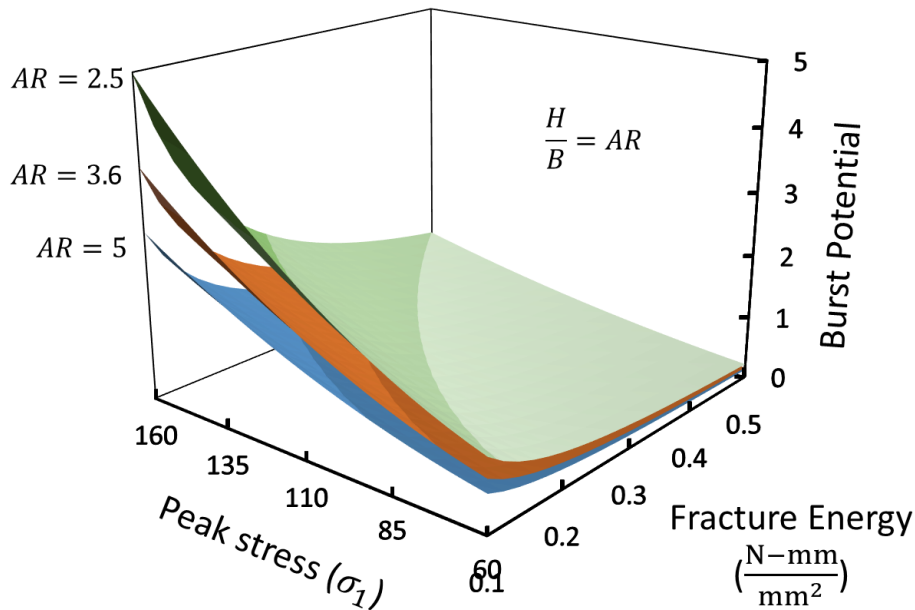


Figure 6.16: Aspect ratio (H/B) effect along with fracture energy and peak stress

The above result shows that, similar to the in-situ σ_1 , the effect of specimen aspect ratio on the overall burst potential (\mathbb{P}) diminishes with the increase in fracture energy. Thus, rock type with relatively higher fracture energy is less likely to undergo burst failure (or with smaller burst magnitude) irrespective of the in-situ stress state and specimen aspect ratio.

6.6.2 Effect of specimen size on burst potential

Similarly, figure 6.17 highlights the importance of specimen size on the overall burst potential. It shows that for any given fracture properties and maximum principal stress, the burst potential of rock (i.e., \mathbb{P}) increases with an increase in specimen size, i.e., keeping the specimen's aspect ratios ($H/B \sim 5$ and $H/W \sim 2.5$) constant.

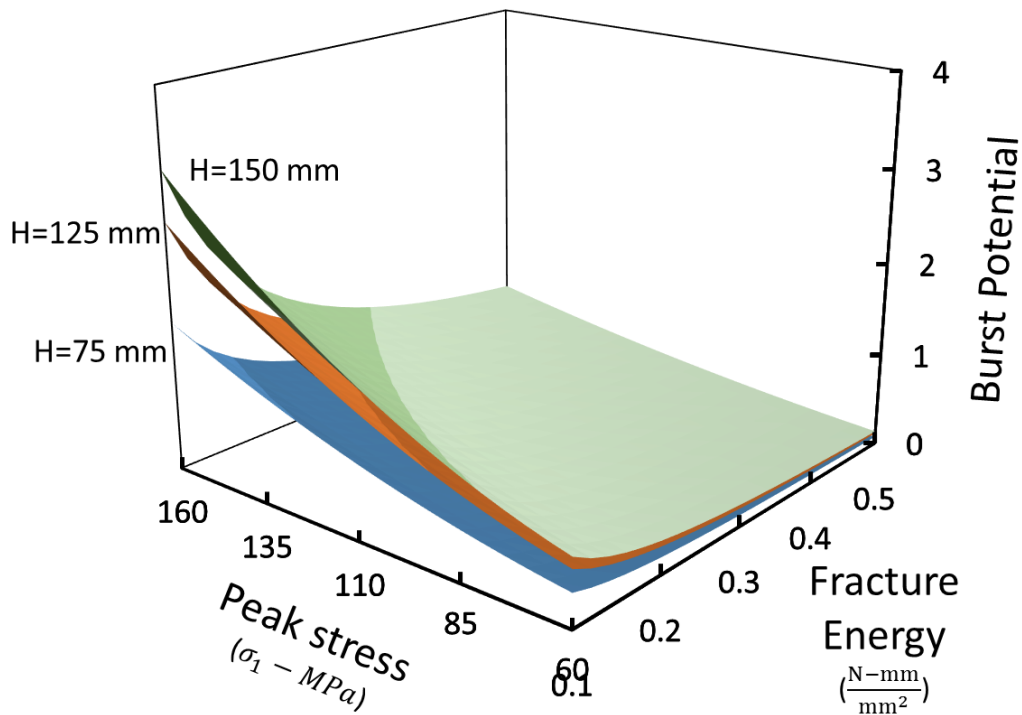


Figure 6.17: Effect of specimen size on the Burst potential

It is because, as we decrease the specimen size, the elastic strain energy stored in the specimen volume at any given stress state decreases. Fracture energy requirement for causing structural failure also reduces but with a lower rate comparatively, i.e., depending upon the fracture surface, as shown in eq. 6.6. In other words, the strain energy storage scales with volume while dissipation due to fracture scales with the surface area. As a result of this pronounced effect of specimen size on the strain energy storing capacity comparatively, the peak load required to cause burst failure also increase. Overall, it enhances the burst potential measured via the P index.

In conclusion, one can observe that the developed energy-based framework is competent in measuring the burst potential of any given rock in quantifiable terms. Also, it explains the critical observations on the effect of material, applied stress state, and specimen geometrical aspects (i.e., including specimen aspect ratio and size) on the overall burst potential. Thus, it provides an effective means to measure the magnitude and analyze the potential reasons behind the burst occurrence.

6.7 Strain burst: the big picture

Theoretical framework development in this chapter enables us to link the critical material, geometrical and in-situ factors with rock's burst potential inside rock mass. To provide a brief overview, we again go back to our conceptual picture of the in-situ strain burst, as presented in section 2.2, chapter-2. Figure 6.18 collaborates this conceptual picture with essential burst controlling factors.

It shows that the burst potential of rock around the underground opening depends upon material properties, in-situ stresses, boundary conditions, and geometrical aspects. In terms of material, this study highlights the role of following fundamental properties, i.e., strength (i.e. σ_{ucs}, σ_t), elastic (i.e., E, ν) and fracture (G_f) properties. The strength and elastic properties signify the strain energy storing characteristics of the rock. While fracture properties indicate its energy dissipation characteristics. Rock with higher energy storing and lower dissipation characteristics (i.e., bigger burst envelope if we keep the specimen geometry constant) signifies higher strain energy availability than its fracture requirement. Thus, such type of rock exhibits higher snap back behavior in controlled laboratory experiments (i.e., chapter-3, AUSBIT approach) and bursting tendency in in-situ conditions, as shown in figure 6.18. The proposed framework further links this material factor with in-situ conditions. It explains the common observation of increasing bursting tendency with mining depth in quantitative terms using a well developed systematic energy-based theoretical framework. The potential of burst increases in rock with comparatively lower fracture energy, situated in deeper underground locations, as shown in figure 6.18. Similarly, one can also link the burst potential of rock with other material properties, including elastic modulus and poisson's ratio, in quantitative terms.

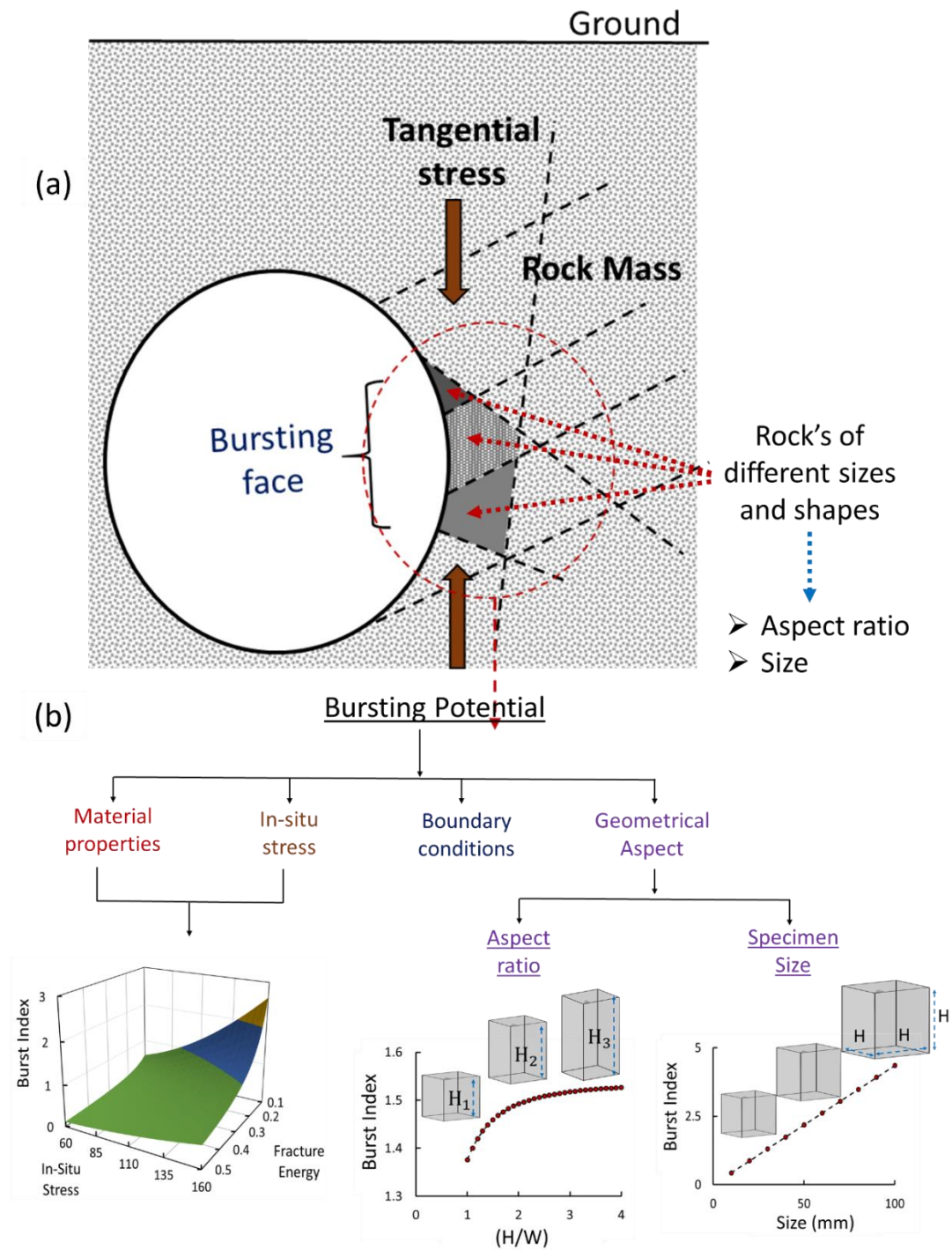


Figure 6.18: (a) Strain burst: Big picture, (b) theoretical link with bursting potential

The other important aspect is the scale dependency of rockburst potential, which has not been addressed adequately in the available literature. The developed theoretical framework is competent in capturing this aspect. To further elaborate this, figure 6.15a shows that rocks inside rock mass are generally in a fractured state with different shapes and sizes. Therefore, one can divide the geometrical aspect into aspect ratio and specimen

size. The variations in the shapes of rocks indicate the variations in aspect ratio. On the other hand, change in specimen size irrespective of aspect ratio is another facet of geometrical influence, which is comparatively more prominent, as shown in figure 6.18(b). This size dependency of burst potential indicates that the burst in the rock inside rock mass is rock's behavioral aspect, which depends upon the total energy stored and the fracture requirement. If rocks around the underground opening are relatively less fractured with bigger sizes, then such rock may have higher energy storage. Consequently, a higher burst index (figure 6.18b), and a higher possibility of strain burst occurrence. This effect of the geometrical aspect can further be quantified in terms of burst potential, thanks to developed size-dependent energy-based strain burst criterion. On the contrary, material characteristics are invariant of size or dimension-independent. We usually evaluate it in terms of strain energy density. These two aspects (i.e., material properties and geometrical aspect) along with in-situ stress state and boundary condition changes, control the overall strain burst mechanism in deep underground conditions. It forms the basis of the energy-based proposed framework for burst predictions.

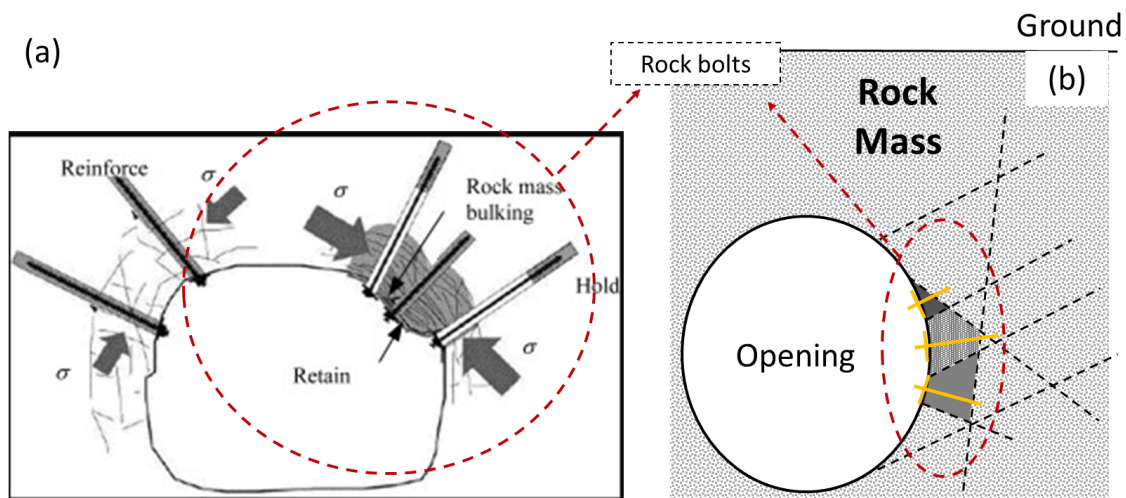


Figure 6.19: Rock bolts - rockburst support system (a) (Kaiser and Cai 2012b), (b) conceptual representation

One can further link all these observations with the functioning of a commonly used rock support system, for instance, rock bolts, as shown in figure 6.19. Kaiser and Cai (2020) stated that no model exists which can thoroughly explain the functioning of rock support systems (Kaiser and Cai 2012b). In this view, the present study could provide valuable insights. When rock bolts or similar support system applies to rock around the opening, these bars/bolts pierce into rock pieces inside rock mass. Consequently, it not

only releases the localized in-situ stresses (i.e., in-situ stress aspect in figure 6.18) but also breaks rocks into smaller sizes and dimensions with smaller aspect ratios. Furthermore, as the geometrical aspects of rock inside rock mass reduces, its burst potential (i.e., can be quantified by the proposed bursting index) also reduces. Consequently, it reduces the stored energy and thus the burst potential making rock bolts effective in retaining rock mass and prevents strain burst occurrence, as shown in figure 6.19(b).

6.8 Conclusions

This chapter proposed an energy-based theoretical framework for strain burst prediction, which enables us to estimate the magnitude/scale of the potential burst. The application and validation of the developed framework illustrated using the Bluestone rock type as an example. This study obtains the required parameters, i.e., strength, elastic, and fracture properties, from unconventional laboratory experiments, including lateral strain-controlled uniaxial compression and AUSBIT (recently patented) indirect tensile strength testing methodology. Details of these experimentation and result analyses have already presented in chapters 3, 4, and 5. Additionally, this study uses the hybrid numerical modeling tool 3DEC-Itasca with a newly developed and implemented cohesive contact model (i.e., details presented in chapter-5) to illustrate and validate the proposed energy-based strain burst framework via virtual strain burst experiments.

Results obtained from the above virtual experiments are in good agreement with the theoretical predictions. It verifies the proposed theoretical framework. This framework further demonstrates that the variation in boundary conditions plays an essential role in burst occurrence. It also shows that burst in deep underground mine condition occurs if the resultant stress state after excavation lies outside the burst envelope developed based on strain energy storing and dissipating characteristics. Furthermore, this study utilizes the above framework to evaluate the scale of bursting under different loading conditions and provides explanations for the key observations, including the increase in peak load and burst scale with the decrease in specimen size. The effect of material properties, including elastic modulus and fracture energy, evaluated using the energy-based strain burst criterion. It also evaluates the influence of specimen's geometrical aspects, including specimen size and aspect ratio on the overall burst potential. These critical aspects of the proposed energy-based framework helped in explaining several laboratory observations

of strain-burst experiments. At last, this chapter successfully links these key laboratory-scale observations with the big picture of in-situ conditions where, in-actual, strain burst incidents occur. This linkage provided a brief explanation of rock-bolts rockburst support system functioning to control or possibly prevent the occurrence of strain-burst in deep underground conditions.

Chapter 7

Conclusions and Future Work

7.1 Summary and Conclusions

“If you want to explore the secrets of the universe, think in terms of energy, frequency, and vibrations”- Nikola Tesla. ‘Energy’ as a concept is undoubtedly a robust tool that can describe everything starting from laboratory scale rock deformation to field-scale deep underground bursting. It forms the basis of the present study, as well. This study aimed to develop a systematic approach to link the energy storage characteristics and dissipation capacity of the materials (i.e., experimentally determined), with the bursting potential of rock. It underpins the larger scale bursting behavior of rock mass around deep underground mine/tunnel openings.

The first objective of this study was to understand the fundamental mechanism of rock deformation and failure. It helped in the assessment of the energy evolution mechanism in rock and identified the critical energy parameters controlling strain energy evolution and typical stress-strain response. For this purpose, this study devised a novel experimentation methodology to investigate and determine the true material properties (tensile strength and fracture energy). It utilized a more straightforward configuration of circular disc based on an indirect tensile testing approach, where the macro dynamic effects removed or minimized for better estimation of intrinsic material properties. It enabled us to quantify the critical fracture properties controlling the energy dissipation characteristics and helped in acquiring a preliminary overview of target rock’s bursting potential. Parallely, this study also developed a hybrid (i.e., continuum-disc-continuum based) numerical modeling approach with the intent to prepare a strong base for determining the link between the more straightforward energy parameters obtained from the laboratory experiments and the bursting potential of rock. In this pursuit, this research makes the following essential contribution:

- ◆ Development of a novel experimental approach to control the dynamics associated with sudden cracking of circular disc sample under diametrical compression, commonly used in indirect tensile strength experiments, including Brazilian disc

tests. The key benefit of this invented methodology is to acquire fracture, elastic, brittleness, and tensile strength properties simultaneously from one simple circular disc test. To the best of author's knowledge, it was not possible before. Consequently, the devised methodology was also patented in Australia as an Innovation Patent under IP Australia. Chapter-3 presented the experimental details and in-depth analysis of the results.

- ◆ Development of a comprehensive approach for analysis of data obtained from advanced experimental approaches, including Digital Image Correlation (DIC) and Acoustic Emission (AE) techniques. It enables us to acquire local scale deformational behavior with the sample scale load-displacement response. Chapter-4 presented a detailed discussion about the principles, methodology, and application of DIC and AE techniques.
- ◆ Development of a hybrid numerical modeling approach that can mimic the realistic rock material behavior at both global and local scales. Numerical modeling tool 3DEC-Itasca was adopted for this purpose. This study also developed a new cohesive contact model to capture the inter-granular cohesive bonding naturally. Chapter-5 presented a detailed discussion about the development, verification, implementation, validation, and applications of the proposed cohesive contact model.
- ◆ Development of a size-dependent energy-based theoretical framework to evaluate the bursting potential of rock specimens under true triaxial loading-unloading conditions. A novel concept of size-dependent and energy-based 'burst envelope' was proposed. It allows us to identify the key parameters affecting the bursting potential of rock. This framework enabled us to link the laboratory scale energy parameters with the bursting potential of the rock mass, utilizing the size, dissipation capacity, and stress conditions of the intact rock bounded by the discontinuities. Chapter-6 presented the details regarding this contribution.

The subsequent section presents a brief discussion about the contributions mentioned above and the key findings of the presented research.

7.1.1 AUSBIT – Adelaide University Snap Back Indirect Tensile Testing approach

The first step towards bursting potential evaluation is to analyze the elastic strain energy-storing/dissipation characteristics of rock on a preliminary basis. After that,

determine essential material parameters related to strength, elastic, and fracture properties as input for the subsequent numerical applications to conduct a thorough analysis of rock's bursting potential. For this purpose, this study developed a new indirect tensile testing methodology named 'AUSBIT,' i.e., Adelaide University Snap-Back Indirect Tensile Testing. AUSBIT enabled to control and exclude the dynamics associated with sudden cracking of disc sample under diametrical compression. It is a challenging task and has never been done before (to the best of our knowledge), especially in simple circular shaped discs where cracking occurs abruptly in a split second-time frame window, e.g., Brazilian disc test. The developed methodology uses lateral deformation as feedback to control the overall axial loading rate. Pairs of the 3D printed plastic holder (or 'holder') designed to carry the Linear Variable Differential Transformer (LVDT) laterally across the sample. Lateral strain feedback coupled with servo-control of the MTS loading frame. All instrumentations fabricated in the School of Civil, Environmental and Mining Engineering at the University of Adelaide. Experiments conducted successfully on circular discs of different rock types with varying dimensions, and results were analyzed to prove the expected performance of the developed methodology.

The immediate benefit of this newly developed methodology is to capture the 'Snap-Back' behavior under an indirect tensile testing framework. It is a much-needed aspect of typical load-displacement response providing an excellent insight to strain energy storage and dissipation characteristics. It also provides useful understandings of strain energy requirements for diametrical cracking and additional energy available at peak load, which, in principle, controls the dynamics associated with sudden cracking in conventional Brazilian disc test. This feature of the developed methodology and obtained results assist in the efficient measurement of intrinsic fracture properties, including fracture energy and toughness of the target rock. Delayed cracking enabled the efficient applications of advanced experimental techniques like Digital Image Correlation (DIC) to obtain material properties at the local scale. Material brittleness and elastic property evaluation are other potential applications of the developed methodology. This study also developed a size-dependent energy-based theoretical framework delineating snapback (S) magnitude, i.e., an indication of bursting potential in the Brazilian disc test. Predictions made using this snapback theoretical framework are in good agreement with experimental data. Determining all such fundamental material properties from a straightforward

experiment is commendable. It further reflects the importance of energy viewpoint as the prime basis for the development of new experimental approaches.

The experiments with snapback indicator \mathcal{S} revealed that the ratio between strain energy stored at peak load and fracture energy required to separate the disc specimen is three times higher in Bluestone rock compared to Hawkesbury sandstone. Therefore, on a preliminary basis, it revealed that Bluestone rock would have a higher tendency to burst under deep conditions. This size-dependent and energy-based snapback indicator \mathcal{S} , formulated based on Brazilian disc tests, is the basis for the establishment of a more general bursting criterion for rock specimens under true triaxial conditions with loading-unloading paths reflecting the effects of underground openings. They all will form a strong base for future investigations towards practical applications in assessing burst potentials of large discontinuous rock masses.

7.1.2 Strength parameter determination from local-scale responses using DIC and AE techniques

This study collaborated the advanced instrumentation, including DIC and AE, with AUSBIT and conventional Brazilian disc experimentations to derive required strength properties quantitatively based on local scale response under a controlled cracking environment. The role of induced dynamics at a local scale in conventional Brazilian disc tests highlights the significance of delayed cracking in AUSBIT. It enabled the determination of local scale material strength (i.e., tensile strength in this case) properties efficiently. The tensile strength determined from local-scale responses observed to be closer to uniaxial strength as compare to indirect tensile strength obtained from conventional Brazilian disc formulation. It provides an efficient alternative to the traditional approach based on peak load measurement from the load-displacement response.

The other potential application of this data analysis approach is to evaluate the link between local-scale dynamics and sample scale AE responses. It demonstrated that sample scale AE events generated were not due to cracking explicitly but due to dynamics associated with the cracking. In a controlled environment, the same rock type sample with similar fracture properties produced entirely different (i.e., of low magnitude) AE events as compared to what generated in an uncontrolled (or conventional) Brazilian disc test approach. This facet is essential for conventional AE application-based approaches,

which usually aim to determine the material damage due to energy dissipation based on AE data analysis primarily. This study considers Hawkesbury sandstone rock for illustration, later extended to the Bluestone rock type. It helped in the finalization of the tensile strength parameter, which eventually used as an input for numerical simulations for bursting potential analysis.

7.1.3 Dis-continuum based numerical modeling development

An essential step towards burst potential evaluation was to develop a numerical modeling framework that can efficiently capture the rock material behavior under any given loading conditions at both local and global scales. Such a robust numerical modeling setup would provide a reliable base to conduct virtual strain burst experiments and explore the bursting aspect of rock. For this purpose, this study develops a hybrid (Discrete-Finite Element) numerical modeling approach for simulating rock fracture and fragmentation using the 3DEC-Itsaca tool. It considers the rock as an aggregate of deformable tetrahedral continuum blocks (i.e., as grain aggregates). Inter-block contacts mimic the rock's inter-granular cohesive bonding, which, in principle, control the overall strength and fracturing behavior. For this purpose, a new cohesive contact model based on elastoplastic-damage coupling was developed and implemented in 3DEC-Itasca. The functioning of the proposed cohesive model verified thoroughly under different loading conditions, including mode-I (or tension), mode-II (or shear), and mixed-mode, and validated against experimental data available in the literature.

After that, laboratory experiments, including uniaxial compression (UCS) tests and conventional Brazilian disc (BD) tests, were performed on Bluestone rock to obtain an excellent experimental data set for calibration and validation purposes. DIC technique used to obtain the full strain evolution for an additional layer of validation, i.e., the double scale validation that includes both macro responses of the specimen and lower scale evolution of strain during localization before complete fracture. It ensures the reliability of the developed numerical modeling framework. Further, experimental data from the UCS test used to calibrate the above developed hybrid numerical modeling framework. This numerical modeling setup utilized the experimentally determined elastic properties (i.e., for continuum elements) and tensile strength parameter (i.e., for contacts) from experiments as input. The experimental stress-strain response used to calibrate the remaining parameters. Overall the results of this numerical simulation are in good

agreement with experimental observations both at local and sample scales. It provides a good insight into the localization mechanism in the cylindrical specimen of Bluestone rock under uniaxial compression. This developed numerical modeling framework was then further extended to simulate a conventional Brazilian disc test. The results of this virtual experiment are also in good agreement with the experimental observations at different scales. Overall, it indicated the reliability of the numerical modeling suit to further extend its applications for analyzing the burst mechanism in rock.

7.1.4 A size-dependent energy-based rockburst criterion

At last, this study formulates and verifies a novel burst potential criterion based on the experimental and numerical developments in the previous chapters. For efficient utilization of the above-developed resources, this study develops a robust theoretical framework based on energy principles. This development resulted in the proposal of the concept of a size-dependent and energy-based burst potential. The resulting burst envelope is a three-dimensional surface in principal stress space derived from energy storing and dissipation characteristics of the rock, taking into account the effect of specimen size. This burst envelope used along with the material yield/failure surface in three-dimensional principal stress space forms the overall conceptual basis of the proposed energy-based framework. It provides a clear picture of strain energy evolution concerning the specimen's bursting potential. This study also proposes a scalar bursting index (\mathcal{P}) to estimate the bursting scale in quantitative terms.

Bluestone rock and its properties were used as an example to illustrate and validate the potential applications of the above size-dependent energy-based bursting framework. Burst envelope for Bluestone rock specimen with predefined dimensions was determined using the elastic, strength, and fracture properties rock already obtained in previous experiments, including UCS and AUSBIT. The Mohr-Columb yield criterion used along with the burst envelope for burst prediction in the Bluestone rock. After that, a hybrid numerical modeling tool, i.e., 3DEC-Itasca, developed in the previous chapters, used to conduct virtual strain burst experiments. Different stress-paths for burst envelope and yield surfaces tested for bursting failure upon unloading in minor principal stress direction, i.e., like deep in-situ conditions where actual strain burst occurs.

Burst predictions and corresponding magnitude (i.e., using busting index \mathcal{P}) obtained from the proposed theory are in good agreement with the observations from virtual

experiments. The effect of the specimen's aspect ratio on overall bursting potential evaluated, which demonstrated good agreement with the theoretical predictions and virtual experiments. Also, the snapback behavior observed in ASUBIT (quantified as snapback factor ξ) and lateral strain-controlled UCS experiments linked with the proposed energy-based framework. Following is the summary of the overall results from the virtual bursting experiments:

- ◆ Variation in boundary conditions plays a more critical role in causing burst failure as compared to the in-situ stress state.
- ◆ Bursting (or strain-burst) in deep underground condition occurs only if the resultant stress state of rock around the potential opening is outside the burst envelope after excavation.
- ◆ Specimens with smaller aspect ratios may need a higher load to cause bursting failure.
- ◆ Peak load requirement for the burst in a specimen with a fixed aspect ratio reduces with an increase in specimen size.
- ◆ The magnitude of burst reduces with an increase in material fracture energy.

These conclusions from the proposed theoretical framework explained key observations in many strain burst experiments reported in the literature. At last, a bigger picture presented to clarify the link between the proposed theoretical conclusions made by the energy-based burst criterion, observations from virtual strain burst experiments, effect of specimen size and aspect ratio, all with the actual in-situ bursting potential of rock in discontinuous rock masses around an underground opening.

7.2 Areas of improvement and recommendations for future work

This research presents a comprehensive approach to evaluate strain energy storing and dissipation characteristics of rock at a laboratory scale and systematically link it with the real in-situ strain-burst potential in deep underground conditions. It is a much-needed requirement in rockburst studies. Results obtained are promising and in good agreement with experimental and numerical data, as well as our expectations. Nevertheless, there have been several simplifying assumptions made during the developments to make a complex theoretical problem practically feasible. Following are the few areas of improvement identified to provide future directions to the research on rockburst:

- ◆ The developed AUSBIT methodology tested on different rock types, including Hawkesbury sandstone, Iranian granite, Bluestone, and concrete (Hon et al. 2018). Considering the promising results obtained from the above analysis, it would be better to further extend the AUSBIT to other brittle rock material types, including glass, ceramic, metals, and even in pharmaceuticals, for instance, tablets. The successful tests on plain concrete have already reported; further investigations on fiber reinforced concrete have also been planned and will be executed next year in Adelaide (Duan et al. 2019). All these areas do use a Brazilian disc test. The mechanism of controlling fracture would be exciting and useful in other fields as well.
- ◆ The current application of AUSBIT in the present research was limited to the Brazilian disc test mainly. It can/should be extended to other indirect tensile testing approaches as well. For instance, in the case of a ring test where tension induced cracks emerge in a relatively gradual manner at the surface of the inner hole, the application of controlled cracking using AUSBIT along with DIC and AE combination would be exciting and beneficial. It may provide further improvement in the local (grain) scale material behavior analysis.
- ◆ The snapback feature of the load-displacement response from AUSBIT can be further used to explore the brittleness index of the different rock. Present work provides a brief overview of this application, which can/should be further explored in different rock or other brittle material types.
- ◆ The presented energy-based size-dependent burst criterion provides a robust approach to evaluate the burst mechanism in a rock under deep underground conditions. However, the following are few assumptions made which future studies can address:
 - (a) Investigate the fracture energy mode transition in uniaxial and true-triaxial experiments as mentioned chapter-6.
 - (b) Determine more quantitative burst indicator in numerical simulation. Presently this research assumes 10% of the maximum displacement, which works well to ensure bursting failure. However, it still requires further improvement to make this scale more quantitative.
 - (c) Reduce the tetrahedral block sizes in strain burst numerical simulation to analyze the fracturing pattern as well during bursting failure.

- ◆ The present study uses two sets of strength parameters to approximate the yield surface. Future studies can improvise it by conducting more laboratory experiments on the same rock under different loading conditions, including biaxial tension, biaxial compression, triaxial compression, and true triaxial compression. It would provide more data points in the three-dimensional principal stress plane and thus more accurate estimation of yield/failure surface.
- ◆ The number of stress paths in virtual true triaxial experiments can be further increased to test more cases of loading-unloading and further investigate the bursting potential.
- ◆ At last, full-field numerical simulation of actual mine/tunnel under deep underground with the same rock type can/should also be done. This process may require parameter transformation from intact rock (as used in laboratory-scale simulations) to rock mass (found in actual underground conditions). One can use Evert Brown's GSI system for this purpose. It would further validate the observations and conclusions from the laboratory scale investigations made in this study.
- ◆ Extension of the presented approach to other rock types and also coal would always be encouraged. It would not only test the functioning of the presented approach in different conditions but also open the possibility of further improvements.

Future work in the highlighted direction will further enhance the robustness of the presented approach and its prospective applications in the field of deep underground exploration.

References

- A NS, Kataka.a M, Mileva A, B ES (2006) Remnant Mining in South African Gold Mines. In: Deep and High Stress Mining
- Abshirini M, Soltani N, Marashizadeh P (2016) On the mode i fracture analysis of cracked Brazilian disc using a digital image correlation method. *Opt Lasers Eng* 78:99–105 . doi: 10.1016/j.optlaseng.2015.10.006
- Aggelis DG, Kordatos EZ, Matikas TE (2011a) Acoustic emission for fatigue damage characterization in metal plates. *Mech Res Commun* 38:106–110 . doi: 10.1016/j.mechrescom.2011.01.011
- Aggelis DG, Soulioti D V., Sapouridis N, et al (2011b) Acoustic emission characterization of the fracture process in fibre reinforced concrete. *Constr Build Mater* 25:4126–4131 . doi: 10.1016/j.conbuildmat.2011.04.049
- Al-ajmi AM, Zimmerman RW (2005) Relation between the Mogi and the Coulomb failure criteria. *Int Journal Rock Mech Min Sci* 42:431–439 . doi: 10.1016/j.ijrmms.2004.11.004
- Aliabadian Z, Zhao G-F, Russell AR (2019a) Failure, crack initiation and the tensile strength of transversely isotropic rock using the Brazilian test. *Int J Rock Mech Min Sci* 122:104073 . doi: 10.1016/j.ijrmms.2019.104073
- Aliabadian Z, Zhao GF, Russell AR (2017) An analytical study of failure of transversely isotropic rock discs subjected to various diametrical loading configurations. *Procedia Eng* 191:1194–1202 . doi: 10.1016/j.proeng.2017.05.295
- Aliabadian Z, Zhao GF, Russell AR (2019b) Crack development in transversely isotropic sandstone discs subjected to Brazilian tests observed using digital image correlation. *Int J Rock Mech Min Sci* 119:211–221 . doi: 10.1016/j.ijrmms.2019.04.004
- ASTM (2000) Annual book of ASTM standards. Philadeplhia, PA, USA
- ASTM (1994) Annual book of ASTM standards. Philadeplhia, PA, USA
- Aubertin M, Rgill D, Simon R (1994) On the use of the brittleness index modified (BIM) to estimate the post-peak behavior of rocks. In: 1st North American Rock Mechanics Symposium. American Rocks Mechanics Association, Austin, Texas, pp

- Barenblatt GI (1962) The Mathematical Theory of Equilibrium Cracks in Brittle Fracture. In: Dryden HL, von Kármán T, Kuerti G, et al. (eds). Elsevier, pp 55–129
- Bažant P, Asce F, Caner FC (2005) Microplane model M5 with kinematic and static constraints for concrete fracture and anelasticity . I : Theory. *J Eng Mech* 131:31–40
- Bažant ZP (1996) Analysis of work of fracture method for measuring fracture energy of concrete. *ASCE* 232:23–29
- Bažant ZP, Yu Q (2004) Size Effect in Fracture of Concrete Specimens and Structures : New Problems and Progress. *Fract Mech Concr Struct* 1:153–162
- Belrhiti Y, Dupre JC, Pop O, et al (2017) Combination of Brazilian test and digital image correlation for mechanical characterization of refractory materials. *J Eur Ceram Soc* 37:2285–2293 . doi: 10.1016/j.jeurceramsoc.2016.12.032
- Blake W (1972) Rock-burst mechanics. *Quart Color Sch Mines* 67:1–64
- Bobet A, A.Fakhimi, Johnson S, et al (2009a) Numerical Models in Discontinuum Media: Review of Advances for Rock Mechanics Applications. *J Geotech Geoenvironmental Eng* 135:1547–1561
- Bobet A, Fakhimi A, Johnson S, et al (2009b) Numerical Models in Discontinuous Media: Review of Advances for Rock Mechanics Applications. *J Geotech Geoenvironmental Eng* 135:1547–1561 . doi: 10.1061/(ASCE)GT.1943-5606.0000133
- Brocca M, Bazant ZP (2000) Microplane constitutive model and metal plasticity. *Am Soc Mech Eng* 53:265–281
- Brugada J, Cheng YP, Soga K, Santamarina JC (2010) Discrete element modelling of geomechanical behaviour of methane hydrate soils with pore-filling hydrate distribution. *Granul Matter* 12:517–525 . doi: 10.1007/s10035-010-0210-y
- Byerlee James d (1968) Brittle-ductile transition in rocks. *J Geophys Res* 73:4741–4750
- Cai M (2013) Principles of rock support in burst-prone ground. *Tunn Undergr Sp Technol* 36:46–56 . doi: 10.1016/j.tust.2013.02.003
- Cai M (2016) Prediction and prevention of rockburst in metal mines - A case study of

- Sanshandao gold mine. *J Rock Mech Geotech Eng* 8:204–211 . doi: 10.1016/j.jrmge.2015.11.002
- Cai MÃ (2008) Influence of intermediate principal stress on rock fracturing and strength near excavation boundaries — Insight from numerical modeling. *Int Journal Rock Mech Min Sci* 45:763–772 . doi: 10.1016/j.ijrmms.2007.07.026
- Candamano S, Sgambitterra E, Lamuta C, et al (2019) Graphene nanoplatelets in geopolymeric systems : A new dimension of nanocomposites. *Mater Lett* 236:550–553
- Cao R, Lin H, Cao P (2018a) Strength and failure characteristics of brittle jointed rock-like specimens under uniaxial compression: Digital speckle technology and a particle mechanics approach. *Int J Min Sci Technol* 28:669–677
- Cao R, Lin H, Cao P (2018b) Strength and failure characteristics of brittle jointed rock-like specimens under uniaxial compression: Digital speckle technology and a particle mechanics approach. *Int J Min Sci Technol* 28:669–677 . doi: 10.1016/j.ijmst.2018.02.002
- Castro LAM, Bewick RP, Carter TG (2012) An overview of numerical modelling applied to deep mining. *Innov Numer Model Geomech* 393–414
- C T Nguyen, Nguyen GD, Das A, Bui HH (2017) Constitutive modelling of progressive localised failure in porous sandstones under shearing at high confining pressures. *Int J Rock Mech Min Sci* 93:179–195
- Chang ching s (1990) Strain tensor and deformation for granular material. *J Eng Mech* 116:790–804
- Chang ching s, Liao ching l (1990) Constitutive relation for a particulate medium with the effect of particle rotation. *Int J Solids Struct* 26:437–453
- Chang BCS, Misra A, Acheampong K (1993) Elastoplastic deformation for particulates with frictional contacts. *J Eng Mech* 118:1692–1707
- Chang CS (1993) Micromechanical modeling of deformation and failure for granulates with frictional contacts. *Mech Mater* 16:13–24
- Chen WF, Han DJ (1988) *Plasticity for Structural Engineers*. Springer, New York Inc.

- Cheng YP, Bolton MD, Nakata Y (2004) Crushing and plastic deformation of soils simulated using DEM. *Géotechnique* 54:131–141 . doi: 10.1680/geot.2004.54.2.131
- Cheng YP, Nakata Y, Bolton MD (2003) Discrete element simulation of crushable soil. *Géotechnique* 53:633–641 . doi: 10.1680/geot.2003.53.7.633
- Cho N, Martin CD, Segoo DC (2007) A clumped particle model for rock. *Int J Rock Mech Min Sci* 44:997–1010 . doi: 10.1016/j.ijrmms.2007.02.002
- Colback PSB (1966) An analysis of brittle fracture initiation and propagation in the Brazilian test. 1st ISRM Congr 385–391
- Colmenares LB, Zoback MD (2002) A statistical evaluation of intact rock failure criteria constrained by polyaxial test data for five different rocks. *Int Journal Rock Mech Min Sci* 39:695–729
- Cook BNGW (1963) The basic mechanics of rockbursts. *J South African Inst Min Metall* 71–81
- Cook NGW (1965) A note on rockburst considered as a problem of stability. *South African Inst Min Metall* 65:437–446
- Correlation Solutions (2006) Vic-3D User Manual
- Cundall PA (1987) Distinct Element Models of Rock and Soil Structure. In: *Analytical and Computational Methods in Engineering Rock Mechanics*. pp 129–163
- Czeczenska KZ, Zuo DK (1986) The rockburst prevention in Polish coal mines. *Min Saf Env Prot* 6:58–63
- Dawidowski P, Dullona C, Naimi Z, Zamparelli M (2015) Analysis of strain localisation and stress distribution in hawkesbury sandstone under uniaxial compression using digital image correlation techniques. The University of Adelaide
- Descamps F, Tshibangu J (2007) Modelling the Limiting Envelopes of Rocks in the Octahedral Plane. *Oil gas Sci Technol* 62:683–694 . doi: 10.2516/ogst
- Diederichs MS (2007) The 2003 Canadian Geotechnical Colloquium: Mechanistic interpretation and practical application of damage and spalling prediction criteria for deep tunnelling. *Can Geotech J* 44:1082–1116 . doi: 10.1139/T07-033
- Dietz M, Oremek GM, Groneberg DA, Bendels MHK (2018) What is rockburst?

- Dinç Ö, Scholtès L (2018) Discrete Analysis of Damage and Shear Banding in Argillaceous Rocks. *Rock Mech Rock Eng* 51:1521–1538 . doi: 10.1007/s00603-017-1397-6
- Dong W, Wu Z, Zhou X, et al (2017) An experimental study on crack propagation at rock-concrete interface using digital image correlation technique. *Eng Fract Mech* 171:50–63 . doi: 10.1016/j.engfracmech.2016.12.003
- Dong X, Karrech A, Basarir H, et al (2019a) Energy dissipation and storage in underground mining operations. *Rock Mech Rock Eng* 52:229–245
- Dong X, Karrech A, Basarir H, et al (2018a) Analytical solution of energy redistribution in rectangular openings upon in- situ rock mass alteration. *Int J Rock Mech Min Sci* 106:74–83 . doi: 10.1016/j.ijrmms.2018.04.014
- Dong X, Karrech A, Basarir H, Elchalakani M (2018b) Extended finite element modelling of fracture propagation during in-situ rock mass alteration. *Am Rock Mech Assoc*
- Dong X, Karrech A, Qi C, et al (2019b) Analytical solution for stress distribution around deep lined pressure tunnels under the water table. *Int J Rock Mech Min Sci* 123:
- Du K, Li X, Li D, Weng L (2015) Failure properties of rocks in true triaxial unloading compressive test. *Trans Nonferrous Met Soc China* 25:571–581 . doi: 10.1016/S1003-6326(15)63639-1
- Duan F, Chen K, Hong M, et al (2019) Digital image corelation technique for fracture properties of concrete. Adelaide
- Dugdale DS (1960) Yielding of steel sheets containing slits. *J Mech Phys Solids* 8:100–104 . doi: 10.1016/0022-5096(60)90013-2
- Durrheim R (2010) Mitigating the risk of rockbursts in the deep hard rock mines of South Africa: 100 years of research. *Extr Sci A century Min Res* 156–171
- Durrheim RJ, Roberts MKC, Haile a T, et al (1998) Factors influencing the severity of rockburst damage in South African gold mines. *J South African Inst Min Metall* 98:53–57
- Einav I, Collins I (2009) A thermomechanical framework of plasticity based on

- probabilistic micromechanics. *J Mech Mater Struct* 3:867–892 . doi: 10.2140/jomms.2008.3.867
- Elices M, Guinea GV, Gómez J, Planas J (2002) The cohesive zone model: advantages, limitations and challenges. *Eng Fract Mech* 69:137–163 . doi: 10.1016/S0013-7944(01)00083-2
- Fairhurst C (1964) On the validity of the “Brazilian” test for brittle materials. *Int J Rock Mech Min Sci Geomech Abstr* 1:535–546 . doi: 10.1016/0148-9062(64)90060-9
- Farnam Y, Geiker MR, Bentz D, Weiss J (2015) Acoustic emission waveform characterization of crack origin and mode in fractured and ASR damaged concrete. *Cem Concr Compos* 60:135–145 . doi: 10.1016/j.cemconcomp.2015.04.008
- Feng X (2018) Rockburst mechanics, monitoring, warning and mitigation
- Feng X, Chen B, Li S, et al (2012) Studies on the evolution process of rockbursts in deep tunnels. *J Rock Mech Geotech Eng* 4:289–295 . doi: 10.3724/SP.J.1235.2012.00289
- Fourmeau M, Gomon D, Vacher R, et al (2014) Application of DIC Technique for Studies of Kuru Granite Rock under Static and Dynamic Loading. *Procedia Mater Sci* 3:691–697 . doi: 10.1016/j.mspro.2014.06.114
- Gentier S, Riss J, Archambault G, et al (2000) Influence of fracture geometry on shear behavior. *Int J Rock Mech Min Sci* 37:161–174 . doi: 10.1016/S1365-1609(99)00096-9
- Gill DE, Aubertin M, Simon R (1993) A practical engineering approach to the evaluation of rockburst potential. In: 3rd International Symposium on Rockbursts and Seismicity in Mines. Rotterdam, Netherlands, pp 63–68
- Gong F, Yan J, Li X, Luo S (2019) A peak-strength strain energy storage index for rock burst proneness of rock materials. *Int J Rock Mech Min Sci* 117:76–89 . doi: 10.1016/j.ijrmms.2019.03.020
- Gong W, He M, Yanyan P (2013) Disaster shearing failure mechanism and threshold based on true-triaxial rockburst experiment. *Disaster Adv* 6:
- Gong W, Peng Y, Wang H, et al (2015) Fracture angle analysis of rock burst faulting planes based on true-triaxial experiment. *Rock Mech Rock Eng* 48:1017–1039 . doi:

10.1007/s00603-014-0639-0

- Goodman RE (1989) Introduction to rock mechanics
- Gopalaratnam VS, Shah SP (1985) Softening response of plain concrete in direct tension. *ACI Mater J* 82:310–323
- Gui Y, Bui HH, Kodikara J (2015a) An application of a cohesive fracture model combining compression, tension and shear in soft rocks. *Comput Geotech* 66:142–157 . doi: 10.1016/j.compgeo.2015.01.018
- Gui Y, Bui HH, Kodikara J (2015b) An application of a cohesive fracture model combining compression, tension and shear in soft rocks. *Comput Geotech* 66:142–157 . doi: 10.1016/j.compgeo.2015.01.018
- Guimatsia I, Nguyen GD (2012) A generic approach to constitutive modelling of composite delamination under mixed-mode loading conditions. *Comput Sci and Technology* 72:269–277 . doi: 10.1016/j.compscitech.2011.11.012
- Guimatsia I, Nguyen GD (2014) A thermodynamics-based cohesive model for interface debonding and friction. *Int J Solids Struct* 51:647–659 . doi: 10.1016/j.ijsolstr.2013.10.032
- Guo Z (2014) Multiaxial Strength and Constitutive Relation. 17:
- HAM VE (1980) Isotropic Yield Surface in Thress dimensions for Use in Soil Mechanics. *Numer Anal Methods Geomech* 4:89–101
- Hammah R, Yacoub T, Corkum B (2008) The practical modelling of discontinuous rock masses with finite element analysis. 42nd US Rock Mech Symp 2nd US - Canada Rock Mech Symp 56–63
- Harrison JP, Hudson JA (2000) Engineering Rock Mechanics Part 2: Illustrative worked examples
- He M, Jia X, Coli M, et al (2012a) Experimental study of rockbursts in underground quarrying of Carrara marble. *Int J Rock Mech Min Sci* 52:1–8 . doi: 10.1016/j.ijrmms.2012.02.006
- He M, Ribeiro L, Miranda T, Zhu G (2015a) Rockburst laboratory tests database — Application of data mining techniques. *Eng Geol* 185:116–130 . doi:

10.1016/j.enggeo.2014.12.008

He M, Ribeiro L, Miranda T, Zhu G (2015b) Rockburst laboratory tests database-Application of data mining techniques. *Eng Geol* 185:116–130 . doi: 10.1016/j.enggeo.2014.12.008

He M, Xia H, Jia X, et al (2012b) Studies on classification , criteria and control of rockbursts. *J Rock Mech Geotech Eng* 4:97–114 . doi: 10.3724/SP.J.1235.2012.00097

He M, Xia H, Jia X, et al (2012c) Studies on classification , criteria and control of rockbursts. *J Rock Mech Geotech Eng* 4:97–114 . doi: 10.3724/SP.J.1235.2012.00097

He MC, Miao JL, Feng JL (2010) Rock burst process of limestone and its acoustic emission characteristics under true-triaxial unloading conditions. *Int J Rock Mech Min Sci* 47:286–298 . doi: 10.1016/j.ijrmms.2009.09.003

He MC, Miao JL, Li DJ, Wang CG (2007) Experimental study of rockburst processes of granite specimen at great depth. *Chinese J Rock Mech Eng* 26:865–876

He W, Hayatdavoudi A (2018a) A comprehensive analysis of fracture initiation and propagation in sandstones based on micro-level observation and digital imaging correlation. *J Pet Sci Eng* 164:75–86 . doi: 10.1016/j.petrol.2018.01.041

He W, Hayatdavoudi A (2018b) A comprehensive analysis of fracture initiation and propagation in sandstones based on micro-level observation and digital imaging correlation. *J Pet Sci Eng* 164:75–86 . doi: 10.1016/j.petrol.2018.01.041

Heal DP (2010) Observations and analysis of incidences of rockburst damage in underground mines. The University of Western Australia

Hoek E, Brown ET (1980a) *Underground Excavations in Rock*. The Institute of Mining and Metallurgy, London

Hoek E, Brown ET (1980b) *Underground in Rock Excavations*. The Institution of Mining and Metallurgy, London

Hoek E, Carranza-torres C, Corkum B (2002) Hoek-brown failure criterion

Hon alvin lau kean, Bong chang yii, Sia D, et al (2018) Analysis of fracture in sandstone

- using digital image correlation. Adelaide
- Hou FL (1989) Criterion and prevention measures on rockburst in circular tunnel. *Appl Rock Mech Eng* 195–201
- Hua A, You M (2001) Rock failure due to energy release during unloading and application to underground rock burst control. *Tunn Undergr Sp Technol* 16:241–246
- Huang D, Li Y (2014) Conversion of strain energy in Triaxial Unloading Tests on Marble. *Int J Rock Mech Min Sci* 66:160–168 . doi: 10.1016/j.ijrmms.2013.12.001
- Huang RQ, Wang XN, Chan LS (2001) Triaxial unloading test of rocks and its implication for rock burst. *Bull Eng Geol Environ* 60:37–41
- Hudson JA, Brown ET, Fairhurst C (1971) Optimizing the control of rock failure in servo-controlled laboratory tests. *Rock Mech* 3:217–224
- Hudson JA, Brown ET, Rummel F (1972a) The controlled failure of rock discs and rings loaded in diametral compression. *Int J Rock Mech Min Sci* 9:241–248 . doi: 10.1016/0148-9062(72)90025-3
- Hudson JA, Crouch SL, Fairhurst C (1972b) Soft, stiff and servo-controlled testing machines: A review with reference to rock failure. *Eng Geol* 6:155–189
- I C, PC P, CM L (1997) Normal/Shear Cracking Model: Application to Discrete Crack Analysis. *Journal Eng Mech* 123:765–773
- ISRM (1978) International society for rock mechanics commission on standardization of laboratory and field tests. *Int J Rock Mech Min Sci Geomech Abstr* 15:99–103 . doi: 10.1016/0148-9062(78)90003-7
- ISRM (2007) The complete ISRM suggested methods for rock characterization, testing and monitoring
- ISRM (1988) International society for rock mechanics commission on testing methods. *Int J Rock Mech Min Sci Geomech Abstr* 25:71–96
- Itasca (2008) Itasca Consulting Group, Inc PFC user manual. Minneapolis, MN, USA.
- Itasca (2011) Itasca Consulting Group, Inc UDEC user manual, Minneapolis, MN, USA

Itasca 3DEC (2016) Version 5.0 user's manuals

Jaeger JC (1967) Failure of Rocks Under Tensile Conditions. *Int J Rock Mech Min Sci* 4:219–227 . doi: [http://dx.doi.org/10.1016/0148-9062\(67\)90046-0](http://dx.doi.org/10.1016/0148-9062(67)90046-0)

Jiang Q, Feng X-T, Xiang T-B (2010) Rockburst characteristics and numerical simulation based on a new energy index : a case study of a tunnel at 2,500 m depth. *Bull Eng Geol Environ* 69:381–388 . doi: [10.1007/s10064-010-0275-1](https://doi.org/10.1007/s10064-010-0275-1)

Jianhong Y, Wu FQ, Sun JZ (2009) Estimation of the tensile elastic modulus using Brazilian disc by applying diametrically opposed concentrated loads. *Int J Rock Mech Min Sci* 46:568–576 . doi: [10.1016/j.ijrmms.2008.08.004](https://doi.org/10.1016/j.ijrmms.2008.08.004)

Jin-shan S, Qi-hu Z, Wen-bo L (2007) Numerical simulation of rock burst in circular tunnels under unloading conditions. *J China Univ Min Technol* 17:0552–0556

Jing L (2003) A review of techniques, advances and outstanding issues in numerical modelling for rock mechanics and rock engineering. *Int J Rock Mech Min Sci* 40:283–353 . doi: [10.1016/S1365-1609\(03\)00013-3](https://doi.org/10.1016/S1365-1609(03)00013-3)

Jing L, Hudson JA (2002) Numerical methods in rock mechanics. *Int J Rock Mech Min Sci* 39:409–427 . doi: [10.1016/S1365-1609\(02\)00065-5](https://doi.org/10.1016/S1365-1609(02)00065-5)

Jinli M, Xuena JIA, Cheng C (2011) The failure characteristics of Granite under true triaxial unloading condition. *Procedia Eng* 26:1620–1625 . doi: [10.1016/j.proeng.2011.11.2346](https://doi.org/10.1016/j.proeng.2011.11.2346)

Johnson S, Morris JP, Tonon F (2009) Numerical models in discontinuous media: Review of advances for rock mechanics applications. *J Geotech Geoenvironmental Eng* 135:1547–1561 . doi: [10.1061/\(ASCE\)GT.1943-5606.0000133](https://doi.org/10.1061/(ASCE)GT.1943-5606.0000133)

Jonsén P, Häggblad H, Sommer K (2007) Tensile strength and fracture energy of pressed metal powder by diametral compression test. *Powder Technol* 176:148–155 . doi: [10.1016/j.powtec.2007.02.030](https://doi.org/10.1016/j.powtec.2007.02.030)

Kaiser PK, Cai M (2012a) Design of rock support system under rockburst condition. *J Rock Mech Geotech Eng* 4:215–227 . doi: [10.3724/sp.j.1235.2012.00215](https://doi.org/10.3724/sp.j.1235.2012.00215)

Kaiser PK, Cai M (2012b) Design of rock support system under rockburst condition. *J Rock Mech Geotech Eng* 4:215–227 . doi: [10.3724/SP.J.1235.2012.00215](https://doi.org/10.3724/SP.J.1235.2012.00215)

- Kang Y, Yu M, Miska SZ, Takach N (2009) Wellbore Stability: A Critical Review and Introduction to DEM. SPE Annu Tech Conf Exhib 4–7 . doi: 10.2118/124669-MS
- Kazerani T (2013) A discontinuum-based model to simulate compressive and tensile failure in sedimentary rock. *J Rock Mech Geotech Eng* 5:378–388
- Kazerani T, Zhao GF, Zhao J (2010) Dynamic fracturing simulation of brittle material using the distinct lattice spring method with a full rate-dependent cohesive law. *Rock Mech Rock Eng* 43:717–726 . doi: 10.1007/s00603-010-0099-0
- Kidybinski A (1981) Bursting liability indices of coal. *Int J Rock Mech Min Sci Geomech Abstr* 18:295–304
- Koldas KS (2003) Rockburst and Fall of Ground Investigations in Deep Level Gold Mines : South African Example. 237–244
- Kwok CY, Bolton MD (2013) DEM simulations of soil creep due to particle crushing. *Géotechnique* 63:1365–1376 . doi: 10.1680/geot.11.p.089
- Labuz JF, Zang A (2012) Mohr – Coulomb failure criterion. *Rock Mech Rock Eng* 45:975–979 . doi: 10.1007/s00603-012-0281-7
- Lacidogna G, Accornero F, Carpinteri A (2019) Influence of snap-back instabilities on Acoustic Emission damage monitoring. *Eng Fract Mech* 210:3–12 . doi: 10.1016/j.engfracmech.2018.06.042
- Lambert C, Coll C (2014) Discrete modeling of rock joints with a smooth-joint contact model. *J Rock Mech Geotech Eng* 6:1–12 . doi: 10.1016/j.jrmge.2013.12.003
- Le linh anh (2019) A mechanism-based approach to constitutive modelling of quasi-brittle geomaterials with and without fibre reinforcement
- Le LA, Nguyen GD, Bui HH, et al (2019) Incorporation of micro-cracking and fibre bridging mechanisms in constitutive modelling of fibre reinforced concrete. *J Mech Phys Solids* 133:103732
- Le LA, Nguyen GD, Bui HH, et al (2018a) Localised failure mechanism as the basis for constitutive modelling of geomaterials. *J Eng Sci* 133:284–310
- Le LA, Nguyen GD, Bui HH, et al (2018b) Localised failure mechanism as the basis for constitutive modelling of geomaterials. *Int J Eng Sci* 133:284–310 . doi:

10.1016/j.ijengsci.2018.09.004

Le LA, Nguyen GD, Bui HH, et al (2017) Modelling jointed rock mass as a continuum with an embedded cohesive-frictional model. *Eng Geol* 228:107–120 . doi: 10.1016/j.enggeo.2017.07.011

Le LA, Nguyen GD, Bui HH, et al (2018c) Localised failure mechanism as the basis for constitutive modelling of geomaterials. *Int J Eng Sci* 133:284–310 . doi: 10.1016/j.ijengsci.2018.09.004

Leplay P, Réthoré J, Meille S, Baietto M (2010) Damage law identification of a quasi brittle ceramic from a bending test using Digital Image Correlation. *J Eur Ceram Soc* 30:2715–2725 . doi: 10.1016/j.jeurceramsoc.2010.05.021

Lesley CA (1995) The origin of massive sandstone facies in an ancient braided river deposits. Durham University

Li C, Cai M, Qiao L, Wang S (1999) Rock complete stress-strain curve and its relationship to rock burst

Li D, Li CC, Li X (2011) Influence of sample height-to-width ratios on failure mode for rectangular prism samples of hard rock loaded in uniaxial compression. *Rock Mech Rock Eng* 44:253–267 . doi: 10.1007/s00603-010-0127-0

Li D, Sun Z, Xie T, et al (2017) Energy evolution characteristics of hard rock during triaxial failure with different loading and unloading paths. *Eng Geol* 228:270–281 . doi: 10.1016/j.enggeo.2017.08.006

Li D, Wong LNY (2013a) The brazilian disc test for rock mechanics applications: Review and new insights. *Rock Mech Rock Eng* 46:269–287 . doi: 10.1007/s00603-012-0257-7

Li D, Wong LNY (2013b) The brazilian disc test for rock mechanics applications: Review and new insights. *Rock Mech Rock Eng* 46:269–287 . doi: 10.1007/s00603-012-0257-7

Li S, Feng X, Li Z, et al (2012) In situ monitoring of rockburst nucleation and evolution in the deeply buried tunnels of Jinping II hydropower station. *Eng Geol* 137–138:85–96 . doi: 10.1016/j.enggeo.2012.03.010

- Li X, Cao W, Zhou Z, Zou Y (2014) Influence of stress path on excavation unloading response. *Tunn Undergr Sp Technol* 42:237–246 . doi: 10.1016/j.tust.2014.03.002
- Liang Y, Li Q, Gu Y, Zou Q (2017) Mechanical and acoustic emission characteristics of rock : Effect of loading and unloading confining pressure at the postpeak stage. *J Nat Gas Sci Eng* 44:54–64 . doi: 10.1016/j.jngse.2017.04.012
- Lisjak A, Grasselli G (2014) A review of discrete modeling techniques for fracturing processes in discontinuous rock masses. *J Rock Mech Geotech Eng* 6:301–314 . doi: 10.1016/j.jrmge.2013.12.007
- Liu C, Lavato ML (2008) Elastic Constants Determination and Deformation Observation Using Brazilian Disk Geometry. *Proc XIth Int Congr Expo*. doi: 10.1007/s11340-009-9281-2
- Liu Q, Deng P (2019) A numerical investigation of element size and loading/unloading rate for intact rock in laboratory-scale and field-scale based on the combined finite-discrete element method. *Eng Fract Mech* 211:442–462 . doi: 10.1016/j.engfracmech.2019.02.007
- Lobo-Guerrero S, Vallejo LE (2010) Fibre-reinforcement of granular materials: DEM visualisation and analysis. *Geomech Geoenjin* 5:79–89 . doi: 10.1080/17486020903348709
- Lockner D (1993) The role of acoustic emission in the study of rock fracture. *Int J Rock Mech Min Sci* 30:883–899 . doi: 10.1016/0148-9062(93)90041-B
- Ma G, Zhou W, Chang XL, et al (2016) Formation of shear bands in crushable and irregularly shaped granular materials and the associated microstructural evolution. *Powder Technol* 301:118–130 . doi: 10.1016/j.powtec.2016.05.068
- Ma Y, Huang H (2018) DEM analysis of failure mechanisms in the intact Brazilian test. *Int J Rock Mech Min Sci* 102:109–119 . doi: 10.1016/j.ijrmms.2017.11.010
- Mahabadi OK (2012) Investigating the influence of micro-scale heterogeneity and microstructure on the failure and mechanical behaviour of geomaterials by Omid Khajeh Mahabadi A thesis submitted in conformity with the requirements for the degree of Doctor of Philosophy Gradu. University of Toronto
- Mahabadi OK, Cottrell BE, Grasselli G (2010) An example of realistic modelling of rock

- dynamics problems: FEM/DEM simulation of dynamic brazilian test on Barre Granite. *Rock Mech Rock Eng* 43:707–716 . doi: 10.1007/s00603-010-0092-7
- Malliga S (2015) Source Location of Rock Burst in the Mines of Kolar Gold Fields. *Int J Sci Res* 4:1925–1929
- Manchao H, Xin C, Guofeng Z, Sousa LR e (2012) Large deformation analysis in deep coal mines in China. *Innov Numer Model Geomech*. doi: 10.13140/2.1.2478.3689
- Masoumi H, Roshan H, Hedayat A, Hagan PC (2018) Scale-size dependency of intact rock under point-load and indirect tensile Brazilian testing. *Int J Geomech* 18:1–15 . doi: 10.1061/(ASCE)GM.1943-5622.0001103
- Matsushima T, Katagiri J, Uesugi K, et al (2008) 3D Shape Characterization and Image-Based DEM Simulation of the Lunar Soil Simulant FJS-1. *J Aerosp Eng* 22:15–23 . doi: 10.1061/(asce)0893-1321(2009)22:1(15)
- Mazel V, Guerard S, Croquelois B, et al (2016a) Reevaluation of the diametral compression test for tablets using the flattened disc geometry. *Int J Pharm* 513:669–677
- Mazel V, Guerard S, Croquelois B, et al (2016b) Reevaluation of the diametral compression test for tablets using the flattened disc geometry. *Int J Pharma* 513:669–677
- Mellor M, Hawkes I (1971) Measurement of tensile strength by diametral compression of discs and annuli. *Eng Geol* 5:173–225 . doi: 10.1016/0013-7952(71)90001-9
- Mitri HS (2007) Assessment of horizontal pillar burst in deep hard rock mines. *Int J Risk Assess Manag* 7:695–707
- MOGI K (1971) Fracture and flow of rocks under high triaxial compression. *J Geophys Res* 76:1255–1269
- MOGI K (1966) Precise measurements of fracture strength of rocks under uniform compressive stress. In: *Experimental Rock Mechanics*. pp 3–16
- Mousavi M, Quentin N, Elia JF, Mohammad G (2018) Experimental study and numerical modeling of gfracture propagation in Shale rocks during Brazilian disk test. *Rock Mech Rock Eng* 51:1755–1775 . doi: 10.1007/s00603-018-1429-x

- Munoz H, Taheri A, Chanda EK (2016) Pre-Peak and Post-Peak Rock Strain Characteristics During Uniaxial Compression by 3D Digital Image Correlation. *Rock Mech Rock Eng* 49:2541–2554 . doi: 10.1007/s00603-016-0935-y
- Mutke G, Stec K (1997) Seismicity in the upper Silesian Coal basin, Poland: Strong regional seismic events. *Rockburst Seism mines* 213–217
- Nath F, Kimanzi RJ, Mokhtari M, Salehi S (2018) A novel method to investigate cement-casing bonding using digital image correlation. *J Pet Sci Eng* 166:482–489 . doi: 10.1016/j.petrol.2018.03.068
- Nath F, Mokhtari M (2018) Optical visualization of strain development and fracture propagation in laminated rocks. *J Pet Sci Eng* 167:354–365
- Needleman A (2013) Some issues in cohesive surface modeling. *Procedia IUTAM* 10:221–246 . doi: 10.1016/j.piutam.2014.01.020
- Nguyen G d, Einav I, Korsunsky A m (2012a) How to connect two scales of behaviour in constitutive model of geomaterials. *Geotech Lett* 2:129–134
- Nguyen GD, Bui HH (2020) A thermodynamics-and mechanism-based framework for constitutive models with evolving thickness of localisation band. *Int J Solids Struct.* 187:100-120. <https://doi.org/10.1016/j.ijsolstr.2019.05.022>
- Nguyen GD, Bui HH (2018) The Roles and Effects of Friction in Cohesive Zone Modelling: A Thermodynamics Based Formulation. In: *Proceeding of the 4th Congres International de Geotechnique.* pp 288–296
- Nguyen GD, Einav I, Korsunsky AM (2012b) How to connect two scales of behaviour in constitutive modelling of geomaterials. *Géotechnique Lett* 2:129–134 . doi: 10.1680/geolett.12.00030
- Nguyen GD, Houlsby GT (2008) A coupled damage-plasticity model for concrete based on thermodynamic principles: Part I: Model formulation and parameter identification. *Int J Numer Anal Methods Geomech* 32:391–413
- Nguyen GD, Korsunsky AM, Einav I (2014a) A constitutive modelling framework featuring two scales of behaviour: Fundamentals and applications to quasi-brittle failure. *Eng Fract Mech* 115:221–240 . doi: .1037//0033-2909.I26.1.78

- Nguyen GD, Korsunsky A m, Einav I (2014b) A constitutive modelling framework featuring two scales of behaviour: fundamentals and applications to quasi-brittle failure. *Eng Fract Mech* 115:221–240
- Nguyen GD, Korsunsky AM (2008) Development of an approach to constitutive modelling of concrete: isotropic damage coupled with plasticity. *Int J Solids Struct* 45:5483–5501
- Nguyen GD, Korsunsky AM, Belnoue JP (2015) A nonlocal coupled damage- plasticity model for the analysis of ductile failure. *Int J Plast* 64:56–75
- Nguyen GD, Nguyen CT, Bui HH, Nguyen VP (2016a) Constitutive modelling of compaction localisation in porous sandstones. *Int J Rock Mech Min Sci* 83:57–72
- Nguyen GD, Nguyen CT, Nguyen VP, et al (2016b) A size-dependent constitutive modelling framework for localised failure analysis. *Comput Mech* 58:257–280
- Nguyen GD, Nguyen CT, Nguyen VP, et al (2016c) A size-dependent constitutive modelling framework for localised failure analysis. *Comput Mech* 58:257–280 . doi: 10.1007/s00466-016-1293-z
- Nguyen NHT, Bui HH, Nguyen GD, Kodikara J (2017a) A cohesive damage-plasticity model for DEM and its application for numerical investigation of soft rock fracture properties. *Int J Plast*. doi: 10.1016/j.applthermaleng.2017.08.158
- Nguyen TB, Amon A (2016) Experimental study of shear band formation: Bifurcation and localization. *Epl* 116:1–6 . doi: 10.1209/0295-5075/116/28007
- Nguyen TB, Mcnamara S, Crassous J, Amon A (2017b) Experimental study of shear bands formation in a granular material. *10001*:1–5
- Nyounguè A, Bouzid S, Dossou E, Azari Z (2016) Fracture characterisation of float glass under static and dynamic loading. *J Asian Ceram Soc* 4:371–380
- Okubo S, Nishimatsu Y (1985) Uniaxial compression testing using a linear combination of stress and strain as the control variable. *Int J Rock Mech Min Sci* 22:323–330
- Ortlepp WD (2005) RaSiM Comes of Age — A review of the contribution to the understanding and control of mine rockbursts. *Proc 6th Int Symp Rockbursts Seism Mines* 3–20

- Ortlepp WD, Stacey TR (1994) Rockburst mechanisms in tunnels and shafts. *Tunn Undergr Sp Technol* 9:59–65
- Ouyang Z, Elsworth D (1991) A phenomenological failure criterion for brittle rock. *Rock Mech Rock Eng* 24:133–153
- Patel S, Martin CD (2018) Application of flattened Brazilian Test to investigate rocks under confined extension. *Rock Mech Rock Eng* 51: . doi: 10.1007/s00603-018-1559-1
- Peng J, Wong LNY, Teh CI (2017) Influence of grain size heterogeneity on strength and microcracking behavior of crystalline rocks. *J Geophys Res Solid Earth* 122:1054–1073 . doi: 10.1002/2016JB013469
- Perras MA, Diederichs MS (2014) A Review of the Tensile Strength of Rock: Concepts and Testing. *Geotech Geol Eng* 32:525–546 . doi: 10.1007/s10706-014-9732-0
- Piratheepan J, Gnanendran CT, Arulrajah A (2012) Determination of c and Φ from IDT and unconfined compression testing and numerical analysis. *J Mater Civ Eng* 24:1153–1164 . doi: 10.1061/(ASCE)MT.1943-5533.0000493
- Potyondy DO, Cundall PA (2004) A bonded-particle model for rock. *Int J Rock Mech Min Sci* 41:1329–1364 . doi: 10.1016/j.ijrmms.2004.09.011
- Pouya A, Bemani Yazdi P (2015) A damage-plasticity model for cohesive fractures. *Int J Rock Mech Min Sci* 73:194–202 . doi: 10.1016/j.ijrmms.2014.09.024
- Qiao CS, Tian ZY (1998) Study of the possibility of rockburst in Dong-gua-shan Copper mine. *Chinese J Rock Mech Eng* 17:917–921
- Ramamurthy T (2007) *Engineering in rocks for slopes, foundations and tunnels*. New Delhi: Prentice-Hall of India Private Limited
- Robertson D, Bolton M and R (2001) Dem simulations of crushable grains and soils. *Powders Grains* 2001 4
- Rodríguez P (2017) Application of acoustic emission monitoring and signal analysis to the qualitative and quantitative characterization of the fracture process in rocks. *ICF 2017 - 14th Int Conf Fract* 1:51–52 . doi: 10.1016/j.engfracmech.2018.06.027
- Rodríguez P, Arab PB, Celestino TB (2016) Characterization of rock cracking patterns in

- diametral compression tests by acoustic emission and petrographic analysis. *Int J Rock Mech Min Sci* 83:73–85 . doi: 10.1016/j.ijrmms.2015.12.017
- Rummel F, Fairhurst C (1970) Determination of the post-failure behavior of brittle rock using a servo-controlled testing machine. *Rock Mech* 2:189–204
- Sabri M, Ghazvinian A, Nejati HR (2016) Effect of particle size heterogeneity on fracture toughness and failure mechanism of rocks. *Int J Rock Mech Min Sci* 81:79–85 . doi: 10.1016/j.ijrmms.2015.11.002
- Saksala T, Hokka M, Kuokkala VT, Mäkinen J (2013) Numerical modeling and experimentation of dynamic Brazilian disc test on Kuru granite. *Int J Rock Mech Min Sci* 59:128–138 . doi: 10.1016/j.ijrmms.2012.12.018
- Scholtès L, Donzé FV (2013) A DEM model for soft and hard rocks: Role of grain interlocking on strength. *J Mech Phys Solids* 61:352–369 . doi: 10.1016/j.jmps.2012.10.005
- Schöpfer MPJ, Abe S, Childs C, Walsh JJ (2009) The impact of porosity and crack density on the elasticity, strength and friction of cohesive granular materials: Insights from DEM modelling. *Int J Rock Mech Min Sci* 46:250–261 . doi: 10.1016/j.ijrmms.2008.03.009
- Schreyer HL (2007) Modelling surface orientation and stress at failure of concrete and geological materials. *Int J Numer Anal Methods Geomech* 31:147–171 . doi: 10.1002/nag
- Shara M, Shen L, Xu Q (2018) Characterisation of mechanical behaviour of 3D printed rock-like material with digital image correlation. *Int J Rock Mech Min Sci* 112:122–138
- Shimizu H, Koyama T, Ishida T, et al (2010) Distinct element analysis for Class II behavior of rocks under uniaxial compression. *Int J Rock Mech Min Sci* 47:323–333 . doi: 10.1016/j.ijrmms.2009.09.012
- Singh B, Goel RK (1999) *Rock mass classification: A practical approach in civil engineering*. Elsevier Publ 48–50
- Singh SP (1988) Technical Note - Burst energy release index. *Rock Mech Rock Eng* 21:149–155

- Solutions C (2009) Vic-2D Reference Manual. 1–59
- Stirling RA, Simpson DJ, Davie CT (2013) The application of digital image correlation to Brazilian testing of sandstone. *Int J Rock Mech Min Sci* 60:1–11 . doi: 10.1016/j.ijrmms.2012.12.026
- Stone DEW, Dingwall PF (1977) Acoustic emission parameters and their interpretation. *NDT Int* 10:51–62 . doi: 10.1016/0308-9126(77)90079-7
- Su G, Chen Z, Ju JW, Jiang J (2017) Influence of temperature on the strainburst characteristics of granite under true triaxial loading conditions. *Eng Geol* 222:38–52 . doi: 10.1016/j.enggeo.2017.03.021
- Tang B (2000) Rockburst control using destress blasting. McGill University, Montreal, Canada
- Tao ZY (1988a) Support design of tunnels subjected to rockbursting. *Rock Mech Power Plants* 407–411
- Tao ZY (1988b) Support Design of Tunnels subjected to rockbursting. *Rock Mech Power Plants* 407–411
- Tarasov B, Potvin Y (2013) Universal criteria for rock brittleness estimation under triaxial compression. *Int J Rock Mech Min Sci* 59:57–69 . doi: 10.1016/j.ijrmms.2012.12.011
- Tarasov BG (2012) New criteria for rock brittleness estimation at triaxial compression. In: *XL International Summer School Conference APM*. pp 367–377
- Tarasov BG, Potvin Y (2012) Absolute, relative and intrinsic rock brittleness at compression. In: *Sixth International Seminar on Deep and High Stress Mining*. Australian Centre for Geomechanics, Perth, pp 313–324
- Tarasov BG, Randolph MF (2011) Superbrittleness of rocks and earthquake activity. *Int J Rock Mech Min Sci* 48:888–898 . doi: 10.1016/j.ijrmms.2011.06.013
- Tomac I, Gutierrez M (2012) Evaluation of the Brazilian test size effect using discrete element modeling. *46th US Rock Mech / Geomech Symp 2012* 2554–2560
- Tran HT, Wang Y, Nguyen GD, et al (2019) Modelling 3D desiccation cracking in clayey soils using a size-dependent SPH computational approach. *Comput Geotech*

116:103209

- Tsangouri E, Aggelis DG, Matikas TE, Mpalaskas AC (2016) Acoustic emission activity for characterizing fracture of marble under bending. *Appl Sci* 6:1–12 . doi: 10.3390/app6010006
- Tuncay E, Hasancebi N (2009) The effect of length to diameter ratio of test specimens on the uniaxial compressive strength of rock. *Bull Eng Geol Environ* 68:491–497 . doi: 10.1007/s10064-009-0227-9
- Tung SH, Sui CH (2010) Application of digital-image-correlation techniques in analysing cracked cylindrical pipes. *Sadhana - Acad Proc Eng Sci* 35:557–567 . doi: 10.1007/s12046-010-0039-4
- Verma RK, Chandra S (2020) Polyaxial strength criterion and closed-form solution for squeezing rock conditions. *J Rock Mech Geotech Eng* 12:507-515. <https://doi.org/10.1016/j.jrmge.2019.06.011>
- Verma RK, Nguyen GD, Karakus M, et al (2018) Numerical Analysis of Fracture Propagation in Brazilian Disc Test. *Aust Conf Comput Mech*
- Verma RK, Nguyen GD, Karakus M, et al (2019a) Snap Back Indirect Tensile Test (AUSBIT)
- Verma RK, Pour AF, Dawidowski P, et al (2019b) Analysing localisation behaviour of rocks using Digital Image Correlation technique. In: 13th International Conference on the Mechanical Behaviour of Materials. Melbourne, pp 11–14
- Wang H, Dyskin A, Dight P, et al (2018) Review of unloading tests of dynamic rock failure in compression. *Eng Fract Mech*. doi: 10.1016/j.engfracmech.2018.12.022
- Wang H, Ren C, Wan Y, et al (2019a) Experimental study on fracture process of sintered Nd-Fe-B magnets during dynamic Brazilian tests. *J Magn Magn Mater* 471:200–208
- Wang J, Xie L, Xie H, et al (2016) Effect of layer orientation on acoustic emission characteristics of anisotropic shale in Brazilian tests. *J Nat Gas Sci Eng* 36:1120–1129 . doi: 10.1016/j.jngse.2016.03.046
- Wang M, Cao P (2016) Numerical analysis of flattened brazilian disc test based on the cusp catastrophe theory. *Math Probl Eng* 2016: . doi: 10.1155/2016/4517360

- Wang QZ, Jia XM, Kou SQ, et al (2004) The flattened Brazilian disc specimen used for testing elastic modulus, tensile strength and fracture toughness of brittle rocks: Analytical and numerical results. *Int J Rock Mech Min Sci* 41:245–253 . doi: 10.1016/S1365-1609(03)00093-5
- Wang XM, Dong LJ, Fu YH (2009) Prediction of possibility and the level of rockburst based on uncertain average graded analysis method. *Sci Technol* 78–81
- Wang Y, Bui HH, Nguyen GD, Ranjith PG (2019b) A new SPH-based continuum framework with an embedded fracture process zone for modelling rock fracture. *Int J Solids Struct* 159:40–57
- Wawersik WR, Brace WF (1971) Post-failure behavior of a granite and diabase. *Rock Mech* 3:61–85
- Wawersik WR, Fairhurst C (1970) A study of brittle rock fracture in laboratory compression experiments. *Int J Rock Mech Min Sci* 7:561–575
- Whyatt J, Blake W, Williams T, White B (2002) 60years of rockbursting in the Coeur D’alene district of Northern Idaho, USA: Lessons learned and remaining issues. *Proc 109th Annu Exhib Meet Soc Mining, Metall Explor* 10
- Wisdom W (1927) *A M ATERIAL C IVILIZATION* * René Guénon. 15–30
- Wu F, Hu X, Gong M, et al (2010a) Unloading deformation during layered excavation for the underground powerhouse of Jinping I Hydropower Station , southwest China. *Bull Eng Geol Environ* 69:343–351 . doi: 10.1007/s10064-010-0308-9
- Wu F, Wu J, Qi S (2010b) Phenomena and theoretical analysis for the failure of brittle rocks. *J Rock Mech Geotech Eng* 2:331–337 . doi: 10.3724/SP.J.1235.2010.00331
- Wu S, Zhang S, Guo C, Xiong L (2017) A generalized nonlinear failure criterion for frictional materials. *Acta Geotech* 12:1353–1371 . doi: 10.1007/s11440-017-0532-6
- Xie H, Li L, Peng R, Ju Y (2009) Energy analysis and criteria for structural failure of rocks. *J Rock Mech Geotech Eng* 1:11–20 . doi: 10.3724/SP.J.1235.2009.00011
- Xing HZ, Zhang QB, Ruan D, et al (2018) Full-field measurement and fracture characterisations of rocks under dynamic loads using high-speed three-dimensional digital image correlation. *Int J Impact Eng* 113:61–72

- Xu YH, Cai M (2017) Influence of loading system stiffness on post-peak stress-strain curve of stable rock failures. *Rock Mech Rock Eng* 50:2255–2275 . doi: 10.1007/s00603-017-1231-1
- Y.M.Alshkane, A.M.Marshall, L.R.Stace (2016) UDEC_Prediction of strength and deformability of an interlocked blocky rock mass using UDEC. *J Rock Mech Geotech Eng* 9:531–542
- Yan G, Yu H, McDowell G (2009) Simulation of granular material behaviour using DEM. *Procedia Earth Planet Sci* 1:598–605 . doi: 10.1016/j.proeps.2009.09.095
- Yang S (2016) Experimental study on deformation , peak strength and crack damage behavior of hollow sandstone under conventional triaxial compression. *Eng Geol* 213:11–24 . doi: 10.1016/j.enggeo.2016.08.012
- Yang X, Ren T, Tan L, et al (2018) Developing coal burst propensity index method for Australian coal mines. *Int J Min Sci Technol* 28:783–790 . doi: 10.1016/j.ijmst.2018.08.008
- Yin Z, Chang CS (2009) Microstructural modelling of stress-dependent behaviour of clay. *Int J Solids Struct* 46:1373–1388 . doi: 10.1016/j.ijsolstr.2008.11.006
- Yin Z, Chang CS, Hicher P (2010) Micromechanical modelling for effect of inherent anisotropy on cyclic behaviour of sand. *Int J Solids Struct* 47:1933–1951 . doi: 10.1016/j.ijsolstr.2010.03.028
- Yin Z, Zhao J, Hicher P (2014) A micromechanics-based model for sand-silt mixtures. *Int J Solids Struct* 51:1350–1363 . doi: 10.1016/j.ijsolstr.2013.12.027
- Yu W, Wu G, An B, Wang P (2019) Experimental Study on the Brittle-Ductile Response of a Heterogeneous Soft Coal Rock Mass under Multifactor Coupling. 2019:
- Yu Y, Zhang J, Zhang J (2009) A modified Brazilian disk tension test. *Int J Rock Mech Min Sci* 46:421–425 . doi: 10.1016/j.ijrmms.2008.04.008
- Zhang C, Feng X-T, Zhou H, et al (2012) Case histories of four extremely intense rockbursts in deep tunnels. *Rock Mech Rock Eng* 45:275–288 . doi: 10.1007/s00603-011-0218-6
- Zhang G, Chen JX, Hu B (2003) Prediction and control of rockburst during deep

- excavation of a gold mine in China. *Chinese J Rock Mech Eng* 22:1607–1612
- Zhang R, Dai F, Gao MZ, et al (2015) Fractal analysis of acoustic emission during uniaxial and triaxial loading of rock. *Int J Rock Mech Min Sci* 79:241–249 . doi: 10.1016/j.ijrmms.2015.08.020
- Zhang X, Yi Y, Zhu H, et al (2018) Measurement of tensile strength of nuclear graphite based on ring compression test. *J Nucl Mater* 511:134–140
- Zhao XG, Cai M (2015) Influence of specimen height-to-width ratio on the strainburst characteristics of Tianhu granite under true-triaxial unloading conditions. *Can Geotech J* 52:890–902
- Zhao XG, Wang J, Cai M, et al (2014) Influence of unloading rate on the strainburst characteristics of beishan granite under true-triaxial unloading conditions. *Rock Mech Rock Eng* 47:467–483 . doi: 10.1007/s00603-013-0443-2
- Zhou GL, Tham LG, Lee PKK, Tsui Y (2001) A phenomenological constitutive model for rocks with shear failure mode. *Int J Numer Anal Methods Geomech* 25:391–414
- Zhou J, Li X, Mitri HS (2018a) Evaluation method of rockburst: State-of-the-art literature review. *Tunn Undergr Sp Technol* 81:632–659
- Zhou J, Li X, Mitri HS (2016) Classification of Rockburst in Underground Projects: Comparison of Ten Supervised Learning Methods. *J Comput Civ Eng* 30:4016003 . doi: 10.1061/(asce)cp.1943-5487.0000553
- Zhou Z, Cai X, Ma D, et al (2018b) Effects of water content on fracture and mechanical behavior of sandstone with a low clay mineral content. *Eng Fract Mech* 193:47–65 . doi: 10.1016/j.engfracmech.2018.02.028

Appendix A

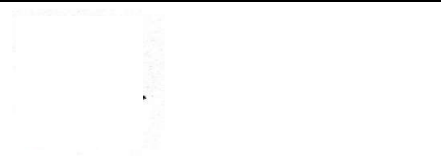
Adelaide University Snap-Back Indirect Tensile Test (AUSBIT)

Adelaide University Indirect Tensile Test (AUSBIT), Innovation Patent, Australia. Patent No: 2019101006. (2019).

Statement of Authorship

Title of Paper	Adelaide University Snap-Back Indirect Tensile Test (AUSBIT)
Publication Status	<input checked="" type="checkbox"/> Published <input type="checkbox"/> Accepted for Publication <input type="checkbox"/> Submitted for Publication <input type="checkbox"/> Unpublished and Unsubmitted work written in manuscript style
Publication Details	Adelaide University Indirect Tensile Test (AUSBIT), Innovation Patent, Australia. Patent No: 2019101006. (2019).


Principal Author

Name of Principal Author (Candidate)	Rupesh Kumar Verma		
Contribution to the Paper	Technical development of invented experimental methodology. Tested and validated its applications using different brittle material types and theoretical framework. Wrote and revised the manuscript. Patent application.		
Overall percentage (%)	40		
Certification:	This paper reports on original research I conducted during the period of my Higher Degree by Research candidature and is not subject to any obligations or contractual agreements with a third party that would constrain its inclusion in this thesis. I am the primary author of this paper.		
Signature		Date	6 th Dec. 2019

Co-Author Contributions

By signing the Statement of Authorship, each author certifies that:

- i. the candidate's stated contribution to the publication is accurate (as detailed above);
- ii. permission is granted for the candidate to include the publication in the thesis; and
- iii. the sum of all co-author contributions is equal to 100% less the candidate's stated contribution.

Name of Co-Author	Giang D. Nguyen		
Contribution to the Paper	Concept & design of experiments and instrumentations to handle Snap-Back in Brazilian disc tests. Technical development and testing of invented experimental methodology. Also developed Snap-Back theoretical framework. Planned & supervised the technical developments & all testing. Evaluated and revised the manuscript. Patent application.		
Signature		Date	06 Dec 2019

Name of Co-Author	Murat Karakus		
Contribution to the Paper	Supervised the technical development. Evaluated and revised the manuscript. Patent application.		
Signature		Date	06/12/2019

Name of Co-Author	Simon Golding		
Contribution to the Paper	Design & 3D print parts of the instrumentations Trial testing & assistance in devising the experiment.		
Signature		Date	06/12/2019

Name of Co-Author	Abbas Taheri		
Contribution to the Paper	Supervised the remaining technical development. Evaluated and revised the manuscript. Patent application.		
Signature		Date	06 Dec 2019



Australian Government

IP Australia

CERTIFICATE OF GRANT INNOVATION PATENT

Patent number: 2019101006

The Commissioner of Patents has granted the above patent on 25 September 2019, and certifies that the below particulars have been registered in the Register of Patents.

Name and address of patentee(s):

THE UNIVERSITY OF ADELAIDE of Adelaide Enterprise, Level 4, Rundle Mall Plaza University of Adelaide SA 5005 Australia

Title of invention:

Snap-Back Indirect Tensile Test

Name of inventor(s):

Verma, Rupesh Kumar; Nguyen, Giang Dinh; Karakus, Murat; Golding, Simon and Teheri, Abbas

Term of Patent:

Eight years from 4 September 2019

NOTE: This Innovation Patent cannot be enforced unless and until it has been examined by the Commissioner of Patents and a Certificate of Examination has been issued. See sections 120(1A) and 129A of the Patents Act 1990, set out on the reverse of this document.



Dated this 25th day of September 2019

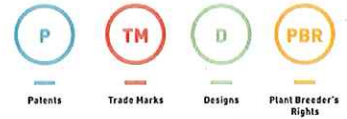
Commissioner of Patents

PATENTS ACT 1990

The Australian Patents Register is the official record and should be referred to for the full details pertaining to this IP Right.



25 September 2019



Delivering a world leading IP system

Phone: 1300 651 010
International: +61 2 6283 2999

www.ipaustralia.gov.au

ABN: 38 113 072 755

Notice of grant for your innovation patent

THE UNIVERSITY OF ADELAIDE

Adelaide Enterprise
Level 4, Rundle Mall Plaza
University of Adelaide SA 5005
Australia

Patent number 2019101006
Patentee name THE UNIVERSITY OF ADELAIDE

Dear Patentee,

The granting of your application has been processed. The date of grant is 25 September 2019 and the Certificate of Grant is enclosed.

What will happen next

- The granted patent number will be published in the next available [Australian Official Journal of Patents](#).
- Your first renewal fee payment, being for the 2nd year anniversary, is due on 4 September 2021.

What you can do

- Request examination** – this is optional and you can request examination at any time during the term of your patent. The fee is currently \$500.

Things to be aware of

- Your patent cannot be legally enforced until it is certified through examination.
- If examination is requested and your patent does not meet the requirements for certification, your patent will cease.
- The term of your innovation patent is 8 years from the date of the patent (4 September 2019).

Your progress

- Filed**
Application is filed
- Acceptance and Grant**
Application is accepted and patent granted
- Examination**
Patent is being examined
- Certification**
Patent is certified
(patent is now enforceable)

- Renewal**
Renewal fees required to maintain patent
(fees are due annually - please refer to the 'paid to' date in AusPat for your next due date)

Need help?

Talk to Alex, our virtual assistant



For further information on this topic, visit our [website](#).

Make an enquiry or provide feedback on our [website](#).



Did you know? Over 98% of customer requests are now received online

- To maintain your innovation patent you have to pay annual renewal fees. The fee can be paid up to 6 months after 4 September 2021 provided it is accompanied by the required late payment fee. Your patent will cease if renewal fees are not paid.

Details of your patent can be viewed on [AusPat](#), our Australian patent search database.

Yours sincerely,

IP Australia

Appendix B


Analysing localisation behaviour of rocks using Digital Image Correlation technique

Verma, R.K., Pour,F.A., Dawidowski, P., Nguyen, G.D., Bui, H.H., Karakus, M., Taheri, A. (2019). “Analyzing localization behavior of rocks using Digital Image Correlation technique”. ICM-13 2019, 13th International Conference on the Mechanics Behavior of Material, RMIT University, Melbourne, Australia.

Statement of Authorship

Title of Paper	Analysing localisation behaviour of rocks using Digital Image Correlation technique
Publication Status	<input checked="" type="checkbox"/> Published <input type="checkbox"/> Accepted for Publication <input type="checkbox"/> Submitted for Publication <input type="checkbox"/> Unpublished and Unsubmitted work written in manuscript style
Publication Details	Verma, R.K., Pour,F.A., Dawidowski, P., Nguyen, G.D., Bui, H.H., Karakus, M., Taheri, A. (2019). "Analyzing localization behavior of rocks using Digital Image Correlation technique". ICM-13 2019, 13 th International Conference on the Mechanics Behavior of Material, RMIT University, Melbourne, Australia.


Principal Author

Name of Principal Author (Candidate)	Rupesh Kumar Verma		
Contribution to the Paper	Results analysis using conventional and DIC experimental data. Wrote and revised the manuscript.		
Overall percentage (%)	50		
Certification:	This paper reports on original research I conducted during the period of my Higher Degree by Research candidature and is not subject to any obligations or contractual agreements with a third party that would constrain its inclusion in this thesis. I am the primary author of this paper.		
Signature		Date	06 Dec 2019

Co-Author Contributions

By signing the Statement of Authorship, each author certifies that:

- i. the candidate's stated contribution to the publication is accurate (as detailed above);
- ii. permission is granted for the candidate to include the publication in the thesis; and
- iii. the sum of all co-author contributions is equal to 100% less the candidate's stated contribution.

Name of Co-Author	Ali Fallah Pour		
Contribution to the Paper	Analysis of DIC data. Wrote part of the manuscript and revised the manuscript.		
Signature		Date	6/12/2019

Name of Co-Author	Pawel Dawidowski		
Contribution to the Paper	Performed laboratory experiments. Revised the manuscript.		
Signature		Date	08/12/2019

Name of Co-Author	Giang D. Nguyen		
Contribution to the Paper	Supervised the experiments & technical developments. Evaluated and revised the manuscript.		
Signature		Date	06 Dec 2019

Name of Co-Author	Ha H. Bui		
Contribution to the Paper	Supervised the technical development. Evaluated and revised the manuscript.		
Signature		Date	06 Dec 2019

Name of Co-Author	Murat Karakus		
Contribution to the Paper	Supervised the technical development. Evaluated and revised the manuscript.		
Signature		Date	06/12/2019

Name of Co-Author	Abbas Taheri		
Contribution to the Paper	Supervised the technical development. Evaluated and revised the manuscript.		
Signature		Date	06 Dec 2019

Analysing localisation behaviour of rocks using Digital Image Correlation technique

Rupesh K. Verma^{1*}, Ali Fallah Pour¹, Pawel Dawidowski¹, Giang D. Nguyen¹, Ha H. Bui², Murat Karakus¹, Abbas Taheri¹

¹School of Civil Environmental and Mining Engineering, The University of Adelaide, Australia

²Department of Civil Engineering, Monash University, Australia

*Corresponding author. Email: rupesh.verma@adelaide.edu.au

Abstract: With the advent of advanced computing technologies, applications of numerical modelling techniques have become popular among the research community. It resulted in the development of numerous constitutive models, the majorities of which are based on the macroscopic material responses simply because of the unavailability of reliable experimental data set which could not only reveal the material behaviour at a global scale but also provide the insight at local scale. Even the use of advanced experimental techniques, despite being efficient, has not furnished well in the direction of revealing localised material behaviour and limited to adding more visual effects. It highlights the importance of comprehensive results interpretation while using advanced experimental techniques. In this direction, this paper presents a new approach to analysing localisation behaviour of rocks using Digital Image Correlation (DIC) technique. For this purpose, lateral strain controlled uniaxial compression tests have been conducted on cylindrical samples of Hawkesbury sandstone. Full field strain data set obtained from DIC have been used to evaluate the localised strain evolution across and around the shear band. It further has been synchronised with macroscopic material response to provide insight into the strain localisation mechanism with reference to the overall sample response. Additionally, strain rate evaluation across the shear band has also been done. These results have been further used to evaluate the thickness of the localisation zone which itself is a much-needed micro-scale parameter for the development of any reliable constitutive model.

Keywords: Shear band, Digital Image Correlation, uniaxial compression test, strain localisation.

1 Introduction

With the advent of advanced computing technologies, applications of numerical modelling techniques in brittle material analysis have become popular among the research community which always requires a good constitutive model for simulation of realistic material behaviour. In this direction, many constitutive models have been developed which mostly are based on the macroscopic sample responses (Zhao, Xie, and Meng 2014; Lanru Jing and Stephansson 2007; Ji, Chen, and Guo 2018; Cheng, Nakata, and Bolton 2003; L Jing and Hudson 2002; Pouya and Bemani Yazdi 2015; Needleman 2013). Such models normally lack the capability to reproduce the realistic material response under loading conditions different from calibration data set. Therefore, the need of constitutive models based on localised material behaviour is quite evident. Examples include cohesive-frictional models representing the localisation zone idealised as a zero-thickness band (Gui, Bui, and Kodikara 2015a; Pouya and Bemani Yazdi 2015; Le et al 2018; N. H. T. Nguyen et al. 2017; Schöpfer et al. 2009; Bobet et al. 2009; Lisjak and Grasselli 2014). Key factor for this limitation could be the unavailability of good experimental data set which could not only provide global sample response but also furnish sufficient information pertaining to localised material strength evolution. This, in return, reflects the limitations of commonly used conventional experimental approaches.

Several advanced experimental approaches have been developed and employed for the characterisation of material behaviour involving localised failure. Examples include Acoustic Emission (AE) techniques (Lockner 1993; Filipussi et al. 2015; Zehnder et al. 2017), X-ray tomography (Viggiani and Desrues 2013; Müter et al. 2014) and other image based approaches (Belrhiti et al. 2017; Stirling, Simpson, and Davie 2013; Shara, Shen, and Xu 2018). However, applications of AE techniques has been limited to assessing energy dissipation mechanism while sample is undergoing damage. Whereas, cost-inefficiency and sample size restriction are the major limitations of X-ray tomography which restrains its applications in the field of rock mechanics. On this ground, techniques based on Digital Image Correlation (DIC) provides an efficient alternative which uses non-contact full field kinematics measurement of planar or non-planar surfaces undergoing deformation (T. B. Nguyen et al. 2017). This approach is based on the principle of tracking pixel displacement on material surface using continuous

images taken by the CCD cameras during the process of deformation. It is one of the easiest and more feasible approach, and despite being able to measure surface strains only, it is much faster than X-ray and can provide much more data than conventional strain gauges.

The above key characteristics of DIC have made its applications popular in various engineering and non-engineering fields. For instance, Munoz et.al. (2017) investigated the strain evolution of sandstone rock under uniaxial compression test (Munoz and Taheri 2017). Bob et.al. (2017) compared the accuracy of the DIC results with conventional experimental data set in case of large cylindrical cement rock fill and demonstrated its reliability as a non-contact full field strain measurement approach (Lingga et al. 2019). He et.al. (2018) explored the fracture initiation and propagation mechanism in disc shaped sample under diametrical compressive loading (He and Hayatdavoudi 2018). Mazela et.al. (2016) investigated the application of DIC in the field of pharmaceutical i.e. studying the mechanical properties of tablets (Mazel et al. 2016). Likewise, many examples can be presented where researchers have explored the application of DIC in studying wide range of material types including concrete, magnet, ceramics, graphene etc. (Jonsén, Häggblad, and Sommer 2007; Wang et al. 2019; Candamano et al. 2019; Nath and Mokhtari 2018; Cao, Lin, and Cao 2018; Zhang et al. 2018; He and Hayatdavoudi 2018; Xing et al. 2018). Despite DIC being an effective approach, to the best of our knowledge the localised behaviour is usually not addressed at length with enough quantitative analyses. In addition, the stability of the experiment involving localised failure can also make the execution of the experiments challenging or even impossible given the instant failure process.

In view of above research gaps, this paper aims to present a new approach to analysing localisation behaviour of rocks using three-dimensional *Digital Image Correlation (DIC)* technique. For this purpose, lateral strain controlled uniaxial compression tests have been conducted on cylindrical samples of Hawkesbury sandstone. One advantage of lateral strain control approach over conventional UCS tests is the delay in fracturing process which enable the application of image processing techniques with lower frame rates. Additionally, full field strain data set obtained from DIC can be used to evaluate the localised strain evolution across and around the shear band. It further has been synchronised with macroscopic material response to provide insight into the strain localisation mechanism with reference to the overall sample response. These results have been further used to evaluate the thickness of the localisation zone which itself is a much needed micro-scale parameter for the development of any reliable constitutive model.

2 Experimental setup: Three-Dimensional Digital Image Correlation (DIC)

Lateral strain controlled uniaxial compressive strength tests were conducted on cylindrical samples of Hawkesbury sandstone where bedding plane orientation were kept vertical (i.e. along loading direction) while coring. The aspect ratio of these samples had been kept 2.5 with 42 mm sample diameter. This test was repeated over five samples to conclude the overall macroscopic properties. Black and white paints were sprayed on each sample to create distinct speckle pattern with good contrast. These speckles were randomly distributed with uniform density maintaining pattern uniqueness to satisfy the pre-requisite of *Digital Image Correlation (DIC)* technique's applicability to full field strain evaluation (Correlation Solutions 2018). The cored sample preparation can be seen in part 'a' of figure 1 below.

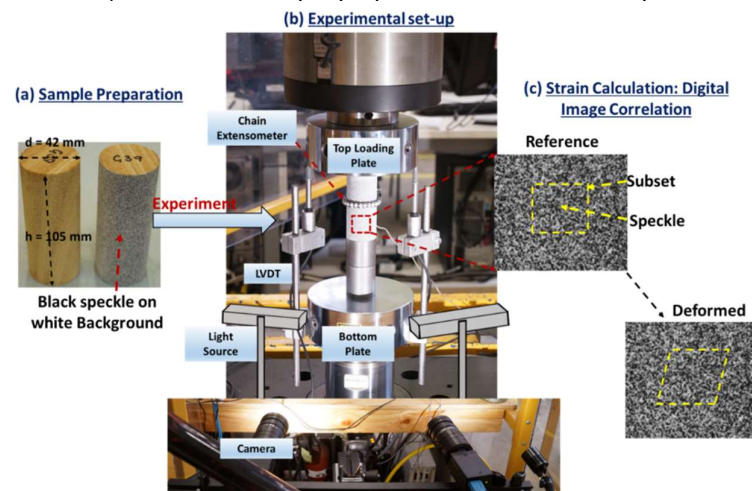


Figure 1: Lateral strain controlled uniaxial compression test on Hawkesbury sandstone

The overall experimental setup is presented in figure 1 'b'. The experiments were conducted on INSTRON – universal compression loading machine where the bottom plate was fixed while the top loading plate was used to apply the axial compression on cylindrical sample. The overall axial (or vertical) displacement of top loading plate had been recorded by two *Linear Variable Differential Transformers* (LVDTs). While chain extensometer had been placed across the central portion of sample to record the overall lateral strain variation under axial compression. The rate of axial movement of top loading plate was controlled to maintain a constant lateral strain rate of 0.16 micron per second. In addition, two CCD cameras were placed in front of the sample and the distance between these cameras and from test sample were adjusted to maintain the overall inclination of 40°. External light source was also provided to ensure uniform brightness throughout the tests.

Further, images at the rate of 1 frame per second were captured continuously during the test. These images were then used to obtain full field strain evolution throughout the test. For post-processing, commercial image processing software package i.e. Correlation solutions – VIC snap three-dimension version (or VIC-3D) was used. The principle behind this approach of strain calculation is to determine the maximum of the correlation array between the subsets of pixel intensity array on reference image and any given image with time. It provides an ease to estimate the both i.e. full field displacement and strain fields. In terms of strain field, one can have all strain types components including Lagrangian strains or Green-Lagrangian strain tensor, engineering, Tresca and Von-Mises strain. So, in principal, DIC measures displacement field which have been further utilised to derive full strain fields via post-processing using VIC-3D software. Detailed description of DIC principles and VIC-snap 3D functioning can be found in (Correlation Solutions 2018).

3 Analysis of results

Detailed discussion about the results obtained from experiment is presented in this section. The intent here is to demonstrate the potential of image processing approach to provide a better insight to rock material's local scale behaviour. Prior to this, it is essential to assess the accuracy of the image-based measurements first. Therefore, four virtual LVDTs are taken across the sample surface on DIC images. The average displacement recorded by these virtual LVDTs are compared with the average of two physical LVDTs used in actual experiment. Overview of above comparison have been presented in figure 2 below.

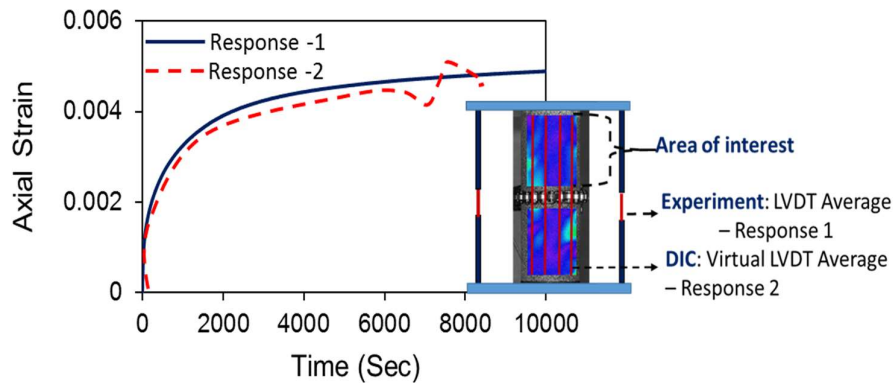


Figure 2: DIC Validation

In figure 2, slight variation between two responses can be perceived after 800 second approximately which gets intensified around/after 7000 seconds. This variation in above responses can be attributed to the fundamental difference between two strain measurement approaches. In actual experiment, LVDTs measure overall vertical displacement of top loading plate and does not get influenced from sample's failure state. On the other hand, virtual strain gauges DIC analysis are the imaginary lines over the image's area of interest (i.e. AOI) which inherits explicit dependency on pixel contrast and corresponding pixel movements. Therefore, as the sample undergoes failure, the corresponding crack creates new surfaces which induces loss of pixels over the localised region, thus affects the overall vertical displacement measurement from virtual strain gauges. Additionally, the chosen area of interest in DIC response does not cover the entire sample portion as in the case of actual LVDTs. Thus, minor variations in above two response can be anticipated and justified. Apart from this, the overall response

of DIC vertical deformation measurement is in good agreement with the experimental observations, hence assures the validity of proposed approach for full field strain evaluation.

In terms of conventional analysis, load-displacement response from uniaxial compression test provide macroscopic sample properties like compressive strength and elastic modulus. Additionally, failure mode (i.e. with prominent shear band in presented case) and crack inclination could also provide a subtle hint towards the stress state around cracked portion. Overview of the above properties have been outlined in table 1 below.

Table 1: Macroscopic material properties

Sr. No.	Sample Property	Value
1	Uniaxial Compression Strength (UCS)	34.9 MPa
2	Elastic Modulus (E)	200 MPa
4	Fracture Angle (θ)	$\sim 66^\circ$

In addition, estimation of cohesion and friction angle can also be derived from Mohr's circle approach provided that more such experiments on samples with different aspect ratio or confining pressure can be performed. Furthermore, energy consumed during the above process of sample failure can also be calculated. However, fracture energy and toughness estimation would not be possible from above tests alone. Overall, one can conclude that the conventional analysis may provide a good overview of sample's global response and its key characteristics. However, it is still not possible to derive any inference regarding sample's material behaviour crucial for determining the local scale material properties. Therefore, this paper has analysed the sample's local scale behaviour using image processing technique and presented the full field strain evolution in collaboration with conventional load-displacement response in figure 3 below. Von-Mises strain is used as an effective indicator of material's distortion and plastic deformation, has been chosen for this purpose. In addition, a virtual section 'x-x' has also been taken across sample height to derive the information regarding strain localisation and evolution in quantitative terms.

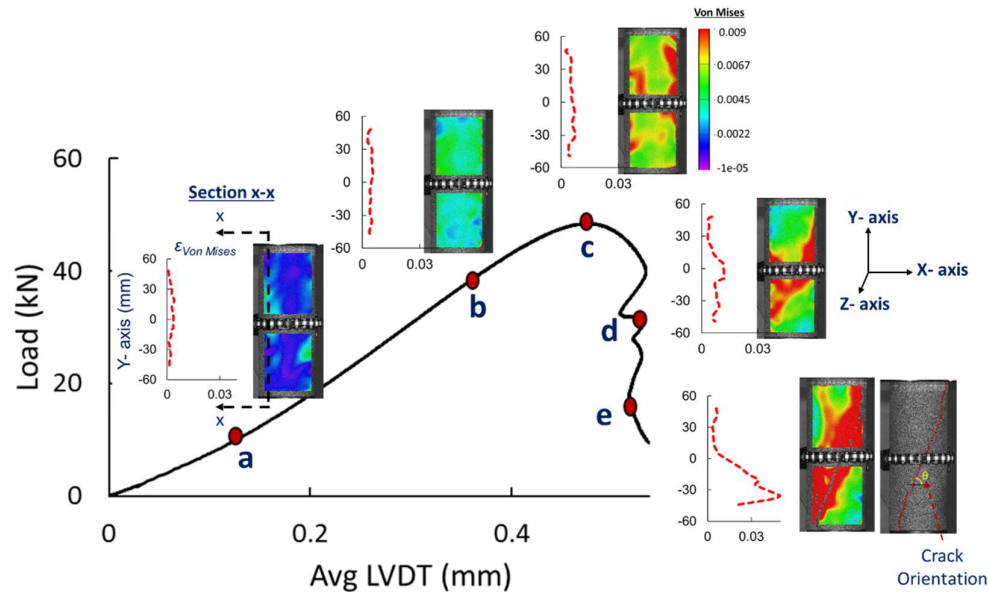


Figure 3: Macroscopic load displacement response synchronised with local scale von-mises strain evolution along x-x axis

For further discussion, the load-displacement response of sample was divided into five main parts. At point 'a', overall strain distribution pattern can be observed to be relatively uniform in major portion of sample with diffused heterogeneity in random order. This irrelevant anisotropy in strain distribution at the early stage can be attributed to the closing of pre-existing pores and heterogeneity of the rock. Thereafter, the rock sample undergoes relatively uniform deformation under external axial symmetric

compressive loading. This can be confirmed from the contour plots at point 'b' which shows relative uniformity in deformation throughout the AOI with about 36% increase in maximum Von-mises strain across 'x-x' section with respect to maximum strain at point 'a'. This point of maximum strain is close to the central portion of sample i.e. $\pm 20\text{mm}$ from centre.

Afterwards, initiation of strain localisation can be observed at point 'c' which is the global peak of load-displacement response. Thereafter, significant degradation in strength at global scale from load-displacement plot can be observed. This global strength reduction can be attributed to the localised material damage which can be confirmed from full field strain evolution plots. Unlike the initial homogeneity in strain distribution at point 'b', significant localisation of material deformation can be observed across sample in the form of cross-band and becomes more visually evident at point 'c'. However, no significant change in strain can be observed in the portion outside this localisation band. The point of maximum strain on section 'x-x' also shifts to -30 mm (i.e. lower portion) from centre.

Eventually, this localised zone evolves into well-developed shear band at point 'e' resulting in the overall structural instability with failure plane inclined (i.e. θ) at 66° with the horizontal line. This can be further confirmed from the strain jump of $\sim 500\%$ across 'x-x' section at -30mm from centre. Besides this localised instability, the overall global loading rate has always been maintained under quasi-static limit. The overall global response of cylindrical sample is just the outcome of this mechanism of localised material deformation. Therefore, capturing material strength evolution at local scale should be the focus for numerical modelling approach to capture the realistic sample response under any given loading conditions. We have further investigated the overall Von-mises strain evolution across shear band region. Sets of reference 7-8 points have been taken across the shear band constituting region-1 for our analysis. In addition, few other regions have also been chosen depending upon its distance from shear band as shown in figure 4.

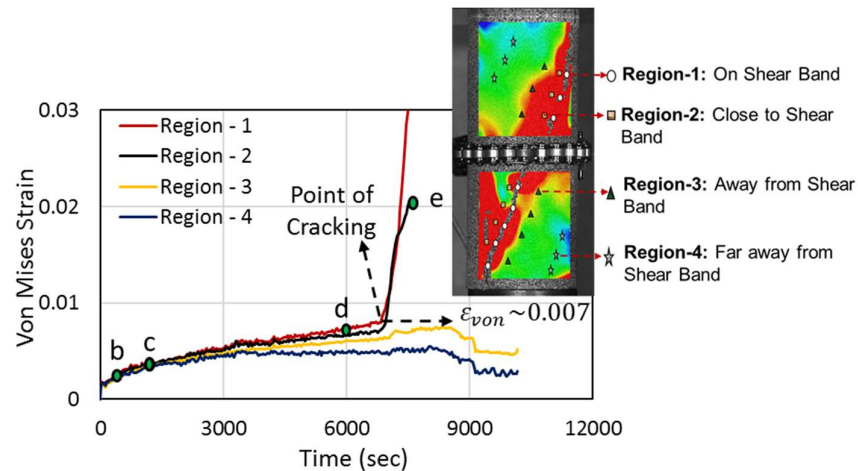


Figure 4: Localized strain evolution with time

In figure 4, one can observe that strain evolution is uniform in all four regions till point 'b' which confirms our previous conclusion of homogeneity of strain distribution in earlier stages. However, later on after point 'b', bifurcation in strain evolution can be observed which continuously increases to point 'c' and becomes evidently high at point 'd'. Additionally, strain magnitude in region 1 is always maximum throughout the test. Thus, one can infer here that under axial symmetric compressive loading with global loading rate under quasi-static conditions, rock material across region 1 experienced much higher strains. Consequently, inter-granular stresses will also get localised in this region resulting in higher localised damage. Eventually, at time 6675 s failure of the material in this localised region resulted in the sudden jump in strain magnitude. The magnitude of maximum localised Von-mises strain at failure is about 0.0075. This localised failure also induces localised dynamics depending upon the width of shear band, affecting the strain evolution in region 2. However, the other portion of sample away from this localised band was under relaxation due to energy release during overall structural failure process. These observation and failure strain quantification would be a representative of material strength property at local scale under mixed-mode loading conditions which is an important material characteristic required constitutive modelling.

In addition to above, we can also extend our discussion to shear band thickness calculation. For this purpose, figure 5 shows the evolution of Von Mises strain along the height of specimens during the test procedure. The purpose of this illustration is to show the development of localization zones in tested specimens. Therefore, two operations were performed on Von Mises strain over covered area by DIC system to present the variation of shear failure plane. Firstly, the average of obtained Von Mises strain was calculated at given section 'x-x' height then these strains were sorted in descending order, ignoring the correlation between strain and position. This is a step needed to condense the rich experimental data to retain only the statistics of the results, and is in line with the statistical homogenisation discussed in Einav and Collins (2009). As it can be seen in this figure, the evolution of Von Mises strain showed more localized behaviour after yielding.

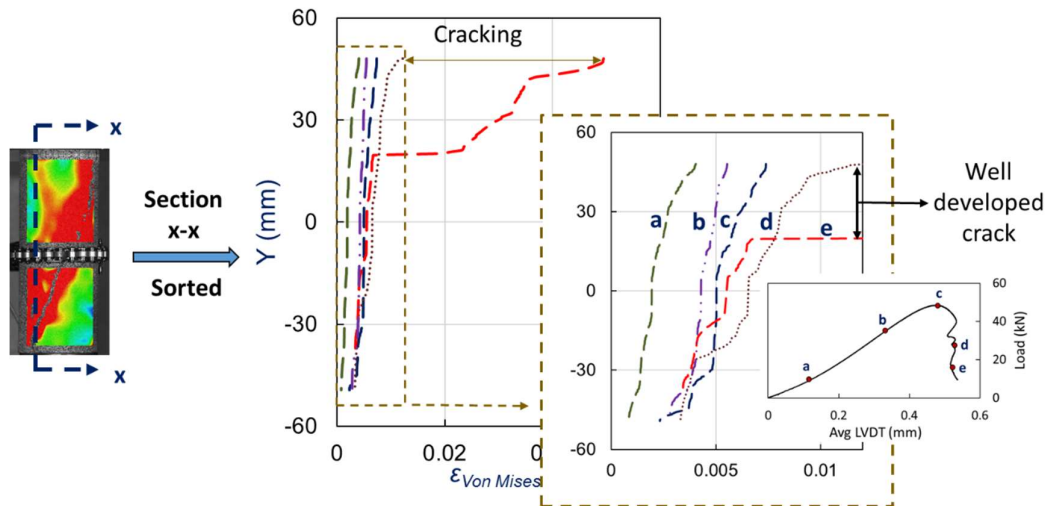


Figure 5: Estimation of shear band thickness

4 Conclusions

This paper has presented an approach to analyse localised failure in conjunction with macroscopic sample response using image processing approach. In this direction, lateral strain controlled UCS test has been conducted to delay the fracturing process to facilitate the application of DIC technique. The obtained full field strain has been used to analyse localised failure process and synchronised with the macroscopic load-displacement response. Synchronised data provides a complete picture on the failure process, while the analysis of shear band evolution supplies more quantitative data for the evaluation of shear band thickness. They are all useful for the development and validation of constitutive models taking into account localised nature of failure in rocks (Giang D. Nguyen, Korsunsky, and Einav 2014; Giang D. Nguyen et al. 2016; G. D. Nguyen, Einav, and Korsunsky 2012; Le et al. 2018).

Acknowledgements

The authors gratefully acknowledge the Australian Research Council (ARC) and OZ Minerals Ltd for their financial support for this research through the Linkage Project LP150100539. Support from the ARC to Giang D. Nguyen & Ha H. Bui (projects FT140100408 & DP170103793) is also acknowledged. The authors also thank honours project students C. Dullona, Z. Naimi & M. Zamparelli for their support in carrying out the experiments.

References

- Belrhiti, Y, J C Dupre, O Pop, A Germaneau, P Doumalin, M Huger, and T Chotard. 2017. "Combination of Brazilian Test and Digital Image Correlation for Mechanical Characterization of Refractory Materials." *Journal of the European Ceramic Society* 37 (5). Elsevier Ltd:2285–93. <https://doi.org/10.1016/j.jeurceramsoc.2016.12.032>.
- Bobet, A., A.Fakhimi, S. Johnson, J.Morris, F.Tonon, and M. Ronald Yeung. 2009. "Numerical Models in Discontinuum Media: Review of Advances for Rock Mechanics Applications." *Journal of Geotechnical and Geoenvironmental Engineering* 135 (11):1547–61.
- Candamano, S, E Sgambitterra, C Lamuta, L Pagnotta, Sudip Chakraborty, and F Crea. 2019. "Graphene Nanoplatelets in Geopolymeric Systems : A New Dimension of Nanocomposites," 1–10.

- Cao, Rihong, Hang Lin, and Ping Cao. 2018. "Strength and Failure Characteristics of Brittle Jointed Rock-like Specimens under Uniaxial Compression : Digital Speckle Technology and a Particle Mechanics Approach," 1–23.
- Cheng, Y. P., Y. Nakata, and M. D. Bolton. 2003. "Discrete Element Simulation of Crushable Soil." *Géotechnique* 53 (7):633–41. <https://doi.org/10.1680/geot.2003.53.7.633>.
- Correlation Solutions. 2018. *VIC-3D Reference Manual - Correlation Solutions*.
- Einav, Itai, and Ian Collins. 2009. "A Thermomechanical Framework of Plasticity Based on Probabilistic Micromechanics." *Journal of Mechanics of Materials and Structures* 3 (5):867–92. <https://doi.org/10.2140/jomms.2008.3.867>.
- Filipussi, D.A., C.A. Guzmán, H.D. Xargay, C. Hucailuk, and D.N. Torres. 2015. "Study of Acoustic Emission in a Compression Test of Andesite Rock." *Procedia Materials Science* 9. Elsevier B.V.:292–97. <https://doi.org/10.1016/j.mspro.2015.04.037>.
- Gui, Y., H. H. Bui, and J. Kodikara. 2015a. "An Application of a Cohesive Fracture Model Combining Compression, Tension and Shear in Soft Rocks." *Computers and Geotechnics* 66. Elsevier Ltd:142–57. <https://doi.org/10.1016/j.compgeo.2015.01.018>.
- He, Wenhao, and Asadollah Hayatdavoudi. 2018. "Journal of Petroleum Science and Engineering A Comprehensive Analysis of Fracture Initiation and Propagation in Sandstones Based on Micro-Level Observation and Digital Imaging Correlation." *Journal of Petroleum Science and Engineering* 164 (November 2017). Elsevier Ltd:75–86. <https://doi.org/10.1016/j.petrol.2018.01.041>.
- Ji, Ming, Kai Chen, and Hong Jun Guo. 2018. "Constitutive Model of Rock Uniaxial Damage Based on Rock Strength Statistics." *Advances in Civil Engineering* 2018. <https://doi.org/10.1155/2018/5047834>.
- Jing, L, and J A Hudson. 2002. "Numerical Methods in Rock Mechanics." *International Journal of Rock Mechanics & Mining Sciences* 39 (4):409–27. [https://doi.org/10.1016/S1365-1609\(02\)00065-5](https://doi.org/10.1016/S1365-1609(02)00065-5).
- Jing, Lanru, and Ove Stephansson. 2007. "Constitutive Models of Rock Fractures and Rock Masses - The Basics." *Developments in Geotechnical Engineering* 85:47–109. [https://doi.org/10.1016/S0165-1250\(07\)85003-6](https://doi.org/10.1016/S0165-1250(07)85003-6).
- Jonsén, P, H Häggblad, and K Sommer. 2007. "Tensile Strength and Fracture Energy of Pressed Metal Powder by Diametral Compression Test" 176:148–55. <https://doi.org/10.1016/j.powtec.2007.02.030>.
- Le, Linh A., Giang D. Nguyen, Ha H. Bui, Abdul Hamid Sheikh, and Andrei Kotousov. 2018. "Localised Failure Mechanism as the Basis for Constitutive Modelling of Geomaterials." *International Journal of Engineering Science* 133:284–310. <https://doi.org/10.1016/j.ijengsci.2018.09.004>.
- Lingga, Bob. A, Derek B. Apel, Mohammadali Sepehri, and Yuanyuan Pu. 2019. "Assessment of Digital Image Correlation Method in Determining Large Scale Cemented Rockfill Strains." *International Journal of Mining Science and Technology*, 7–12.
- Lisjak, A., and G. Grasselli. 2014. "A Review of Discrete Modeling Techniques for Fracturing Processes in Discontinuous Rock Masses." *Journal of Rock Mechanics and Geotechnical Engineering* 6 (4). Elsevier Ltd:301–14. <https://doi.org/10.1016/j.jrmge.2013.12.007>.
- Lockner, D. 1993. "The Role of Acoustic Emission in the Study of Rock Fracture." *International Journal of Rock Mechanics and Mining Sciences & Geomechanics* 30 (7):883–99. <http://www.sciencedirect.com/science/article/pii/014890629390041B>.
- Mazel, V, S Guerard, B Croquelois, J B Kopp, J Girardot, H Diarra, V Busignies, and P Tchoreloff. 2016. "Reevaluation of the Diametral Compression Test for Tablets Using the FI Attened Disc Geometry" 513:669–77.
- Munoz, H, and A Taheri. 2017. "Specimen Aspect Ratio and Progressive Field Strain Development of Sandstone under Uniaxial Compression by Three-Dimensional Digital Image Correlation." *Journal of Rock Mechanics and Geotechnical Engineering* 9 (4). Elsevier Ltd:599–610. <https://doi.org/10.1016/j.jrmge.2017.01.005>.
- Müter, D, H O Sørensen, D Jha, K N Dalby, and S L S Stipp. 2014. "X-Ray Tomography and Finite Elements Simulations of Rock Mechanics" 20 (Suppl 3):818–19. <https://doi.org/10.1017/S1431927614005819>.
- Nath, Fatick, and Mehdi Mokhtari. 2018. "Optical Visualization of Strain Development and Fracture Propagation in Laminated Rocks," 1–26.
- Needleman, A. 2013. "Some Issues in Cohesive Surface Modeling." *Procedia IUTAM* 10. Elsevier B.V.:221–46. <https://doi.org/10.1016/j.piutam.2014.01.020>.
- Nguyen, G. D., I. Einav, and A. M. Korsunsky. 2012. "How to Connect Two Scales of Behaviour in Constitutive Modelling of Geomaterials." *Géotechnique Letters* 2 (3):129–34. <https://doi.org/10.1680/geolett.12.00030>.

- Nguyen, Giang D., Alexander M. Korsunsky, and Itai Einav. 2014. "A Constitutive Modelling Framework Featuring Two Scales of Behaviour: Fundamentals and Applications to Quasi-Brittle Failure." *Engineering Fracture Mechanics* 115:221–40. <https://doi.org/10.1037/0033-2909.126.1.78>.
- Nguyen, Giang D., Chi T. Nguyen, Vinh P. Nguyen, Ha H. Bui, and Luming Shen. 2016. "A Size-Dependent Constitutive Modelling Framework for Localised Failure Analysis." *Computational Mechanics* 58 (2). Springer Berlin Heidelberg:257–80. <https://doi.org/10.1007/s00466-016-1293-z>.
- Nguyen, Nhu H.T., Ha H. Bui, Giang D. Nguyen, and Jayantha Kodikara. 2017. "A Cohesive Damage-Plasticity Model for DEM and Its Application for Numerical Investigation of Soft Rock Fracture Properties." *International Journal of Plasticity*. <https://doi.org/10.1016/j.applthermaleng.2017.08.158>.
- Nguyen, Thai Binh, Sean Mcnamara, Jérôme Crassous, and Axelle Amon. 2017. "Experimental Study of Shear Bands Formation in a Granular Material" 10001:1–5.
- Park, J. W., C. Park, J. W. Song, E. S. Park, and J. J. Song. 2017. "Polygonal Grain-Based Distinct Element Modeling for Mechanical Behavior of Brittle Rock." *International Journal for Numerical and Analytical Methods in Geomechanics* 41 (6):880–98. <https://doi.org/10.1002/nag.2634>.
- Pouya, Ahmad, and Pedram Bemani Yazdi. 2015. "A Damage-Plasticity Model for Cohesive Fractures." *International Journal of Rock Mechanics and Mining Sciences* 73. Elsevier:194–202. <https://doi.org/10.1016/j.ijmms.2014.09.024>.
- Report, A. 1998. "APPLICATION OF X-RAY TOMOGRAPHY TO MEASUREMENT OF FRACTURES IN ROCKS," no. June.
- Schöpfer, Martin P.J., Steffen Abe, Conrad Childs, and John J. Walsh. 2009. "The Impact of Porosity and Crack Density on the Elasticity, Strength and Friction of Cohesive Granular Materials: Insights from DEM Modelling." *International Journal of Rock Mechanics and Mining Sciences* 46 (2):250–61. <https://doi.org/10.1016/j.ijmms.2008.03.009>.
- Shara, Mansour, Luming Shen, and Qingfeng Xu. 2018. "Characterisation of Mechanical Behaviour of 3D Printed Rock-like Material with Digital Image Correlation." *International Journal of Rock Mechanics and Mining Sciences* 112 (April):122–38.
- Stirling, Ross A, David J Simpson, and Colin T Davie. 2013. "International Journal of Rock Mechanics & Mining Sciences The Application of Digital Image Correlation to Brazilian Testing of Sandstone." *International Journal of Rock Mechanics and Mining Sciences* 60. Elsevier:1–11. <https://doi.org/10.1016/j.ijmms.2012.12.026>.
- Viggiani, Gioacchino, and Jacques Desrues. 2013. "X-Ray Micro toMography as a Tool for Studying Localized Damage / Deformation in Clay Rock," 91–98.
- Wang, Huanran, Chunying Ren, Yin Wan, and Danian Chen. 2019. "Experimental Study on Fracture Process of Sintered Nd-Fe-B Magnets during Dynamic Brazilian Tests."
- Xing, H Z, Q B Zhang, D Ruan, S Dehkhoda, G X Lu, and J Zhao. 2018. "Full-Field Measurement and Fracture Characterisations of Rocks under Dynamic Loads Using High-Speed Three-Dimensional Digital Image Correlation," 1–31.
- Zehnder, Alan T, Jay Carroll, Kavan Hazeli, Ryan B Berke, Garrett Pataky, Matthew Cavalli, and Alison M Beese. 2017. *Fracture, Fatigue, Failure and Damage Evolution, Volume 8*. Vol. 8. <https://doi.org/10.1007/978-3-319-42195-7>.
- Zhang, Xiaojuan, Yanan Yi, Haibin Zhu, Guangyan Liu, Libin Sun, Li Shi, Han Jiang, New Energy Technology, and Applied Mechanics. 2018. "Measurement of Tensile Strength of Nuclear Graphite Based on Ring Compression Test," 1–16.
- Zhao, Guangming, Lixiang Xie, and Xiangrui Meng. 2014. "A Damage-Based Constitutive Model for Rock under Impacting Load." *International Journal of Mining Science and Technology* 24 (4). China University of Mining & Technology:505–11. <https://doi.org/10.1016/j.ijmst.2014.05.014>.

Appendix C


Numerical Analysis of Fracture Propagation in Brazilian Disc Test

Verma, R.K., Nguyen, G.D., Karakus, M., Taheri, A., Bui, H.H. (2018).
“Numerical Analysis of Fracture Propagation in Brazilian Disc Test”.
ACCM 2018, 3rd Australian Conference on Computational Mechanics,
Deakin University, Melbourne, Australia.

Statement of Authorship

Title of Paper	Numerical Analysis of Fracture Propagation in Brazilian Disc Test
Publication Status	<input checked="" type="checkbox"/> Published <input type="checkbox"/> Accepted for Publication <input type="checkbox"/> Submitted for Publication <input type="checkbox"/> Unpublished and Unsubmitted work written in manuscript style
Publication Details	Verma, R.K., Nguyen, G.D., Karakus, M., Taheri, A., Bui, H.H. (2018). "Numerical Analysis of Fracture Propagation in Brazilian Disc Test". ACCM 2018, 3rd Australian Conference on Computational Mechanics, Deakin University, Melbourne, Australia.


Principal Author

Name of Principal Author (Candidate)	Rupesh Kumar Verma		
Contribution to the Paper	Development of constitute model from the provided generic framework. Numerical implementation of model, performed numerical analysis and result analysis. Wrote and revised the manuscript		
Overall percentage (%)	70		
Certification:	This paper reports on original research I conducted during the period of my Higher Degree by Research candidature and is not subject to any obligations or contractual agreements with a third party that would constrain its inclusion in this thesis. I am the primary author of this paper.		
Signature		Date	06 Dec 2019

Co-Author Contributions

By signing the Statement of Authorship, each author certifies that:

- i. the candidate's stated contribution to the publication is accurate (as detailed above);
- ii. permission is granted for the candidate to include the publication in the thesis; and
- iii. the sum of all co-author contributions is equal to 100% less the candidate's stated contribution.

Name of Co-Author	Giang D. Nguyen		
Contribution to the Paper	Development of generic framework for constitute model. Supervised the technical development. Evaluated and revised the manuscript.		
Signature		Date	06 Dec 2019

Name of Co-Author	Murat Karakus		
Contribution to the Paper	Supervised the technical development. Evaluated and revised the manuscript.		
Signature		Date	06/12/2019

Name of Co-Author	Abbas Taheri		
Contribution to the Paper	Supervised the technical development. Evaluated and revised the manuscript.		
Signature		Date	06 Dec 2019

Name of Co-Author	Ha H. Bui		
Contribution to the Paper	Development of generic framework for constitute model. Supervised the technical development. Evaluated and revised the manuscript.		
Signature		Date	06 Dec 2019

Numerical Analysis of Fracture Propagation in Brazilian Disc Test

Rupesh K. Verma^{1,a}, Giang D. Nguyen^{1,b*}, Murat Karakus^{1,c}, Abbas Taheri^{1,d}
and Ha H. Bui^{2,e}

¹Department of Civil, Mining and Environment Engineering, University of Adelaide, Australia.

²Department of Civil Engineering, Monash University, Australia.

^arupesh.verma@adelaide.edu.au, ^bg.nguyen@adelaide.edu.au, ^cmurat.karakus@adelaide.edu.au,
^dabbas.taheri@adelaide.edu.au, ^eha.bui@monash.edu

Keywords: Brazilian disc test, Crack initiation, Quasi-brittle material, Dis-continuum, Cohesive Joint Model, Plasticity, Damage.

Abstract.

Brazilian disc test is an indirect approach for determining tensile strength of quasi-brittle geo-materials such as rocks. This test is practically more convenient to perform as compared to uniaxial tensile strength test, making it relatively more popular. However, determining crack initiation position and crack pattern in Brazilian disc test sample still requires more attention. Theoretically, crack should initiate at the center of the sample as a result of material tensile failure under uniform tensile stress generated by diametrical compressive loading. However, majority of experimental data suggests crack initiation occurs close to the point of loading. This deviation of experimental observations from theoretical consideration could be better understood in terms of material damage distribution. In this view, this paper presents a three dimensional numerical modelling approach to replicate Brazilian disc test, explaining crack initiation and propagation mechanism in rock. In the proposed methodology, rock sample is replicated as a combination of deformable tetrahedral blocks in dis-continuum based numerical modelling tool 3DEC by Itasca. These tetrahedral blocks interact with each other via cohesive boundaries controlling the basic characteristics of block separation and frictional contact, facilitating the realistic simulation of material failure under given loading conditions. The effect of plastic deformation and material damage has also been incorporated via a damage-plasticity based cohesive joint model controlling the behavior of cohesive boundaries of tetrahedral blocks. For this purpose, a subroutine for cohesive joint model has been written in C++ programming language and implemented in 3DEC as a DLL file. This model is capable of capturing the rock behavior under Mode-I, Mode-II and mixed mode loading conditions. This entire setup is further used to complement the Brazilian disc experimental data available in the literature and for numerical investigations on the effects of rock properties on the fracture pattern. Characteristics of stress, strain and material damage distributions across the sample in three dimensional space are used as the key parameters to explain the crack initiation and propagation mechanism.

Introduction

Brazilian disc test is an indirect approach of testing tensile strength of quasi-brittle material e.g. rock. It was proposed by Carneiro et. al. (1943) based on the experimental fact that under bi-axial loading conditions with compression (i.e. three times smaller than principal tensile stress) in one direction and tensile loading in other, majorities of rock specimen fails in tension [1, 2]. Initially the purpose of this test was to determine the tensile strength of concrete by applying diametrical compressive load on disc shaped specimen which generates uniform tensile stress perpendicular to vertical diametrical axis. As concrete is weak in tension, this tensile stress across vertical axis exceeds material strength and results in splitting failure. Strength to resist this failure i.e. Brazilian tensile strength in MPa (σ_t) can be calculated from following equation [2].

$$\sigma_t = \frac{2P}{\pi Dt} \quad (1)$$

Where, ' P ' is the peak load (kN), ' D ' is the specimen diameter (mm), ' t ' is the specimen thickness (mm). Later on, Rock Mechanics (ISRM-1978) recommended it for testing rock material's tensile strength based on the assumptions of material homogeneity, isotropy and pre-peak linear elasticity [2, 3]. This test was practically more convenient to perform as compared to uniaxial tensile strength test, thus become widely popular.

Despite widespread popularity, Brazilian disc test has always been in controversy since its inception. Main reason for the controversy is difference in Brazilian disc and uniaxial tensile strength test results which many researchers attempted to explain on the basis of crack initiation point in disc specimen. Ideally, crack in disc under uniform tensile stresses should initiate from specimen's center [3]. However, Fairhurst in 1964 used Griffith type fracture criterion to prove that for small loading angles, failure may occur away from specimen's center resulting in under-estimate the material's tensile strength [4]. Colback (1966) used high speed photography to determine the point of fracture initiation and suggested that for any valid Brazilian disc test, crack must initiate from the disc's center to cause axial splitting of specimen [5]. Hudson (1972) used scanning electron micrograph to analyze the point of crack initiation and concluded that use of flat steel plate in Brazilian test will always cause failure initiation beneath the loading point, thus questioned its feasibility [6].

On contrary, Jaeger et.al. (1967) supported the feasibility of Brazilian disc test on the basis of theoretical and experimental results of tensile strength tests on three different rocks [7]. Yanagidani et. al. (1978) analyzed strain variation on specimen surface using transient recorder (TR) and observed that crack initiated from tensile stress zone [8]. Mellor et. al. (1971) suggested the use of curved-jaw loading plate to make Brazilian disc test results comparable with uniaxial tensile strength test [9]. Wang et. al. (2003) suggested the use flattened Brazilian disc specimen in spite of conventional round shaped specimen to ensure the crack generation at specimen center [10]. Yong et. al. (2009) proposed to replace steel bars from spacers for load application which can reduce the stress concentration near loading point [11]. In numerical modelling, Yu. et. al. (2005) performed three dimensional Finite Element analysis (3D-FEM) to analyze the failure mechanism of Brazilian disc sample and concluded that crack initiation will always occur away from center, thus, discarded the use of Brazilian disc test for tensile strength measurement [12]. Van De Steen et. al. (2005) used Boundary element code to simulate Brazilian disc test and proposed that fracture in disc initiate in close vicinity to loading plates [13].

Despite many such efforts, consensus on crack initiation and propagation mechanism in Brazilian disc have not been made yet. In this view, this paper aims to analyze the material damage distribution in Brazilian disc specimen using three dimensional dis-continuum based numerical modelling technique i.e. 3DEC-Itasca(2013) [14]. To capture the realistic behavior of rock material, a coupled elastic-plastic-damage cohesive crack model, which was developed for the purpose of fracture analysis and rock burst studies in [15], has been implemented in 3DEC as DLL file. This model is efficient in capturing the influence of 'process zone' in front of actual crack under complex loading conditions. Here, this competent tool is further used to understand the characteristics of rock fracturing and explain crack initiation/propagation mechanism in Brazilian disc specimen.

Methodology

Intact rock can be considered as granular material with assembly of minerals interacting via inter-granular cementitious forces responsible for overall material strength. As stresses at inter-granular scale overcome material strength, it results in degradation of cementitious forces which eventually cause crack initiation. To capture this mechanism of material damage, this paper proposes to use a dis-continuum based three dimensional numerical modelling tool i.e. 3DEC-Itasca, where rock sample is idealized as an assembly of deformable tetrahedral blocks interacting via interface elements i.e. joint constitutive model. Here, joint constitutive model plays crucial role in simulating crack initiation mechanism. However, currently available joint models in 3DEC e.g. Mohr-Coulomb, Continuously Yielding etc. are not efficient in capturing the actual post-peak material behavior incorporating gradual decay of material strength, crucial for realistic crack initiation and propagation mechanism.

Therefore, an elastic-plastic-damage coupled cohesive joint model proposed by Verma et al. [15] have been implemented in 3DEC as a DLL file [15]. This model is efficient in capturing the influence of damage on gradual degradation of material strength in terms of in-elastic inter-block relative displacement. Here, material damage coupled with in-elastic displacement physically signifies degradation in inter-granular cementitious forces which directly influences normal (σ_n) and shear (\mathbf{t}_s) components of stress state at each intergranular contacts as follows [15].

$$\sigma_n = (1 - D)k_n^0 u_n^e - Dk_n^0 \langle u_n^e \rangle = \begin{cases} (1 - D)k_n^0 u_n^e & \text{Tension} \\ k_n^0 u_n^e & \text{Compression} \end{cases} \quad (2)$$

$$\mathbf{t}_s = (1 - D)k_s^0 \mathbf{u}_s^e \quad (3)$$

where, D denotes material damage parameter with maximum value of 1, k_n^0 and k_s^0 are contact stiffness in normal and shear direction, $u_n^e = u_n - u_n^p$ and $\mathbf{u}_s^e = \mathbf{u}_s - \mathbf{u}_s^p$ are elastic components, as the difference between total (u_n and \mathbf{u}_s) and plastic (u_n^p and \mathbf{u}_s^p) relative contact displacements in normal and shear directions, respectively. As the shear displacements are in two directions, all shear displacements are represented in vector (bold) forms. Furthermore, the following expression (i.e. Eq. 4) of yield surface which evolves with material damage is used.

$$f = \sqrt{\mathbf{t}_s \cdot \mathbf{t}_s} + \sigma_n (c - \sigma_n \tan^2 \Phi) - \sigma_t (c - \sigma_t \tan^2 \Phi) = 0 \quad (4)$$

In the above equation, c , σ_t and Φ denote material strength parameters i.e. contact's cohesion, tensile strength and friction angle, respectively. At each contact, material damage is coupled with relative plastic displacements of contact by following expression.

$$dD = \sqrt{A (du_n^p)^2 + B (\mathbf{du}_s^p \cdot \mathbf{du}_s^p)} \quad (5)$$

Where, dD increment in damage, A and B controls rate of damage in normal and shear direction. Further, direction of relative plastic contact displacements have been controlled by following plastic potential (g) expression i.e. non-associated flow rule.

$$g = \sqrt{\mathbf{t}_s \cdot \mathbf{t}_s} + \sigma_n (c - \sigma_n \tan^2 \Psi) - \sigma_t (c - \sigma_t \tan^2 \Psi) = 0 \quad (6)$$

where, Ψ denotes dilation angle. This model is capable of capturing the realistic material behavior in mode-I, mode-II and mixed model loading conditions. For interested readers, further detailed of the above cohesive joint model with verification, validation and applications can be found in [15].

Numerical Simulation of Brazilian Disc test

This section presents the numerical investigation of Brazilian disc test on medium grained soft rock (i.e. Gosford sandstone) sample of diameter (d) 50 mm and thickness (t) of 25 mm [16]. The aim here is to understand the crack initiation and propagation mechanism on the basis of damage evolution in Brazilian disc sample under bi-axial loading conditions. To conduct the above analysis in computationally efficient way, this paper adopts specimen with smaller thickness/diameter ratio ($t/d = 0.08$). Size of the tetrahedral blocks (i.e. 2 mm) in disc sample is adopted on the basis of computational feasibility and mesh sensitivity.

Boundary conditions. Load is applied via flat steel plate with elastic properties i.e. density (ρ_{steel}), young's modulus (E_{steel}) and poisson's ratio (ν_{steel}) are presented in table 1. Top plate is given downward velocity while keeping the bottom plate fixed. Downward velocity of top plate is determined on the basis of quasi-static strain rate (i.e. $\dot{\epsilon} = 10^{-4}$ or less) conditions as follows.

$$v = (\dot{\epsilon}) (d) = (10^{-4}) (50) = 5 \times 10^{-3} \text{ mm/s.} \quad (7)$$

Therefore, downward velocity of 5×10^{-4} mm/s (i.e. 10 times smaller than required) is applied to top steel plate (i.e. velocity control).

Model calibration. At first, tetrahedral blocks are assigned in-built elastic material model with properties i.e. density (ρ), young's modulus (E), poison's ratio (ν), from experiments (table-1). Now, the setup of 3DEC with implemented cohesive joint model has to be calibrated with experimental data to obtain the micro-parameters of joint constitutive model. In this view, first step is to calibrate model's elastic response with experimental data which is primarily controlled by normal (k_n^0) and shear contact stiffness (k_s^0) and relative contact displacement. Ideally, in the given assembly of deformable blocks (representing rock minerals), magnitude of contact stiffness should be infinite to ensure negligible contribution of relative contact displacement in overall elastic deformation. However, numerically it is not feasible. Thus, a very high value to contact stiffness should be assigned in such a way that further increase in its magnitude results negligible change in overall material's elastic response.

On the other hand, cohesion (c), tensile strength (σ_t) and friction (Φ) are strength parameters controlling the peak of load-displacement plot. On individual basis, tensile strength controls the initiation and density of tensile cracks while cohesion and friction collaboratively controls the shear induced cracks, crucial for structural stability of sample. Thus, these parameters should be calibrated to compliment peak strength of experimental observation along with appearance of anticipated crack pattern. Damage parameters i.e. A and B , controls material damage rate in normal and shear direction of any contact plane. It should calibrated on the basis fracture energy in mode-1 (i.e. pure tension) and mode-2 (i.e. pure shear) loading conditions. Thus, parameter ' A ' here has been calibrated using mode-1 fracture energy (i.e. 0.722 Nmm/mm^2) via analytical solution of pure tension loading conditions [15]. However due to unavailability of mode-2 fracture energy, parameter ' B ' has been calibrated to match the peak, post-peak response of simulation with experimental observation. Here, in this test alone, influence of dilation angle (Ψ) is not very significant. Thus a very small value of dilation angle is being adopted. All the calibrated cohesive joint micro parameters are presented in table 1 as follows.

Table 1 Calibrated Parameters

ρ_{steel}	8050 [kg/m ³]	ρ	2600 [kg/m ³]	σ_t	4 [MPa]
E_{steel}	208 [GPa]	E	2.4 [GPa]	Φ	30
ν_{steel}	0.25	ν	0.25	Ψ	5
		k_n^0	8E6 [MPa/mm]	A	312
		k_s^0	6.89E6 [MPa/mm]	B	20
		c	6 [MPa]		

Results and discussion

This section presents the detailed results of Brazilian disc simulation on Gosford sandstone i.e. soft rock. As per literature, experimental response of load-displacement curve has been shifted left to remove initial non-linear section due to early compaction of sample [16]. Results of 3DEC numerical simulation have been digitized and scaled up to compare it with experimental response.

Fig. 1(a) presents the final results of the above simulation and its comparison with experimental data. It can be seen that the peak strength prediction by 3DEC simulation is in close agreement with experimental observation. Material response in terms of pre-peak and post peak load displacement curve also agrees well with experiment. In addition, final crack and corresponding damage pattern of numerical simulation sample shows similar resemblance with actual failed disc specimen from experiment i.e. fig. 1(b) and 1(c). Thus, overall numerical simulation of Brazilian disc test can capture the trend in response and the cracking patterns experimentally observed. We also acknowledge the

results are not a perfect match in terms of crack pattern (more centered in the experiment than in the simulation) and will improve it in the future.

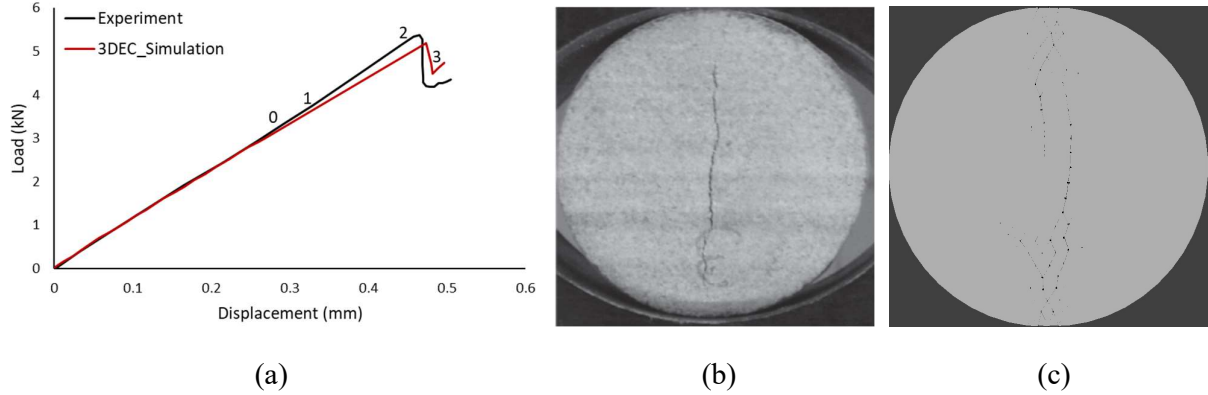


Fig. 1. (a) Load-displacement comparison between experiment [16] and numerical simulation. (b) Experiment_crack pattern [16], (c) 3DEC_crack pattern

Now, to address the question of Brazilian disc test feasibility, it is inevitable to compare it with the tensile strength of the material. Ideally, this actual tensile strength should characterize the material's resistance at inter-granular level to pure tensile loading which in above simulation is represented by inter-block tensile strength micro-parameter (i.e. $\approx \sigma_t = 4$ MPa). On the other hand, material strength obtained by Brazilian disc test is computed as follows.

$$\sigma_t = \frac{2P}{\pi Dt} = \frac{2(5400)}{\pi(50)(25)} = 2.75 \text{ MPa.} \quad (7)$$

Thus, on comparing the calculated strength with actual value, it can be observed that the computed tensile strength from Brazilian Disc test is roughly 31% smaller than the actual value which is a serious under-estimation of material strength. This results is in accord with [11] which reported Brazilian disc strength to be 41% smaller than uniaxial tensile strength. This is a serious anomaly in Brazilian disc test results which can be better understood in terms of stress distribution and material damage evolution in sample, as presented in the following sub-section.

Stress distribution and damage evolution. The proposed three dimensional numerical modelling approach provides an ease to have a thorough view through the sample throughout the test which is impossible in experimental approaches. Using this advantage, principal stresses across specimen have been recorded at three stages i.e. stage 1 to 3, as shown in fig. 1(a) and point '0' denotes stress state at which damage in material started, signifying the beginning of pre-peak in-elastic deformation. These stresses are in equilibrium with contact stresses, establishing direct correlation between observed principal stresses and cohesive joint strength degradation via damage. This degradation in cohesive joint strength parameters is the primary cause of crack initiation and propagation in sample. In addition, thanks to the three dimensional numerical modelling tool approach, point of maximum contact normal (i.e. u_n^{max}) and shear (i.e. u_s^{max}) displacement across the sample have also been identified at each stage throughout the test which is crucial for the analysis of damage evolution.

Fig. 2 presents principal stress distribution with tension taking positive sign. All plots are presented with scale on left end denoting vertical distance in millimeter (or 'mm') from specimen's center and contour scale on right end showing magnitudes of corresponding recorded parameters. In case of displacement vector plots, normal and shear displacement vectors are scaled to achieve better visibility. Length and color of each vector in these plots denotes its magnitude as per contour scale at right end, while arrow showing direction of corresponding displacement. The damage distribution plots are virtually dissected through central diametrical axis and rotated by 90° at each stage to have a clear view of damage distribution across specimen.

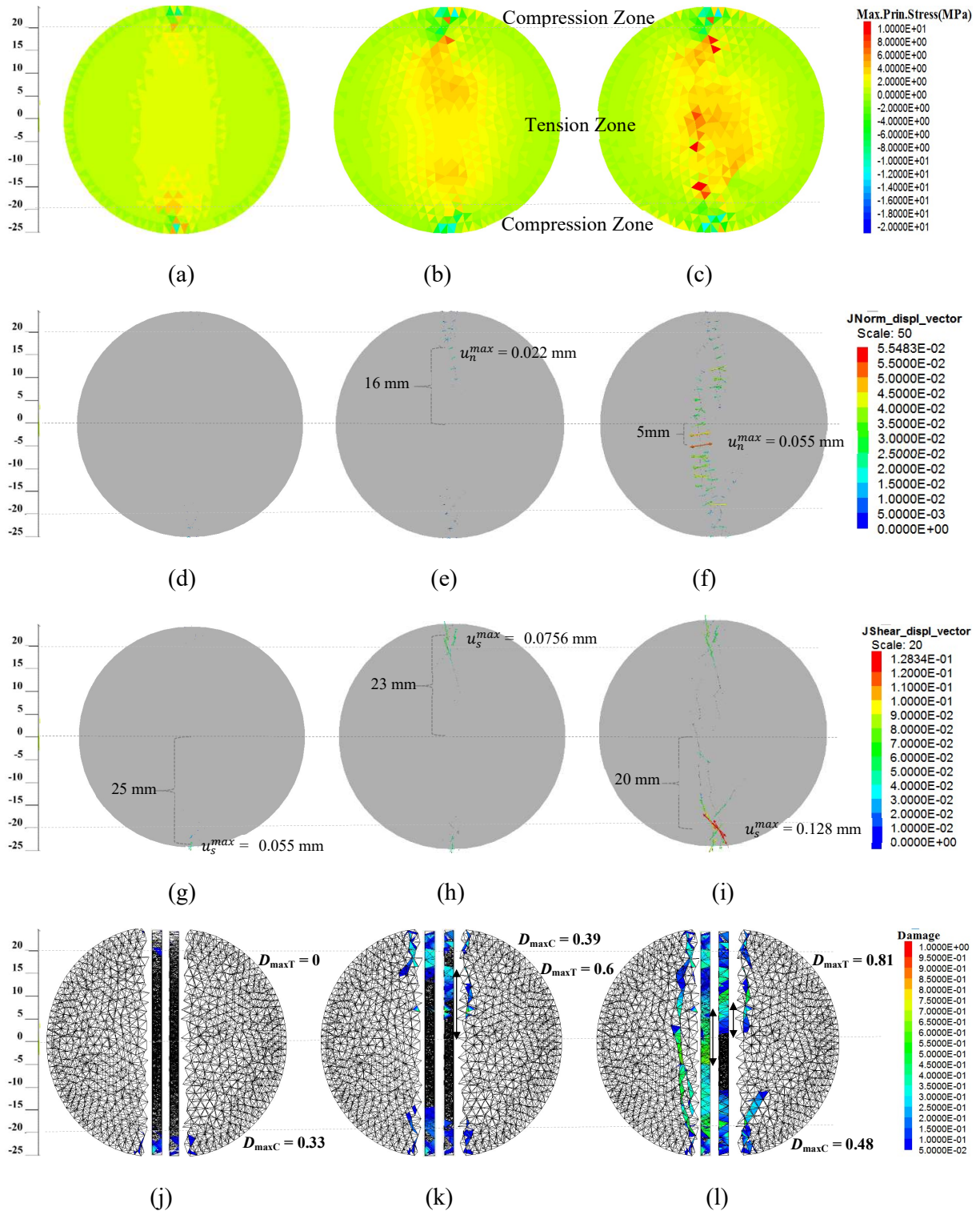


Fig. 2. Principal stress -(a) Stage_1, (b) Stage_2, (c) Stage_3; Normal displacement vectors-(d) Stage_1, (e) Stage_2, (f) Stage_3; Shear displacement vectors-(g) Stage_1, (h) Stage_2, (i) Stage_3; Damage distribution-(j) Stage_1, (k) Stage_2, (l) Stage_3

From the preliminary view of above fig. 2(a)-(c), one can clearly observe that stress distribution across disc specimen along loading direction is quite non-uniform with tensile stresses across central portion of sample and compressive near loading plates. A clear transition from tension to compression can be observed at vertical distance of ± 20 mm from specimen center. Thus, it is convenient here to

name *tension zone* to specimen's central portion (i.e. ± 20 mm vertical distance from specimen center) and *compression zone* to specimen's loading end portion (i.e. 5mm from load points) for our following discussion.

Now at stage 1, fig. 2(a) shows that principal stresses in *tension zone* are uniformly distributed across central diamterical axis with overall magnitude smaller than 4 MPa i.e. tensile strength of cohesive joint model (table 1). In addition, fig. 2(d) shows no sign of contact normal displacement across this zone at this stage. This can be further verified by the observation of no damage in *tension zone* from damage distribution plot as well i.e. fig. 2(j), where ' $D_{\max T}$ ' denotes maximum damage in this zone which is currently zero. Thus, it is appropriate to conclude here that at stage-1, material is undergoing uniform tensile elastic deformation in *tension zone* (i.e. mode-1 loading). On the other hand, tetrahedral blocks beneath in *compression zone* are severely stressed by maximum principal stress of -14 MPa (i.e. compression) which have resulted in maximum interfacial shear displacements (i.e. u_s^{\max}) of 0.055 mm at 25 mm vertical distance from specimen center i.e. fig. 2(g). As a results, material damage has also been observed in this region with a maximum value (i.e. ' $D_{\max C}$ ') of 0.33 at this stage i.e. fig. 2(j). This shows that localized compression has resulted in shear failure which has already exceeded the contact shear strength of cohesive joint model, resulting in material damage. This damage due shearing is the primary reason for crack initiation at loading point in *compression zone* i.e. fig. 2(g). These observations are in accordance with [6] which also shows crack initiation point to be within 5mm from vertical distance from loading points.

Further at stage 2, it can be observed that the tensile stress distribution in *tension zone* has now started exhibiting non-uniformity with overall magnitude close to cohesive joint tensile strength of 4MPa in region 5 to 20 mm (or -5 to -20 mm) from specimen center fig. 2(b). However, in central portion of specimen i.e. ± 5 mm from disc center, tensile stresses are still under this tensile strength cap. As a result, relative normal displacements of tetrahedral block started taking place in above mentioned region of ± 5 to ± 20 mm vertical distance from center. Consequentially, u_n^{\max} has also raised to a magnitude of 0.022 mm at vertical distance of 16 mm away from specimen center i.e. fig. 2(e). This further justifies the increase in $D_{\max T}$ from zero to 0.6 in *tension zone* at vertical distance of 16 mm from specimen center i.e. fig. 2(k). On the other hand, localized compressive stress in top *compression zone* have also increased u_s^{\max} to 0.0756 mm at 23 mm vertical distance from specimen center i.e. fig. 2(h). It resulted increase in $D_{\max C}$ from 0 to 0.39 indicating crack initiation in top *compressive zone* too i.e. fig. 2(k). Here, it important to notice that magnitude of u_s^{\max} is approximately 2.5 times of u_n^{\max} . Still, damage effect of u_n^{\max} is more evident comparatively. This further explains the severity of tensile crack as compare to shear cracks in *compression zone*. As shear crack initiated prior to tension crack, thus, here it appears that crack is propagating from loading ends towards specimen center i.e. fig. 2(d) and 2(e).

Finally at stage-3, fig. 2(c) shows that tensile stresses in specimen have increased across central diamterical axis of sample causing significant damage throughout the *tension zone*. Fig. 2(e) and 2(f) shows the drastic increase in u_n^{\max} from 0.022 mm at stage 2 to a value of 0.055 mm at stage-3. This maximum relative contact normal displacement occurs at 5mm vertical distance from specimen center i.e. fig. 2(f). On average basis also, interfacial normal displacement have been significantly increased in this stage as compare to previous stage. It further justifies the significant increase in material damage from 0 to 0.7 in central portion of tension zone i.e. ± 5 mm from specimen center, where point of maximum material damage (i.e. $D_{\max T} \approx 0.81$) at 6 mm from specimen center i.e. fig. 2(l). In addition, u_s^{\max} has also increased from 0.58 mm to 0.128 mm. This maximum shear displacement took place at a vertical distance of 5 mm from bottom steel plate resulting in increased $D_{\max C}$ from 0.39 to 0.48 in *compression zone*. However, it is still smaller than $D_{\max T}$ i.e. maximum damage in *tension zone* indicating dominance of tensile cracks on structural failure of specimen resulting in softening of load-displacement plot i.e. fig. 1(a).

Thus, it can be inferred that failure mechanism in Brazilian disc sample is a collaborative effort of tensile and compressive (i.e. causing shear failure) stresses. Here, influence of localized compressive stresses is significant in earlier stages resulting crack initiation and generating damaged material in *compression zone*. This compression induced damage does not cause structural failure but results in

re-distribution of applied loading across central *tension zone*, resulting in reduction of load-displacement plot peak. On the other hand, tension induced damage initiated in later stages but it cause material damage at central portion of specimen with much higher rate comparatively which eventually dominates the structural failure of specimen i.e. fig. 2(j)-(l). Thus, it is clear that despite early beginning of damage due to shear in localized *compression zone*, central diametrical tensile loading is the primary cause of specimen's structural failure. Localized stresses near loading ends only assists diametrical tensile loading in specimen failure which certainly under-estimates material's actual tensile strength, justifying results from eq. 7.

Conclusion

From the above discussion two important conclusions can be made: First, the implemented cohesive joint model has naturally captured the crack initiation and propagation mechanism in disc sample. This proves its efficiency in realistic simulation of material response under given loading conditions. Secondly, load concentration in above specimen of Gosford sandstone (i.e. soft rock) due to experimental set up results in crack initiation at loading ends. Eventually, central diametrical tensile stresses in combination with shear in localized compression zones cause structural failure of specimen. Thus, computed strength in tension naturally under-estimates the actual tensile strength of material. Therefore, it would be convenient from here to question the Brazilian disc test feasibility. Further studies are still needed to quantify the results for more practical purposes.

Acknowledgements

The authors gratefully acknowledge the Australian Research Council and OZ Minerals Ltd for their financial support for this research through the Linkage Project LP150100539.

References

- [1] D. Li, L.N.Y. Wong, The brazilian disc test for rock mechanics applications: Review and new insights, *Rock Mech. Rock Eng.* 46 (2013) 269–287. doi:10.1007/s00603-012-0257-7.
- [2] F.L.L. Carneiro, A new method to determine the tensile strength of concrete, *Proc. 5th Meet. Brazilian Assoc. Tech. Rules (“Associaçãõ Bras. Normas Técnicas—ABNT”)*. 3d. Sectio (1943).
- [3] Z.T. Bieniawski, I. Hawkes, Suggested Methods For Determining Tensile Strength of Rock Materials, *Int. Soc. Rock Mech. Comm. Stand. Lab. F. Tests.* 15 (1978) 99–103. doi:10.1016/0148-9062(78)90003-7.
- [4] C. Fairhurst, On the validity of the “Brazilian” test for brittle materials, *Int. J. Rock Mech. Min. Sci. Geomech. Abstr.* 1 (1964) 535–546. doi:10.1016/0148-9062(64)90060-9.
- [5] P.S.B. Colback, An analysis of brittle fracture initiation and propagation in the Brazilian test, *1st ISRM Congr.* (1966) 385–391. <http://www.onepetro.org/mslib/servlet/onepetropreview?id=ISRM-1CONGRESS-1966-066>.
- [6] J.A. Hudson, E.T. Brown, F. Rummel, The controlled failure of rock discs and rings loaded in diametral compression, *Int. J. Rock Mech. Min. Sci.* 9 (1972) 241–248. doi:10.1016/0148-9062(72)90025-3.
- [7] J.C. Jaeger, Failure of Rocks Under Tensile Conditions, *Int. J. Rock Mech. Min. Sci.* 4 (1967) 219–227. doi:http://dx.doi.org/10.1016/0148-9062(67)90046-0.
- [8] T. Yanagidani, O. Sano, M. Terada, I. Ito, The observation of cracks propagating in diametrically-compressed rock discs, *Int. J. Rock Mech. Min. Sci.* 15 (1978) 225–235. doi:10.1016/0148-9062(78)90955-5.
- [9] M. Mellor, I. Hawkes, Measurement of tensile strength by diametral compression of discs and annuli, *Eng. Geol.* 5 (1971) 173–225. doi:10.1016/0013-7952(71)90001-9.
- [10] Q.Z. Wang, X.M. Jia, S.Q. Kou, Z.X. Zhang, P.A. Lindqvist, The flattened Brazilian disc

- specimen used for testing elastic modulus, tensile strength and fracture toughness of brittle rocks: Analytical and numerical results, *Int. J. Rock Mech. Min. Sci.* 41 (2004) 245–253. doi:10.1016/S1365-1609(03)00093-5.
- [11] Y. Yu, J. Zhang, J. Zhang, A modified Brazilian disk tension test, *Int. J. Rock Mech. Min. Sci.* 46 (2009) 421–425. doi:10.1016/j.ijrmms.2008.04.008.
- [12] Y. Yu, J. Yin, Z. Zhong, Shape effects in the Brazilian tensile strength test and a 3D FEM correction, *Int. J. Rock Mech. Min. Sci.* 43 (2006) 623–627. doi:10.1016/j.ijrmms.2005.09.005.
- [13] B. van de Steen, A. Vervoort, J.A.L. Napier, Observed and simulated fracture pattern in diametrically loaded discs of rock material, *Int. J. Fract.* 131 (2005) 35–52. doi:10.1007/s10704-004-3177-z.
- [14] Itasca Consulting Group Inc., 3DEC-3 Distinct Element Code, (2013).
- [15] R. Verma, G. Nguyen, M. Karakus, A. Taheri, H. Bui, A 3D Dis-continuum Approach to Fracture Initiation and Propagation in Hard Rocks, *Rock Mech. Rock Eng.* (2018), to be submitted.
- [16] Y. Gui, H.H. Bui, J. Kodikara, An application of a cohesive fracture model combining compression, tension and shear in soft rocks, *Comput. Geotech.* 66 (2015) 142–157. doi:10.1016/j.compgeo.2015.01.018.